Ph. D Thesis

Spatially Adaptive Image Denoising Techniques Using Directionlets

Submitted to the

Cochin University of Science and Technology

in partial fulfillment of the requirements for the award of the degree of

Doctor of Philosophy

in the Faculty of Technology

By
Sethunadh R

Under the guidance of
Dr. Tessamma Thomas

DEPARTMENT OF ELECTRONICS
COCHIN UNIVERSITY OF SCIENCE AND TECHNOLOGY
KOCHI, KERALA, INDIA-682022

August 2014

Image Processing

Spatially Adaptive Image Denoising Techniques Using Directionlets

Ph. D Thesis in the field of Image Processing

Author

Sethunadh R
Research scholar
Department of Electronics
Cochin University of Science and Technology
Kochi-682022
Kerala, India
email:r_sethunadh@vssc.gov.in

Research Advisor

Dr. Tessamma Thomas
Professor
Department of Electronics
Cochin University of Science and Technology
Kochi-682022
Kerala, India
email:tess@cusat.ac.in

Audio and Image Research Lab
Department of Electronics
Cochin University of Science and Technology
Kochi, 682022, India
www.doe.cusat.edu

August 2014

Cover: Global Coverage by Satellite image of Osceansat-2, ISRO

Dedicated to my Parents and Teachers

DEPARTMENT OF ELECTRONICS
COCHIN UNIVERSITY OF SCIENCE AND TECHNOLOGY
COCHIN-22

Certificate

This is to certify that this thesis entitled '**Spatially Adaptive Image Denoising Techniques Using Directionlets'** is a bonafide record of the research work carried out by **Mr. Sethunadh R** under my supervision in the Department of Electronics, Cochin University of Science and Technology. The results presented in this thesis or parts of it have not been presented for the award of any other degree.

Cochin-22
18-08-2014

Prof.(Dr.) Tessamma Thomas
(Supervising guide)
Department of Electronics
Cochin University of Science and Technology
Cochin 682022

Declaration

I hereby declare that this thesis entitled '**Spatially Adaptive Image Denoising Techniques Using Directionlets**' is based on the original research work carried out by me under the supervision of **Dr. Tessamma Thomas** in the Department of Electronics, Cochin university of Science and Technology. The results presented in this thesis or parts of it have not been presented for the award of any other degree.

Cochin-22
18-08-2014

Sethunadh R
Research Fellow
Cochin University of Science & Technology
Cochin 682022

ACKNOWLEDGEMENT

Preface

Digital imaging has found multifaceted applications in our day to day life. Revolutionary changes have been brought to the arena of digital photography by the integration of digital cameras into mobile phones and other personal gadgets. Satellite imaging based on Synthetic Aperture Radar (SAR) which can operate day and night under all weather conditions is another thrust area that has wide range of applications like homeland security, environmental protection, biomass estimation, traffic monitoring, 3-D map generation, land resource management etc. Unfortunately, many a time these images do not serve the purpose to the required level of satisfaction due to the undesirable coexistence of an extraneous entity called noise. So denoising, or in a more confined sense for SAR images, despeckling is an important pre-processing step in any image processing application to have an application friendly image.

Image denoising imposes a compromise between noise reduction and preservation of significant image details. To achieve a good performance in this respect, a denoising algorithm has to adapt to image discontinuities. Geometrical features in images, like edges and contours, play one of the most important roles in the human visual system, since they carry most of the perceptual information. Even though Wavelet Transform (WT) was established as a landmark of multi resolution analysis, it can only effectively capture point singularities and cannot capture the 1-D discontinuities like edges and contours in natural images, resulting in an inefficient sparse representation. This is due to the spatial isotropy of 2-D WT and its construction only along vertical and horizontal directions. Owing to the fact that multi-scale transforms with directivity provide image representations of high-energy concentration, the image denoising methods based on these transforms generally outperform 2-D WT based methods. Recently many directional transforms viz. Contourlet, Curvelet, Shearlet, Bandlet etc were introduced for image representation. However, most of these transforms often require oversampling, have higher computational complexity when compared to the standard 2D-WT, and require non-separable convolution and filter design. Also in some of these schemes the transform directions are not adaptive to the dominant

directions and filtering is done in continuous domain making it difficult to use them on discrete images.

The directionlet transform is one among these directional transforms which was proposed as an anisotropic, perfect reconstruction and critically sampled basis functions with directional vanishing moments along any two directions. It retains the computational efficiency and the simplicity of 1-D processing and filter design of the standard separable 2-D WT. It has good approximation properties as compared to the approximation achieved by other over complete transform constructions and is superior to the performance of the standard separable 2-D WT while having similar complexity. Thus image denoising schemes based on directionlet transform can perform better in terms of preserving image features and computational efficiency. This thesis is about image denoising schemes based on directionlet transform.

The main objectives covered in this thesis are:-

1. To develop efficient denoising algorithms for images corrupted with Gaussian noise, to effectively retain the significant features in images and thereby providing better visual qualities along with good performance metrics.

2. To develop efficient despeckling algorithms for SAR images in directionlet domain, which perform equally well both in homogeneous and heterogeneous areas.

Both the above objectives are thoroughly studied. Different denoising and despeckling algorithms are developed as a result of the study. All these schemes suitably adjust the transform directions based on local dominant directions of spatially segmented image and successfully capture the oriented features. These schemes are verified by testing them with original and synthetic images corrupted with noise.

Contents

Principal Symbols

F	:	Clean SAR image
G	:	SAR image with Speckle noise
V	:	Multiplicative speckle noise
$\check{F}$	:	Filtered SAR image (despeckled image)
f	:	Clean image
g	:	Digital Image with AWGN
v	:	AWGN
$\hat{f}$	:	Filtered Digital Image or Estimate of clean image
f_j	:	DT at level j of clean image
g_j	:	DT at level j of noisy image
v_j	:	DT at level j of noise
$\hat{f}_j$	:	DT at level j of estimate of clean image
W_{f_j}	:	WT at level j of clean image
$\boldsymbol{f_j}$	:	Inter and intra scale dependence vector of DT of clean image at level j
L	:	Number of looks in SAR image
$P_f(f)$	:	PDF of random variable f
$d_1 = \dfrac{a_1}{b_1}$	:	First direction of DT
$d_2 = \dfrac{a_2}{b_2}$	:	Second direction of DT
$\rho = n_1{:}n_2$	:	Anisotropic ratio
$H(Z_1)$	:	Filter
$j = 1, 2, ..J$	:	Number of DT levels
i	:	Segment number of segmented image
M_Λ	:	Generator Matrix
$N_s = p \times q$	:	Size of the image
p	:	Number of pixels in one vertical line of image
q	:	Number of pixels in one horizontal line of image
L_f	:	Length of the filter /Number of filter coefficients
(x, y)	:	Pixel position

μ	:	Mean
σ	:	Variance
σ^2	:	Standard Deviation
$\bar{s}(x, y)$	:	Strong point pixel value in SAR image
β	:	Edge correlation parameter
N_{ID}	:	Number of ideal edge pixels
N_{DE}	:	Number of default edge pixels
$\mathbb{Z}^2$	:	Discrete space
$L(r, n)$	:	Digital line
r	:	Slope of line
c	:	Intercept of line
k_1, k_2	:	Mondrian line directions
λ	:	GCV Threshold

Abbreviations

1D	:	1- Dimensional
2D	:	2- Dimensional
AWGN	:	Additive White Gaussian noise
AWT	:	Anisotropic Wavelet Transform
BLS-GSM	:	Bayesian Least Squares, Gaussian Scale Mixture (a denoising algorithm)
BM3D	:	Block Matching 3D filtering (a denoising algorithm)
CWT	:	Continuous Wavelet Transform
DCT	:	Discrete cosine Transform
DFT	:	Discrete Fourier Transform
DT	:	Directionlet Transform
DTCWT	:	Dual Tree Complex Wavelet Transform
DVM	:	Directional Vanishing Moment
DWT	:	Discrete Wavelet Transform
EPI	:	Edge Preservation Index
EPLL	:	Expected patch log-likelihood (a denoising algorithm)
ESI-H	:	Edge Save Index – Horizontal
ESI-V	:	Edge Save Index – Vertical
FOM	:	Figure of Merit
FSWT	:	Fully Separable Wavelet Transform
GCV	:	Generalized Cross Validation
GGD	:	Generalized Gaussian Distribution
GSM	:	Gaussian Scale Mixture
HMT	:	Hidden Markov Tree
i.i.d	:	independent identically distributed
KSVD	:	K-Singular Value Decomposition
MAD	:	Median Absolute Deviation
MAP	:	Maximum A Posteriori
MLE	:	Maximum Likelihood Estimation
MMSE	:	Minimum Mean Squared Error
MRA	:	Multi- Resolution Analysis

MRI	:	Magnetic Resonance Imaging
MRF	:	Markov Random Field
MSE	:	Mean Squared Error
MSSIM	:	Mean Structural Similarity Index
NL-means	:	Non-Local means (a denoising algorithm)
NLSC	:	Non-Local Sparse Coding (a denoising algorithm)
NSCT	:	Non-Sub sampled Contourlet Transform
OCV	:	Ordinary Cross Validation
pdf	:	probability density function
PSNR	:	Peak SNR
RMSE	:	Root Mean Squared Error
SAR	:	Synthetic Aperture Radar
SCR	:	Signal to Clutter Ratio
SNR	:	Signal to Noise Ratio
SSIM	:	Structural Similarity Index Matrix
SURE	:	Stein's Unbiased Risk Estimate
UDT	:	Undecimated Directionlet Transform

List of Figures

List of Tables

Chapter 1

Introduction

The chapter provides a brief overview of the image denoising and despeckling techniques. It gives an insight into the motivation behind the present research and its objectives. This is followed by a brief discussion of various state of the art innovations in image denoising and despeckling which are related to the present study. The chapter concludes with the summary of contributions of the thesis and its organization.

1.1 Introduction

The use of digital imaging in applications ranging from personal archival to remote sensing has now become widespread. One of the major problems regarding the use of these images is their corruption during acquisition and transmission phase. There are different types of noises which can affect digital images like Gaussian noise in digital cameras due to the discrete nature of light and thermal behaviour of camera sensor, multiplicative speckle noise in SAR and ultrasound medical images due to the coherent nature of the scattering phenomenon etc. The denoising of digital images corrupted by different types of noises is a well researched problem in image processing. Here the ultimate aim is to remove noise while preserving important signal features.

A number of denoising methods have been proposed in literature for removing various types of noises. These include linear and non-linear techniques. Noise having Gaussian-like distribution is very often encountered in real-world images. The zero mean property of the Gaussian distribution allows such noise to be removed by locally averaging pixel values. Conventional linear filters such as arithmetic mean filter and Gaussian filter smooth noises effectively but distort

edges and contours [1]. The Wiener filter is the mean square error-optimal stationary linear filter for images degraded by additive noise and blur. A common drawback of the practical use of this method is that they usually require some *a priori* knowledge about the spectra of noise and the original signal. Unfortunately, such information is very often not available. This makes the linear or spatial techniques less attractive for image denoising.

The effect of speckle in SAR images can be reduced either during the image formation time or later. The former method is based on multi-look incoherent averaging [2, 3], which improves the SAR image by averaging the uncorrelated images from non-overlapping spectrum at the cost of reduction in spatial resolution. The later method is based on image domain filtering like spatial filtering or transform-domain filtering. The spatial filtering schemes include Frost filter [4], Kuan Filter [5], Lee filter [6, 7], enhanced Lee filter [8] Gamma MAP filter [9, 10], Kalman filter [11] etc. These schemes use a defined filter window to estimate the local noise variance of the speckled image and perform individual unique filtering process. Even though these techniques, with low computational complexity, greatly reduce the speckle level in homogeneous areas they over smooth heterogeneous areas in the image due to losses at contours and edges in images.

Alternatively, non-linear methods were proposed for image denoising and despeckling. They are mostly based on multi-resolution analysis using wavelet transform [12, 13]. Separable two-dimensional (2-D) wavelets have been one of the major research tools for image representation over Fourier basis. Over the past two decades many image denoising and despeckling schemes based on Wavelet Transform (WT) were proposed. Comparative study between spatial and wavelet transform-domain filtering for SAR images show that the wavelet-based approach is among the best for noise removal [14, 15]. The WT based image denoising methods can be broadly classified into two: the threshold based methods and the statistical model based methods. In threshold based methods, a WT coefficient is compared with a given threshold and is set to zero if its magnitude is less than the threshold; otherwise it is kept unmodified or modified depending on hard or soft thresholding rules, respectively. These methods rely on the principle that the noise

will predominantly dominate the wavelet coefficients at finer scales and a few large coefficients only will represent the relevant information of the image. The effectiveness of these methods depends on the estimation of the correct threshold. Of the various thresholding strategies, soft-thresholding is the most popular one which was theoretically justified by Donoho and Johnstone [16, 17, 18]. The statistical model based denoising methods are mainly based on statistical modelling of WT coefficients with prior probability distribution functions [19]. The noise free coefficients are then estimated using this *a priori* information with Bayesian estimation techniques, such as the *maximum a posteriori* (MAP) estimator. Here the main problem is effectively modelling the image and noise coefficients. If these models are well chosen, the noise can be removed efficiently.

Despite the considerable success of WT based image analysis, intense research in the last few years have shown that WT based multi-resolution ideas are far from being universally effective. The 2-D wavelet functions are isotropic and have directional vanishing moments (DVMs) only along horizontal and vertical directions. Wavelets are the optimal bases for functions with point singularity like 1-D piecewise smooth signals, but they have serious limitations in dealing with high-dimensional signals like images as it cannot utilize the advantages of geometrical features present in images. It means that the WT is unsuited to exploit the correlation along edges and contours in images and has limited directional selectivity. Thus WT decomposition cannot produce an optimal sparse representation of images. This limits the performance of wavelet-based denoising algorithms, particularly in preserving sharp edge features. Therefore the requirement of a more effective transform with spatially anisotropic basis functions and multi-directional vanishing moments for real-world images was felt to properly capture the geometrical coherence of edges and contours present in them. Towards this end various multi-scale transforms with directional selectivity were developed over the past decade for image representations. Some of the examples are curvelet [20], contourlet [21], directional filter banks [22], wedgelets [23, 24], Dual Tree Complex WT (DTCWT) [25], orientation adaptive WT [26], directional lifting WT [27-28], Shearlet [29-31], curved wavelets [32], bandelets [33-35], directionlets [36-37], etc. However, most of these directional transforms often require oversampling, have higher computational complexity when compared to the

standard discrete WT, and require non-separable convolution and filter design. Also in some of these schemes the transform directions are not adaptive to the local dominant directions in images and filtering is done in continuous domain making it difficult to use them on discrete images.

Denoising schemes based on some of these transforms like curvelet, contourlet, DTCWT etc are already available in literature. The wedge shaped basis functions of curvelet and contourlet transforms provide good sparse representations for high dimensional singularities and thereby better denoising performance. However the sub sampling operations involved in the multi-scale partition and directional filter processing of these transforms causes pseudo-Gibbs phenomenon and lack of shift invariance which will adversely affect the denoising performance. Also they have much higher computational complexity as compared to separable 2-D WT. The DTCWT exhibits approximate shift invariant property and better directional selectivity in multiple directions with reduced computational complexity. It is an over complete wavelet transform, which is implemented by two wavelet filter banks operating in parallel. The performance gains provided by the DTCWT come from designing the filters in the two filter banks appropriately. The DTCWT of a 2-D image results in an approximation subband and six directional subbands at each level, which are strongly oriented at angles of $\pm15°$, $\pm45°$ and $\pm75°$. However the DTCWT is not adaptive to the local dominant directions in the image resulting in an inefficient sparse representation.

The directional WT and curved WT are based on directional lifting and keep the down sampling pattern same as that of standard WT, i.e., vertical down sampling followed by horizontal down sampling or vice-versa, and vary the filtering direction locally. However, due to the possible mismatch between the down sampling and the filtering directions, these transforms may suffer from aliasing. On the other hand, orientation adaptive WT and directionlets apply both filtering and down sampling along the dominant directions. The orientation adaptive WT allows filtering and down sampling along any two arbitrary directions using an invertible re-sampling involving interpolation of pixels at arbitrary locations, whereas, directionlets allow filtering and down sampling along any two arbitrary rational directions by applying 1-D WT along the lines defined on integer lattices without

any interpolation. Both these conceptually similar methods apply spatially varying re-sampling followed by separable filtering, and hence, are forced to process on segmented image [38]. Recent works on directionlets focus on its application in solving different image processing problems like super resolution [39], fusion [40], enhancement [41] etc.

1.2 Motivation & Objectives

Image denoising imposes a compromise between noise reduction and preserving significant image details. To achieve a good performance in this respect, a denoising algorithm has to adapt to image discontinuities. Geometrical features in images, like edges and contours, play one of the most important roles in the human visual system, since they carry most of the perceptual information. An efficient image representation has to be capable of precise modelling and of providing a sparse description of this geometrical information. Recently many multi resolution schemes for image decompositions with better directional properties have been presented by many authors. Since these transforms provide image representations of high-energy concentration, the image denoising methods based on these transforms generally outperform DWT based ones.

Directionlet Transform (DT) is one such representation which has gained popularity over the last few years as an anisotropic, perfect reconstruction and critically sampled basis function with directional vanishing moments along any two directions. It retains the computational efficiency and the simplicity of 1-D processing and filter design of the standard separable 2-D WT. It has good approximation properties as compared to the approximation achieved by other over complete transform constructions and is superior to the performance of the standard separable 2-D WT while having similar complexity. This has motivated us to design denoising algorithms based on Directionlet transform.

The performance of denoising schemes based on thresholding depends on the estimation of the correct threshold. There are different methods available for computing a proper threshold. However in most of these methods, the knowledge of noise variance is must for computing the threshold. Unfortunately this is not

available in most of the practical cases. The Generalised Cross Validation (GCV) based threshold computation can avoid this limitation. Thus here despeckling algorithms based on GCV threshold are developed in directionlet domain.

The effective modelling of the statistics of signal and noise plays a major role in the performance of statistical model based denoising schemes. If these models are well chosen, the noise can be efficiently removed. In literature several models have been considered for the noise-free wavelet coefficients and Gaussian model for the noise coefficients. In most of these models the WT coefficients are assumed to be independent. However it was well established that there are inter and intra scale statistical dependency in wavelet coefficients of natural images because if a WT coefficient has small magnitude the adjacent coefficients are very likely to be small, and the small coefficients tend to propagate across the scales [18]. Thus the models which consider the WT coefficient as independent cannot efficiently model the transform coefficients of natural images and thus may not provide good denoising performance. The performance of denoising schemes based on multi-resolution analysis would be significantly improved if the multi-scale correlation among the transform coefficients is also taken into account. Theoretically this is true for any transform with multi resolution representation for images. This has motivated us to investigate the interscale and intrascale dependency of DT coefficients across different levels and to develop image denoising schemes based on this dependency.

The main objectives covered in this thesis are:-

1. To develop efficient denoising algorithms for images corrupted with Gaussian noise, to effectively retain the significant features in images and thereby providing better visual qualities along with good performance metrics.

2. To develop efficient despeckling algorithms for SAR images in directionlet domain, which perform equally well both in homogeneous and heterogeneous areas.

1.3 Related Work

In this section a brief description of famous and efficient state of the art denoising and despeckling schemes in transform domain is given. These schemes are used for comparing the presented schemes in this thesis mainly because of three reasons. The first and foremost reason is their state of the art competitive performance. The second reason is that these schemes are some way related to the presented schemes in this thesis and the final one is the availability of their results for comparison.

Denoising of images corrupted with Gaussian noise using wavelet based thresholding is very popular. There are ample of literature available on finding out an effective threshold. Of the various thresholding strategies, soft-thresholding is the most popular and has been theoretically justified by Donoho and Johnstone [20]. For denoising applications with known noisy function, it is often ideal to search for the optimal minimum mean-square error risk estimate using *a priori* information. Thus Donoho and Johnstone proposed an optimal threshold value by minimizing Stein's unbiased risk estimator (SURE) [42]. The Bayesian threshold proposed by Chang et al [43] is based on an empirical observation in which the wavelet coefficients in each subband are modelled as independent and identically distributed random variables with Generalised Gaussian Distribution (GGD). Later they have presented batter results with the same scheme with context modelling of the wavelet transform coefficients for variance estimation [44]. The denoising based on generalised cross validation (GCV) based thresholding in wavelet domain proposed by M. Jansen et al [45] also provided promising results. These schemes are still considered as the best schemes in threshold based denoising schemes in wavelet domain.

There are efficient denoising schemes available in literature which considers the dependency of the transform coefficients across scales. Chen et al [46-47] have proposed methods which take into account the intra scale dependency of the WT coefficients for image denoising. Crouse et al. [48] developed a framework for statistical signal processing based on Hidden Markov Models (HMM), where the interscale dependency of WT coefficients was exploited to find out an effective threshold. Sendur et al [49] developed a subband adaptive bivariate shrinkage function for image denoising in the wavelet domain based on the parent

coefficients. Later they published better results using the same bivariate shrinkage function with local variance estimation [50]. Luisier et al [51] proposed an image denoising algorithm using a point wise threshold based on SURE that takes into account interscale dependencies of oriented pyramid coefficients. These schemes are considered as the state of the art schemes in interscale dependency model based denoising.

There are efficient denoising schemes available in literature which make use of various directional transforms like curvelets [20], contourlets [21], Dual Tree Complex WT (DTCWT) [25], shearlet [29], steerable pyramids [52], etc. As compared to the regular 2-D separable wavelet transform, these tailored, multi-scale and directional redundant transforms can more effectively capture edge structures, therefore the representation coefficients are sparser, and thus provide a better denoising performance in terms of edge and feature enhancement. Sendur et al [50] presented a denoising scheme based on DTCWT using a bivariate shrinkage function and reported good results. Here the performance improvement was mainly due to the use of DTCWT and incorporation of a local variance parameter in the shrinkage function. The scheme proposed by G. Chen et al. [53] exploits the statistical dependency between a complex wavelet coefficient and its parent and children across three scales in the thresholding process. A denoising scheme based on steerable pyramids was proposed by Portilla et al. [54], in which they modelled the neighbourhoods of WT coefficients at adjacent positions and scales based on a Gaussian Scale Mixture (GSM) and estimated the noise free transform coefficients using Bayes least squares (BLS) estimator. Their denoising method is known as BLS-GSM scheme. Furthermore, threshold based denoising schemes in curvelet domain [55], contourlet domain [56-57] and shearlet domain [58] were reported by some authors. A denoising algorithm in directionlet domain was proposed by V. Velisavljević [37], which is a combination of smooth denoising and oriented denoising using GSM. Here the image was taken as a single unit and an isotropic transform was taken along some pre fixed directions. Due to these reasons, this scheme provided only comparable results with the BLS-GSM scheme, but with a lower computational complexity. The BLS-GSM scheme is still one among the best available denoising schemes and is the state of the art in transform domain denoising schemes.

Various despeckling schemes based on multi resolution analysis tools have been developed over the last few years. These schemes can be broadly classified as threshold based schemes and statistical model based schemes. In most of these schemes, to take advantage of the denoising algorithms already available for additive white Gaussian noise (AWGN), the multiplicative speckle noise is converted into additive one by a logarithmic transformation. The threshold based schemes compute a proper threshold mostly based on minimum mean square error criterion and applies this threshold to the transform coefficients using soft or hard thresholding strategy [15]. Most of the statistical model based schemes are based on the *maximum a posteriori* (MAP) probability criterion by modelling the transform coefficients using various probability distributions like the generalized Gaussian (GG) distribution [59-60], Laplacian distribution [61-63], Cauchy's distribution [64] etc. The MAP despeckling in the undecimated wavelet domain with GG distribution was proposed by F. Argenti et al. [59]. This method was later refined by the same authors [60] by classifying the wavelet coefficients according to their texture energy. One of the major drawbacks of GG-based MAP solutions is the numerical computation of the estimate of noise free coefficient, leading to a high computational cost. To overcome this issue, alternative models were considered. Motivated by the use of Laplacian–Gaussian (LG) assumption to derive MAP and minimum mean square error (MMSE) estimators for ultrasound despeckling [61], similar schemes were developed for SAR images also [63]. This has resulted in a reduction in computational cost by one order of magnitude with respect to the solution obtained numerically with the GG assumption, without significantly affecting the performance in terms of speckle reduction.

A spatially adaptive homomorphic despeckling scheme based on modelling of wavelet coefficients of the log-transformed reflectance using a Cauchy prior with a zero-valued location parameter was proposed by M. Bhuiyan et al. [64]. Here the spatial dependence of the wavelet coefficients was incorporated in the estimation process using a linear predictive model. This method using the minimum mean square absolute error (MMAE) estimator provides a better speckle reduction in homogeneous regions, while still preserving the edge and line structures well. A despeckling scheme based on modelling of DTCWT coefficients using a bivariate Cauchy *pdf* was proposed recently by J J Ranjani et al [65]. Here the significant

dependences of the wavelet coefficients across different scales were considered in the MAP estimation process. Mellin transform of two dependent random variables is utilized to estimate the dispersion parameter of the bivariate Cauchy *pdf* from the noisy observations. Later the same authors have proposed a DTCWT based despeckling algorithm using multivariate statistical theory [66]. The DTCWT coefficients in each subband are modelled with a multivariate Cauchy *pdf* which takes into account the statistical dependency between the wavelet coefficients, their neighbours and coefficients across scales.

SAR image despeckling using WT results in unexpected pseudo contours due to the fact that 2-D WT can only provide three directional subbands in a certain resolution. To overcome this issue despeckling schemes based on directional transforms have been introduced very recently. A simple curvelet based despeckling scheme proposed by Biao Hou et al [67] has provided very good results as compared to wavelet based schemes. A despeckling scheme by exploiting the multidirectional capabilities of non sub sampled contourlet transform (NSCT) was presented by F. Argenti et al. [68]. Here the noise–free NSCT coefficients are estimated from the observed ones according to either the MAP or the MMSE criterion. The main drawback here is that the computational complexity of this scheme is much higher due to the non separable filtering of NSCT. Similar to this scheme, a non-sub sampled shearlet transform (NSST) based adaptive despeckling scheme was proposed by Biao Hou et al.[69]. In this scheme the NSST coefficients in each subband are classified to identify the signal of interest. This scheme has provided reasonably good despeckling performance when compared to the WT and NSCT based methods while preserving details and texture information. An edge detection and despeckling algorithm in bandlet domain was proposed by Biao hou et al [70]. Later a similar scheme based on multi scale products of bandlet coefficients was proposed by W G Zhang et al. [71]. Here the edge is first detected and the edge removed image is used for despeckling. Finally the removed edge is added to preserve edges while despeckling. Both these schemes provided very good despeckling results while preserving the edges and contours well. These schemes are considered as the state of the despeckling schemes based on directional transforms.

1.4 Summary of contributions and publications

The main aim of image denoising is to remove noise while preserving the important signal features. The focus of this thesis is to develop directionally adaptive image denoising schemes which can preserve the important image features while diluting noise. This problem is referred here as spatially adaptive image denoising. Here the directionlet transform is used for decomposing the image into multi resolution levels. Such denoising schemes have wide applications in various fields. Common application areas are in SAR imaging, digital photography, medical imaging etc., where noise enters during acquisition or transmission of these images. In all these cases the preservation of image features while denoising is important. To take care of several such applications, here different image denoising schemes based on directionlet transform are presented. The contributions of the thesis are summarized here.

1.4.1 Denoising of images corrupted with Gaussian noise

Here four different denoising schemes for images corrupted with Gaussian noise are presented. Two of these schemes are threshold based ones and the other two are statistical model based ones. All these schemes are compared with the state of the art transform domain denoising schemes.

14.1.1 Subband adaptive denoising scheme based on SURE risk

A simple, threshold based subband adaptive denoising scheme in directionlet domain is presented here to establish the concept of denoising in directionlet domain. The image is first spatially segmented and for each spatial segment the directionlet transform was computed along six different directions. Then a directional map that provides the best match between the transform and locally dominant directions is generated by identifying the minimum energy in the high-pass subband. The decomposed images with directional energy are then used for the computation of scale dependent subband adaptive optimal threshold based on SURE risk. The threshold applied sub-bands with the unprocessed first sub-band (LLL) are given as input to the inverse directionlet algorithm for getting the

denoised image. Experimental results show that this method outperforms the standard wavelet-based denoising methods in terms of numeric and visual quality.

Published paper related to this work is given in '*List of Publications 1.6*'

1.4.1.2 Subband adaptive denoising scheme based on Bayes shrinkage

In the previous scheme the directional map is estimated by computing the directionlet transform along all the directions. This is time consuming especially when more directions are considered. To avoid this, here the directionality of the spatially segmented image is first computed using a parameter called *directional variance* for selecting the optimum pair of directions for decomposing the image. Due to this the DT needs to be computed along the dominant directions only, leading to a computationally efficient scheme. The decomposed images with directional energy are used for thresholding using sub band adaptive Bayesian threshold. The threshold corrected sub-bands with the unprocessed first sub-band are given as input to the inverse directionlet algorithm for getting the denoised image. Due to the processing in the directionlet domain the image features are concentrated on fewer coefficients so that more effective thresholding is possible. Experimental results show that this scheme outperforms the standard wavelet-based denoising methods in terms of perceptual and numerical estimates.

Published paper related to this work is given in '*List of Publications 1.3*'

1.4.1.3 Image denoising based on inter and intra scale dependency of Directionlet coefficients

Here a locally adaptive image denoising algorithm based on the dependences of the directionlet coefficients across different scales is proposed. The spatially segmented image is first decomposed along the local dominant directions using DT. The DT coefficients so obtained are then modelled using a modified bivariate function with a local variance parameter, which takes into account the inter and intra scale dependency of these coefficients. A nonlinear threshold function is derived from the modified bivariate models of the signal and noise employing a *maximum a posteriori* (MAP) estimator using Bayesian theory. The denoised image is obtained from the estimate of the noise free coefficients using directional information and inverse directionlet transform. Here it is established that, allowing

for spatial segmentation and choosing transform directions in each segment independently, directionlets outperform the other oriented transforms such as steerable pyramids and DTCWT in image denoising.

Published paper related to this work is given in '*List of Publications 1.1*'

1.4.1.4 Image denoising based on adaptive spatial segmentation and multi scale correlation

The main drawback with the DT based denoising schemes is the high computation cost. To make the previous method more computationally efficient, here two techniques are employed. One is the adaptive spatial segmentation based on the content directionality and the other one is the local variance parameter estimation based on classification of DT coefficients using context modelling. Also a simple bivariate model is used here to model the heavy-tail behaviour of natural images and the interscale properties of DT coefficients. In addition, the intrascale dependency of directionlets is also well exploited in the enhancement process due to the computation of local variance using classification of DT coefficients. The proposed algorithm is competitive with the existing transform based algorithms with better results in terms of output peak signal-to-noise ratio while having lower computational complexity. It exhibits good capability to preserve edges, contours and textures especially in images with abundant high frequency contents.

1.4.2 Despeckling of SAR images

Here six different despeckling schemes for SAR images are presented. Three of these schemes are threshold based ones and the other three are statistical model based ones. All these schemes are compared with the state of the art transform domain despeckling schemes.

1.4.2.1 SAR image despeckling based on GCV thresholding

The effectiveness of a despeckling algorithm basically depends on two factors: one is the efficient representation of the image to be despeckled using a directional and multi resolution expansion and the other is the efficient computation of an optimal threshold. Here the first requirement is met by using a locally adaptive directionlet

transform and the second by optimal scale dependent subband adaptive threshold computation using Generalized Cross Validation (GCV) technique. The GCV method doesn't require the knowledge of the noise variance as it is only based on the input data and its minimum is a good approximation for the optimal threshold. Here the directionlets are constructed adaptively so that the chosen directions are maximally aligned with locally dominant directions across image. Due to this the transform generates a sparser representation with a reduced energy in the high-pass subbands allowing for a more robust estimation of the noise free coefficients. Experimental results on simulated and actual SAR images show that minimizing GCV in the directionlet domain results in better despeckling performance when compared to minimizing it in the wavelet domain.

Published paper related to this work is given in '*List of Publications 1.7*'

1.4.2.2 SAR image despeckling based on Edge detection

Since geometrical features in images, like edges and contours carry most of the perceptual information, they play important roles in the human visual system. So retaining of this information is very important in despeckling. This scheme efficiently extracts edge information along dominant directions from the spatially segmented SAR image. Then an optimal scale dependent subband adaptive GCV threshold is applied to the edge removed image. The despeckled image is finally synthesized using the extracted edge information to preserve the sharpness of edges and the texture. The algorithm adapts the transform directions to dominant directions across the image domain and successfully captures oriented features. Due to this the transform generates sparser representation, allowing for more robust estimation of edge characteristics and optimal threshold for despeckling. This scheme outperforms the traditional despeckling schemes and the wavelet and bandlet based edge detection methods in terms of numeric and perceptual quality.

Published paper related to this work is given in '*List of Publications 1.5*'

1.4.2.3 SAR despeckling based on multiscale products thresholding

The performance of the despeckling schemes based on multi-resolution analysis would be significantly improved if the multiscale correlation among the transform

coefficients is taken into account. If a DT coefficient generated by a true signal has a large magnitude at a finer scale, its ascendants at coarser scales will probably be significant as well, while the magnitude of the noise coefficients may decay rapidly along the scales. Hence, the multiscale products at adjacent scales of DT would strengthen the significant features while diluting noise. This property of the DT is exploited here to strengthen significant signal features before computing the GCV threshold. The proposed scheme outperforms many of the traditional despeckling schemes in terms of speckle reduction and edge preservation.

Published paper related to this work is given in '*List of Publications 1.4*'

1.4.2.4 Despeckling based on Laplacian-Gaussian modelling

The generalized Gaussian shape parameters relative to the reflectivity and to the speckle noise in SAR images suggest that their distributions can be approximated as a Laplacian and a Gaussian function, respectively. Under these hypotheses, a nonlinear threshold function is derived from these models of the signal and noise, employing a *maximum a posteriori* (MAP) estimator using Bayesian theory. The algorithm adapts the transform directions to local dominant directions and thus efficiently captures the geometrical information present in images. This results in better sparsity which aids for efficient estimation of noise free coefficients. The despeckled image is obtained from the estimated noise free coefficients using directional information and inverse directionlet transform. The effectiveness of the proposed scheme is illustrated by comparing it with traditional and similar wavelet based schemes.

1.4.2.5 Despeckling based on Cauchy-Gaussian modelling

This scheme is conceptually similar to the earlier scheme. The main difference is that the impulsive heavy tailed behaviour of the log transformed high resolution SAR image is modelled here using a heavy tailed Cauchy distribution. The DT is first computed along the dominant directions of the spatially segmented image. The signal and the noise coefficients are then modelled using Cauchy-Gaussian bivariate distributions which take into account the statistical dependence between the adjacent scale coefficients. The nonlinear threshold functions derived from the

models employing a MAP estimator are then used for estimating the noise free coefficients. Since the directionlets possess spatial anisotropy and better directional capabilities, statistical interscale dependency modelling in directionlet domain results in visually appealing despeckling results, with improved performance parameters.

Published paper related to this work is given in '*List of Publications 2.1*'

1.4.2.6 SAR image despeckling based on bivariate shrinkage

Here a spatially adaptive despeckling algorithm for SAR images is presented, which takes into account the statistical interscale dependency of DT coefficients. The algorithm spatially adapts the transform directions to dominant directions across the image domain and successfully captures the oriented features. The interscale dependency of the DT coefficients is then modelled using a non-Gaussian bivariate distribution to effectively compute the noise free coefficients. Experimental results show that the proposed method achieves effective despeckling performance compared with other directional transform based despeckling schemes in terms of both subjective visual quality and details preservation.

Published paper related to this work is given in '*List of Publications 1.2*'

Altogether ten different denoising schemes have been developed within the frame work of directionlet transform and all these schemes were compared with the state of the art technologies available for standard benchmark images and original images corrupted with noise. It is well established that, allowing for spatial segmentation and choosing transform directions in each segment independently, directionlets outperform the standard 2D WT and other oriented transforms such as steerable pyramids, contourlet, shearlet, bandlet, DTCWT etc. in image denoising and despeckling.

This research has resulted so far in a publication of seven papers in international journals and one paper in an international conference proceeding. Most recent research results, presented in section 4.5 and 5.5, are submitted to two international journals.

1.5 Thesis Outline

The main goal of the thesis is to develop new image denoising and despeckling schemes capable of capturing geometrical features in images, based on multi directional anisotropic transform called directionlets. Here various image denoising and despeckling schemes in directionlet domain are presented. These schemes are broadly classified into two, viz. threshold based and statistical model based ones. The effectiveness of each of these schemes over the competing state of the art methods is illustrated. The thesis is organized into six chapters as below:-

Chapter 1: Introduction

The first chapter serves as a preamble to the work, which gives an insight into the motivation behind the present research and its objectives. It also describes the importance and relevance of this work in the area of image denoising and despeckling**.** A summary of contributions and publications are also highlighted here.

Chapter 2: Image denoising

This chapter presents the different types of noises which are common in digital images and SAR images. The evolution of different image denoising and despeckling schemes are also highlighted here, giving special emphasis on different types of spatial and transform domain schemes. In the transform domain methods, the threshold and statistical model based schemes are described. The state of the art methods in each area are also highlighted along with the pros and cons of each of these schemes. At the end various measures of image denoising performance are also explained.

Chapter 3: Directionlet Transform

In the beginning of this chapter the background knowledge on wavelet theory is reviewed. The requirement of a multi resolution anisotropic transform with directional vanishing moments along multiple directions is then analysed. This follows the directionlet theory and construction of directionlet transform. The sparsity due to the anisotropy and any direction nature of directionlet is also illustrated. Then the polyphase representation of directionlet transform is

presented. Finally an analysis on the computational complexity of directionlet transform as compared to wavelet transform and other directional transforms is presented.

Chapter 4: Spatially adaptive image denoising techniques

In this chapter the main contributions of the thesis to image denoising are presented. Here four different denoising schemes in the directionlet domain, for images corrupted with additive white Gaussian noise are presented and the results are compared with the state of the art technologies. The computational complexity of these schemes is also analysed here.

Chapter 5: Spatially adaptive SAR image despeckling techniques

This chapter presents the main contributions of the thesis to SAR image despeckling. Here six different despeckling schemes in directionlet domain are presented, which include threshold based and statistical model based schemes. These schemes are compared with the state of the art technologies available for standard benchmark images corrupted with noise and also original SAR images. The comparison is made in terms of speckle reduction, edge and feature preservation and computational efficiency.

Chapter 6: Conclusions and future perspectives

In this concluding chapter the whole work is summarised and a thought for the scope of further research in the area of image denoising is presented.

The remaining portions of the thesis include the bibliography followed by a list of publications by the author in the related field.

Chapter 2

Image Denoising

This chapter presents the different types of noises which are common in digital images and SAR images. The evolution of different image denoising and despeckling schemes are also highlighted here, giving special emphasis on spatial and transform domain techniques. In the transform domain methods, the threshold and statistical model based schemes are described. The state of the art methods in each area are also highlighted along with the pros and cons of each of these schemes. At the end, various measures of image denoising performance are also explained.

2.1 Introduction

Image denoising refers to the recovery of a digital image that has been contaminated by noise. The presence of noise in images is unavoidable. It may be introduced during image formation, recording or transmission phase. Further processing of the image often requires that the noise must be removed or at least reduced. Even a small amount of noise is harmful when high accuracy is required. The noise can be of different types. The most popular ones are additive white Gaussian noise (AWGN), speckle noise, impulse noise, Poisson noise etc. Mathematically the degradation process can be denoted as $G = F \& V$. Here F is the clean image, G the noisy image and V, the noise. $'\&'$ is a mathematical operation which can be additive or multiplicative depending upon the type of noise. An image denoising algorithm attempts to obtain the best estimate of F from G. The optimization criterion can be mean squared error (MSE)-based one or perceptual quality driven.

This chapter is subdivided into three sections. In the first section, different types of noises which are encountered in digital images and SAR images are explained. In the second section the evolution of image denoising and despeckling over the years and the recent advances in this area are presented. In the last section the different metric parameters which are used for assessing the performance of different denoising and despeckling algorithms are explained.

2.2 Sources and Types of Noises

During any physical measurement, it is likely that the measured quantity is corrupted by some amount of noise. The sources and types of this noise are depending upon the physical measurement. Noise often comes from a source that is different from the one to be measured, but sometimes it is due to the measurement process itself. In case of images, the example of former one is read-out noise in digital cameras and later one is speckle noise in SAR images. Sometimes, noise might be due to the mathematical manipulation of a signal, as is the case in image de-convolution or image compression. Often, a measurement is corrupted by several sources of noise and it is usually difficult to fully characterize all of them. In all these cases, noise is the undesirable part of the image. Ideally, one seeks to reduce noise by manipulating the image acquisition process, but when such a manipulation is impossible, denoising algorithms become mandatory.

The characteristics of noise mainly depend on the image acquisition process. This include digital and analog cameras of various kinds for visible or infra-red light, radar imagery such as Synthetic Aperture Radar (SAR), Magnetic Resonance Imaging (MRI), Computer Tomography (CT), Positron Emission Tomography (PET), ultra-sonography, electron microscopy etc. Here we concentrate mainly on two types of images viz. SAR images and images from digital and analog cameras.

2.2.1 Noise in Camera Imaging

Images taken with both digital cameras and conventional film cameras will pick up noise from a variety of sources. The types of noise possibly corrupting images are too numerous to list here. The Gaussian noise [72] and the salt and pepper noise are the two most common noises in this category. In either case, the noise at different

pixels can be either correlated or uncorrelated. In many cases, noise values at different pixels are modelled as being independent and identically distributed, and hence uncorrelated. The most common noises affecting the digital images are described here.

2.2.1.1 Additive White Gaussian Noise

In image denoising, the most common setting is to use black-and-white images corrupted with Additive White Gaussian Noise (AWGN). The images with AWGN are used as the benchmark images for assessing the performance of image denoising algorithms. Gaussian noise is a statistical noise that has a probability density function (*pdf*) of the normal distribution (also known as Gaussian distribution). For each pixel, a random value drawn from a normal distribution is added to the clean pixel value. The distribution is the same for every pixel (i.e. the mean and variance are the same) and the noise samples are drawn independently of each other. The read-out or amplifier noise of digital cameras is often approximately AWGN. In case of Gaussian noise, an amount of noise is added to every part of the picture i.e., each pixel in the image will be changed from its original value by a small amount. Gaussian noise is the most common noise and can be produced by the thermal agitation of charged carriers (usually the electrons) inside an electrical conductor. It is properly defined as the noise with a Gaussian amplitude distribution with a bell-shaped probability density function, known as the Gaussian function or informally as the bell curve [73] shown in figure 2.1. This is defined as:

$$P_f(f) = \frac{1}{\sigma\sqrt{2\pi}} \; e^{-\frac{1}{2}\left(\frac{f-\mu}{\sigma}\right)^2} \qquad\qquad (2.1)$$

The parameter μ is the mean or expectation (location of the peak) and σ^2 is the variance. σ is known as the standard deviation. The distribution with $\mu = 0$ and $\sigma^2 = 1$ is called the standard normal distribution or the unit normal distribution. A normal distribution is often used as a first approximation to describe real-valued random variables that cluster around a single mean value. The normal distribution is considered the most prominent probability distribution in statistics. There are

several reasons for this: First, the normal distribution arises from the central limit theorem, which states that under mild conditions, the mean of a large number of random variables independently drawn from the same distribution is distributed approximately normally, irrespective of the form of the original distribution. Secondly, the normal distribution is very tractable analytically, that is, a large number of results involving this distribution can be derived in explicit form.
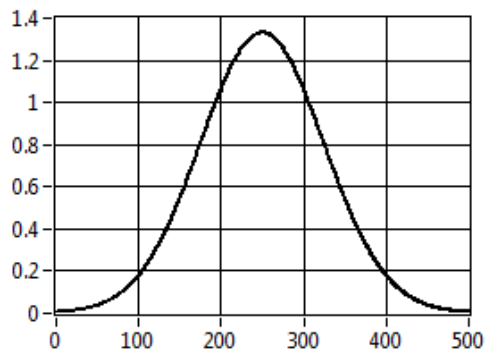
Figure 2.1. The bell curve of Gaussian distribution

2.2.1.2 Salt-and-pepper noise

Salt-and-pepper noise is having a fat-tail distribution. It is also known as impulsive noise or spike noise [72]. This noise is normally generated due to the loss of pixels during transmission. Here the pixels in the image are very different in colour or intensity from their surrounding pixels. This will appear as dark and white dots in images. Generally this type of noise will only affect a small number of image pixels. It is a type of noise where the image contains a certain percentage of noisy pixels, where the noisy pixels are randomly either completely dark (pixel value zero) or saturated (highest possible pixel value). The value of the noisy pixels is therefore completely uncorrelated with the value of the same pixels in the clean image. Typical sources include flecks of dust inside the camera, overheated or faulty CCD elements, analog-to-digital converter errors etc. Salt-and-pepper noise can also arise due to errors during transmission of an image like bit errors in transmission. Denoising schemes based on median filtering are usually effective on this kind of noise.

2.2.1.3 Photon Shot Noise

The dominant noise in the lighter parts of an image from an image sensor is typically that caused by statistical quantum fluctuations, that is, variation in the number of photons sensed at a given exposure level. This noise is known as photon shot noise [74]. Shot noise has a root-mean-square value proportional to the square root of the image intensity, and the noises at different pixels are independent of one another. Shot noise follows a Poisson distribution, which is usually not very different from Gaussian. When the mean is high the Poisson distribution looks similar to a Gaussian distribution with equal mean and variance. In that setting, removing Poisson noise is similar to removing Gaussian noise, where each pixel has a variance which depends on the pixel value of the underlying clean image. For lower mean values, the two distributions do not look similar. Due to the advancements in technology the pixel size of image sensors is getting smaller resulting in decrease in number of photons captured per pixel. Hence, photon shot noise is becoming a major issue in modern imaging systems.

In addition to photon shot noise, there can be additional shot noise from the dark leakage current in the image sensor; this noise is sometimes known as dark-current shot noise. The dark current is normally highest at hot pixels within the image sensor. This variation in dark current of normal and hot pixels can be subtracted off (using dark frame subtraction), leaving only the shot noise of the leakage. If dark-frame subtraction is not done, or if the exposure time is long enough that the hot pixel charge exceeds the linear charge capacity, the noise will appear as salt-and-pepper noise.

2.2.1.3 Thermal Noise

Thermal noise arises due to the thermal energy of a chip. The thermally generated electrons accumulate in the chip are indistinguishable from photoelectrons resulting in noise. Thermal noise occurs even in the absence of light and is therefore sometimes referred to as dark-current noise. This type of noise is strongly dependent on the temperate of the sensor, but also on exposure time as well as the ISO setting of the camera. Each pixel can be approximately modelled as Gaussian. Thermal noise is an example of noise which can be reduced by modifying the

signal acquisition process. One of the most common ways for reducing thermal noise is the cooling of the camera sensor.

2.2.1.4 Compression Artefacts

Digital images are usually stored in a compressed format such as JPEG. The compression algorithm gives rise to artefacts, which is considered as a type of noise. For example the JPEG algorithm, which is the most commonly used compression algorithm, causes blocking artefacts in the compressed image. This type of noise is non-linearly related to the clean image.

2.2.2 Noise in SAR Imaging

SAR imaging uses a coherent imaging process, which results in a multiplicative noise called speckle noise. It is caused by constructive and destructive interference of coherent waves reflected by the many elementary scatterers contained within the imaged resolution cell. For distributed targets, the signal received by the radar is a superposition of many small reflections. Here it is assumed that in each resolution cell no single scatterer dominates over all others combined and the number of scatterers is large and the scatterers are statistically identical and independent. Moreover to have different phases for the scatterers, the maximum range extent of the target shall be many wavelengths across. The vector sum of the backscattered electric field is equivalent to a 2-D random walk process with independently and identically Gaussian distributed real and imaginary components [75].

2.2.2.1 Speckle Noise and its Characterisation

It was established that the speckle noise can be characterized as a random variable using a statistical model [75-76]. As explained earlier, since the SAR images are formed by coherent imaging process they are affected by speckle noise. The undesirable effects of speckle in a SAR image can be easily reduced during the image formation phase itself through multi look averaging. The obvious disadvantage of such an approach is the loss in spatial resolution. The statistical distribution of the resultant speckle in the degraded-resolution image is given by the Gamma distribution in the case of intensity data, and by the multi convolution of the Rayleigh probability density in the case of amplitude data.

Speckle in SAR images is generally modeled as multiplicative random noise, whereas most available filtering algorithms were developed for additive white Gaussian noise (AWGN) in the context of image denoising and restoration, as additive noise is most common in imaging and sensing systems. To take advantage of the available noise models it is necessary to apply a logarithmic transform to convert the multiplicative noise model into an additive one in most cases. As a nonlinear operation, the logarithmic transform totally changes the statistics of SAR images, and thus the original speckle statistics cannot be directly used to the log-transformed images. Prior to the subsequent analysis and processing, several factors need to be considered, such as the change in probability density function (*pdf*) of the log-transformed random variable, the new statistical characteristics of the transformed data etc. SAR images are usually available in two formats: intensity format and amplitude format. The characteristics of the SAR images in these formats have been studied by many authors [77-79] and these models have been widely used in the processing of SAR images. A review of the statistical characteristics of speckle in amplitude and intensity formats and the derivation of its *pdf*, mean values, and variances is given here.

2.2.2.1.1 SAR Image in Intensity Format

If we use G to denote the image intensity that the SAR measures for a given pixel whose backscattering coefficient is F, and assume that the SAR image represents an average of L looks (independent samples or pixels), then G is related to F by the following multiplicative model [76]

$$G = FV \tag{2.2}$$

where V is the normalized fading random variable in the intensity image, following a Gamma distribution with unit mean and variance $1/L$. The *pdf* of V is given by

$$P_V(V) = \frac{L^L V^{L-1} e^{-LV}}{\Gamma(\mathrm{L})}, \quad V \geq 0, \qquad L \geq 0 \tag{2.3}$$

where $\Gamma(\cdot)$ denotes the gamma function.

The natural logarithmic transformation converts (2.2) into

$$g = f + v \tag{2.4}$$

where $g = \ln(G), f = \ln(F)$ and $v = \ln(V)$. Given that the logarithmic function is monotonic, the *pdf* of the random variable v can be obtained from

$$p_v(v) = p_v(e^v)e^v \tag{2.5}$$

which leads to

$$p_v(v) = \frac{L^L e^{vL} e^{-Le^v}}{\Gamma(L)} \tag{2.6}$$

and the mean of v is given by

$$E(v) = \psi(L) - \ln(L) \tag{2.7}$$

where $\psi(\cdot)$ is the Digamma function [80] defined as

$$\psi(x) = \frac{d}{dx}\ln\Gamma(x) \tag{2.8}$$

When L is an integer, the equation (2.7) can further be simplified as

$$E(v) = \sum_{m=1}^{L-1} \frac{1}{m} + \psi(1) - \ln(L), \quad \psi(1) = -C \tag{2.9}$$

where C is Euler's constant ($C = 0.577215$).

The new variance is given by

$$var\,(v) = \psi(1, L) \tag{2.10}$$

where $\psi(1, L)$ is known as the first-order Polygamma function of L. A general n^{th} Poly gamma function is defined as the nth derivative of the Digamma function [80]

$$\psi(n, x) = \frac{d^n}{dx^n}\,\psi(x) = \frac{d^{n+1}}{dx^{n+1}}\ln\Gamma(x) \tag{2.11}$$

$$var\,(v) = \psi(1,1) - \sum_{m=1}^{L-1} \frac{1}{m^2}, \qquad \psi(1,1) = \frac{\pi^2}{6} \tag{2.12}$$

2.2.2.1.2 SAR Image in Amplitude Format

For an amplitude image, the multiplicative model $G = FV$ still holds, where F is the speckle-free value of the magnitude of the electric field of the backscattered signal and G is the voltage measured when a linear detector is used. For a single-look image, the normalized fading random variable V obeys the Rayleigh *pdf* [76], which can be written as

$$p_V(V) = \frac{\pi V}{2} e^{-\frac{\pi V^2}{4}}, \qquad V \geq 0, \qquad L = 1 \qquad (2.13)$$

Its mean and variance are

$$E(V) = 1, \qquad var(V) = \frac{4}{\pi} - 1 \qquad (2.14)$$

After the logarithmic transform, the *pdf* of the random variable $v = \ln(V)$ becomes

$$p_v(v) = \frac{\pi e^{2v}}{2} e^{-\frac{\pi e^{2v}}{4}}, \qquad L = 1 \qquad (2.15)$$

The density function defined in (2.15) is called the double exponential or Fisher-Tippet density function [81]. The mean and variance of v are

$$E(v) = \frac{1}{2} \ln\left(\frac{4}{\pi}\right) + \frac{1}{2} \psi(1) = \frac{1}{2} \ln\left(\frac{4}{\pi}\right) - \frac{1}{2} C \qquad (2.16)$$

$$var(v) = \frac{1}{4} \psi(1,1) = \frac{\pi^2}{24} \qquad (2.17)$$

By averaging L uncorrelated amplitude samples from linear detection, a multiple L-look amplitude image can be generated. Here a square operation will not provide the same results as an intensity image. For the corresponding multiplicative L-look fading random variable denoted by v_L, its mean is unit magnitude and the variance is $(4/\pi - 1)$ decreased by a factor of L. The common practice to derive its *pdf* is to use the characteristic function. Unfortunately, it is not possible to derive a closed analytical form for the *pdf*. As far as the log-transformed speckle random variable is concerned, there does not exist a closed-form expression for its *pdf* either. One straightforward way to obtain its *pdf* is to employ the histogram estimation technique, but the numerical procedure involves multiple steps including the simulation of Rayleigh distributed random variables, multi-look averaging, the logarithmic transform, and the final histogram generation. In [79], other than the

conventional characteristic function method, an alternative approach is provided to derive the *pdf* of interest. This is the approximation method based on the edge worth expansion.

2.2.2.1.3 Gaussian Distribution Approximation

It has been established that, as the number of looks increases, the *pdf* of a speckle random variable approaches the Gaussian *pdf* [76]. The distances between the original speckle or the log-transformed speckle distributions and the Gaussian distribution were computed to determine which one approaches the Gaussian distribution more precisely [79]. Based on this analysis it was clearly demonstrated that, for intensity data, the *pdf* of the log-transformed noise approaches the Gaussian *pdf* much faster than that of the original speckle. Therefore, it is more appropriate to apply those Gaussian-noise-based image analysis algorithms to the noisy image after a logarithmic transform, than directly to the original intensity image. Figure 2.2 shows the *pdf* of speckle noise and the corresponding log-transformed speckle noise for intensity image. Similar plots are shown in figure 2.3 and 2.4 for amplitude image and square-root intensity image respectively. For both the amplitude image and the square-root intensity image, although the log-transformed speckle noise approaches the Gaussian *pdf* slightly slower than the original speckle noise, the former is already statistically very close to the Gaussian *pdf*. Thus the application of any Gaussian noise based image analysis algorithm will work equally well on the log-transformed amplitude data also.
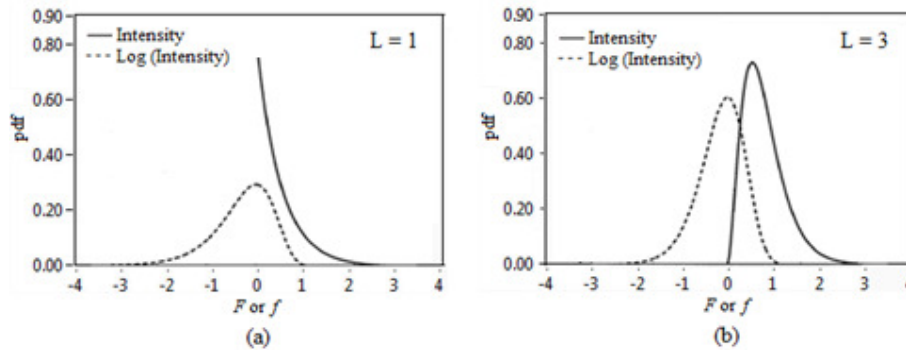
Figure 2.2 The *pdf* of speckle and the log-transformed speckle for SAR image in the intensity format (a) L = 1 (b) L = 3.
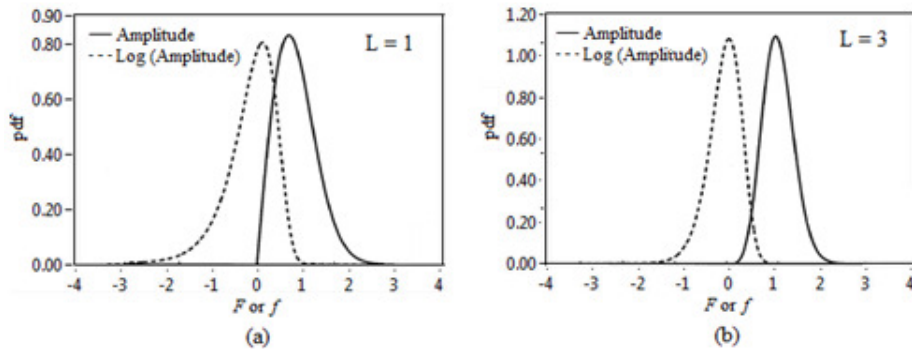
Figure 2.3 The *pdf* of speckle and the log-transformed speckle for SAR image in the amplitude format (a) L = 1 (b) L = 3.
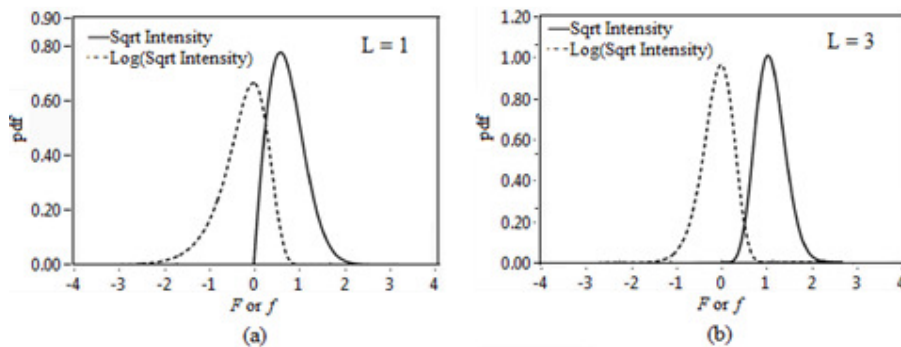
Figure 2.4 The *pdf* of speckle and the log-transformed speckle for SAR image in the square-root intensity format (a) L = 1 (b) L = 3.

2.3 Image Denoising Schemes

Over the last decades, a variety of methods have been proposed for image denoising. This includes spatial filtering methods, transform based methods, variational methods and techniques based on the solution of partial differential equations. There are various factors which need to be considered in selecting a noise reduction algorithm. They are the available computer power and time, whether sacrificing some real detail is acceptable if it allows more noise to be removed and the characteristics of the noise. For example a digital camera must apply noise reduction in a fraction of a second while a desktop computer has much

more power and time for denoising. Here we address the image denoising problems in two different application areas viz. images acquired using digital or conventional cameras and images from synthetic aperture radar (SAR). The later one is more specifically known as despeckling as the SAR images are inherently affected with speckle noise. In this section a survey of different denoising and despeckling schemes is done.

2.3.1 Denoising of Images with AWGN

The denoising of images affected with additive white Gaussian noise is a well known problem in image processing. Image denoising studies were started way back in 1970s by computer vision pioneers such as S. Zucker and Azriel Rosenfeld. In early 1980s, J. S. Lee proposed image enhancement schemes by using local statistics [6]. The invention of wavelet transforms in late 1980s has led to dramatic progress in image denoising in 1990s. The Bayesian view towards image denoising was put forward by Simoncelli & Adelson in 1996 and since then, many wavelet-domain denoising techniques have been proposed. The simple yet elegant Gaussian scalar mixture (GSM) algorithm published by Portilla et al. in 2003 [54] and the nonlocal mean (NLM) algorithm by Buades et al. in 2005 [88] have renewed the interest into this classical inverse problem. In the past few years, many more powerful denoising algorithms have appeared. Among them the patch-based nonlocal schemes, BM3D has shown outstanding performance. The directional transform based denoising schemes proposed very recently also have given outstanding results. Here an overview of the popular image denoising algorithms for images corrupted with AWGN is provided.

2.3.1.1 Wavelet Domain Techniques

Since their introduction in the late 1980s, *wavelets* have been universally recognized as extremely powerful tools for the analysis of non-stationary signals and images [12]. Wavelet based denoising algorithms basically involve three steps. First, an image is transformed into a wavelet domain. Next, denoising is effected on the wavelet coefficients, and finally the denoised image is obtained by applying the inverse wavelet transform on the denoised wavelet coefficients. The wavelet based denoising schemes can be broadly classified into two; the threshold based

schemes and statistical model based schemes. In threshold based methods, a WT coefficient is compared with a given threshold and is set to zero if its magnitude is less than the threshold; otherwise it is kept unmodified or modified depending on hard or soft thresholding rules, respectively. The statistical model based schemes model the WT coefficients with prior probability distribution functions (*pdf*) and the noise free coefficients are estimated using this *a priori* information with Bayesian estimation techniques, such as MAP or MMSE estimators.

Undecimated version of WT is commonly used for image denoising. It has both advantages and disadvantages over decimated one. Performing an undecimated WT is more computationally demanding than performing a decimated transform. Another advantage of decimated transform is that they preserve the inner-product so that the white noise in the input image remains white after the transform. However in the other case white noise in the image becomes correlated in the transform domain. However, undecimated transforms have the advantage of introducing fewer aliasing or ringing artefacts. Ringing artefacts occur due to the Gibbs phenomenon when coefficients of a decimated transform are set to zero.

2.3.1.1.1 Threshold Based Denoising in Wavelet Domain

Wavelet coefficient thresholding scheme of denoising is based on the idea that the energy of the signal to be defined concentrates on some of the wavelet coefficients, while the energy of noise spreads throughout all wavelet coefficients. Similarity between the basic wavelet and the signal to be defined plays a very important role, making it possible for the signal to concentrate on fewer coefficients. The concept of threshold based denoising in wavelet domain is illustrated in figure 2.5. Here after transforming an image into wavelet domain, denoising is effected by thresholding of the wavelet coefficients. The effectiveness of these methods depends on the estimation of the correct threshold.

There are ample of literature available on finding out an effective threshold. Of the various thresholding strategies, soft-thresholding is the most popular and has been theoretically justified by Donoho and Johnstone [17, 18]. These authors have shown that the shrinkage rule is near-optimal in the *minimax* (minimum of maximum mean square error) sense and provided the expression of the optimal

threshold called universal threshold as a function of the noise power when the number of samples is large. The use of the universal threshold to denoised images in the wavelet domain is known as *VisuShrink.* For image denoising, however, *VisuShrink* is known to yield overly smoothed images. This is because its threshold value, $\sqrt{2\sigma^2 \log N}$ can be unwarrantedly large due to its dependence on the number of samples N, which is very high for typical test images. Yet, despite its theoretical appeal, *minimax* is different from mean-squared error (MSE) as a measure of error.
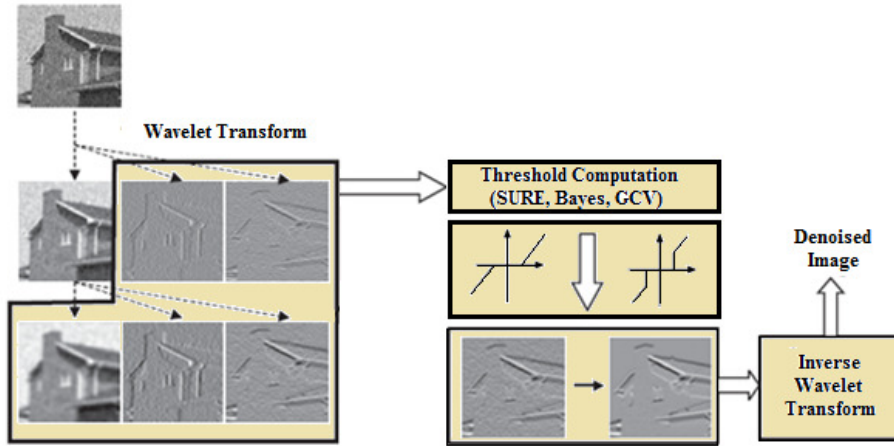
Figure 2.5. Concept of threshold based denoising in wavelet domain.

For denoising applications with known noisy function, it is often ideal to search for the optimal minimum mean-square error risk estimate using *a priori* information. Donoho and Johnstone proposed an optimal threshold value by minimizing Stein's unbiased risk estimator (SURE) [17]. SURE risk is a very good estimate of the true risk when the true function is not known [42]. Later a hybrid approach between the universal threshold and SURE threshold was proved to be more efficient and is known as SURE shrink [18]. Later Chang et al [43] have proposed Bayesian threshold in wavelet domain. This is based on an empirical observation in which the wavelet coefficients in each subband are modelled as independent and identically distributed random variables with Generalised Gaussian Distribution (GGD).

The major drawback in most of these thresholding schemes is that they require the prior knowledge of the amount of noise present in the image to compute an optimum threshold. The Generalised Cross Validation (GCV) technique proposed by Jansen et al [45] was proven to be an effective statistical way for estimating an optimum threshold for noise removal in many denoising application. The main advantage of GCV technique is that it can be used to estimate the optimal threshold without having the knowledge of the noise variance. The GCV is only based on the input data and its minimum is a good approximation for the optimal threshold. It was well established that the minimum of the GCV is an asymptotically optimal threshold for denoising applications [45].

In GCV technique, the original image *f* is assumed to be regular so that each pixel f_i can be approximated by a linear combination of its neighbours. So by considering the estimate of the noisy component g_i (represented as $\breve{g}_i$), as a combination of its neighbours, one can eliminate the noise in this particular component. This is repeated for all the components and the compromise can be estimated as Ordinary Cross Validation (OCV). The estimate of g_i can be computed in many ways. By generalizing it one can get the Generalized Cross Validation (GCV). This is a function of known parameters of the input image and is independent of the noise variance. It was established that minimizing the mean square error is equivalent to minimizing the GCV. So the value corresponding to the minimum of the GCV function can be used as an optimal threshold value.

In wavelet based denoising schemes substantial improvements in perceptual quality were reported later by translation invariant methods based on thresholding of undecimated WT coefficients. Further, many investigators have experimented with variations on the basic schemes like modified thresholding functions, level-dependent thresholding, block thresholding, adaptive thresholding etc and reported better results.

2.3.1.1.2 Bayesian Denoising in Wavelet Domain

The statistical model based schemes model the WT coefficients with prior probability distribution functions and the noise free coefficients are estimated using this *a priori* information with Bayesian estimation techniques, such as the MMSE

or MAP estimators. Here the main challenge lies in the accurate modelling of the image and noise coefficients using suitable *pdf*. If these models are well chosen, the noise can be removed efficiently. In literature several models have been considered for the noise-free wavelet coefficients and Gaussian model for the noise coefficients. Figure 2.6 shows the concept of Bayesian denoising in wavelet domain.

Consider a classical estimation problem as to estimate an unknown signal f from its noisy observation g. The probability density governing the observation process is the conditional density $P_{G|F}(g|f)$. The unknown signal f is treated as a realization of a random vector F. The Bayes estimate $\check{f}$ is the estimate that minimizes the Bayes risk, $\mathcal{R}$, which is the expected value of a cost function, $C(f, \check{f})$

$$\mathcal{R} \triangleq E\{C(f, \check{f})\} = \int\limits_{-\infty}^{\infty} \int\limits_{-\infty}^{\infty} C(f, \check{f}) P_{F,G}(f, g) df dg \qquad (2.18)$$
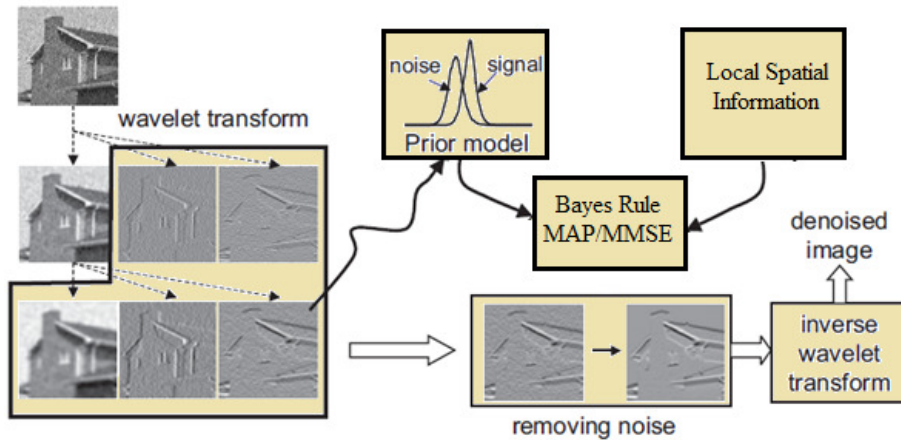
Figure 2.6: Concept of Bayesian denoising in wavelet transform domain.

In a given problem one chooses a cost function to accomplish two objectives. The first objective is that the cost function should measure user satisfaction adequately

and the second one is to assign one that results in a tractable problem. One usually starts by assuming that the cost depends only on the error of the estimate $f_e = \check{f} - f$; the cost function $C(f, \check{f})$ is then reduced to a function of a single variable. Since the joint density can be rewritten as $P_{F,G}(f, g) = P_G(g) . P_{F|G}(f|g)$, the risk becomes

$$\mathcal{R} = \int_{-\infty}^{\infty} P_G(g) dg \int_{-\infty}^{\infty} C(f - \check{f}) P_{F|G}(f|g) df \qquad (2.19)$$

The estimate that minimizes this risk follows from differentiating the inner integral and setting it zero.

$$\frac{d}{d\check{f}} \int_{-\infty}^{\infty} C(f - \check{f}) P_{F|G}(f|g) df = 0 \qquad (2.20)$$

To proceed, the cost function needs to be specified. One possible cost function is the square of the error, $C(f_e) = f_e{}^2$, and is commonly referred to as the squared error or the quadratic cost function. It accentuates the effects of large errors. The corresponding estimate is called the *minimum mean squared error* (MMSE) estimate $\check{f}_{ms}$. Basically it is the conditional mean and can be defined as

$$\check{f}_{ms} = \int_{-\infty}^{\infty} f P_{F|G}(f|g) df \qquad (2.21)$$

One other possible cost function is the uniform cost function, which assigns zero cost to all errors less than $\pm {}^{\Delta}\!/_2$. It means an error f_e less than ${}^{\Delta}\!/_2$ in magnitude is as good as no error. If $| f_e| > {}^{\Delta}\!/_2$, the cost has a uniform value of one. Of particular interest is the case where Δ is arbitrarily small but a nonzero number. One can show that the risk in this case is minimized by choosing the value f at which the posterior density $P_{F|G}(f|g)$ has its maximum. Hence the name the *maximum a posteriori* (MAP) estimate

$$\check{f}_{map} = argmax P_{F|G}(f|g) \qquad (2.22)$$

The above expression can be rewritten by separating the role of the observation g and of the *a priori* knowledge as follows

$$P_{F|G}(f|g) = \frac{P_{G|F}(g|f)P_F(f)}{P_G(g)} \qquad (2.23)$$

Here $P_G(g)$ is not a function of f. Thus the expression in (2.22) can be rewritten as

$$\check{f}_{map} = argmaxP_{G|F}(g|f)P_F(f) \qquad (2.24)$$

The limiting case of the MAP estimate, in which the prior is not available is the *maximum likelihood* (ML) estimate, $\check{f}_{ml} = argmaxP_{G|F}(g|f)$. In many cases of interest the MAP and the MMSE estimates coincide. For a large class of cost functions the optimum estimate is the conditional mean whenever the *a posteriori* density is symmetric about the conditional mean.

For natural noise-free images, the histograms of wavelet coefficients are typically sharply peaked at zero. S. Mallat [82] proposed to model the marginal prior distribution of image wavelet coefficients, $P_F(f)$ as a generalized Laplacian distribution as

$$P_F(f) = \frac{\beta}{2\alpha\Gamma(\frac{1}{\beta})} e^{-\left|\frac{f}{\alpha}\right|^{\beta}} \qquad \alpha, \beta > 0 \qquad (2.25)$$

where $\Gamma(x) = \int_0^{\infty 1} t^{x-1}e^{-t} \, dt$ is the Gamma function. The above model is often used in image processing applications. In some literature it is referred as the generalized Gaussian distribution (GGD). The model parameters α and β can be computed from the histogram of noise-free wavelet coefficients. Specifically, if σ_f^2 is the sample variance and K_f the kurtosis of the noise-free histogram, then α and β can be estimated from the following equations [19].

$$\sigma_f^2 = \alpha^2 \frac{\Gamma(\frac{3}{\beta})}{\Gamma(\frac{1}{\beta})} \qquad (2.26)$$

$$K_f = \frac{\Gamma(\frac{1}{\beta})\Gamma(\frac{5}{\beta})}{\Gamma^2(\frac{3}{\beta})} \qquad (2.27)$$

In practice the histogram of noise-free wavelet coefficients is not available and the model parameters need to be estimated from the noisy coefficients, g. In case of additive white Gaussian noise (AWGN), and for the above prior model, it is a simple task. The variance σ_g^2 and the fourth moment $m_{4,g}$ of the generalized Laplacian signal corrupted by AWGN are [19]

$$\sigma_g^2 = \sigma_v^2 + \sigma_f^2 = \sigma_v^2 + \alpha^2 \frac{\Gamma(\frac{3}{\beta})}{\Gamma(\frac{1}{\beta})} \qquad (2.28)$$

$$m_{4,g} = 3\sigma_v^4 + \frac{6\sigma_v^2 \alpha^2 \Gamma(\frac{3}{\beta})}{\Gamma(\frac{1}{\beta})} + \alpha^4 \frac{\Gamma(\frac{5}{\beta})}{\Gamma(\frac{1}{\beta})} \qquad (2.29)$$

where σ_v^2 is the noise variance. For natural images, the shape parameter β is typically $\beta \in [0, 1]$. In practice, the Laplacian prior, where $\beta = 1$, is often used due to simplicity. The scale parameter is then simply computed as

$$\alpha = [0.5(\sigma_g^2 - \sigma_v^2)]^{1/2} \qquad (2.30)$$

The Generalized Gaussian Distribution (GGD) and the α-stable prior are the most commonly used priors. The GGD prior suffers from not capturing the heavy tail behavior of the observed wavelet coefficients densities. The α-stable prior shows superiority in fitting the mode and the tail behavior of the wavelet coefficients distributions. But their hyper-parameters estimator is poor in the presence of contaminating noise. Only two special cases of α-stable distributions have a closed form expression, namely the Gaussian and Cauchy *pdf*. The Gaussian *pdf* is obviously not suitable to represent the signal coefficients. On the other hand the Cauchy *pdf* is unimodal and symmetric having a sharp peak around zero with heavy tail [83]. This is suitable for high resolution SAR images as they exhibit impulsive behavior indicative of underlying heavy tailed distributions [84]. For both the GGD and the alpha-stable priors, the derived Bayesian estimator has no closed analytical form in general, and also, it involves intensive numerical

integration. Other long-tailed distributions of wavelet coefficients have been proposed for specific types of images. Examples are the Pearson distributions for SAR images [85] and α-stable distributions for medical ultrasound images [86] etc.

A large class of Bayesian wavelet domain filtering techniques assumes an orthogonal wavelet transform and approximates the wavelet coefficients as mutually independent. In such a condition, the optimum Bayes estimates act as simple 'shrinkers' of the coefficients. Such Bayesian shrinkage rules are often similar to soft-thresholding, but are less ad-hoc and usually outperform the classical thresholding in terms of the mean square error. If the wavelet coefficients are assumed to be *i.i.d.*, their MAP estimates are same as presented earlier, since the same procedure is applied to each coefficient in a given subband. Efforts were made to study the relationship between such *i.i.d.* MAP estimators and wavelet thresholding [87]. There it was shown that the soft-thresholding method is equivalent to the MAP estimation assuming a Laplacian prior on the wavelet coefficients, with standard deviation equal to $\sigma_f = \sigma_v^2 T_U^{-1}\sqrt{2}$, where σ_v^2 is the noise variance and T_U is the universal threshold. Under the minimum mean square error (MMSE) criterion, the optimum estimate is the conditional mean as follows

$$\check{f}_{mmse} = \int_{-\infty}^{\infty} P_{F|G}(f|g)df = \frac{\int_{-\infty}^{\infty} f P_{G|F}(g|f)P_F(f)df}{\int_{-\infty}^{\infty} P_{G|F}(g|f)P_F(f)df} \qquad (2.31)$$

Simoncelli and Adelson [19] applied the above MMSE estimator in the context of image denoising, assuming the generalized Laplacian prior from equation (2.25). In case of AWGN, the above equation becomes

$$\check{f}_{mmse} = \frac{\int_{-\infty}^{\infty} f P_V(g-f)P_F(f)df}{\int_{-\infty}^{\infty} P_V(g-f)P_F(f)df} \qquad (2.32)$$

Where, $P_V(v)$ is the normal distribution $V(0, \sigma_v^2)$. For the Laplacian prior $P_F(f)$ the above estimator has no closed form solution and is computed numerically. This operation was implemented in an oriented multi resolution representation, known as the steerable pyramid by some authors [19] and reported to outperform classical

Wiener filtering. A related approach, but with an orthogonal 2D-DWT was later applied to medical ultrasound images [86].

In practice, generally, two problems arise with the Bayesian approach when an accurate but complicated *pdf* is used. The first issue is it can be difficult to estimate the parameters for a specific image, especially from noisy data, and the second problem is the estimators for these models may not have simple closed form solution. The solution for these problems usually requires numerical techniques. Thus the modeling of wavelet coefficients shall be carefully done in Bayesian denoising.

2.3.1.1.3 Interscale Dependency Model in Wavelet Domain

In most of the statistical model based denoising schemes, the WT coefficients are assumed to be independent. However it was well established that there are inter and intra scale statistical dependency in wavelet coefficients of natural images due to the fact that if a WT coefficient has small magnitude the adjacent coefficients are very likely to be small, and the small coefficients tend to propagate across the scales. Thus the models which consider the WT coefficient as independent cannot efficiently model the transform coefficients of natural images.

Several researchers have proposed many interscale dependency models for WT coefficients. Sendur et al [49] have proposed four different non-Gaussian models to characterize the interscale dependency and the corresponding bivariate MAP estimators based on noisy wavelet coefficients were derived. These models were developed based on the dependency of a coefficient and its parent at adjacent coarser scale locations and the coefficients at adjacent spatial locations. These models are based on the joint empirical coefficient-parent histograms of a large numbers of images taken from the Corel image database. Daubechies length-8 (Db4) wavelet was used to compute the wavelet transform. Using this empirical data a shrinkage function was derived numerically which depends on both parent and child. It was difficult to find an accurate model for the empirical histogram. However an approximate bivariate *pdf* was proposed. If the noise is assumed to be independent and identically distributed the joint probability function of noise vector $\boldsymbol{v_j} = (v_j, v_{j+1})$ can be written as a bivariate *pdf* as

$$p_v(\boldsymbol{v_j}) = \frac{1}{\left(\sqrt{2\pi}\sigma_v\right)^2} \; e^{-\left(\frac{v_j^2+v_{j+1}^2}{2\sigma_v^2}\right)} \tag{2.33}$$

The joint *pdf* for the signal coefficient vector $\boldsymbol{f_j} = (f_j, f_{j+1})$ can be defined as

$$p_f(\boldsymbol{f_j}) = \frac{3}{\left(\sqrt{2\pi}\sigma\right)^2} \; e^{-\left(\frac{\sqrt{3}}{\sigma}\sqrt{f_j^2+f_{j+1}^2}\right)} \tag{2.34}$$

Apply this to the MAP estimator in equation (2.22), we can get the value of $\hat{f}_j$ as

$$\hat{f}_j(g_j, g_{j+1}) = \frac{\left(\sqrt{g_j^2+g_{j+1}^2}-\frac{\sqrt{3}\sigma_v^2}{\sigma}\right)_+}{\sqrt{g_j^2+g_{j+1}^2}} \cdot g_j \tag{2.35}$$

Sendur et al [49] developed a subband adaptive image denoising in the wavelet domain based on this bivariate shrinkage function. Later they published better results using the same bivariate shrinkage function with local variance estimation [50].

There are other efficient denoising schemes available in literature which considers the dependency of the transform coefficients across scales. Chen et al [46-47] have proposed methods which take into account the intra scale dependency of the WT coefficients for image denoising. Crouse et al. [48] developed a framework for statistical signal processing based on Hidden Markov Models (HMM), where the interscale dependency of WT coefficients was exploited to find out an effective threshold. Luisier et al [51] proposed an image denoising algorithm using a point wise threshold based on SURE risk that takes into account interscale dependencies of oriented pyramid coefficients. The scheme proposed by G. Chen et al. [53] exploits the statistical dependency between a complex wavelet coefficient and its parent and children across three scales in the thresholding process. Portilla et al. [54] have modeled the neighborhoods of WT coefficients at adjacent positions and scales based on a Gaussian scale mixture (GSM) and estimated the noise free coefficients using Bayes least squares (BLS) estimator. Their denoising method, known as BLS-GSM, is still one among the best available denoising schemes in transform domain.

2.3.1.1.4 Directional Transform Based Denoising Schemes

Among the directional transform based denoising algorithms, the one based on steerable pyramid representation [52] is an important one. Decomposing an image into a steerable pyramid is a linear operation. A steerable pyramid is conceptually similar to a Laplacian pyramid. In both cases an image is represented using several scales. The coarsest scale contains the lowest frequencies of the image and the finer scales contain subsequently higher frequencies. A difference between the two representations is that in the steerable pyramid, each scale contains several orientation sub-bands. Each orientation sub-band corresponds to the response of a directional derivative operator. The steerable pyramid transform is over complete. A similarity between the steerable pyramid and orthogonal transforms is that the steerable pyramid decomposition is self-inverting; the inverse transformation can be performed by applying the transpose of the matrix performing the forward transform. The steerable pyramid has frequently been used in image denoising. Two properties of steerable pyramid decompositions are particularly useful for image denoising. The first property is that the distribution of coefficients in steerable pyramid decomposition is highly peaked. The other property is that edges in the input image cause a clustering activity. This has the effect that the absolute values of neighbouring coefficients are mutually dependent. This property holds for spatially adjacent coefficients, but also for coefficients corresponding to the same image location in different scales or orientations. The steerable pyramid based denoising scheme was proposed by J. Portilla et al. [54]. This has provided better results in terms of PSNR and better edge preservation. There are efficient denoising schemes available in literature which are based on directional transforms like DTCWT, curvelet, contourlet, shearlet etc. [55-58]

2.3.1.2 Non-local Techniques

The wavelet-based denoising techniques explained in the previous section estimate the denoised pixel intensities based on the information provided in a limited surrounding neighborhood. These methods only exploit the spatial redundancy in a local neighborhood and are therefore referred to as *local* methods. One of the most important innovations of recent years in image denoising has been the introduction of non-local approach. These methods estimate the intensity of every pixel based on information from the *whole* image thereby exploiting the presence of similar

patterns and features in an image. This approach relies on the observation that most natural images present clear self-similarities. If the image is divided into small patches, then most patches repeat almost identically over and over in the image. Once these similar patches are identified, they can be exploited to carry out noise filtering. This relatively new class of denoising methods originates from the Non-Local Means (NL Means), introduced by Buades at al. [88-89].

The most popular non-local denoising techniques are Non-Local Means (NLM) algorithm and Block Matching 3-D algorithm. These schemes are not considered as the transform based techniques and thus they are not compared with the schemes presented in this thesis. The performance improvement in these methods is basically due to the non-local averaging strategy employed. A brief introduction of these schemes is given in this section

2.3.1.2.1 Non-Local Means (NLM) Algorithm

In NLM algorithm, the filtering is carried out through the weighted mean of all the pixels in a certain search area; the weight associated with each given pixel, however, depends not on its geometrical distance from the reference pixel but on its contextual similarity with it, measured by the Euclidean distance between the patches surrounding the selected and the reference pixel.

The weight $w(s,t)$ defined by comparing two patches A_s and A_t centered respectively around the pixel s and t, is represented as

$$w(s,t) \triangleq e^{\frac{-1}{h}\sum \alpha_k |c_{s,k}-c_{t,k}|^2} \tag{2.36}$$

where $c_{s,k}$ and $c_{t,k}$ are the kth neighbor in the patch A_s and A_t, respectively, α_k define a centered symmetric Gaussian kernel and h controls the decay of the exponential function. The similarity measure is a weighted Euclidean distance over the two windows, well-adapted and robust in the AWGN model. Basically, the NLM filter estimates a noise-free pixel intensity as a weighted average of all pixel intensities in the image, and the weights are proportional to the similarity between the local neighborhood of the pixel being processed and local neighborhoods of surrounding pixels. This type of non-local means approach is known as point wise

approach, which provides the estimate for a single point only, that is the reference pixel in this case.

This technique, despite being intuitive and potentially very powerful, has some limitations. One is that the objective and visual quality of this scheme is inferior to the other recent non-local techniques like BM3D and the other most important issue is that the computational complexity of this scheme is quadratic in the number of pixels in the image, making it computationally intensive and even impractical in real applications. These issues were addressed by different researchers and improvements for enhancing the visual quality with reduced computation time have been proposed. Towards this end, modifications in the basic scheme with better similarity measures [90-92], adaptive local neighborhoods [93], or refinement in similarity estimates in different iterations [94] were proposed. The improvement in computational efficiency of NLM filters based on different techniques [95-98] were investigated out of these the neighborhood pre classification [95] and FFT-based computation of the neighborhood similarities [96] are the best ones.

2.3.1.2.2 Block-Matching 3D (BM3D) Algorithm

BM3D can be arguably considered as the state-of-the-art for AWGN denoising. The BM3D algorithm [99] is an extension of NLM with a multipoint rather than point wise filtering. It combines three basic ideas in a multipoint approach: the non-local approach, the wavelet domain shrinkage and the Wiener denoising in two steps [100]. Here the last two steps work not on local neighborhoods, but on groups of blocks drawn from different image locations and collected on the basis of their similarity. The resulting 3D groups are highly redundant allowing for a sparser WT representation and a more effective separation between signal and noise through hard thresholding in the first step. Due to grouping the statistics can be more reliably estimated, and the Wiener filtering on the 3D groups of the second step turns out to be extremely effective.

The BM3D algorithm involves two steps with each step composed of three different phases. The three phases in the first step are as follows

a) Grouping: for each reference block, the most similar blocks are located in the image according to a minimum Euclidean distance criterion;

b) Collaborative filtering: each 3D group undergoes WT, hard thresholding and inverse WT;

c) Aggregation: all filtered blocks are returned to their original location and contribute with suitable weights to the basic estimate of noise free image.

The second step comprises the same three stages, with the following differences

a) Grouping: blocks are located based on the basic estimate provided by the first step;

b) Collaborative filtering: each 3D group of noisy blocks undergoes DCT or WT, Wiener filtering and inverse transform

c) Aggregation: like in step one.

2.3.1.3 Dictionary-based Methods

Several denoising algorithms rely on dictionaries for denoising. These methods learn or adapt a dictionary. Here denoising is performed patch-wise with each patch denoised separately and inserted into the denoised image. Usually, averaging is performed in areas of overlapping patches. In these methods the denoising performance relies on an over-complete dictionary. The dictionary contains a set of atoms, which can be thought of as basis functions. The idea here is to denoising by approximating the noisy patch using a sparse linear combination of atoms. Good approximations to the true solution can usually be found using orthogonal matching pursuit (OMP) [101], which is a greedy procedure and therefore is quite fast. The quality of the denoising result of a dictionary based method is highly dependent on the choice of the dictionary. The dictionary can be selected mainly in three ways, viz. by design, by global learning on a dataset of noise-free images, or by learning adaptively from the noisy image itself.

The dictionary based methods usually provide very good denoising performance but are computationally very intensive. The most popular dictionary based denoising schemes are K-Singular Value Decomposition (KSVD), Non-Local Sparse Coding (NLSC) and Expected Patch Log Likelihood (EPLL). These schemes are briefly described here.

2.3.1.3.1 K-Singular Value Decomposition (KSVD)

K-Singular Value Decomposition (KSVD) [102-103] is an iterative algorithm that learns a dictionary on the noisy image at hand. One iteration of the algorithm consists of two steps, viz. finding the coefficient of approximation for each patch in the image using OMP and updating the dictionary one column at a time. Usually ten iterations are sufficient to achieve good results. Here the dictionary updating step relies on a singular value decomposition, hence the name of the algorithm. Dictionaries learned in such a way often contain features of the image on which the dictionary was learned.

2.3.1.3.2 Non-Local Sparse Coding (NLSC)

Non-Local Sparse Coding (NLSC) [104] is another dictionary-based method that is similar to K-SVD. Here the dictionary is adapted to the noisy image at hand. The main difference with the KVSD scheme is that the NLSC employs simultaneous sparse coding [105], which encourages similar-looking noisy patches to be approximated using the same sparse decomposition. The idea underlying this approach is that the natural images contain self-similarities. That is similar-looking patches are expected to be found at several locations in an image. NLSC is one of the best currently available denoising algorithms in terms of quality of the results, but with a much higher computational complexity.

2.3.1.3.3 Expected Patch Log Likelihood (EPLL)

Many denoising methods denoise image patches independently and apply averaging or other similar techniques in areas of overlapping patches. Dictionary denoising methods such as KSVD are examples of such methods. The main problem with this approach is that the averaging process may create patches in the resulting images. Expected Patch Log Likelihood (EPLL) [106] contrasts itself from methods that denoise patches independently by keeping each patch under a given patch prior, while staying close to the noisy image. EPLL takes a *maximum a posteriori* (MAP) approach to denoising. The EPLL is not the expected log-likelihood of a full image, but it is the sum over the expected patch log-likelihoods of many sliding window patches in an image. Here the optimization is performed using half-quadratic splitting, which introduces auxiliary variables and alternates between two steps viz. updating the auxiliary variables while keeping the image

patches fixed and updating the image patches while keeping the auxiliary variables fixed. This procedure is repeated for a small number of iterations.

2.3.2 SAR Image Despeckling

SAR imaging is an important source of information, which provides high resolution images of earth in all weather and illumination conditions. It has wide range of applications like home land security, environmental protection, land resource management, disaster management, archaeology etc., which require different image processing tasks like image segmentation and classification, target detection etc. The performance of these image processing tasks is heavily dependent on the quality of the source images. SAR images are inherently susceptible to speckle, caused by constructive and destructive interference between waves returned from elementary scatterers within each resolution cell [2]. This will greatly affect the radiometric resolution of SAR images and degrade the human interpretation and computer-aided scene analysis. Thus, speckle reduction is a critical preprocessing step for any SAR image processing and applications. SAR image despeckling has been the active research topic over the last few years due to the launch of large number of radar satellites.

The effect of speckle in SAR images can be reduced either during the image formation phase or later. The former method consists of multi-look processing by averaging several statistically dependent looks of the same scene during image focusing in the frequency domain [2]. The main drawback of this method is that it enhances the radiometric resolution at the expense of spatial resolution, resulting in blurring of the image. The post-image-formation approaches of SAR despeckling can be grouped into three broad categories, viz. spatial, transform based and nonlocal filtering. These techniques are explained in this section.

2.3.2.1 Spatial Domain Techniques

The despeckling of SAR images can be considered as a statistical estimation problem, wherein the estimate of the radar reflectivity is carried out through the direct manipulation of the noisy image [107]. This is equivalent to the measurement of a stochastic process in a finite interval. Here the estimation

process will be meaningful only if the process involved is ergodic and stationary. This ensures that the estimations computed on a finite interval approximate the estimations on the whole process. Thus speckle filtering can be described as a function of the stationarity and non stationarity nature of the scene, speckle, and observed signals. Usually most of the speckle filters assume that the speckle noise is multiplicative unit mean wide sense stationary process. This assumption simplifies the processing since speckle statistics, which are constant on the whole scene, need to be estimated only once. Thus the despeckling filters can be categorized based on the stationarity-non stationarity nature of the speckle random process as Stationary Multiplicative Speckle Model Filters (SMSM) and Non-stationary Multiplicative Speckle Model Filters (NSMSM) [108]. The examples of SMSM Filters are the Lee [6] and Kuan [5] MMSE filters and the Frost [4] filter and that of NSMSM is the MAP Gaussian filter [109].

The SMSM filters carry out the despeckling in the original domain in a non-homomorphic way. They operate in the spatial domain with linear filters developed under a minimum mean-square error (MMSE) approach. The MMSE solution becomes a linear function of the covariance matrix of the signal and noise through the assumption of Gaussian signals. In this case it is called linear MMSE (LMMSE) filtering [110]. The LMMSE approach is based on the first two moments of the *pdf* and is computationally very efficient. The SAR images are not generally stationary due to the spatial variations of the scene signal. However these images are locally stationary. Thus the first two moments required to apply the LMMSE approach can be accurately estimated within a moving window. The idea of adaptive filtering by applying the LMMSE filtering in a local way was introduced by Lee [6], Kuan [5] and Frost [4]. These standard filters made it clear that some kind of local adaptivity is necessary to account for the non stationarity of the image. Even though these filters perform well to reduce speckle in homogeneous areas they typically exhibit limitations in preserving sharp features and details of the original image due to losses at contours and edges. To overcome these disadvantages contextual information of the image need to be taken into account in the despeckling algorithm. This was done in various ways in the works reported in [7], [8] and [111].

In contrast to SMSM speckle filters, the NSMSM filters are statistical model based and thus require the knowledge of the *a priori* probability density function. Here the simple MMSE estimation is replaced with the more sophisticated and promising Bayesian *maximum a posteriori* (MAP) approach. The challenging part of these schemes is the effective modelling of the statistics of the SAR images. If these models are well chosen, the noise can be efficiently removed. The most well known NSMSM filters are the ones proposed in [109], [9] and [112]. The method proposed in [109] uses a Gaussian MAP filter and the one proposed in [9] uses a Gamma MAP filter. The variety of situations encountered in SAR images cannot be accurately modeled using a simple parametric model [113]. The accuracy of the parameter estimation is heavily dependent on the volume of available data. The inaccuracies in it results in artifacts and artificial biases in the reconstructed scene. A large processing window will lead to an accurate estimate of the *pdf* parameters, on the other hand if the number of independent samples is not large enough a radiometric bias may be introduced. In particular this bias depends on the number of window samples but also on the texture autocorrelation included in the window.

2.3.2.2 Wavelet Transform Domain Techniques

The transform domain techniques are mainly based on wavelet transform. Here noise is assumed to be white and independent of the noise-free image. In case of SAR despeckling, to take advantage of the denoising algorithms already available for additive white Gaussian noise (AWGN), the multiplicative speckle noise has to be converted into additive one. Based on this the despeckling techniques can be broadly put into two main categories: the homomorphic and non homomorphic approach. These techniques are available in decimated and undecimated wavelet domain. The advantage of using undecimated wavelets for denoising signal-independent noise is equivalent to that of a translation-invariant denoising (TID). The TID consists of applying wavelet denoising to circularly shifted versions of the noisy image and of averaging the results after shifting them back [114]. It yields superior performance with respect to conventional hard and soft thresholding in terms of noise suppression, sharpness preservation, and absence of ringing impairments. Therefore, transform domain despeckling is mostly performed in the undecimated wavelet domain.

2.3.2.2.1 Homomorphic Wavelet Approach

The homomorphic approach consists in applying a logarithmic transform of the data to convert the multiplicative noise to an additive one. The main problem here is that in this process the statistics of SAR images are totally changed due to the non linearity of the logarithmic transform. This necessitates a detailed analysis of the distribution and statistics of the log-transformed speckle. Over the years many authors have conducted studies to describe the characteristics of the log-transform random variables. Arsenault et.al [115], showed that the logarithm of speckle noise approaches a Gaussian distribution as the number of look increases. Detailed studies were carried out to characterize the log-transformed speckle and to analyze the problems introduced by the logarithmic transformation of SAR images [116]. It was established that the log-transformed speckle is non-Gaussian, especially in the important single-look case and has non-zero mean. However many of the despeckling schemes available with homomorphic approach assume a zero mean AWGN noise. In general, mean bias problem should not be ignored especially for SAR images with high noise levels, for the purpose of radiometric preservation. So it is necessary to correct the biased mean within the processing stages. More importantly, the logarithm changes radically the data dynamics, leading to unavoidable radiometric distortions during the denoising process.

The homomorphic approach of despeckling using simple hard and soft thresholding are presented in [15]. Even though these schemes use an empirical threshold value they outperformed the spatial-domain adaptive filters especially for the most common single look SAR images. Further to this many works were proposed to find out an appropriate threshold selection such as adaptive thresholding [117], empirical shrinkage in an adaptive fashion [118] etc. Later performance improvements in despeckling were achieved by optimizing the shrinkage parameter through a statistical Bayesian approach by assuming *a priori* hypothesis on the reflectivity of the scene. For this several solutions were proposed based on MAP criterion and different distributions like the Γ-distribution [119], the alpha-stable distribution [120], the normal inverse Gaussian [121], or the simpler Cauchy distribution [64], for the log-transformed reflectance in the wavelet domain. Since the alpha-stable distribution [120] does not have a closed-form expression, the estimation of the *pdf* parameters from the noisy image is hampered and the

Bayesian estimator obtained does not have a closed-form. This results in a high computational complexity. In [64] it was shown that two special cases of the alpha-stable distribution have closed-form expressions, the Gaussian and Cauchy *pdfs*. Based on this a simple Cauchy prior was proposed, which has the advantage to be symmetric, to have a sharp peak around zero with heavy tails and to have only dispersion parameter to estimate. This prior leads to the derivation of both a MAP and MMSE Bayesian estimators.

In homomorphic approach, after denoising an exponential operation is employed to convert the log-transformed images back to the non logarithmic format. However, the mean of log-transformed speckle noise does not equal to zero resulting in a bias in the mean of reconstructed signal. This means the backscatter mean is not preserved in homogeneous areas when the logarithm is inverted after filtering. This needs to be corrected to avoid extra distortion in the restored image. A solution to this problem was proposed by Xie et al. [122], which adjusts the mean value by adding a further processing step. The other major issue with homomorphic filtering is that the signal variations are damped by the logarithm, resulting in an unlikely flatness after filtering.

2.3.2.2.2 Non-Homomorphic Wavelet Approach

The non-homomorphic approaches use the multiplicative noise model to develop the denoising algorithm. To one side this brings the advantage that all the issues related to the homomorphic approach are avoided, on the other side there are some serious modeling issues to be solved with the multiplicative model. In the early days the multiplicative model were not as well developed as the techniques for additive noise. Over the years lot of non homomorphic techniques have been proposed [6-8] enumerating only the spatial domain approaches. All these techniques simplify the multiplicative noise model in various ways.

In order to overcome the drawbacks of the homomorphic approach, several authors look to the additive signal-dependent speckle model in the wavelet domain. When the noise is signal independent, the MMSE Wiener filtering can be simply formulated and efficiently performed in the wavelet domain. Here it is done as a

rescaling of wavelet coefficients by a space-varying factor depending on the SNR of the coefficients themselves [123]. A low complexity MMSE estimation procedure is proposed in [124] to derive the shrinkage factor for each wavelet coefficient. Later MMSE filtering was extended to multiplicative noise in undecimated wavelet domain [125]. Foucher et al. [85] used the Pearson distribution to model the *pdf* of stationary WT wavelet coefficients and reconstructed the despeckled image using the MAP criterion. Although this algorithm has sound performance, the high computational complexity of the Pearson distribution makes this approach less appealing in practice. M. Dai et al [126] presented an efficient non-homomorphic despeckling scheme with edge preservation. F. Argenti et al [59] proposed a despeckling scheme in wavelet domain based on generalized Gaussian (GG) distribution, characterized by two spatially-varying parameters. These parameters of the speckle-free reflectivity and the signal-dependent noise are derived, through the relationships between these moments and the moments of observable noisy variables. The main problem here is that the cross correlation of the reflectivity pixel is neglected to enable a more simple estimation of GG parameters. This assumption is justified in homogeneous areas, but no longer in textured ones. To overcome these issues the same scheme was extended by classification of wavelet coefficients based on their level of heterogeneity [60]. Information about scene heterogeneity is very important because the local stationarity and ergodicity assumptions, to obtain the statistical estimation of parameters, may no longer be verified. Moreover, in case of extremely heterogeneous areas, like point targets, being the speckle not fully developed, leaving the area as such without any processing will be a better strategy.

One of the major drawbacks of GG-based MAP solutions, either with or without classification of wavelet coefficients, is that they can be achieved only numerically, thereby leading to a high computational cost. A Laplacian–Gaussian (LG) assumption was used to derive MAP and minimum mean square error (MMSE) estimators for despeckling of medical ultrasound images [61]. This was based on homomorphic filtering, which may induce a biased estimation. Later based on the assumption that the estimated distributions of the wavelet coefficients relative to the speckle free reflectivity and to the speckle noise approximately follow a

Laplacian and a Gaussian distribution, respectively, a MAP despeckling scheme was proposed [62]. As in the case of the GG-based MAP solution, here also classification of wavelet coefficients according to their texture content was carried out. Here the computational cost was reduced by one order of magnitude with respect to the solution obtained numerically with the GG assumption, without significantly affecting the performance in terms of speckle reduction.

2.3.2.2.3 Bayesian Despeckling in the Wavelet Domain

From a signal processing perspective, despeckling filters aim at performing an estimation of the radar reflectivity (signal of interest), based on the speckled image (observed signal). Bayesian estimation techniques can be used to solve this problem. As explained earlier the Bayesian solution can be obtained basically using MMSE or MAP equations. The MMSE requires only the second order moments of the noise component while the MAP requires the precise knowledge of the *pdf* of the random variables involved.

Under Gaussian signals assumptions, the MMSE solution becomes a linear function of the covariance matrices of the signal and of the noise and it is referred to as *linear* MMSE (LMMSE) filtering. The underlying hypothesis of uncorrelated noise yields a spatial LMMSE filtering, by locally modeling the covariance matrix of the signal. The further assumption of uncorrelated signal variations around its space-varying mean yields the *local* LMMSE (LLMMSE) filter. When non-Gaussianity assumptions are made on the first-order distribution of reflectivity, the LMMSE solution is no longer optimal. Consequently, the LLMMSE solution is a maximum likelihood (ML) approximation of the MMSE estimate. In the non-Gaussian case the MMSE estimator may be formulated as a *maximum a posteriori* (MAP) estimator. As explained earlier, if the number of looks is not too large, SAR reflectivity is non-Gaussian distributed. Hence, better estimators like the Gamma-MAP filter is required where the underlying assumption of Gamma-distributed texture allows a closed-form MAP solution.

There are many despeckling schemes available in literature, which are based on Bayesian estimation techniques. Many of these schemes are already covered in the previous two sections.

2.3.2.3 Directional Transform based Techniques

SAR image despeckling using WT results in unexpected pseudo contours due to the fact that 2D WT can only provide three directional subbands in a certain resolution. To overcome these issues despeckling schemes based on different directional transforms were introduced very recently. The prominent among these are the DTCWT [65-66], curvelet [67], contourlet [68], shearlet [69] and bandlet [70-71] based schemes. These schemes provided better results as compared to WT based ones. A brief description of these schemes is presented here.

The DTCWT has the advantage of improved directional selectivity, approximate shift invariance, and perfect reconstruction over the discrete wavelet transform. J J Ranjani et al. proposed a despeckling algorithm based on DTCWT by considering the dependences of the wavelet coefficients across different scales [65]. Here the DTCWT coefficients in each subband are modelled with a bivariate Cauchy *pdf* which takes into account the statistical dependence among the DTCWT coefficients. A MAP estimator is used to compute the noise free coefficients. Mellin transform of two dependent random variables is utilized to estimate the dispersion parameter of the bivariate Cauchy *pdf* from the noisy observations. Later the scheme was refined by the same authors with a multivariate Cauchy *pdf*, which takes into account the statistical dependency between the DTCWT coefficients, their neighbours and coefficients across scales [66].

F. Argenti et al. proposed an efficient despeckling scheme by exploiting the multidirectional capabilities of non-sub sampled contourlet transform (NSCT) [68]. Here the noise free NSCT coefficients are estimated from the observed ones according to MAP and LMMSE criterion. Even though this scheme has provided better results, the computational complexity of the scheme is much higher due to the non separable filtering of NCST. Later an adaptive despeckling method based on non-sub sampled shearlet transform (NSST) was proposed [69], in which the NSST coefficients in each subband are classified to identify the signal of interest. Here the quantitative analysis of noise variance is made by considering the interaction of Laplacian pyramid with Directional Filter Bank used in NSST. This has improved the spatial adaptability of the scheme. The classification of different regions in SAR image was carried out to reduce the shrinkage ratio for

heterogeneity regions while removing speckle effectively. This method has provided reasonably good despeckling performance when compared to the previously mentioned NCST based scheme while preserving details and texture information well.

The bandelets have adaptability as compared with wavelet, curvelet, contourlet, shearlet etc. Also the number of its optional directions outperforms other multiscale geometric analysis tools. A despeckling algorithm based on Translation Invariant Bandlet Transform (TIBT) using edge detection and Fuzzy C Means (FCM) clustering was proposed by Biao Hou et al. [70]. Later a similar despeckling scheme was reported with edge detection based on multiscale products of bandlet transform [71]. Both these schemes provided very good despeckling results as compared to WT and other directional transform based schemes.

2.3.2.4 Non-local Despeckling Techniques

One of the most important innovations of recent years in denoising has been the introduction of non-local approach. Non-local filtering represents a complete change of perspective in image denoising, since the "true" value of the current pixel is no more estimated from the pixels closest to it, but from those pixels, located anywhere in the image, which have the most similar context. This approach relies on the observation that most natural images including SAR images present clear self-similarities. In images most patches repeat almost identically over and over in the image. Once these similar patches are identified, they can be exploited to carry out noise filtering.

By exploiting image self similarity, nonlocal filtering mimics a true statistical averaging of pixels, thus allowing strong speckle reduction and accurate preservation of features. On the down side, it requires the computation of a large number of block-similarity measures and is therefore computationally demanding. SAR despeckling schemes based on non-local approach are presented here.

2.3.2.4.1 Probabilistic Patch-Based (PPB) Filtering

PPB can be considered as an evolution of NLM for speckle noise [127-128]. Here a similarity measure is developed which is well suited to SAR images. PPB is

developed by a more general approach for patch-based denoising in the framework of Weighted Maximum Likelihood Estimation (WMLE). The WMLE has first been applied to image denoising by Polzehl et al. [129]. Contrary to this, in PPB the weights are defined following a statistical patch-based approach. Here a suitable patch-based weight is defined to generalize the Euclidean distance based weight used in the Non-local means algorithm. In PPB the distance between two patches is based on the speckle distribution model. This scheme has provided reasonably good despeckling results.

2.3.2.4.2 SAR Version of BM3D

The BM3D scheme was extended to SAR despeckling by taking a non-homomorphic approach [130]. For images with a small number of looks, this kind of approach does not work well, being the hypothesis of Gaussian noise not satisfied in this case. Since the logarithmic operation changes the data dynamics and, therefore, the distances among patches, a homomorphic approach is used here. The original BM3D algorithm was modified with respect to the criterion used to collect blocks in the 3D groups and the thresholding process. In the AWGN setting the grouping based on Euclidean distance makes perfect sense because a smaller Euclidean distance corresponds to a higher likelihood that the two signal blocks without noise be equal. However, once the noise statistics change, as happens with SAR images, the Euclidean distance loses its significance.

2.3.3 Strengths and Weaknesses of Different Schemes

The denoising algorithms cannot always be clearly assigned to one category and might sometimes belong to several categories. Linear smoothing, median filtering, wiener filter, anisotropic diffusion and bilateral filtering are considered to be filtering-based methods. BLS-GSM and KSVD are based on a decomposition of the image though KSVD can also be said to rely on prior knowledge. EPLL, BM3D and NLSC rely on prior knowledge about images. Methods based on prior knowledge about images can be further divided into external knowledge based ones and   internal knowledge based ones. The former one is based on knowledge about all natural images and the later one is based on knowledge about the noisy

image itself. EPLL belongs to the category exploiting external knowledge, whereas BM3D and NLSC belong to the category exploiting internal knowledge.

Methods based on internal knowledge are a more recent development than methods based on external knowledge. The idea underlying methods exploiting internal knowledge is to look for regions within an image that are similar in appearance. This idea was extended to image patches and looks for similar patches within a given noisy image and performs a weighted average of the center pixels for denoising in NL-means approach. BM3D also exploits the idea of grouping patches that are similar in appearance, but performs a more effective denoising step on the group of patches rather than a single patch in NL-means. NLSC is a further example of a method exploiting this idea. There similar-looking patches are grouped and denoised together using simultaneous sparse coding, where a dictionary is used that is adapted to the noisy image itself. Dictionary-based methods can belong to either the category exploiting external or internal knowledge, depending on what kind of dictionary is used for sparse representation. If the dictionary is learned on a large dataset of images, the method belongs to the category of methods exploiting external knowledge. If the method learns a dictionary on the noisy image at hand, such as KSVD, the method belongs to the category of methods exploiting internal knowledge. NLSC employs a dictionary that is learned on a dataset of noise-free images, but adapts this dictionary to the noisy image at hand, similarly to KSVD. NLSC can therefore be said to belong both to the category employing internal and to the category employing external knowledge. In case the dictionary is hand-crafted as opposed to learned on either a larger dataset or a single noisy image, the method belongs to the same category as methods based on wavelet-decompositions. They rely on a decomposition of the image that is useful, but do not rely on learning.

These denoising methods have complementary strengths and weaknesses. They vary in terms of denoising results and the computational complexity of the algorithm. The computationally most intensive methods learn or adapt a dictionary. The KSVD and NLSC schemes require long computation times (up to an hour on a modern machine for images of size 512x512). The BM3D requires the computation of a large number of block-similarity measures and is therefore computationally

demanding. The BLS-GSM and the directional transform based schemes are relatively fast. The computational complexity of directional transform based schemes depends mainly on the type of transform used. If the transform is a separable one and non redundant, then it will be computationally more efficient. Most methods like EPLL lie somewhere in the middle of these two extremes and require a few minutes of computation for images of size 512x512. The methods relaying on internal knowledge are particularly effective on images with repeating structure, whereas methods relying on external knowledge are usually more effective on images with more complex structures which are not identical within the same image.

The importance of the image denoising problem goes beyond the evident applications it serves. Being the simplest possible inverse problem, it provides a convenient platform over which image processing ideas and techniques can be tested and perfected. Thus the aim shall be to concentrate on weather and how can we develop a generalized framework of image restoration which is not only suitable to solve image denoising problem, but also has potential ability to retain the visually important features like contours, edges etc in a computationally efficient manner.

2.3.4 State of the art Denoising & Despeckling Schemes

In case of denoising of images with AWGN, the bivariate shrinkage with local variance in DTCWT domain [50], BLS-GSM scheme [54] and BM3D scheme [99] are considered as the state of the art techniques. The first one is the simplest algorithm with a very less computation time. The BLS-GSM is considered as the state of the art in transform domain image denoising, but the computation time is high. The BM3D algorithm achieves the largest PSNR among the existing denoising algorithms. This algorithm uses a highly complicated image noise model and uses a non local approach for denoising. The BM3D algorithm has much high computational complexity than the other schemes mainly because of the computation of a large number of block-similarity measures, grouping similar 2-D fragments of the image into 3-D data array and the collaborative filtering to deal with these 3-D data arrays. The details of these schemes are already presented in the previous sections.

Among the wavelet based SAR despeckling schemes, the one based on generalized Gaussian Distribution (GGD) [60], Laplacian distribution [63] and Cauchy's distribution [64] are considered as the state of the art. In the first scheme, the wavelet coefficients are partitioned into classes having different degrees of heterogeneity and different GG parameters are used for different sets of coefficients. Even though this scheme outperformed the previously proposed schemes in terms of speckle reduction, the high computational cost due to the numerical estimation of noise free coefficients has limited its practical applications. To overcome this, a Laplacian–Gaussian (LG) assumption was used to derive MAP and MMSE estimators in the second scheme. As in the previous case here also classification of wavelet coefficients according to their texture content was carried out. Here the computational cost was reduced by one order of magnitude with respect to the solution obtained numerically with the GG assumption, without significantly affecting the performance in terms of speckle reduction. In the third scheme Cauchy's distribution is used to model the heavy tailed behavior of SAR images. This scheme also provided reasonably good results.

SAR image despeckling using WT results in unexpected pseudo contours due to the fact that 2D WT can only provide three directional subbands in a certain resolution. To overcome these issues despeckling and denoising schemes based on directional transforms were introduced very recently. Among the directional transform based SAR despeckling schemes, the one based on DTCWT [65-66], contourlet [68], shearlet [69] and bandlet [71] are considered as the state of the art techniques. The despeckling scheme proposed by J J Ranjani et al. [65] used a MAP estimator by modelling the significant dependences of the DTCWT coefficients across different scales with a bivariate Cauchy *pdf*. Later the same authors refined this scheme by introducing a multivariate Cauchy *pdf* [66]. In the contourlet based scheme a non-sub sampled contourlet transform (NSCT) is used in Bayesian framework to estimate the noise free image [68]. The computational complexity of the scheme is much higher due to the non separable filtering of NSCT. In the shearlet based scheme the non-sub sampled shearlet transform (NSST) coefficients in each subband are classified to identify the signal of interest [69]. An edge detection and despeckling algorithm based on multi scale products in bandlet domain was proposed by W G Zhang et al. [71]. Here the edge is first

detected and the edge removed image is used for despeckling. Finally the removed edge is added to preserve edges while despeckling.

Among the non-local techniques for SAR image despeckling, the probabilistic patch based filtering (PPB) [128] and the SAR version of BM3D (SAR-BM3D) [130] are considered as the state of the art despeckling schemes. The details of these schemes are given in section 2.3.2.4.

2.4 Measures of Image Denoising Performance

The measures of denoising performance are different for different types of images. The performance measures used for SAR images may not be a good performance indicator for images corrupted with Gaussian noise. A good SAR despeckling technique should have basically four important characteristics [3] viz. speckle reduction in homogeneous areas; preservation of scene features such as texture, edges, point target etc.; radiometric preservation and absence of artifacts. To assess the capacity of a despeckling technique to achieve such results, a set of suitable measures are used in the literature, which can be classified as no-reference measures and full-reference measures. The no-reference measures are applied on real-world SAR images and the full-reference measures are applied when a reference SAR image is generated by simulation. In some approaches, despeckling quality is judged based on the results of subsequent tasks, such as classification or segmentation, but these are obviously application-dependent and hence not very general. Many of these measures can be used to assess the performance of denoising algorithms for images corrupted with AWGN also.

Here let us consider the following model of a discrete noisy image:-

$$G = F.V \hspace{3cm} (2.37)$$

Where F is the clean image or the reference image, G is the noisy image and V is the multiplicative speckle noise. Let $\check{F}$ be the denoised or the despeckled image. The no reference measures require only G and $\check{F}$ while the full reference measures require F and $\check{F}$.

2.4.1 No-Reference Measures

The no reference measures are applicable for real SAR images. Due to the lack of a reference, these measures make sense only if referred to areas of the SAR image that can be clearly characterized in terms of their signal content as homogeneous, heterogeneous, or extremely heterogeneous regions. There are basically four different types of quantitative evaluation indicators which can be used to evaluate the performance of SAR images.

2.4.1.1 Effective Number of Looks (ENL)

Homogeneous regions in SAR images are the most simple to analyze as in these areas the randomness of the observed signal is only caused by speckle, which is fully developed. Here for each pixel the multiplicative noise model is valid and the speckle can be modeled as Gamma distributed with unit mean and variance = 1/L, where L is the number of looks. ENL is a commonly used parameter to measure the smoothing effects in the de-speckled image in homogeneous regions. The ENL is defined as

$$\text{ENL} = A\left(\frac{\mu^2}{\sigma^2}\right) \tag{2.38}$$

where $A = 1$ for SAR images in intensity format and $A = (\frac{4}{\pi} - 1)$ for SAR images in amplitude format and μ and σ^2 are the mean and variance values respectively over the homogeneous area. Since the mean value reflects the average brightness of a SAR image, the sustainment of it is important to image calibration. Variance of image denotes the range at which the pixels in an image deviate from the mean. A lower Variance gives a cleaner and smoother image. So the denoised image should sustain the mean of image and decrease its variance. A large ENL value corresponds to better speckle suppression, with infinity corresponding to ideal filtering. In a homogeneous region, one can also evaluate the radiometric preservation by comparing the value of the local mean backscattering reflectivity in the original and filtered images. A successful speckle reducing filter should not significantly alter the mean intensity within a homogeneous region.

ENL is preferred in many cases as it is the most commonly used measure, which provides an immediate insight about speckle reduction ability. Also it has a

compelling physical meaning as the number of looks needed to reach the same speckle suppression level guaranteed by filtering; and it can be computed also in the absence of a reference image, provided a flat region can be identified. However, on the down side it is not a good measure of despeckling performance in heterogeneous areas of an image as it depends on the presence and detectability of a relatively large flat region of the image. Also because of the variation of the incidence angle between near and far range, homogeneous areas exhibit a slight amplitude variation along the range direction, which obviously affects the ENL measures. Thus the subjective quality of the despeckled image through visual examination is also important. A refined version of ENL, referred to as ENL* [131] is also used in literature, which removes the image amplitude variation along range, by dividing values on each fixed-range line by their average, before computing the ENL. When the despeckling is very effective ENL* can differ significantly from the conventional ENL.

2.4.1.2 Mean of Ratio Image (MoRI)

In SAR images, when dealing with heterogeneous regions like textured areas and edges, the analysis becomes more complex. Texture, which represents the intrinsic spatial variability of a natural scene, is a precious feature to discriminate among different land-use types. Measuring its preservation, however, is not an easy task [107]. In case of edges, one can apply an edge detector on the filtered images and observe the resulting edge map.

Since speckle in SAR imagery is multiplicative noise, the ratio of the original SAR image to the despeckled one is the speckle. So the statistical characteristics of the ratio image can indicate the performance of the despeckling methods. For ideal filtering, the ratio image should be pure speckle. Thus, its mean should equal one, and its variance should be the inverse of the number of looks [121]. The mean of ratio image, MoRI is usually used to measure the degree of radiometric preservation. The mean closer to one means a better performance of radiometric preservation. In addition, this comparison provides information regarding a possible bias and whether the speckle is insufficiently filtered (the variance is lower than the theoretical value) or the scene texture is smoothed (the variance becomes larger than the theoretical value). In addition, the visual inspection of the

ratio image can provide information on the degree of edge-preservation in a region, as the presence of structures in ratio image indicates that they are filtered out from the original data. The ratio image can also give important indications on filtering artifacts which is often not so visible in the filtered image.

2.4.1.3 Edge Save Index (ESI)

The effectiveness of a despeckling algorithm in edge preservation can be assessed using a parameter called Edge Save Index, ESI [132]. It reflects the edge save ability in horizontal (ESI$_H$) or vertical (ESI$_V$) direction of the despeckling algorithm. The bigger the ESI, the stronger the edge save ability. The ESI can be computed using the following formulae:-

$$ESI_H = \frac{\sum_{x=1}^{p}\sum_{y=1}^{q-1}|\breve{F}_{x,y+1} - \breve{F}_{x,y}|}{\sum_{x=1}^{p}\sum_{y=1}^{q-1}|G_{x,y+1} - G_{x,y}|} \qquad (2.39)$$

$$ESI_V = \frac{\sum_{y=1}^{q}\sum_{x=1}^{p-1}|\breve{F}_{x+1,j} - \breve{F}_{x,y}|}{\sum_{y=1}^{q}\sum_{x=1}^{p-1}|G_{x+1,j} - G_{x,y}|} \qquad (2.40)$$

where G is the original noisy image, $\breve{F}$ is the reconstructed image, p is the row number and q is the column number of the image.

2.4.1.4 Signal-to-Clutter Ratio (SCR)

In SAR images, the speckle noise in extremely heterogeneous areas such as point targets, strong edges, or buildings, does not obey to a fully developed model. So during despeckling these areas should not be filtered at all, and their original value should be preserved. The performance assessment using the above mentioned measures cannot be applied to these areas. Here a new measure known as Signal to Clutter Ratio (SCR) can be used to evaluate the performance of preservation of strong point targets in SAR images [69]. SCR in decibels (dB) is defined as

$$SCR = 10\log_{10}\frac{\sum_i\sum_j|\breve{s}(x,y)|}{N\sigma_C} \qquad (2.41)$$

where $š(x, y)$ is the point target pixel value, N is the total number of point target pixels, and σ_C is the clutter standard deviation. A large SCR value corresponds to better speckle suppression.

2.4.2 Full-Reference Measures

The performance assessment becomes much simpler when a clean reference is available. In literature, both natural optical images and synthetic images with simple features such as uniform regions, textures, edges or strong scatterers are used as references. Synthetic SAR images are generated by applying a fully developed speckle field. In this case, one can easily compute all sorts of full-reference global distortion measures on the filtered image from the traditional mean-square error (MSE) up to most recent measures, like the structural similarity index, which try to provide more meaningful information about the closeness of two images. The proposed measures can be calculated globally or locally, if one is interested on the performance on specified areas. Through the clean reference, several objective measures are proposed to assess the edge-preservation capacity of the filters. In particular, one can generate synthetic images with edges of different slope, orientation and thickness and define indexes on a certain region of interest.
Here G, F and $\check{F}$ are available. Since all the three types of images are available, the no reference measures explained in the previous section also can be applied here.

2.4.2.1 Peak Signal-to-Noise Ratio (PSNR)

For synthetic speckle images and images corrupted with AWGN, the peak signal-to-noise ratio (PSNR) can be used to evaluate the performance. It is defined as

$$PSNR = 10 \log_{10}\left(\frac{R^2}{MSE}\right) \tag{2.42}$$

where R is the maximum fluctuation in the denoised image and *MSE* is representing the Mean Square Error between the despeckled image $\check{F}$ and the original reference image F. For an 8 bit image the value of R is 255.

$$MSE(\check{F}, F) = \frac{\sum_{x,y}\left(\check{F}(x, y) - F(x, y)\right)^2}{p \times q} \tag{2.43}$$

where p and q are the size of the image. To improve readability, the above result can be shown on a logarithmic scale by means of the related despeckling gain measure (DG) defined as

$$DG = 10 \, log10 \frac{MSE(\check{F},G)}{MSE(\check{F},F)} \tag{2.44}$$

Larger number of DG indicate better speckle rejection. The PSNR is the most commonly used full reference measure and this single measure can give the best assessment of any denoising or despeckling scheme.

2.4.2.2 Edge-correlation Factor (β-index)

The edge correlation parameter β is a metric which assesses the quality of the edge preservation [133]. It evaluates the correlation index between the high pass versions of the original and filtered images.

$$\beta = \frac{\sum_{i,j}\left(\Delta\check{F} - \Delta\bar{\check{F}}\right)(\Delta F - \Delta\bar{F})}{\sqrt{\sum_{i,j}\left(\Delta\check{F} - \Delta\bar{\check{F}}\right)^2 \sum_{i,j}(\Delta F - \Delta\bar{F})^2}} \tag{2.45}$$

where $\Delta\check{F}$ and ΔF are the high pass filtered outputs of $\check{F}$ and respectively obtained with a 3× 3 pixel standard approximation of the Laplacian operator. The over line operator represents the mean value. If the edges are optimally preserved in the despeckled or denoised image, then the value of β will be close to one.

2.4.2.3 Mean Structural Similarity Index Matrix (MSSIM)

Mean Structural Similarity Index Matrix (MSSIM) is a performance indicator which measures the structural similarity between a reference image and the despeckled or denoised image [134]. It is reported to be a more reliable metric for assessing the visual quality.

$$MSSIM(F,\check{F}) = \frac{1}{M}\sum_{j=1}^{M} SSIM(F_j, \check{F}_j) \tag{2.46}$$

where F and $\breve{F}$ are the reference and the despeckled images, respectively, M is the number of local windows in the image, SSIM is the Structural Similarity Index Matrix, $F_{j,}$ and $\breve{F}_j$ are the image contents at the jth local window. The SSIM is defined as

$$SSIM(F, \breve{F}) = \frac{(2\mu_F \mu_{\breve{F}} + C_1)(2\sigma_{F\breve{F}} + C_2)}{(\mu_F^2 + \mu_{\breve{F}}^2 + C_1)(\sigma_F^2 + \sigma_{\breve{F}}^2 + C_2)} \quad (2.47)$$

where μ_F and $\mu_{\breve{F}}$ are the estimated mean intensities and σ_F and $\sigma_{\breve{F}}$ are the standard deviations of the original reference image and the despeckled image respectively. The constants C_1 and C_2 are given as $C_1 = (K_1 D)^2$ and $C_2 = (K_2 D)^2$, respectively where $K_1, K_2 \ll 1$ and D is the dynamic range of the pixel values. $\sigma_{F\breve{F}}$ can be estimated as

$$\sigma_{F\breve{F}} = \frac{1}{N-1} \sum_{i=1}^{N} (F_i - \mu_F)(\breve{F}_i - \mu_{\breve{F}}) \quad (2.48)$$

where N is the size of the image.

2.4.2.4 Figure of Merit (FOM)

Pratt's figure of merit (FOM) is a performance measure for SAR images used to measure edge preservation in the despeckled SAR image [135]. It measures the distance of a given edge map from the reference edge map, penalizing both the suppression of true edges and the detection of false ones

$$P = \frac{100}{Max\{N_{DE}, N_{ID}\}} \sum_{i=1}^{N_{DE}} \frac{1}{1 + Kd_i^2} \quad (2.49)$$

where N_{ID} is the number of ideal edge pixels. N_{DE} is the number of detected pixels, and d_i is the distance between the ith detected edge pixel and the closest true edge

pixel. Here K is a calibration constant, which is an arbitrary penalty parameter and can be set as two for a stronger penalization of misplaced edge pixels. The factor $Max\{N_{DE}, N_{ID}\}$ penalizes the number of false edges. The smearing and offset effects are also included in the Pratt's measure to provide an impression of overall quality.

2.4.2.5 Edge-Preservation Index (EPI)

There are several objective performance measures available to assess the edge-preservation capacity of the filters. One can generate synthetic images with edges of different slope, orientation and thickness and define indexes on a certain region of interest. The edge-preservation index (EPI) [136] is one such parameter which is defined as follows:

$$EPI = \frac{\sum_{i=1}^{n}|\breve{F}_{i,1} - \breve{F}_{i,2}|}{\sum_{i=1}^{n}|F_{i,1} - F_{i,2}|} \tag{2.50}$$

where $F_{i,1}$, $F_{i,2}$, $\breve{F}_{i,1}$, and $\breve{F}_{i,2}$ are the values of the reference and filtered images, respectively, observed on the one pixel wide lines on both sides of the edge. Larger values correspond to a better edge retaining ability of the filter. Recently, a modified version of *EPI* called Edge-Preservation Index based on Ratio of Average (EPI-ROA) [137] was proposed. This is based on ratios rather than differences.

All of the above parameters need not be used for assessing the performance of a denoising or despeckling algorithm as some of these parameters give only redundant information. Thus in this thesis some of these parameters are only used for assessing the performance. These are selected based on the use of these parameters in the competing referred works.

<div align="right">

Chapter 3

Directionlet Transform

</div>

In the beginning of this chapter the background knowledge on wavelet theory is reviewed. The requirement of a multi resolution anisotropic transform with directional vanishing moments along multiple directions is then analysed. This follows the directionlet theory and construction of directionlet transform. The sparsity due to the anisotropy and any direction nature of directionlet is also illustrated. Then the polyphase representation of directionlet transform is presented. Finally an analysis on the computational complexity of directionlet transform as compared to wavelet transform and other directional transforms is presented.

3.1 Introduction

Over the last two decades the standard two-dimensional (2-D) wavelet transform (WT) has emerged as an efficient multi resolution analysis tool for images. But it fails to provide a compact representation in the presence of one-dimensional (1-D) discontinuities, like edges or contours. The main reason for this inefficiency is the *spatial isotropy* of the construction of the standard 2-D WT, that is, filtering and subsampling operations are applied equally along both the horizontal and vertical directions at each scale. The corresponding filters, obtained as direct products of the 1-D counterparts, are isotropic at all scales. However, discontinuity curves present in images are having highly anisotropic features and they are characterized by a geometrical coherence that cannot be properly captured by the isotropic transforms. Many wavelets that intersect such anisotropic objects generate many large magnitude wavelet coefficients. This is illustrated in a simple example in Figure 3.1. A simple image with one discontinuity along a smooth curve is represented by the two types of basis functions: isotropic and anisotropic. The

support of these basis functions is shown schematically as black rectangles. Figure 3.1 (a) shows the spatial frequency tiling of Standard 2-D WT for two iteration and figure 3.1 (b) shows its basis functions. The spatial frequency tiling of an anisotropic transform with anisotropic ratio of 1:2 along horizontal to vertical direction is shown in figure 3.1(c) for two iterations and figure 3.1 (d) shows its basis functions. It can be seen from these figures that the isotropic basis functions generate a large number of significant coefficients around the discontinuity, but the anisotropic basis functions trace the discontinuity line and produce just a few significant coefficients. Thus the requirement is anisotropic basis functions that can match anisotropic objects in images. However, the design of the anisotropic transforms that ensures an efficient matching between the basis functions and objects in images is challenging.

(a) (b)

(c) (d)
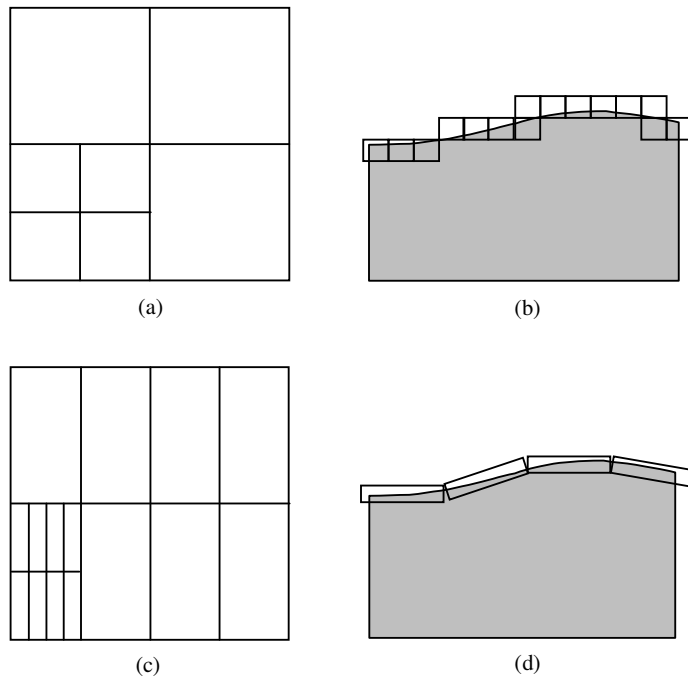
Figure 3.1 Representation efficiency of isotropic and anisotropic basis functions (a) frequency decomposition of 2-D WT for two iterations and (b) its basis functions. (c) frequency decomposition of an anisotropic transform with anisotropic ratio of 1:2 for two iterations and (d) its basis functions.

Anisotropic basis functions have already been tried in many transforms. This includes adaptive or signal dependent schemes like bandelets [34-35] and non-adaptive schemes like curvelet [20], contourlet [21], directional filter banks [22], wedgelets [23-24], Dual Tree Complex WT (DTCWT) [25], Shearlet [29-31] etc. These methods build dictionaries of anisotropic basis functions that provide a sparse representation of edges in images. However, most of these directional transforms often require oversampling, have higher computational complexity when compared to the standard DWT, and require non-separable convolution and filter design. Also in some of these schemes the transform directions are not adaptive to the dominant directions and filtering is done in continuous domain making it difficult to use them on discrete images.

3.2 2-D Wavelet Transform

The 2-D WT is designed in such a way that the filter bank used in it is fully separable. This enables to get the associated basis functions as the direct product of two independent 1-D basis functions in the horizontal and vertical directions. This method is conceptually simple and has very low computational complexity. The construction of the standard 2-D WT is shown in figure 3.2. The filtering and subsampling operations in the transform are iterated with an equal number of steps along both the horizontal and vertical directions at each scale. At the first stage the rows of the image to be transformed are low pass (L) and high pass (H) filtered and down sampled by two. In the next step each column of the row filtered image is again low pass (L) and high pass (H) filtered and down sampled by two. The output of this will have four sub band images labelled as LL, HL, LH and HH. Now the LL subband image goes through the same process of filtering and down sampling to form the next stage of the structure. The basic 1-D high-pass (HP) and Low Pass (LP) filters used in the transform are denoted as $H_1(z)$ and $H_2(z)$, respectively. The resulting filters, obtained as direct products of the 1-D counterparts, are isotropic at all scales resulting in four frequency bands as shown in figure 3.3(a). The corresponding isotropic basis functions for Haar and Biorthogonal wavelets and its Fourier transform are shown in figure 3.3(b), (c) and (d) respectively. The main limitation of such a construction is that it cannot properly capture the anisotropic features in images leading to an inefficient sparse representation in transform domain.
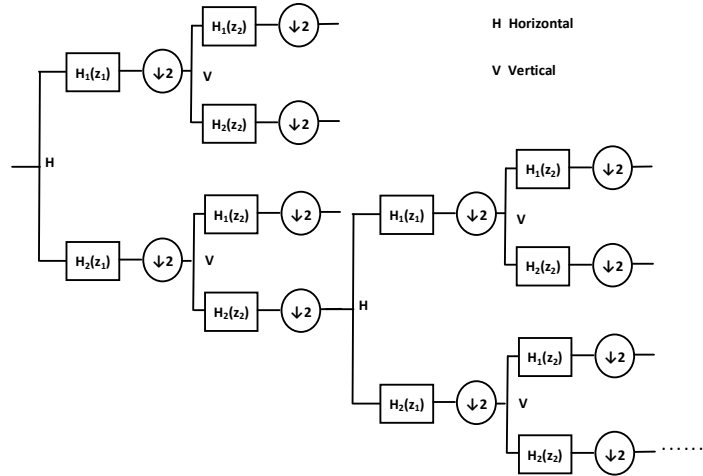
Figure 3.2 The filtering and subsampling operations in standard 2-D WT with two steps in each direction.
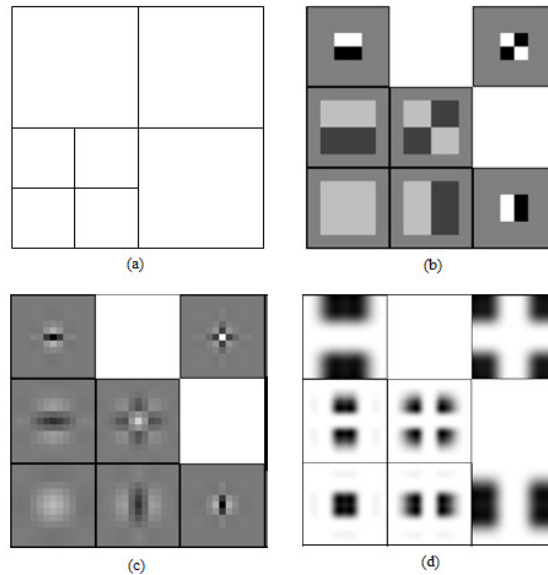
Figure 3.3 (a) The frequency decomposition of 2-D WT. The corresponding basis functions for (b) Haar and (c) biorthogonal - 9/7 wavelets (d) Fourier transform of the basis functions obtained from the biorthogonal - 9/7 1-D filters.

3.3 Fully Separable 2-D Wavelet Transform

To overcome the limitations of 2-D WT, a fully separable 2-D WT (FSWT) was proposed, which will improve compactness of the representation of images with discontinuities. In this transform a full 1-D WT is applied in the horizontal direction (each row of image) and then, on each output a full 1-DWT is applied in the vertical direction (each column). The decomposition scheme is shown in Figure 3.4. This type of decomposition is referred to as tensor wavelet basis [138-139]. The frequency decomposition of 2D FSWT with four steps in horizontal and vertical directions is shown in figure 3.5(a) and the corresponding anisotropic basis functions are shown in figure 3.5(b, c). The Fourier transform of the basis function is shown in figure 3.5(d). The FSWT are better adapted to the anisotropic objects such as the discontinuities in images. Due to this the representation efficiency is strongly improved in case of FSWT. However this also could not fully deal with the discontinuities in images resulting in an inefficient representation in the frequency domain.
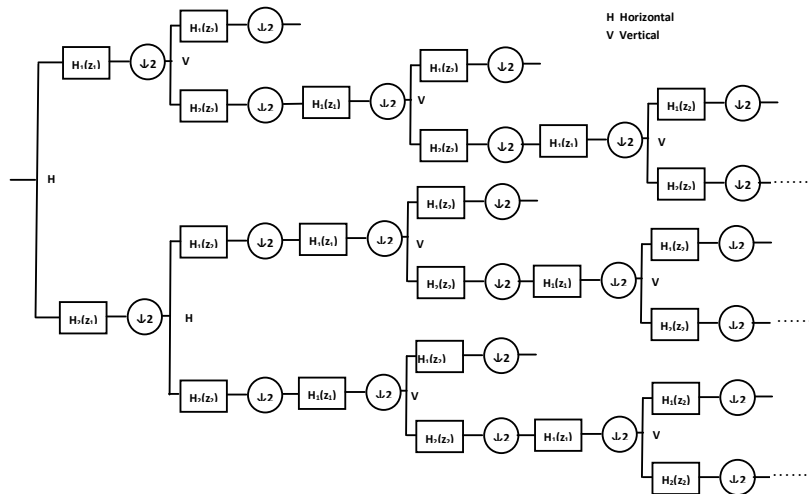
Figure 3.4 The filtering and subsampling operations in FSWT with two steps shown in each direction.
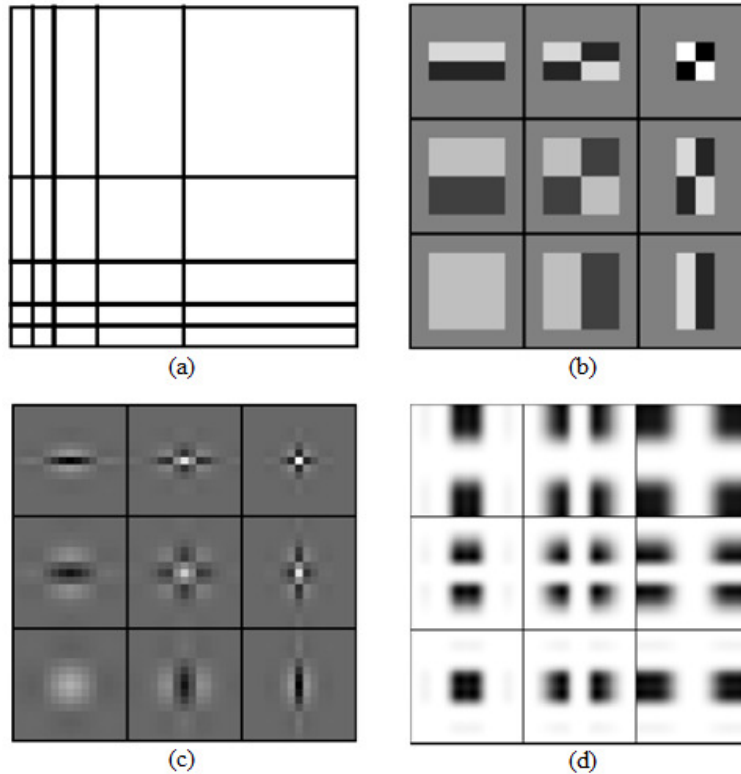
Figure 3.5 (a) The frequency decomposition of FSWT with 4 steps in horizontal and vertical directions. The anisotropic basis functions obtained from the (b) Haar and (c) biorthogonal-9/7 wavelet functions. (d) The corresponding Fourier transform of the basis functions obtained from biorthogonal-9/7 filters.

3.4 Anisotropic 2-D Wavelet Transform

In anisotropic WT (AWT) the number of transforms applied along the horizontal and vertical directions is unequal, that is, there are n_1 horizontal and n_2 vertical transforms at a scale, where n_1 is not necessarily equal to n_2. The unequal number of horizontal and vertical transforms will continue in the low pass sub-band, like in the standard wavelet transform. Such an anisotropic transform can be denoted as AWT(n_1, n_2). The anisotropy ratio $\rho = n_1/n_2$ determines elongation of the basis functions of the AWT(n_1, n_2). An example of construction of AWT is shown in

figure 3.6, where the AWT (2, 1) is used. The corresponding frequency decomposition and basis functions are shown in figure 3.7. The standard WT and the FSWT can be expressed in terms of the AWT. The standard WT is simply obtained by AWT (1, 1). However, the representation of the FSWT is more complex and it needs concatenation of two AWTs. The first transform is $\text{AWT}(n_{1max}, 0)$ that produces $n_{1max} + 1$ subbands and it is followed by the $\text{AWT}(n_{2max}, 0)$ applied on each subband. The arguments n_{1max} and n_{2max} determine the maximal number of transforms in the two directions and depend on the size of the image.

Even though the AWT is not the most appropriate representation for natural images, it improves approximation of more general classes of images. This type of transform can trace the discontinuity efficiently with fewer significant coefficients compared with standard WT due to the spatial anisotropy of its construction.
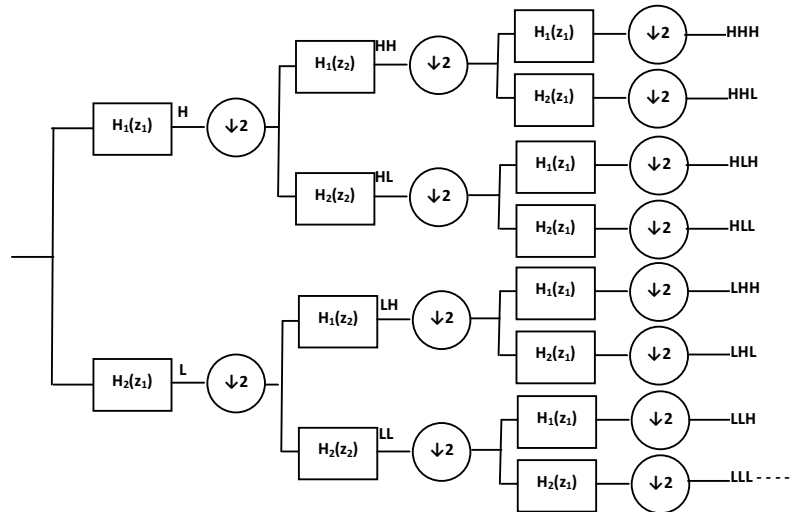
Figure 3.6 The filtering and subsampling operations in an AWT with anisotropic ratio of 1:2 is shown.
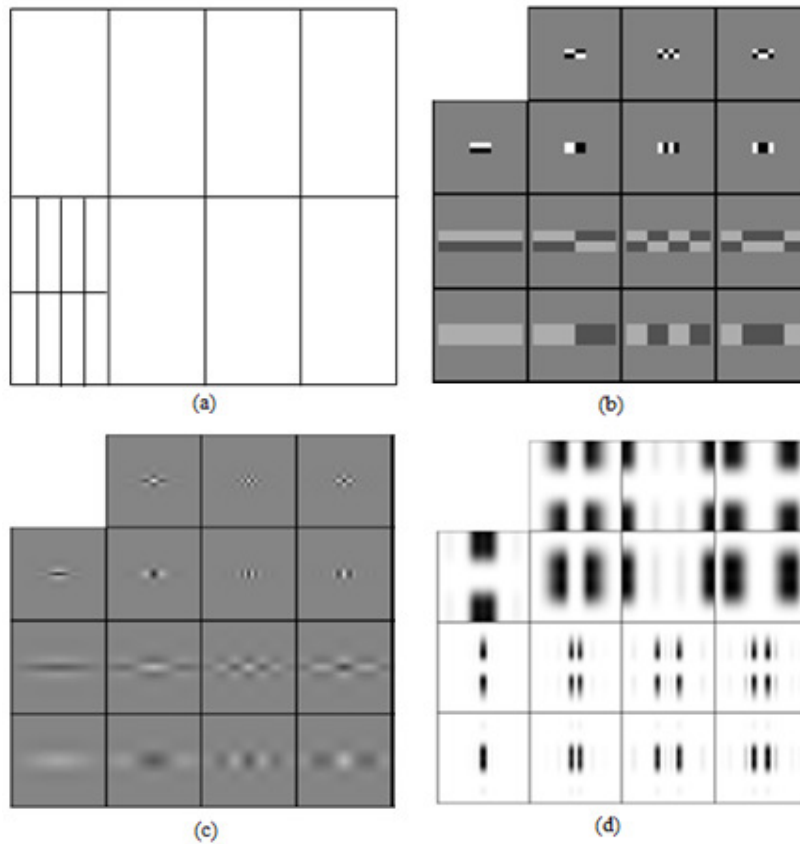
Figure 3.7 (a) The frequency decomposition of AWT(2,1) with one step of iteration. The corresponding basis functions obtained from the (b) Haar and (c) biorthogonal 9/7 1-D wavelet (d) The corresponding Fourier transform of the basis functions obtained from the biorthogonal 9/7 wavelet.

The main limitation with the above three transforms viz, WT, FSWT and AWT is that they are applied in the horizontal and vertical directions only and not along any other directions. Transforms involving more than the standard two directions will provide efficient representation of more general classes of images. These types of general transform can be obtained by imposing vanishing moments along different directions. Such a transform construction is explained in the next section.

3.5 Skewed Anisotropic 2-D Wavelet (Directionlet) Transform

The transform constructions that lead to anisotropic basis functions as explained in previous sections use only the horizontal and vertical directions. Due to this the high-pass (HP) filters in these transforms have vanishing moments only along these two directions. Since characterization of features in synthetic and natural images involves many more than these two standard directions, multi-directionality (M-DIR) and directional vanishing moments (DVM) are very important in achieving a good sparse representation. In this section a lattice-based anisotropic transform, which exploits multi directionality as proposed in [36] is presented.

To apply a discrete transform in the discrete space $\mathbb{Z}^2$ in a certain direction, the pixels that approximate the chosen direction need to be defined. This problem of defining the pixels in a particular direction was considered in computer graphics [140-142].

The set of points $(x, y) \in \mathbb{R}^2$ represents a continuous line with the slope r and intercept c if the following equality is satisfied:

$$y = rx + c \qquad (3.1)$$

A digital line $L(r, n)$ can be defined from the above equation by a discrete approximation as follows:-

$$y = \lceil rx \rceil + n, \ \forall x \in \mathbb{Z} \ for \ |r| \leq 1 \ or$$

$$x = \left\lceil \frac{y}{r} \right\rceil + n, \ \forall y \in \mathbb{Z} \ for \ |r| > 1. \qquad (3.2)$$

For every rational slope r, the set of digital lines $L(r, n): n \in \mathbb{Z}$ completely partitions the 2D discrete space $\mathbb{Z}^2$, meaning every pixel $(x, y) \in \mathbb{Z}^2$ is associated to only one of the digital lines with slope r. This is a mandatory requirement to preserve critical sampling in the transform. The concept of digital lines is useful for undecimated multi-directional representation. However they do not provide an efficient framework when transforms are applied in different directions and critical sampling is enforced. This is basically due to two issues. The first one is the

directional interaction and the other one is lack of *systematic subsampling*. These issues are discussed here.

Let us consider an image with two dominant directions with the rational slopes $d_1 = \frac{b_1}{a_1}$ and $d_2 = \frac{b_2}{a_2}$, where a_1, b_1, a_2, b_2 are integers. To simplify the notation, the two slopes can be jointly denoted by the following matrix:-

$$M(r_1, r_2) = \begin{bmatrix} a_1 & b_1 \\ a_2 & b_2 \end{bmatrix} = \begin{bmatrix} d_1 \\ d_2 \end{bmatrix} \tag{3.3}$$

To provide a sparse representation of this image, a 1-D WT is applied along the digital lines, $L(r, n): n \in \mathbb{Z}$. This produces two types of nonzero coefficients, that is, the coefficients corresponding to the discontinuities with the slopes d_1 and d_2.

Since the HP filter has vanishing moments along digital lines with the slope d_1, the coefficients along this direction are annihilated in the HP subband, while the coefficients along the second direction with the slope d_2 are retained in both the subbands. However, after subsampling, unlike in the case of the standard directions, the coefficients along the second direction are not aligned, that is, they cannot be clustered in the digital lines with the slope d_2. Therefore, the following 1-D WT applied along the digital lines with the slope d_2 does not annihilate the coefficients along the second direction, and, hence, it yields a non-sparse representation. This phenomenon is called *directional interaction*. To illustrate this phenomenon, a simple class of piecewise polynomial image known as $Mondrian(k_1, k_2)$ is used. This image contains $M \times M$ piecewise polynomial images with k_1 horizontal and k_2 vertical discontinuities. A 1-D WT is applied on an image from the class S-Mondrian $(M(-1/2, 2/3)1,1)$ along the digital lines $L(-1/2, n)$ and is shown in figure 3.8. The HP filtering annihilates the digital line with the slope $-1/2$. However, the nonzero coefficients produced by the other line with the slope $2/3$ are not aligned in the digital lines $L(2/3, n)$. Also the concept of digital lines does not provide a systematic rule for subsampling in the case of iteration of the filtering and subsampling operations along the directions with the slopes and when critical sampling is enforced. Although the transform along digital lines is efficient when applied in oversampled schemes, it fails to provide a systematic subsampling method when critical sampling is enforced. To overcome

the *directional interaction* and to carry out an organized iterated subsampling, the concept of integer lattices can be used.

$$M_\Lambda = \begin{bmatrix} 2 & -1 \\ 3 & 2 \end{bmatrix}$$
Haar high pass filtering along $-\frac{1}{2}$
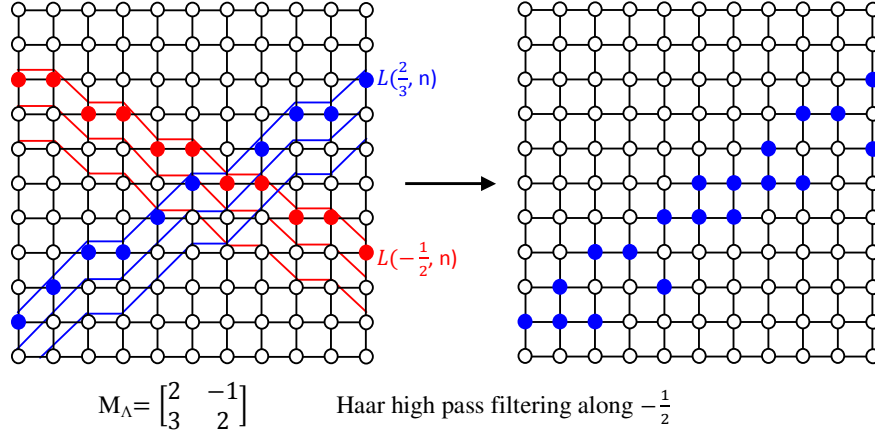
Figure 3.8 Illustration of directional interaction when filtering is done along digital lines

Instead of applying a transform along digital lines, integer lattices [143] based transform can be used. Any integer lattice Λ is a sub-lattice of the cubic lattice $\mathbb{Z}^2$. Here the lattice Λ can be represented by a non-unique generator matrix M_Λ.

$$M_\Lambda = \begin{bmatrix} a_1 & b_1 \\ a_2 & b_2 \end{bmatrix} = \begin{bmatrix} d_1 \\ d_2 \end{bmatrix} \tag{3.4}$$

Where a_1, b_1, a_2, $b_2 \in \mathbb{Z}$. and d_1 and d_2 are two linearly independent integer vectors. The linear combination of these two vectors will form the points of the lattice Λ.

In lattice based transform the discrete space is first partitioned using integer lattices before performing 1-D filtering along lines across the lattice. The integer lattice Λ is a sub-lattice of discrete space $\mathbb{Z}$ which can be partitioned into $|M_\Lambda|$ cosets, where each coset is determined by the shift vector, $S_k \in \mathbb{Z}$, for $k = 0, 1, 2, ... |M_\Lambda| - 1$. The integer lattice Λ with the corresponding generator matrix given by (3.4) partitions each digital line with slopes d_1 and d_2 into co-lines $CL_{sk}(d_1, n)$ and $CL_{sk}(d_2, n)$ respectively as shown in Figure 3.9. The intersection between a coset and a digital

line is known as a co-line. The filtering and sub sampling operations are applied on the pixels in each of the cosets separately. Note that each filtering operation is purely 1D. After subsampling, the retained points belong to the sub lattice $\Lambda^{'}$ of the lattice Λ ($\Lambda^{'} \subset \Lambda$) with the corresponding generator matrix given by (3.5)

$$M_{\Lambda'} = Ds * M_{\Lambda} = \begin{bmatrix} 2d_1 \\ d_2 \end{bmatrix} \qquad (3.5)$$

Here, Ds is the horizontal subsampling operator, that is $\quad D_s = \begin{bmatrix} 2 & 0 \\ 0 & 1 \end{bmatrix}$

Applying the 1-D filtering and sub sampling on the co-lines $CL_{sk}(d_1, n)$ will not disturb those operations along $CL_{sk}(d_2, n)$, means the retained pixels after these operations belong to the same co-lines as they were before. The filtering and sub sampling operations are applied on the pixels along the vector d_1 in each of the cosets separately. Since these operations are applied in each coset separately, the pixels retained after this operations are clustered along the vector d_2. The direction of vector d_1 is called the transform direction and d_2 the alignment direction. Here, since the filtering and subsampling are applied in each coset separately, the pixels retained after the subsampling are clustered in co-lines along the alignment direction. This is shown in figure 3.10. The nonzero pixels obtained after one step of the lattice-based filtering operation applied on the same example as in Figure 3.8 are clustered now in the digital lines with the slope 2/3. Due to this the directional interaction is avoided here.

The lattice-based transforms can avoid directional interaction and are capable of providing the same order of approximation as the FSWT achieves for the same class of image. The skewed versions of the standard WT, FSWT, and AWT can be constructed using integer lattices. Given a lattice Λ , the skewed transforms are applied along co-lines in the transform and alignment directions of the lattice Λ, retaining the same frequency decompositions as the corresponding transforms along the standard directions. Notice that the skewed transforms are applied in all cosets of the lattice Λ separately. The basis functions of the skewed transforms have DVM in *any* two directions with rational slopes. The corresponding basis functions are shown in Figure 3.11 for the directions along the vectors $d_1 = [1, 1]$ and $d_2 = [-1, 1]$.

$$M_\Lambda = \begin{bmatrix} 2 & 1 \\ -1 & 1 \end{bmatrix}$$

$$Det(M_\Lambda) = 3$$

$$r_1 = \tfrac{1}{2} \qquad r_2 = -1$$

★$CL_{[0,0]}\left(\tfrac{1}{2},n\right)$ ◆$CL_{[0,1]}\left(\tfrac{1}{2},n\right)$ ●$CL_{[1,1]}\left(\tfrac{1}{2},n\right)$ ◆$CL_{[0,0]}(n,-1)$ ★$CL_{[0,1]}(n,-1)$ ●$CL_{[1,1]}(n,-1)$
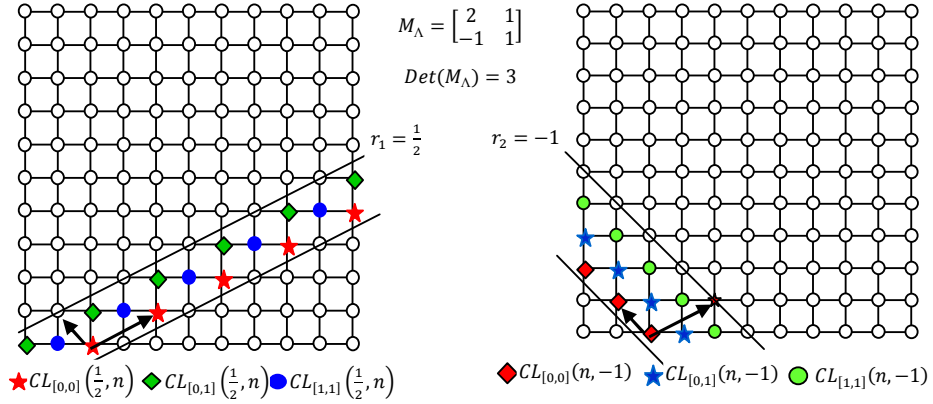
Figure 3.9 The intersections between the 3 cosets of the lattice Λ given by the generator matrix M_Λ and the digital lines with slope $r_1 = {}^1/_2$. The co-lines are $CL_{[0,0]}\left(\tfrac{1}{2},n\right), CL_{[0,1]}\left(\tfrac{1}{2},n\right)$ and $CL_{[1,1]}\left(\tfrac{1}{2},n\right)$.

$L(\tfrac{2}{3}, n)$

$L(-\tfrac{1}{2}, n)$

$$M_\Lambda = \begin{bmatrix} 2 & -1 \\ 3 & 2 \end{bmatrix}$$ Haar high pass filtering along $-\tfrac{1}{2}$
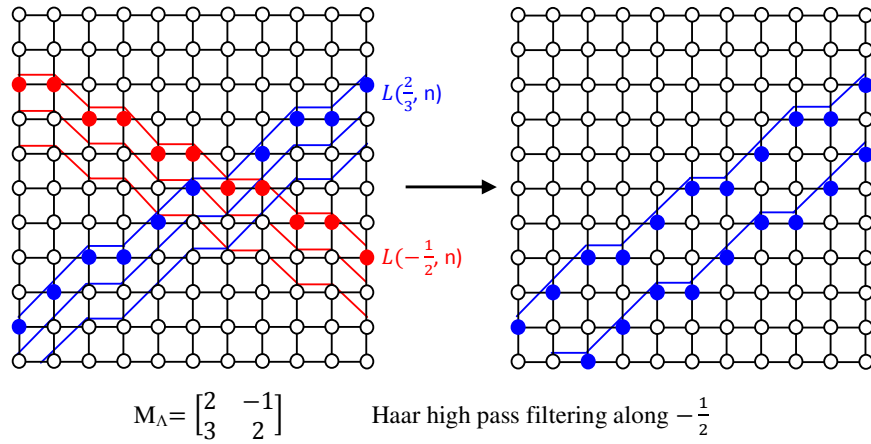
Figure 3.10: The lattice-based filtering and subsampling which has avoided the directional interaction.

79
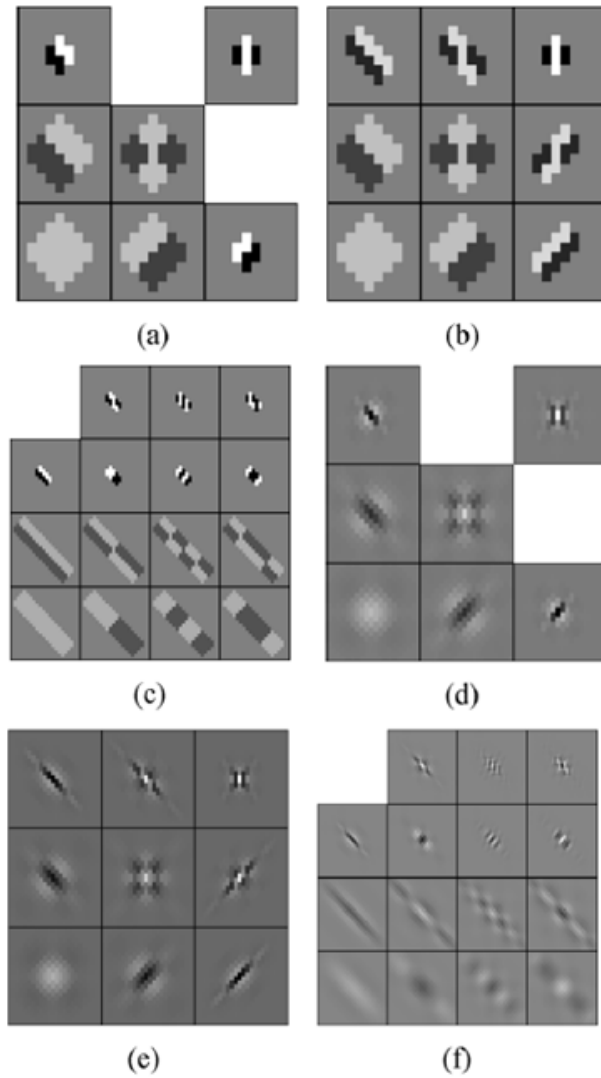
Figure 3.11 Basis functions obtained by the skewed transforms using the Haar 1-D scaling and wavelet functions: (a) S-WT, (b) S-FSWT, and (c) S-AWT ($\mathbf{M}_\Lambda, 2, 1$) (directionlets). The same, but with the biorthogonal-9/7 1-D scaling and wavelet functions: (d) S-WT, (e) S-FSWT, and S-AWT ($\mathbf{M}_\Lambda, 2, 1$) (directionlets).

The lattice based anisotropic transform, which will avoid directional interaction, is called Skewed AWT, denoted as SAWT($\mathbf{M}_\Lambda, n_1, n_2$). The basis functions of S-AWT are called directionlets, which can be effectively used for directional analysis of images. An example of construction of directionlets based on integer lattices is shown in figure 3.12 for pair of direction ($45°$, $135°$) with anisotropic ratio of 1:1 and 1:2. Here the two cosets are shown in white and black circles.

Coset 1 ○   Coset 2 ●

$$M_\Lambda = \begin{bmatrix} 1 & 1 \\ -1 & 1 \end{bmatrix} \qquad M'_{\Lambda_1} = \begin{bmatrix} 2 & 2 \\ -1 & 1 \end{bmatrix} \qquad M_{\Lambda_1} = \begin{bmatrix} 4 & 4 \\ -2 & 2 \end{bmatrix}$$
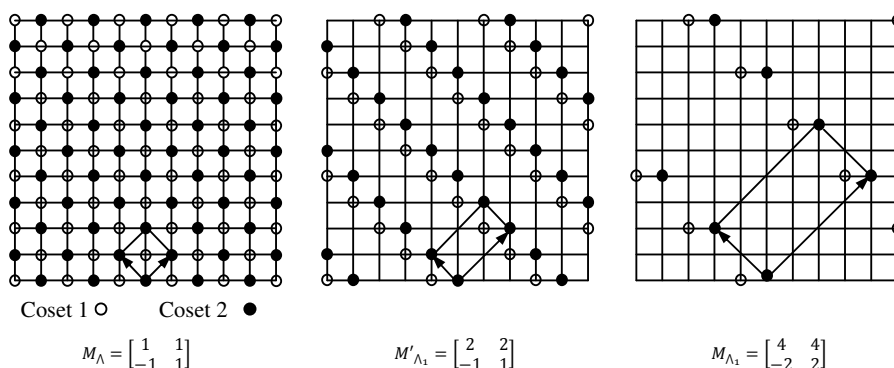
Figure 3.12 Construction of directionlets based on integer lattices for pair of directions ($45°$, $135°$) with anisotropic ratio of 1:1 and 1:2. Here $d_1 = [1,1]$ and $d_2 = [-1,1]$.

The SAWT($\mathbf{M}_\Lambda, n_1, n_2$) is implemented as a stage transformation. In every scale, it decomposes an image into ($2^{n_1+n_2} - 1$) detail subbands and one approximation subband. The approximation subband will have ($2^{n_1+n_2} - 1$) number of orientations. All these subbands are anisotropic with an anisotropic ratio of $n_2 : n_1$. The corresponding basis functions in the space domain will have an aspect ratio of $n_1 : n_2$ in the horizontal-to-vertical directions. This scheme is iterated on the approximation subband to obtain coarser subbands and can be implemented by a 2-D separable filter bank. As an example, the AWT (2, 1) produces eight subbands as shown in figure 3.6. At the first stage the rows of the image to be transformed are low pass (L) and high pass (H) filtered and down sampled by two. In the next step each column of the row filtered image is again low pass (L) and high pass (H) filtered and down sampled by two. The output of this will have four sub band images labelled as LL, HL, LH and HH. As a next step each row of these sub band images are again low pass (L) and high pass (H) filtered and down sampled by two.

This will produce eight bands viz. HHH, HHL, HLH, HLL, LHH, LHL, LLH, and LLL. Now the LLL subband image goes through the same process of filtering and down sampling to form the next stage of the structure.

Efficiency of representation of an image by a skewed transform depends on matching between the directions of discontinuities in the image and the directions used in the transform. The skewed versions of the transforms SWT, SFSWT & $SAWT(M_\Lambda, 2, 1)$, where $M_\Lambda = M(d_1, d_2)$ are applied to the image S-Mondrian $(M(d_1, d_2)k_1, k_2)$ and the different resolution levels are shown in Figure 3.13. For the case of class S-Mondrian $(M(d_1, d_2)k_1, k_2)$ the orders of nonzero coefficients in band-pass subbands are given in Table 3.1. Table 3.2 summarizes the orders of nonzero coefficients in band-pass subbands in the case of both matched and mismatched directions.
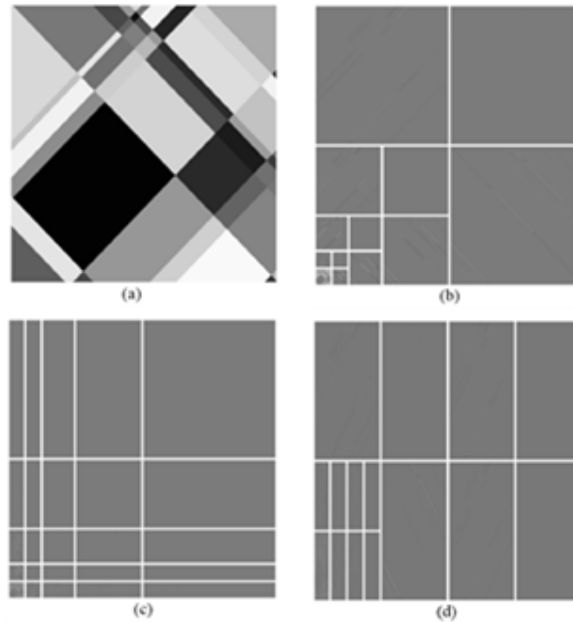
Figure 3.13 (a) Example of an image from the class S-Mondrian $(M(d_1, d_2)k_1, k_2)$, for $M = [v_1 ; v_2]^T$, where $v_1 = [1; 1]$ and $v_2 = [-1; 1]$. The image is transformed using (b) S-WT, (c) S-FSWT, and (d) $SAWT(M_\Lambda, 2, 1)$, where all the transforms are built on the lattice Λ determined by the generator matrix $M_\Lambda = M(d_1, d_2)$.

TABLE 3.1 Orders of approximation by the standard WT, FSWT and AWT
applied on the *class S-Mondrian* (k_1, k_2)

Standard WT	FSWT	AWT
$(k_1 + k_2)M$	$(k_1 + k_2)(\ln M)^2$	$\left(k_1 a + {k_2}/{a}\right)M$

TABLE 3.2 Orders of approximation by the standard WT, FSWT and AWT
applied on the *class S-Mondrian* $(M(d_1, d_2)k_1, k_2)$

	Standard WT	FSWT	AWT
Matched Direction	$(k_1 + k_2)M$	$(k_1 + k_2)(\ln M)^2$	$\left(k_1 a + {k_2}/{a}\right)M$
Un matched Direction	$(k_1 + k_2)M$	$(k_1 + k_2)M$	$(k_1 + k_2)M$

In the multi scale DT decomposition, each coefficient, except the ones at the finest scale, has a certain number of children. The number of children that each coefficient can have varies depending on the anisotropic ratio of the transform. The DT with two horizontal transforms and one vertical transform will have eight children at the next scale. The WT will always have four children. The interscale dependency is shown in figure 3.14(a) in case of WT and in figure 3.14(b) in case of DT. Here the case of $DT(\mathbf{M}_{\Lambda J}, 2, 1)$ is considered, where the generator matrix $\mathbf{M}_{\Lambda J} = \begin{bmatrix} d_1 & d_2 \end{bmatrix}^T$ with $d_1 = \begin{bmatrix} 1 & 1 \end{bmatrix}$ and $d_2 = \begin{bmatrix} 0 & 1 \end{bmatrix}$. The dependent children are identified as in the case of standard zero tree structure. Here the children correspond to the same spatial location and orientation as the parent coefficient. In the case of WT, the set of children is isotropic and aligned along the horizontal and vertical directions. On the other hand, in the case of DT, since directionlets are anisotropic and oriented in different directions, the corresponding children are grouped in anisotropic and oriented sets. The corresponding parent-children relation is illustrated in figure 3.15 for WT and in figure 3.16 for DT. The anisotropy and orientation of the sets of children is the same as that used in the construction of directionlets. But it still retains the property of grouping coefficients across scales that belong to the same spatial location.

The directionlet transform is not shift invariant because of the decimation operation involved in the transform construction. In image processing applications, a small shift in the input signal can cause very different output wavelet coefficients. One way of overcoming this is by taking the transform without decimation. The drawback of this approach is that it is computationally inefficient, especially in multiple dimensions. In the multi resolution analysis, the oversampled transforms have been shown to lead to better denoising performance than critically sampled transforms. For that reason, undecimated versions of transforms are preferred for denoising algorithms. In undecimated directionlet transform the oversampling is imposed in the same way as in the case of the undecimated wavelet transform, that is, by discarding the sub-samplers in the filter-banks of figure 3.6. The filters used for DT are up sampled across scales. Thus, if the LP filter $H_2(Z_1)$ is used in first level 1-D wavelet filter-bank, the equivalent LP filter at the jth scale is $H_2\left(Z_1^j\right)$, where $j = 1….J,$ corresponds to the scale index sweeping from the finest to the coarsest scale. Such a construction results in a shift-invariant transform with a preserved number of coefficients in each subband.

(a)   (b)
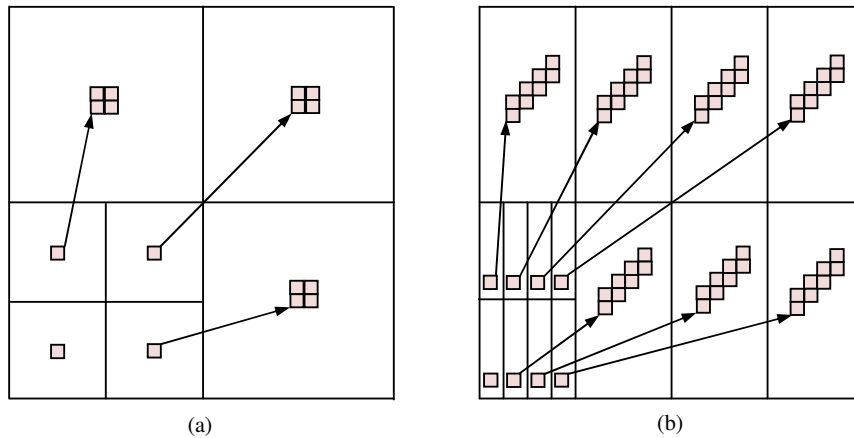
Figure 3.14 Interscale dependencies of a) wavelet transform coefficients and b) directionlet transform coefficients along 90º and 45º.

$$M_{\Lambda_j} = \begin{bmatrix} 1 & 1 \\ 0 & 1 \end{bmatrix} \qquad\qquad M_{\Lambda_{j+1}} = \begin{bmatrix} 4 & 4 \\ 0 & 2 \end{bmatrix}$$
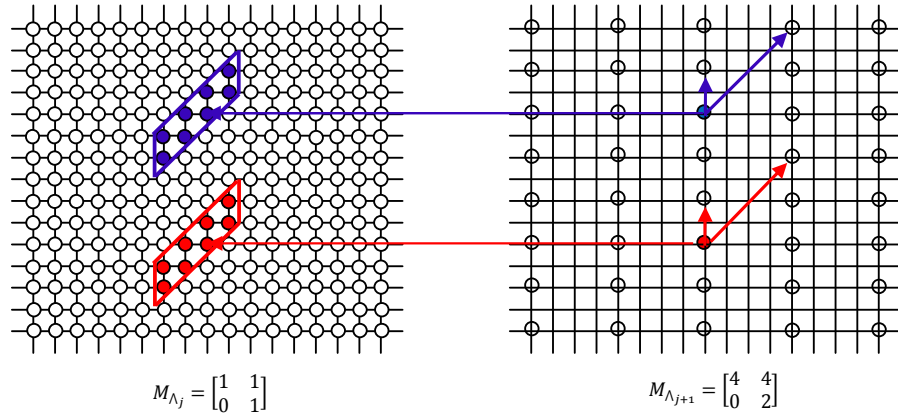
Figure 3.15 The parent child relationships for DT($\mathbf{M}_{\Lambda_J}$, 2, 1). The subbands at the coarser scale $j+1$ are defined across the lattice Λ_{j+1} with the generator matrix $M_{\Lambda_{j+1}}$. Each coefficient has a set of children at the next finer scale j. The children belong to the same orientation as their parent and are located in the parallelepiped around the spatial location of their parent.

$$M_{\Lambda_j} = \begin{bmatrix} 1 & 0 \\ 0 & 1 \end{bmatrix} \qquad\qquad M_{\Lambda_{j+1}} = \begin{bmatrix} 2 & 0 \\ 0 & 2 \end{bmatrix}$$
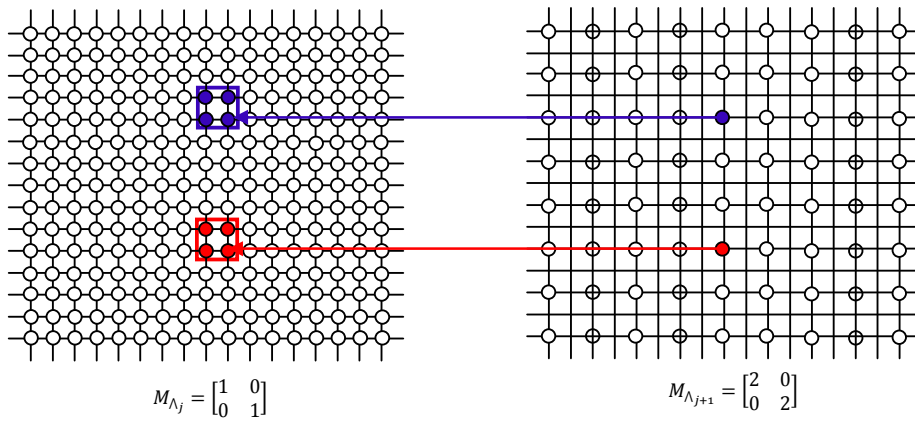
Figure 3.16 Zero-tree hierarchical structure of wavelet transform coefficients

2.4 Polyphase Representation of Directionlets

The lattice based filtering and sub sampling operations in directionlet transform can be efficiently represented in the polyphase domain. A two-channel 1-D filter-bank with transfer function $[H_0(z), H_1(z)]$ followed by a sub sampler by the factor 2 can be given in terms of the polyphase components [143] as

$$H_0(z) = H_{00}(z^2) + zH_{01}(z^2) \text{ and}$$

$$H_1(z) = H_{10}(z^2) + zH_{11}(z^2)$$

Here, H_{00}, H_{01}, H_{10}, and H_{11} are the polyphase components of the filters $H_0(z)$ and $H_1(z)$ that correspond to even and odd samples of the impulse response, respectively. The corresponding polyphase representation is shown in Figure. 3.17.
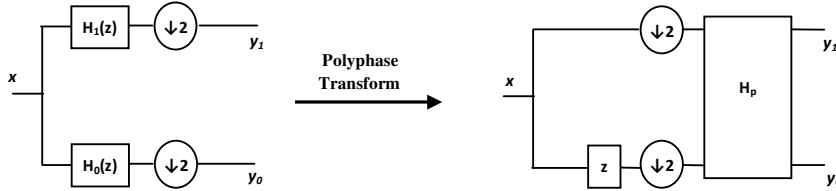
Figure. 3.17. One-dimensional filter-bank $[H_0(z), H_1(z)]$ with the subsampling factor 2 is represented in the poly phase domain with the corresponding poly phase components, H_{00}, H_{01}, H_{10}, and H_{11}

$$H_p = \begin{bmatrix} H_{00}(z) & H_{01}(z) \\ H_{10}(z) & H_{11}(z) \end{bmatrix}$$

The equivalent polyphase components of a 2-D filter-bank $[H_0(z), H_1(z)]$, where $= (z_1, z_2)$, can be found for the lattice-based scheme of DT. Here the filters $H_0(z)$ and $H_1(z)$ used are are purely 1-D filters, that is, $H_0(z) = H_0(z_1)$ and $H_1(z) = H_1(z_1)$. Since the lattice-based filtering and subsampling in DT are applied in each coset of the lattice separately, the equivalent scheme has two sections. The first section does the separation into two cosets and the second one do 1-D filtering and sub-sampling in the transform direction. This is illustrated in Figure. 3.18(a) for DT($\mathbf{M}_\Lambda, 2, 1$), where the generator matrix, $\mathbf{M}_\Lambda =$

$[d_1 \quad d_2]^T$ with $d_1 = [1 \quad 1]$ and $d_2 = [-1 \quad 1]$ and sub sampling matrix $D_s = [r_1 \quad r_2]^T$ with $r_1 = [2 \quad 0]$ and $r_2 = [0 \quad 1]$. Notice that filtering in the transform direction is performed as horizontal filtering proceeded by rotation by the generator matrix. Since the total subsampling rate is $|Det(D_s. \mathrm{M}_\Lambda| = 4$, the polyphase representation of such a filter-bank consists of four polyphase components. The equivalent polyphase representation is shown in Figure. 3.18(b), where the polyphase transform H_p is block-diagonal as given below.

$$H_p = \begin{bmatrix} H_{00}(Z_1) & H_{01}(Z_1) & 0 & 0 \\ H_{10}(Z_1) & H_{11}(Z_1) & 0 & 0 \\ 0 & 0 & H_{00}(Z_1) & H_{01}(Z_1) \\ 0 & 0 & H_{10}(Z_1) & H_{11}(Z_1) \end{bmatrix}$$
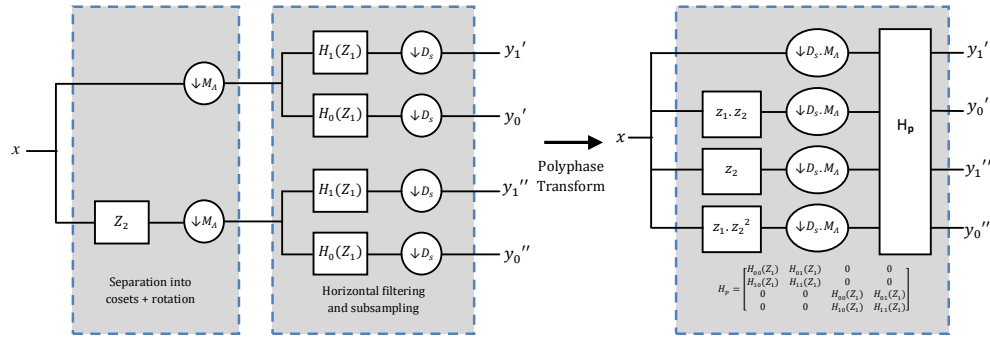
Figure 3.18. 2-Dimensional two-channel filter-bank of $DT(\mathbf{M}_\Lambda, 2, 1)$ and its equivalent polyphase representation

Notice that the block-diagonal polyphase transform with two identical blocks is a consequence of the separable transforms applied across cosets. This property allows for a simple filter design and computational efficiency in the polyphase domain. Such separability in the polyphase domain has also been used in other 2-D filter-bank designs [144-145].

2.5 Computational Complexity of Directionlets

The computational complexity of DT is similar to that of 2-D WT which is in the order of $N^2.L$. Each filtering operation is performed in $N.L$ multiplications and $N.L$ additions. Here N is the number of input samples and L is the length of the applied filter. The extra computation is due to the anisotropic nature of DT. The computational complexity is substantially lower than other similar schemes like bandlets, which require $N^2(log_2N)^2$ operations and contourlets, which require $L_1.L_2N^2$ operations, where $L_1\ and\ L_2$ is the size of the 2-D filters. The Wedgeprints require N^2log_2N operations. Thus as compared to other popular directional transforms, the directionlet transform require only less number of computations. However the true benefit of DT comes from the identification of local dominant directions in an image by spatial segmentation and decomposition of these spatial segments using the anisotropic transform along the dominant direction. Thus for the better identification of directional features using DT, extra computations are required for segmentation and content direction identification. This adds to the computational complexity of DT based applications. So there is always a trade off between the computational efficiency and denoising performance in DT based denoising schemes.

2.6 Conclusions

In this chapter, the concept of anisotropic transform construction is presented through fully separable WT and anisotropic WT. These transforms retain the simplicity of separable filtering and subsampling from the standard 2-D WT and provide anisotropic basis functions that can capture more efficiently anisotropic features in images, like edges and contours. Further to this an anisotropic transform with directional vanishing moments along any two directions is presented. The lattice based construction and the polyphase representation of this transform is also presented. The computational complexity of directionlet transform as compared to other directional transforms is also analyzed here.

Chapter 4

Spatially Adaptive Image Denoising in Directionlet Domain

In this chapter the main contributions to image denoising are presented. Four different denoising schemes in directionlet domain are presented for images corrupted with additive white Gaussian noise. The results are compared with the state of the art transform domain denoising techniques. The computational complexities of these schemes are also analysed here.

4.1 Introduction

This chapter presents the main contributions of the thesis in the area of image denoising. The images corrupted with additive white Gaussian noise (AWGN) are considered here. Four different denoising schemes in directionlet domain are presented here. These include two threshold based schemes and two statistical model based schemes. All these schemes are in line with wavelet transform based schemes with several modifications due to the implementation in directionlet domain. The presented schemes are compared with the similar schemes in wavelet domain and also with other directional transform based denoising schemes.

As in any transform based denoising, the directionlet based denoising algorithms basically involve three steps. First, an image is transformed into directionlet domain. Next, denoising is effected on the directionlet coefficients, and finally the denoised image is obtained by applying the inverse directionlet transform on the denoised directionlet coefficients. The principle of denoising in directionlet domain is illustrated in figure 4.1.
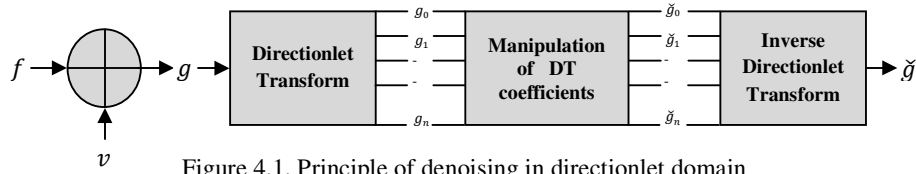
Figure 4.1. Principle of denoising in directionlet domain

The directionlet based denoising schemes can be broadly classified into two; the threshold based schemes and statistical model based schemes. In threshold based methods, a DT coefficient is compared with a given threshold and is set to zero if its magnitude is less than the threshold; otherwise it is kept unmodified or modified depending on hard or soft thresholding rules, respectively. As like Wavelet based denoising schemes, these schemes are based on the idea that the energy of the signal to be defined concentrates on some of the transform coefficients, while the energy of noise spread throughout all coefficients. Similarity between the basic wavelet and the signal to be defined plays a very important role, making it possible for the signal to concentrate on fewer coefficients. The effectiveness of these methods depends on the estimation of the correct threshold. In statistical model based schemes, the WT coefficients are modelled using a suitable prior probability distribution function and the noise free coefficients are estimated using this *a priori* information with Bayesian estimation techniques, such as the *maximum a posteriori* (MAP) estimator. The challenging part of these schemes is the effective modelling of the statistics of the images. If these models are well chosen, the noise can be efficiently removed. In literature several models have been considered for the noise-free wavelet coefficients and Gaussian model for the noise coefficients. The main thrust here is the computation of a proper threshold in threshold based schemes and the accurate modelling of the directionlet transform coefficients in case of statistical model based schemes.

4.2 SURE Thresholding in Directionlet Domain

Here a novel denoising scheme which is in line with the 3-band 2-D wavelet transform based schemes is presented. This scheme is evidently not better than the state of the art denoising schemes. However through this scheme we intent to introduce the concept of denoising in directionlet domain. It is noteworthy that as

compared to the similar schemes in wavelet domain, this simple scheme in directionlet domain is much better in terms of numerical and visual qualities.

The proposed algorithm involves mainly three steps. First transform the input image using directionlet transform, then threshold the transform coefficients using a non-linear algorithm and finally reconstruct the image using the modified coefficients. The effectiveness of a denoising algorithm basically depends on two factors- one is the efficient representation of the image to be denoised using a local, directional and multi resolution expansion and second is the efficient computation of an optimal threshold. Here the first requirement is met by using a locally adaptive directionlet transform and the second by optimal threshold computation using Steins' Unbiased Risk Estimate (SURE).

4.2.1 Image Noise Model & SURE Threshold Computation

Suppose that the image f, with N number of pixels, is polluted by independent and identically distributed (*i.i.d*) white Gaussian noise, v with zero mean and σ^2 variance, the observed image g is described as

$$g = f + v \tag{4.1}$$

In denoising applications, the performance is often measured in terms of peak signal-to-noise ratio (PSNR). The aim of image denoising is naturally to maximize the PSNR and, thus, to minimize the minimum mean square error (MSE). Here the objective is to estimate image f with minimum MSE, i.e., to minimize l_2 risk, $R(\hat{f}, f)$ for a given noisy image, as follows

$$R(\hat{f}, f) = \frac{1}{N} \left\| \hat{f} - f \right\|^2 = \frac{1}{N} \sum_{i=0}^{N-1} (\hat{f}_i - f_i)^2 \tag{4.2}$$

where $\hat{f}$ is the estimate of f from g. Here mean is used instead of mathematical expectation, because the optimal solution is desired for each individual noisy function. Here, f can be estimated using a point wise function of g as

$$\hat{f} = x(g) \tag{4.3}$$

where $x(g)$ is a function from $\mathbb{R}^N$ to $\mathbb{R}^N$. Here the goal is to find the function $x(g)$ that minimizes the MSE and thus $R(\hat{f}, f)$.

$$R(\hat{f}, f) = \frac{1}{N} \left\| \hat{f} - f \right\|^2 = \frac{1}{N} \left\| x(g) - f \right\|^2 \tag{4.4}$$

$$R(\hat{f}, f) = \frac{1}{N} \left(\|x(g)\|^2 - 2\|x(g)f\| + \|f\|^2 \right) \tag{4.5}$$

In practice, the noisy signal, g only is accessible and not the original signal, f. Thus the explicit dependence on f need to be removed from equation (4.5). Note that, since $\|f\|^2$ has no influence in the minimization process of $R(\hat{f}, f)$, this need not be estimated. Charles Stein [42] introduced a method for estimating the loss $\left\| \hat{f} - f \right\|^2$ in an unbiased fashion. For a nearly arbitrary, nonlinear, biased estimator one can nevertheless estimate its loss unbiased. When $x(g)$ is weakly differentiable, then

$$E_f \left\| x(g) - f \right\|^2 = N + E_f \left\{ \|x(g)\|^2 + 2\nabla_g x(g) \right\} \tag{4.6}$$

where,

$$\nabla_g x(g) = \sum_{i=0}^{N} \frac{\partial x_i}{\partial g_i} \tag{4.7}$$

Now consider the soft threshold estimator which is illustrated in figure 4.2(a)

$$x(g) = \eta(g, t) = sign(g)(|g| - t)_+ \tag{4.8}$$

where $\quad (|g| - t)_+ = \max(0, |g| - t) \tag{4.9}$

and $\quad sign(g) = \frac{1}{1 + e^{-g}} \tag{4.10}$

Here $x(g)$ is weakly differentiable in Stein's sense, and thus using equation (4.7)

$$R_s(t) = \sigma_v{}^2 - \frac{1}{N} \left(2\sigma_v{}^2. \neq \{i : |g_i| \le t\} + \sum_{i=1}^{N} Min(|g_i|, t)^2 \right) \tag{4.11}$$

This is an unbiased estimator of the risk, $E_f \left\| x(g) - f \right\|^2$. Thus it provides a means for unbiased estimate of the true MSE, but it also requires the knowledge of noise variance, $\sigma_v{}^2$, whose exact value is hard to be known in practical case. It was well established that the minimum of MSE & SURE correspond to the optimal threshold. From figure 4.2 (b) it can be seen that the MSE curve and SURE curve closely follow and the minimum of both correspond to the same threshold value. Thus the estimator of risk $R_s(t)$ can be used to select the near optimal threshold as

$$\underset{t \in \{g_0, g_1 .. g_{N-1}\}}{t_S} = \arg \min R_s(t) \tag{4.12}$$

Here t_s is selected as the value of g which makes the $R_s(t)$ minimum. This is a suboptimal threshold for the risk because it is selected within a finite set.
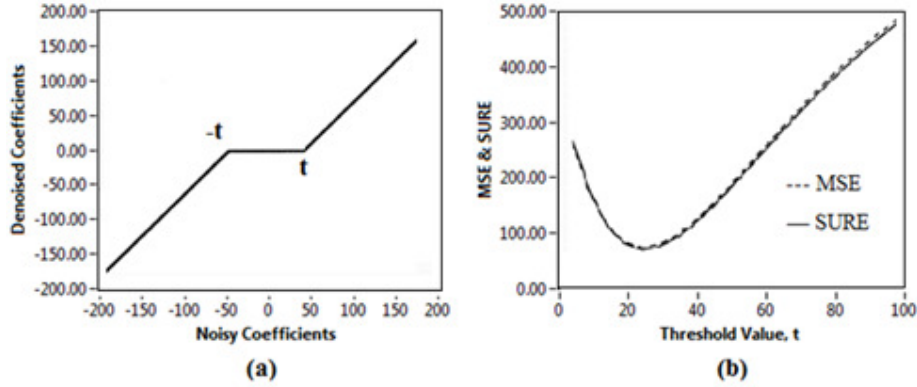
Figure 4.2 (a) Soft thresholding (b) The MSE & SURE values plotted against threshold, t

A transform domain shrinkage method relies on the basic idea that the energy of a function will often be concentrated in a few coefficients in transform domain while the energy of noise is spread among all coefficients. Therefore, the nonlinear thresholding function in transform domain will tend to keep a few larger coefficients representing the function, while the noise coefficients will tend to reduce to zero. Here the equation for l_2 risk for a given noisy image can be extended to the transform coefficients also provided the transform is orthogonal. Then the risk function given in (4.2) can be expressed in transform domain as

$$R(\hat{f}, f) = \frac{1}{N}\sum_{i=0}^{N-1}(\hat{f}_i - f_i)^2 = \frac{1}{N}\ \Sigma_{i,j}(\hat{F}_{i,j} - F_{i,j})^2 \qquad (4.13)$$

Apply the directionlet transform to the vector g and obtain the empirical directionlet coefficients $G_{i,j}$ at scale j where $j = 1, 2 .... J$. Apply the soft-thresholding function as given in equation (4.8), to the directionlet coefficients $G_{i,j}$ at each scale j where $j = 1, 2 .... J$. Then the estimate coefficients $\hat{F}_{i,j}$ are obtained based on the selected threshold, $t = [t_1, t_2 ... t_J]^T$. Here t_j is the threshold for directionlet coefficients at scale j. Here t is selected for each scale as the value of the directionlet coefficient at that scale which makes the SURE

risk $R_s(t)$ minimum. This is done for each detail subband. So this is a scale dependent sub band adaptive threshold. Now take the inverse directionlet transform on the threshold applied DT coefficients and obtain the estimate of the function.

4.2.2 Denoising Algorithm

The edge information in images has great influence on human visual effect and reflects the main direction of texture for the most part. Wavelet is the optimal bases for functions with point singularity. But in the case of two dimensional functions like images, wavelet analysis cannot take advantages of the geometrical features in it. Thus it is not the optimal or the sparsest representation tool for analysing images. When the direction of the directionlet bases matches with the geometrical features in images, then the directionlet can represent images well, otherwise bases of directionlet will degenerate into wavelets and will have poor approximation power. But the main problem in natural images is that the directional information in them varies over space. Thus, directionality can be considered as a local feature, defined in a small neighbourhood. Therefore, to extract directional variations of an image it has to be analysed locally. This necessitates the need for spatial segmentation of the image into smaller segments before identifying the dominant directions for that segment. If these dominant directions match with the transform directions then the transform can efficiently capture the geometrical information present in images.

In the proposed scheme the input image is subdivided into small patches of size 32x32, before applying the directionlet transform. Even though the construction of directionlets allow for anisotropy and directional vanishing moments along any two directions with rational slopes, here the transform directions are taken only from the set of directions, $D = \{(0°, 90°), (0°, 45°), (0°, -45°), (90°, 45°), (90°, -45°)\}$. This restriction is imposed to avoid the division of cubic lattice into more cosets as explained earlier. The best pair of directions $d_n^* \in D$ is then chosen for each segment indexed by n as

$$d_n^* = arg\ min_{d \in D} \sum_i \left| W_{n,i}^d \right|^2 \tag{4.14}$$

where, the directionlet coefficients $W_{n,i}^d$ are produced by applying directionlets to the nth segment along the pair d of directions. The assigned pair of transform

directions of each patch across the input image forms a directional map of that image and provides the best matching between the transform and the locally dominant directions for that segment. For segments with no apparent dominant directions, the pair $(0°, 90°)$ is assigned by default to smooth the segments for the reason of simplicity of implementation of DT. To avoid a blocking effect in the transform caused by many small segments, the pixels from the neighbour segments are used for filtering across the segment borders. Here a symmetric extension is performed as it seems to provide better results. The size of extension is fixed based on the segment size and the length of wavelet used for filtering.

After identifying the dominant directions in each spatial segment, the directionlet transform coefficients corresponding to the dominant directions are selected for thresholding. In the directionlet decomposition, the subbands $LHH_j, LHL_j, LLH_j, HLL_j, HLH_j, HHL_j$ and HHH_j, $j = 1,2,3 …. J$ are called the *details*, where j is the *scale*, with J being the largest or coarsest scale in the decomposition. The subband LLL_j is the low resolution residual. Like wavelet transform, the directionlet transform is also orthogonal and the coefficients in the subbands are independent and identically distributed with zero mean. The directionlet coefficient $G_{i,j}$ from the detail subbands are used for optimal threshold computation as explained in section 4.2.1 with soft threshold function to obtain $\hat{F}_{i,j}$. The denoised estimate is then obtained as $\hat{f} = D^{-1}\hat{F}_{i,j}$, where D^{-1} is the inverse directionlet transform operator.

The noise variance is not known in many cases. So it needs to be computed from the noisy image. This can be computed as the robust median estimator from HHH_1 coefficients. The directionlet transform is not shift invariant because of the decimation operation involved in the transform construction. In image denoising, a small shift in the input signal will result in significant performance degradation. This can be avoided by using an undecimated version of the transform. The main drawback of such an approach is the computational complexity, especially when applied in multiple dimensions. Unlike the discrete version of directionlet transform, which down samples the approximation coefficients and detail coefficients at each decomposition level, the Undecimated Directionlet Transform

(UDT) does not incorporate the down sampling operations. Thus, the approximation coefficients and detail coefficients at each level are having the same length as the original signal. Denoising with the UDT is shift-invariant. The denoising result of the undecimated directionlet transform has a better balance between smoothness and accuracy than its discrete version. In case of UDT, the oversampling is imposed in the same way as in the case of the undecimated wavelet transform, that is, by discarding the sub-samplers in the filter-banks. The filters used for DT are up sampled across scales. Thus, if the LP filter $H_2(Z_1)$ is used in the corresponding 1-D wavelet filter-bank, then the equivalent LP filter at the jth scale is $H_2(Z_1^{J-j})$, where *j = 1….J*, corresponds to the scale index sweeping from the finest to the coarsest scale. Such a construction results in a shift-invariant transform with a preserved number of coefficients in each subband.

The developed denoising algorithm, which is referred as *DT-SURE* is summarised in three steps as follows.

Step 1: **Directionlets and Directional Map**

- The noisy image is first divided into spatial segments of smaller size, say 32 by 32.
- Apply directionlet transform to segments along the pair of directions $D = \{(0°, 90°), (0°, 45°), (0°, -45°), (90°, 45°), (90°, -45°) \}$ with an anisotropic ratio of 1:2
- Compute optimal pair of direction using equation (4.14)
- Compute the multi scale directionlet transform along dominant directions.

Step 2: **Threshold Computation**

- For each subband, except the LLL_J subband, compute the SURE threshold using the equation (4.12) which minimizes the SURE risk
- Apply the computed threshold to the subband using soft thresholding rule to estimate the best value for the noise-free coefficients

Step 3: **Reconstruction**

- Reconstruct the image from the above processed sub-bands and the low-pass residual (LLL_J) using inverse directionlet transform and the direction map to obtain the denoised image.

4.2.3 Experimental Analysis and Results

In this section, the performance of the *DT-SURE* scheme is compared with similar wavelet based schemes like SureShrink [42], Bayes shrink [43] and HMT scheme [48]. The SureShrink and BayesShrink are the SURE and Bayesian threshold based denoising scheme in wavelet domain respectively. HMT scheme is the hidden Markov tree approach of denoising in wavelet domain. All these schemes are subband adaptive schemes. Standard greyscale images of size 512x512 are used for evaluating the performance of the developed algorithm. The test images are contaminated with zero mean white Gaussian noise with standard deviation $\sigma = 10$, 15, 20, 25 & 30. In all the schemes the popular Db4 wavelet with three decomposition levels are used. The performance improvement was quantified in terms of Peak Signal to Noise Ratio (PSNR). The denoising process has been performed over ten different noise realizations for each standard deviation and the resulting PSNRs averaged and given in Table 4.1. The parameters of each method have been set according to the values given by their respective authors in the corresponding referred papers. Variations in output PSNRs are, thus, only due to the denoising techniques themselves. From the results it is clear that the *DT-SURE* scheme outperforms the other compared schemes for all the test images. As compared to SureShrink, the performance improvement of *DT-SURE* is more than 1 dB on average for *Lena* image. This difference is higher for *Barbara* and *Boat* images as they contain more edges and textures.

A visual comparison of *Lena* image is given in Figure 4.3 and Boat image in Figure 4.4 for $\sigma = 20$. Although there is no consensual objective way to judge the visual quality of a denoised image, two important criteria are widely used: the visibility of processing artifacts and the conservation of image edges. Processing artifacts usually result from the modification of the spatial correlation between wavelet coefficients mainly caused by the zeroing of small neighboring coefficients. The edge distortions in images usually arise when the transform directions are not matched with the edges in images. Since the directionlet transform was taken along the local dominant directions in the image, the DT based denoising algorithms shall perform better in both the above aspects. This is evident from the visual quality of the denoised images with *DT-SURE* scheme as they are characterized by fewer

artifacts and are having sharper edges and texture than the output images from other schemes. The zoomed portions of the denoised images substantiate this.

Table.4.1 PSNR (dB) comparison of DT-SURE scheme with other denoising algorithms

Standard devn. σ	Noisy	SureShrink [42]	BayesShrink [43]	HMT [48]	DT-SURE
Lena					
10	28.13	33.27	33.33	33.83	**34.24**
15	24.61	31.36	31.39	31.74	**32.36**
20	22.11	30.19	30.15	30.38	**31.01**
25	20.17	29.14	29.21	29.25	**29.94**
30	18.59	28.36	28.48	28.36	**29.15**
Boat					
10	28.13	31.18	31.78	32.26	**32.37**
15	24.61	29.28	29.84	30.30	**30.46**
20	22.11	28.12	28.43	28.83	**28.94**
25	20.17	27.27	27.37	27.66	**27.88**
30	18.59	26.53	26.56	26.84	**26.95**
Barbara					
10	28.13	30.21	30.84	31.35	**31.96**
15	24.61	28.12	28.50	29.21	**29.86**
20	22.11	25.91	27.11	27.81	**28.21**
25	20.17	25.71	26.00	25.97	**26.99**
30	18.59	24.33	25.14	25.12	**26.01**

Even though DT-SURE has performed well in terms of PSNR, it has got a serious drawback with respect to the higher computation time. The actual time taken by these algorithm using an Intel Core i5 CPU @ 2.4 GHz with 4GB RAM for *Barbara* image of size 512x512 with a standard deviation of 20 is given in Table 4.2. As can be seen from these figures the computation time taken by the DT-SURE scheme is more than ten times that of the SureShrink. The computational inefficiency of the scheme is basically due to two reasons: one is the use of undecimated version of the transform and the other is due to the computation of transform along five different sets of directions with an anisotropic ratio of 1:2.

Table 4.2 Computation time taken by different algorithms

Method	SureShrink [42]	BayesShrink [43]	DT-SURE
Time (sec)	**1.2**	1.4	15.1

Figure.4.3. Image denoising result of *Lena* image. (a) Noise free image (b) noisy image with $\sigma = 20$, (c) denoised image using WT-SURE (d) denoised image using DT-SURE (e) enlarged portion of (c) and (f) enlarged portion of (d)
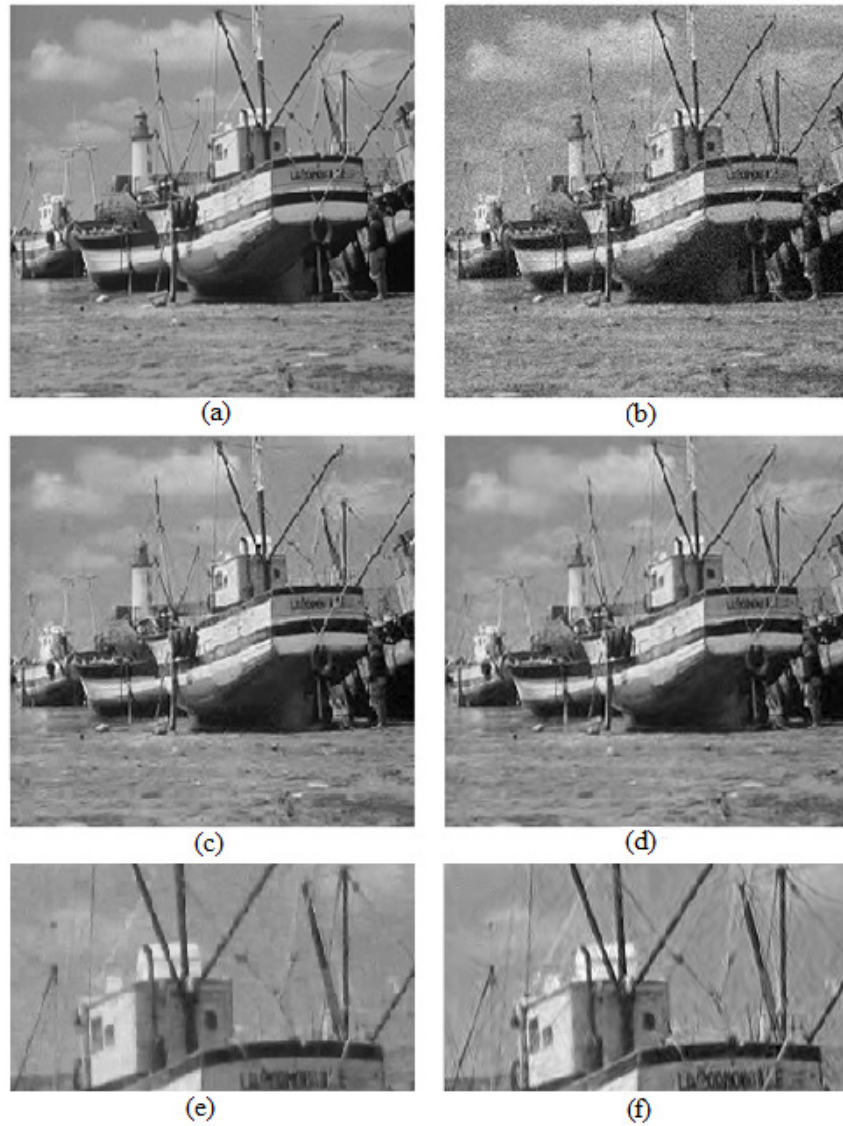
Figure.4.4. Image denoising result of *Boat* image. (a) Noise free image (b) noisy image with $\sigma = 20$, (c) denoised image using WT-SURE (d) denoised image using DT-SURE (e) enlarged portion of (c) and (f) enlarged portion of (d)

4.3 Subband Adaptive Bayes Thresholding in Directionlet Domain

In the previous section, a simple denoising scheme in directionlet domain is presented, which uses a threshold computed based on SURE risk. As compared to the previous scheme, two major modifications are made here to make the scheme more efficient. One is the use of Bayesian threshold and the second one is a more efficient way of identification of local dominant directions in the image.

The directionlet based denoising scheme proposed here is an extension of the wavelet based denoising techniques. The undecimated version of directionlet transform is used here to have better denoising performance. The directionlet has directional vanishing moments along two directions only. So for identifying the best pair of directions, directionlet transform has to be taken along multiple directions. This is computationally intensive and data expansive. Thus if the texture direction is known a priori, the construction of directionlet can be limited to two dominant directions only, making it a computationally efficient scheme. However natural images can have different texture at different areas. This restriction implies a need for spatial segmentation of image and adaptation of the pair of directions in each segment based on the dominant direction of image. Here a scheme is presented in which the directional information of the spatially segmented image is first identified and then directionlet transform is computed for each of these spatial segments along the dominant directions. A subband adaptive Bayesian threshold is then computed from these transform coefficients and applied to the detail subbands using soft thresholding rule. Finally the denoised image is reconstructed from the modified subband coefficients.

4.3.1 Identification of Local Dominant Directions Using Directional Variance

As explained earlier, there are adaptive and non adaptive directional transforms for image representation. The former ones are fixed transforms with anisotropic directional basis, independent of image being transformed. In this case a fixed decomposition is applied irrespective of the signal, and these try to make the

directional features in images more explicit. The later ones do signal adaptive directional decompositions. In most of these schemes, the adaptation is done by searching exhaustively all possible directions using Lagrangian multiplier based Rate-Distortion (RD) optimization. Motivated by the need to estimate the content direction in a faster and efficient way, a scheme was proposed by D. Jayachandra et al [146], which compute the variance along discrete lines, as a means to measure content directionality. This parameter is known as directional variance, '*DirVar*'.

Given any rational slope r, the digital line $L(r, n)$ where $n \in \mathbb{Z}$, *is* defined as the set of pixels (x, y) such that

$$y = \lceil rx \rceil + n, \ \forall \ x \in \mathbb{Z} \ for \ |r| \leq 1 \ or$$

$$x = \left\lceil \frac{y}{r} \right\rceil + n, \ \forall \ y \in \mathbb{Z} \ for \ |r| > 1. \tag{4.15}$$

For every rational slope r, the set of digital lines $L(r, n): n \in \mathbb{Z}$ completely partitions the 2D discrete space $\mathbb{Z}^2$, meaning every pixel $(x, y) \in \mathbb{Z}^2$ is associated to only one of the digital lines with slope r.

Given the definition of digital line $L(r, n)$ with rational slope r, the directional variance [146] for a given image segment S, along the lines with rational slope r, is defined as

$$DirVar(S, r) = \frac{1}{N} \sum_{x=1}^{n} \sum_{y=1}^{k_x} \left(S_y - S_{L(r,x)} \right)^2 \tag{4.16}$$

where, (x, y) is the set of pixels, $S_{L(r,x)}$ is the mean of the digital line with slope r and offset x and S_y is the pixel in the same line. N is the total number of pixels and n is the total number of lines in the segment S. k_x is the number of pixels in the line x.

$DirVar(S, r)$ measures the normalized sum of variances along each digital line with the given slope r and hence is very sensitive to content directionality. It measures spatial activity along the given direction. That is, if the content has edges along some direction then the $DirVar$ measured along a direction slightly different from that will result in a larger value than when measured along the content direction. Figure.4.5 shows the *DirVar* plot along 12 directions for three images

with different directionality. The directions selected are $(x,\ y) = (1,0),(3,1),(2,1),(1,1),(1,2),(1,3),(0,1),(-1,3),(-1,2),(-1,1),(-2,1),(-3,1)$. For the first image with two regions separated by a line edge along the direction (1,2), the *DirVar* plot shows a dip at direction number 5 which corresponds to (1,2). Moving away from this direction shows increase in *DirVar*, hence clearly showing the difference between the content direction and others. For the next image with two dominant directions, *DirVar* shows minima at those two directions, showing its ability to respond to more than one direction. For the next image with uniform region which doesn't have specific directionality, *DirVar* doesn't vary much from direction to direction.
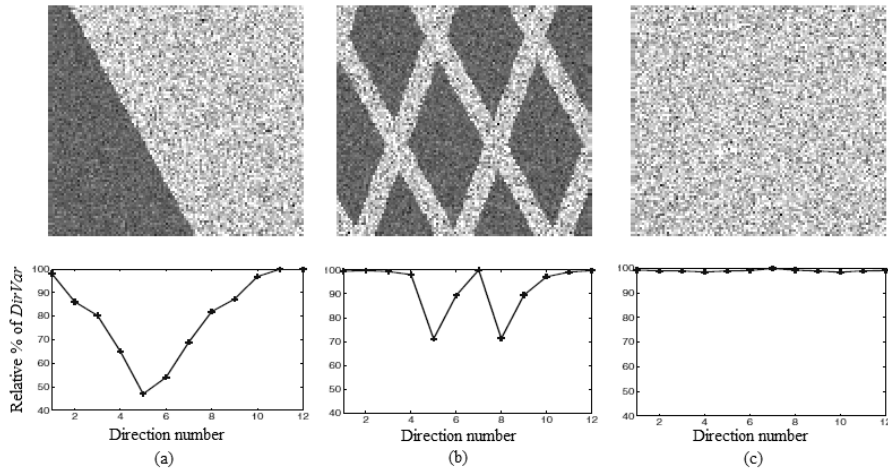
Figure.4.5. The directional variance for different images (a) an image with one edge (b) an image with two edges and (c) an image with no specific edges.

In the proposed scheme, the *DirVar* was computed along the rational directions $(x, y) = (1,\ 0),\ (2,\ 1),\ (1,\ 1),\ (1,\ 2),\ (0,\ 1),\ (-1,2),\ (-1,\ 1)$ and $(-2,1)$ which corresponds to 0º, 30º, 45º, 60º, 90º, 120º, 135º and 150º. This was carried out for each spatial segment of the image and the directions corresponding to the two minimum directional variances were identified and these were selected as the optimal pair of directions (transform direction and alignment direction) for computing the directionlet transform. The segments where the *DirVar* for all the directions comes

within 5% are considered to have no apparent dominant directions. For such segments, the pair (0º, 90º) is assigned by default as the transform directions for the reason of simplicity of implementation of DT.

4.3.2 Image Noise Model and Bayes Threshold Computation

The Generalised Gaussian Distribution (GGD) has been widely used to model the coefficients in many wavelet based denoising applications. For most of the natural images, the WT coefficients from each subband except LL subband can be well described by the zero mean GGD. Based on this distribution many attempts were made to find out the best threshold for denoising applications. The Bayes threshold based on GGD was first proposed by Chang et al [43] in the wavelet domain. The same scheme can be extended to the directionlet domain also as DT is an extended version of WT. The threshold estimation problem in directionlet domain can be formulated as follows.

Suppose that the image f is polluted by independent and identically distributed $(i.i.d)$ white Gaussian noise v with zero mean and σ_v^2 variance, the observed image g can be described as:

$$g = f + v \qquad (4.17)$$

Since the directionlet transform is a linear operator, we can get the corresponding observation model in the directionlet domain as

$$g_j = f_j + v_j \qquad (4.18)$$

where g_j, f_j and v_j are the directionlet transforms of g, f and v respectively.

It has been observed that for a large class of images, the coefficients from each subband except LL subband form a symmetric distribution that is sharply peaked at zero [82], well described by the zero-mean GGD.

The GGD is

$$GG_{\sigma_f,\beta}(f) = C(\sigma_f,\beta)e^{-[\propto(\sigma_f,\beta)|f|]^\beta} \qquad (4.19)$$

where, $\qquad\qquad -\infty < f < \infty, \quad \sigma_f > 0, \quad \beta > 0$

$$\propto (\sigma_f, \beta) = \sigma_f^{-1} \left[\frac{\Gamma(3/\beta)}{\Gamma(1/\beta)} \right]^{1/2}$$

$$C(\sigma_f, \beta) = \frac{\beta. \propto (\sigma_f, \beta)}{2\Gamma(1/\beta)}$$

and $\Gamma(1/\beta) = \int_0^\infty e^{-u} u^{t-1} du$ is the gamma function. The parameter σ_f is the standard deviation and β is the shape parameter.

For each subband, the signal coefficients f_j are modeled as independent samples of generalized Gaussian distribution, $P_f(f_j) = GG_{\sigma_f, \beta}(f_j)$ and since the wavelet transform is orthogonal, the noise coefficients v_j are modeled as independent samples of the Gaussian distribution, $p_v(v_j) = \frac{1}{\sqrt{2\pi}\sigma_v} e^{-\left(\frac{v_j^2}{2\sigma_v^2}\right)}$

Let the estimator be restricted to the *soft-threshold* estimator of the form $\eta(g, T) = sign(g)(|g| - T)_+$, where T is called the threshold. For a given set of parameter the objective is to find a soft threshold T which minimises the Bayes risk $R(T)$, which is defined as

$$R(T) = E(\check{f} - f)^2 = E_f E_{g/f}(\check{f} - f)^2 \qquad (4.20)$$

The optimal threshold T^* can be obtained by minimising the Bayes risk $R(T)$.

$$T^*(\sigma_f, \beta) = \arg\min R(T) \qquad (4.21)$$

This is a function of σ_f and β. There is no closed form solution for $T^*(\sigma_f, \beta)$ for this chosen pair.

It was established that at least for the range of $\beta \in [0.5, 4]$, T^* can be well approximated by the following equation [43]

$$T_B(\sigma_f) = \frac{\sigma_v^2}{\sigma_f} \qquad (4.22)$$

It was well established that a GGD with the shape parameter, β ranging from 0.5 to 1 can adequately describe the wavelet coefficients of a large set of natural images. This range of shape parameter, β is well within the range requirement for $T_B(\sigma_f)$ defined earlier. Thus in case of wavelet based denoising the threshold value mentioned in equation (4.22) can be effectively used. Now it has to be established that the directionlet coefficients also follow the non-Gaussian statistical properties, whose probability density function can be modelled using Generalized Gaussian Distribution. Figure. 4.6 shows the histogram of the wavelet and directionlet coefficients of *Lena* and *Barbara* images. These histograms are approximated to the generalized Gaussian curve and the corresponding standard deviation, σ and shape parameter, β are computed in each case. From these figures it is clear that the directionlet coefficients of natural images show a strong non-Gaussian statistical properties, whose probability density function can be modelled with the use of Generalized Gaussian Distribution. Also as in the case of wavelet coefficients, the β values in the case of directionlet coefficients also lie within the range of 0.5 to 1. This justifies the use of the Bayesian threshold as defined in equation (4.22) to the directionlet coefficients also.

The Bayesian threshold $T_B(\sigma_f)$ is a function of GGD parameters σ_f and β and is adaptive to different subband characteristics. Here the parameter β doesn't explicitly enter into the expression of $T_B(\sigma_f)$, only the standard deviation of signal σ_f does. The noise variance σ_v^2 can be computed from the high frequency sub band coefficients at level1 (HHH_1) in the directionlet decomposition by the robust median estimator as

$$\sigma_v = \frac{Median\left(|K_{ij}|\right)}{0.6745}, where\ K_{ij} \in HHH_1 \tag{4.23}$$

The next parameter to be estimated is σ_f. From the image noise model as given in equation (4.17) and assuming that f and v are independent of each other,

$$\sigma_g^2 = \sigma_f^2 + \sigma_v^2 \tag{4.24}$$

where σ_g^2 is the variance of the noisy image.
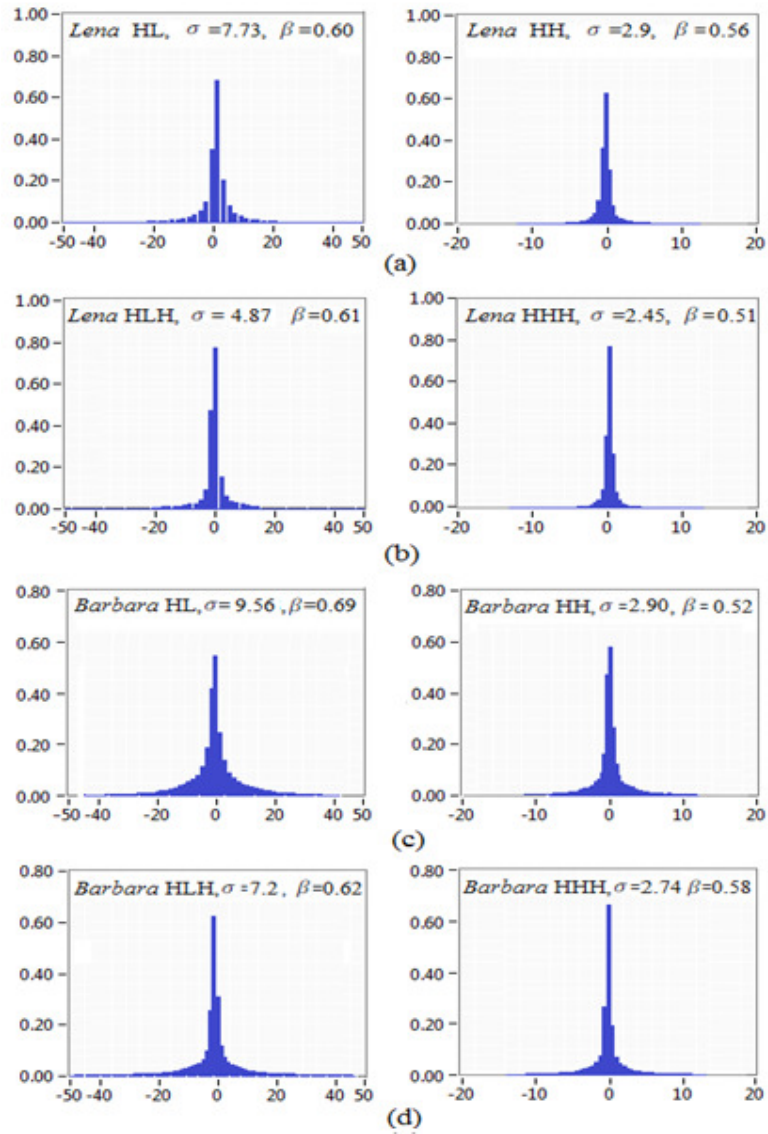
Figure 4.6. Histogram at scale 1 of (a) WT coefficients of HL & HH subbands of *Lena* (b) DT coefficients of HLH & HHH subbands of *Lena* (c) WT coefficients of HL & HH subbands of *Barbara* (d) DT coefficients of HLH & HHH subbands of *Barbara*

Since the noisy image is modelled as zero mean, σ_g^2 can be computed using the following empirical formula:-

$$\breve{\sigma}_g^2 = \frac{1}{n^2} \sum_{i,j=1}^{n} g_{ij}^2 \qquad (4.25)$$

where $n \times n$ is the size of the subband under consideration. σ_f can now be computed as

$$\breve{\sigma}_f = \sqrt{max(\breve{\sigma}_g^2 - \breve{\sigma}_v^2, 0)} \qquad (4.26)$$

From the computed values of σ_f and σ_v the threshold can be calculated using equation (4.22). The computed threshold is data driven and subband dependent. The denoising scheme based on Bayes thresholding in directionlet domain is referred as *DT-Bayes*.

4.3.3 Denoising algorithm

The *DT-Bayes* image denoising algorithm is summarized as follows:-

Step 1: Divide the noisy image into spatial segments of smaller size, say 32 by 32.

Step 2: Compute the $DirVar$ along eight directions 0º, 30º, 45º, 60º, 90º, 120º, 135º and 150º using equation (4.16) for each segment and choose the directions corresponding to two minimum $DirVar$ values as the pair of transform and alignment directions.

Step 3: Decompose the image segments into sub-bands using directionlet transform along the chosen pair of directions.

Step 4: Compute the noise variance from the HHH_1 subband using equation (4.23)

Step 5: For each subband, except the LLL subband, compute the Bayes threshold using the equation (4.22).

Step 6: Apply the computed threshold to the subbands using soft thresholding rule to estimate the best value for the noise-free coefficients.

Step 7: Reconstruct the image from the above processed sub-bands and the low-pass residual (LLL) to obtain the denoised image.

4.3.4 Results and Analysis

Standard greyscale images of size 512 x 512 are used for evaluating the performance of the developed algorithm. The test images are contaminated with zero mean white Gaussian noise with standard deviation of 10, 15, 20, 25 and 30. The performance of the *DT-Bayes* scheme is compared mainly with *BayesShrink* [43], which is a scheme with Bayesian thresholding in wavelet domain. This is a subband adaptive scheme with no spatial adaptation or correlation. In both the schemes popular Db4 wavelet was used for filtering. The performance improvement was quantified in terms of Peak Signal to Noise Ratio (PSNR). The directions estimated by minimizing the directional variance for the *Lena* and *Barbara* images are shown in Figure 4.7. Here the image was segmented into small patches of size 32x32 and the directional variance was computed along eight different directions. It is evident from these figures that the directional variance has correctly identified the directions that are close to the content directionality of the image in most of the spatial segments.
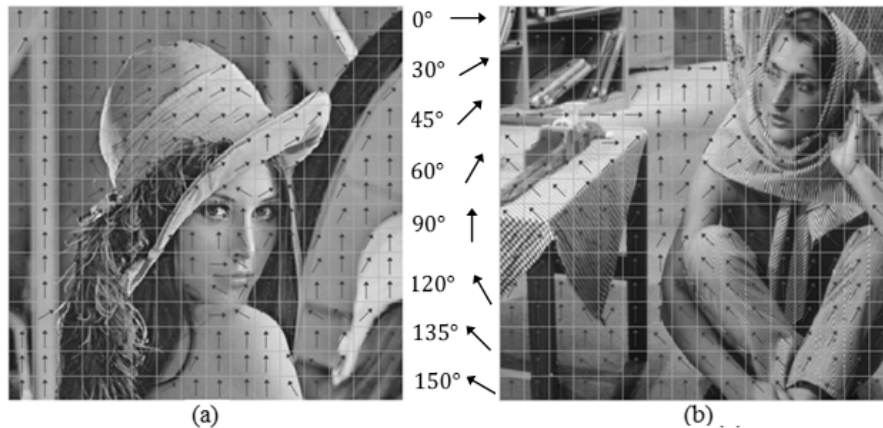
Figure 4.7 Directions estimated by minimizing *DirVar* for (a) *Lena* and (b) *Barbara* image

The PSNR comparison of *Lena*, *Boat* and *Barbara* images is given in Table 4.3. The PSNR values provided are the average of 10 different noise realisations for each standard deviation. The proposed method outperforms the other compared scheme for all the test images. From the PSNR values it is seen that the performance difference with the *BayesShrink* scheme is more for *Barbara* and *Boat*

images. This is basically due to the fact that these images have more high frequency content and so more directional features. The DT has effectively captured these directional features and aided for efficient denoising. Extracted and enlarged portions of *Barbara, Lena* and *Boat* images are shown in figure 4.8, figure 4.9 and figure 4.10 respectively for analysing the visual performance of the *DT-Bayes* scheme**.** It can be seen from these figures that the visual quality of the denoised images using DT is evidently better because of sharper edges and texture. The *BayesShrink* blurs image details especially at edges and contours. The *DT-Bayes* scheme suppresses noise effectively while preserving the image details equally well. The performance improvement of the directionlet based scheme as compared to WT based schemes is more evident especially when the local dominant directions in the image are neither horizontal nor vertical. This can be seen clearly from the stripes in the scarf of *Barbara*, edges of the hat of *Lena* and the rods and ropes in *Boat* image. In all these cases the lines and edges are retained with the best quality in the resulting images from *DT-Bayes* scheme.

Table.4.3. PSNR (dB) comparison of DT-Bayes scheme with other denoising algorithms for *Lena, Boat & Barbara* images of size 512x512

σ	Noisy	SureShrink [42]	BayesShrink [43]	HMT [48]	DT-SURE	DT-Bayes
Lena						
10	28.13	33.27	33.33	33.83	34.24	**34.56**
15	24.61	31.36	31.39	31.74	32.36	**32.68**
20	22.11	30.19	30.15	30.38	31.01	**31.39**
25	20.17	29.14	29.21	29.25	29.94	**30.26**
30	18.59	28.36	28.48	28.36	29.15	**29.50**
Boat						
10	28.13	31.18	31.78	32.26	32.37	**32.72**
15	24.61	29.28	29.84	30.30	30.46	**30.92**
20	22.11	28.12	28.43	28.83	28.94	**29.44**
25	20.17	27.27	27.37	27.66	27.88	**28.27**
30	18.59	26.53	26.56	26.84	26.95	**27.36**
Barbara						
10	28.13	30.21	30.84	31.35	31.96	**32.66**
15	24.61	28.12	28.50	29.21	29.86	**30.47**
20	22.11	25.91	27.11	27.81	28.21	**28.95**
25	20.17	25.71	26.00	25.97	26.99	**27.57**
30	18.59	24.33	25.14	25.12	26.01	**26.68**
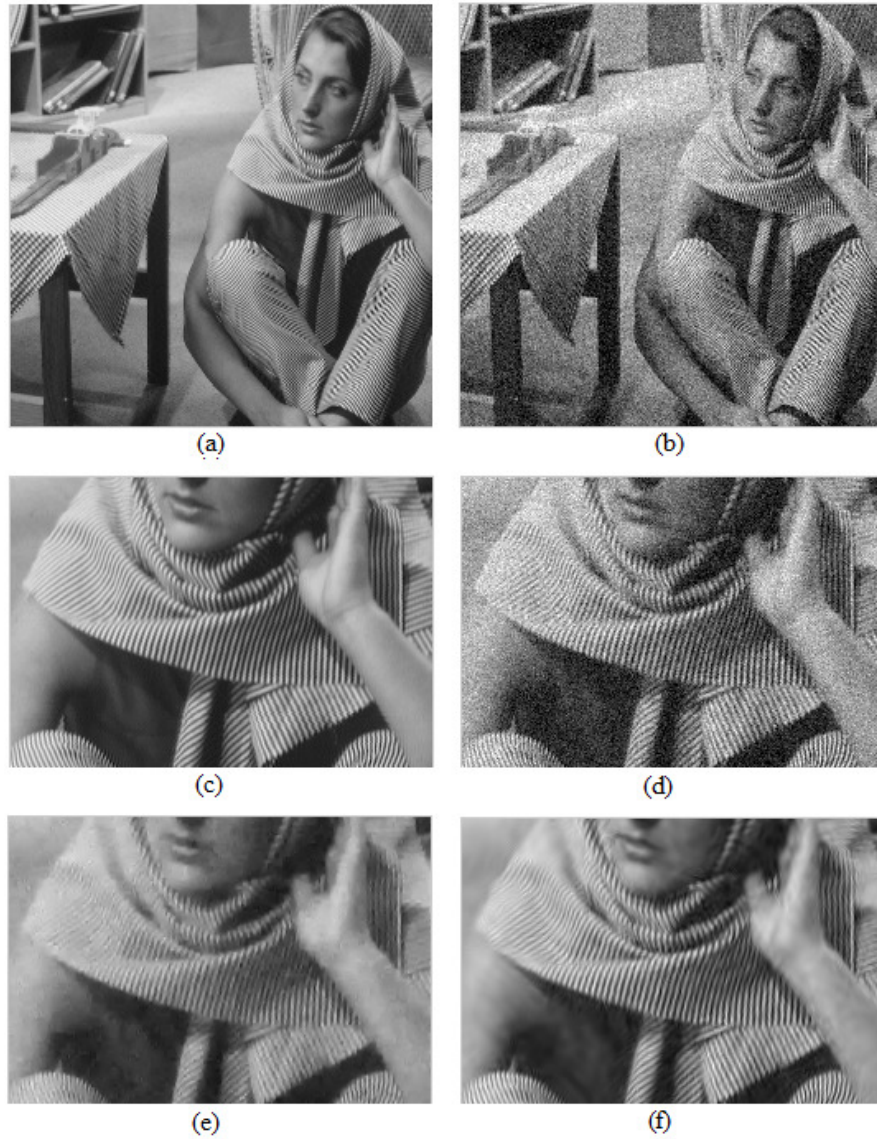
Figure.4.8 Image denoising result of *Barbara* image. (a) noise free image (b) noisy image with $\sigma = 20$, (c) enlarged portion of noise free image (d) enlarged portion of noisy image (e) denoised image using BayesShrink (f) denoised image using *DT-Bayes*.
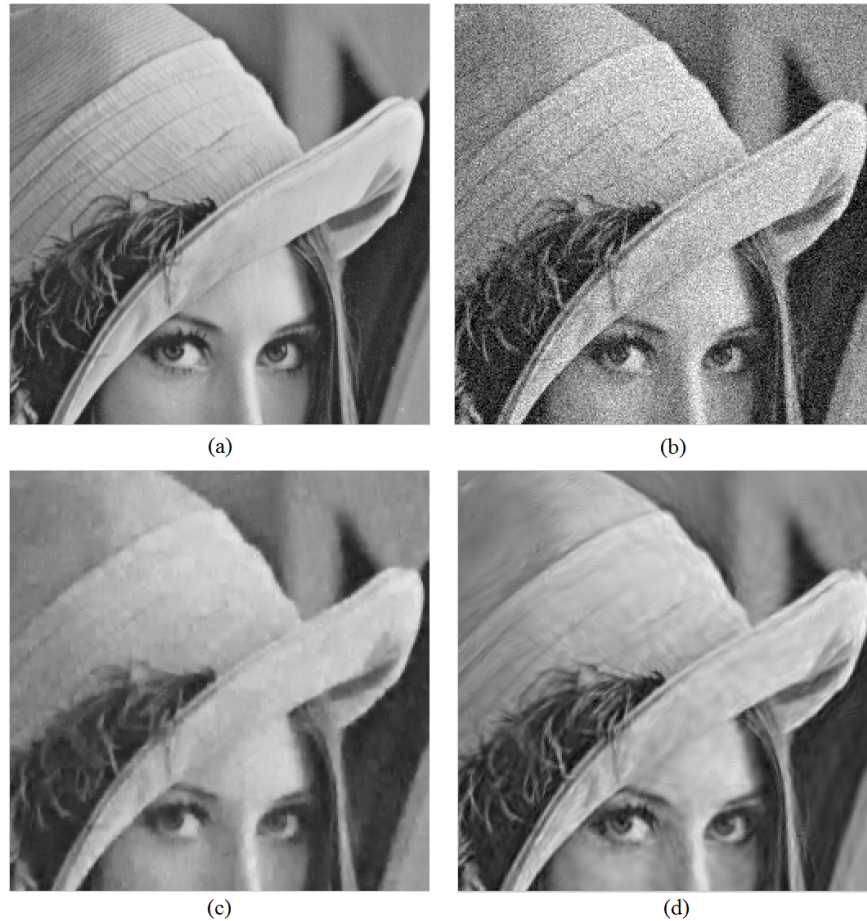
Figure.4.9. Image denoising result of *Lena* image. (a) Noise free image (b) noisy image with $\sigma = 20$, (c) denoised image using wavelet based BayesShrink in [43] and (d) denoised image using Bayes thresholding in directionlet domain.

The time taken by the *DT-Bayes* algorithm is noticeably very less from the previous scheme mainly due to the use of directional variance for estimation of dominant directions. The actual time taken by these algorithm in an Intel Core i5 CPU @ 2.4 GHz with 4GB RAM for *Barbara* image of size 512x512 with a standard deviation of 20 is given in Table 4.4.

Table 4.4. Computation time taken by different algorithms

Method	SureShrink [42]	BayesShrink [43]	DT-SURE	DT-Bayes
Time (sec)	**1.2**	1.4	15.1	8.3
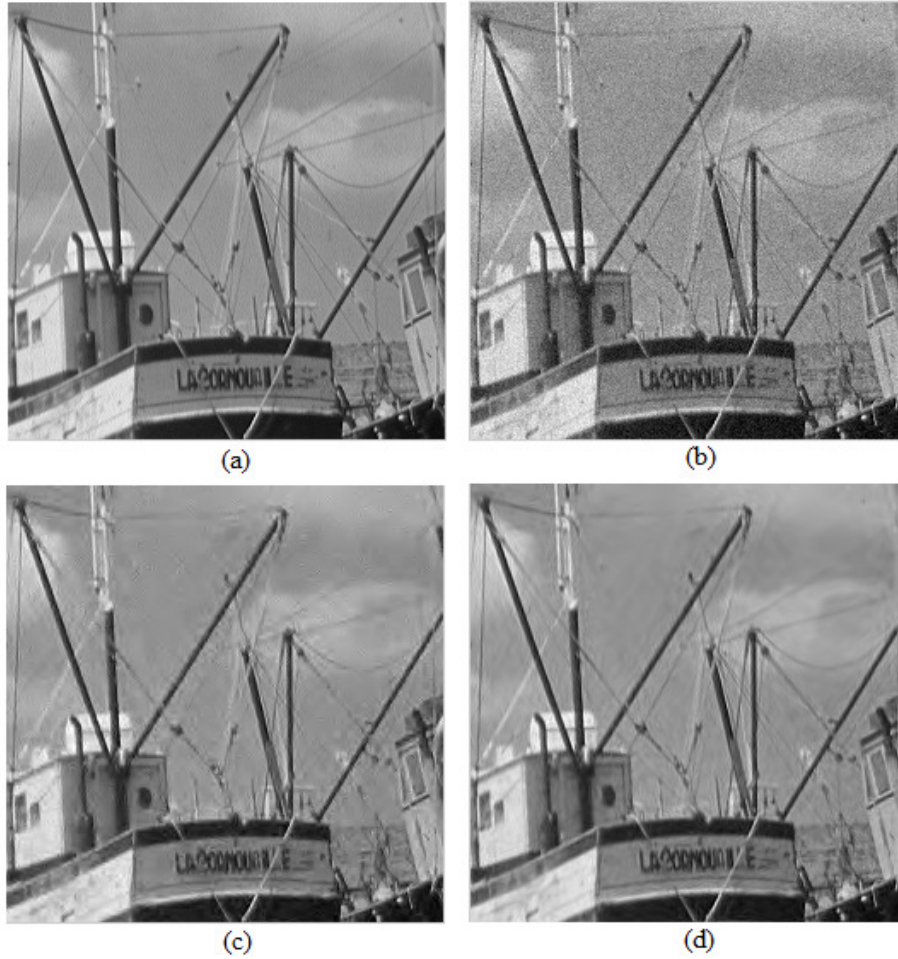
Figure 4.10 Visual performance of DT-Bayes algorithm. (a) Noise free part of *Boat* image (b) Noisy parte with $\sigma = 10$, (c) Denoised image using wavelet based BayesShrink [43] and (d) Denoised image using *DT-Bayes*.

4.4 Image Denoising Using Interscale Dependency in Directionlet Domain

In this section a statistical model based denoising scheme is presented in directionlet domain. This scheme is different from the earlier two schemes in three major aspect. The first one is that it is a statistical model based scheme as against the threshold based schemes presented earlier. The second speciality is that the interscale dependency of the transform coefficients is taken into account in the modelling process. The third difference is the use of spatial adaptation instead of the subband adaptation used in the earlier schemes.

The statistical model based schemes model the signal and noise coefficients using appropriate prior probability distribution functions and the noise free coefficients are estimated using this *a priori* information with Bayesian estimation techniques, such as the MAP estimator. Here the main challenge lies in the accurate modelling of the image and noise coefficients. If these models are well chosen, the noise can be removed efficiently. In literature several models have been considered for the noise-free wavelet coefficients and Gaussian model for the noise coefficients. In most of these models the WT coefficients are assumed to be independent. However it was well established that there are inter and intra scale statistical dependency in wavelet coefficients of natural images due to the fact that if a WT coefficient has small magnitude the adjacent coefficients are very likely to be small, and the small coefficients tend to propagate across the scales. Thus the models which consider the transform coefficient as independent cannot efficiently model natural images and thus may not provide good denoising performance. Motivated by this here the interscale dependency of transform coefficients is incorporated in the estimation process. Also here spatial adaptation is used instead of subband adaptation. In the earlier two schemes, if two noisy coefficients from the same subband are of equal magnitudes then they are shrunk by the same amount without considering their spatial position and local surroundings. Here a local variance parameter, computed from the neighboring coefficients are used in the estimation process thereby the intrascale dependency of the transform coefficients is also made use of. This scheme is conceptually simple and computationally efficient with better directional features as against other directional transform based schemes.

The directionality of the spatially segmented image is first computed using directional variance to adapt the transform direction to the content direction. DT is then computed along these directions. The DT coefficients so obtained are then modelled using a bivariate function with a local variance parameter, which takes into account inter and intra scale dependency of these coefficients. A nonlinear threshold function is derived from the bivariate models of the signal and noise employing a *maximum a posteriori* (MAP) estimator using Bayesian theory. The denoised image is obtained from the modified transform coefficients using directional information and inverse directionlet transform.

4.4.1 Image Modelling & MAP Estimation

The statistical model of a noisy image can be written as

$$g(x,y) = f(x,y) + v(x,y) \tag{4.27}$$

Here $g(x,y)$ is the $(x,y)^{th}$ pixel of the noisy image, $f(x,y)$ the corresponding noise free image and $v(x,y)$ is independent and identically distributed white Gaussian noise with zero mean and σ_n^2 variance. The aim of denoising is to estimate $f(x,y)$ from $g(x,y)$.

Let us denote the *J*-level DT with generator matrix $\mathbf{M}_{\Lambda J}$ and anisotropic ratio of $n_2 : n_1$ as DT($\mathbf{M}_{\Lambda J}, n_1, n_2$). Then as an example, DT($\mathbf{M}_{\Lambda J}, 1, 2$) of a 2-D image results in an approximation subband LLL_J as well as $7 \times J$ detail subbands viz. $LHH_j, LHL_j, LLH_j, HLL_j, HLH_j, HHL_j \text{ and } HHH_j$, where $j = 1,2,3 \ldots J$. The approximation subband contains the low frequency portion of the image and thus possesses most of the information of the image. The detail subbands provide the directional information in the image specific to the spatial location resulting in an efficient energy compaction or sparse representation.

Since DT is a linear operation like 2-D WT, the equation in (4.27) can be written as

$$g_j^i(x,y) = f_j^i(x,y) + v_j^i(x,y) \tag{4.28}$$

Here $g_j^i(x,y)$, $f_j^i(x,y)$ and $v_j^i(x,y)$ denote the DT at level j for segment i of the segmented noisy image, noise free image and noise components respectively. From now onwards, we will omit the superscript i and index (x,y) for simplicity.

Now we have to consider the interscale dependency of DT coefficients in the modelling process. Assume that $DT(\mathbf{M}_{\Lambda J}, n_1, n_2)$. is applied on an image, where $\mathbf{M}_{\Lambda J} = [d_1 \quad d_2]^T$. The transform is applied in each of $|\det(\mathbf{M}_{\Lambda J})|$ cosets independently. The number of HP subbands produced at each scale of DT is $(2^{n_1+n_2} - 1)$ and these subbands are said to have $(2^{n_1+n_2} - 1)$ distinct orientations. Consider two subbands of the same orientation at two adjacent scales. We denote the index of the finer scale as j and that of the coarser scale as $(j + 1)$. The two subbands are defined across the corresponding lattices given by the generator matrices

$$M_{\Lambda_j} = \begin{bmatrix} 2^{jn_1}.d_1 \\ 2^{jn_2}.d_2 \end{bmatrix} \text{ and } M_{\Lambda_{j+1}} = \begin{bmatrix} 2^{(j+1)n_1}.d_1 \\ 2^{(j+1)n_2}.d_2 \end{bmatrix}$$

Notice that the lattice Λ_{j+1} is a sublattice of the lattice Λ_j and recall that the coefficients in the two subbands are separated into $|\det(M_{\Lambda_j})|$ cosets. A coefficient in the Cth coset of the subband at the coarser scale $(j + 1)$ is parent of a set of children that belong to the same coset C in the subband at the next finer scale j. The children belong to the same orientation as their parent and are located within the parallelepiped around the spatial location of their parent. The children are defined by the following equation

$$m_1.2^{jn_1}.d_1 + m_2.2^{jn_2}.d_2 \text{ for } -\frac{1}{2} \leq m_1, m_2 < \frac{1}{2} \qquad (4.29)$$

The similar hierarchical structure of subbands across scales is shown in Figure 4.11(a) for the case of $DT(\mathbf{M}_{\Lambda J}, 2, 1)$, where the generator matrix $\mathbf{M}_{\Lambda J} = [d_1 \quad d_2]^T$ with $d_1 = [1 \quad 1]$ and $d_2 = [-1 \quad 1]$. The corresponding parent-children relation is illustrated in Figure 4.11(b) for the same transform.

As in the case of WT, adjacent scale coefficients in the directionlet domain are also strongly correlated. The noise level decreases rapidly across scales while signal structures are strengthened. To take advantage of this property we model the DT coefficients using this dependency. Let us consider the coefficients of $DT(\mathbf{M}_{\Lambda J}, n_1, n_2)$ at scale j. Here each DT coefficient will have one parent at scale $(j + 1)$ and $2^{n_1+n_2}$ children at scale $(j - 1)$. If we consider this interscale

dependency or the parent child relationship in the model in equation (4.28), it can be written as

$$\boldsymbol{g}_j = \boldsymbol{f}_j + \boldsymbol{v}_j \tag{4.30}$$

where $\boldsymbol{g}_j = \left(A_{g_{jpc}}, g_j\right)$, $\boldsymbol{f}_j = \left(A_{f_{jpc}}, f_j\right)$, and $\boldsymbol{v}_j = \left(A_{v_{jpc}}, v_j\right)$, are the interscale dependence vectors of noisy, noise-free and noise coefficients respectively.

Here $A_{g_{jpc}}$ is the average of one parent at scale $(j+1)$ and $2^{n_1+n_2}$ children at scale $(j-1)$ of g_j and can be expressed as

$$A_{g_{jpc}} = \frac{1}{2}\left(\sum_k \frac{g_{j-1}^{(k)}}{2^{n_1+n_2}} + y_{j+1}\right) \tag{4.31}$$

where $g_{j-1}^{(k)}$, $k = 0,1 \dots (2^{n_1+n_2} - 1)$ are the children and g_{j+1} is the parent of g_j.

Similarly, $\qquad\qquad A_{v_{jpc}} = \frac{1}{2}\left(\sum_k \frac{v_{j-1}^{(k)}}{2^{n_1+n_2}} + v_{j+1}\right) \tag{4.32}$

and $\qquad\qquad A_{f_{jpc}} = \frac{1}{2}\left(\sum_k \frac{f_{j-1}^{(k)}}{2^{n_1+n_2}} + f_{j+1}\right) \tag{4.33}$

Coset 1 ○   Coset 2 ●

$M_{\Lambda_j} = \begin{bmatrix} 1 & 1 \\ -1 & 1 \end{bmatrix}$ $M_{\Lambda_{j+1}} = \begin{bmatrix} 4 & 4 \\ -2 & 2 \end{bmatrix}$

(a)   (b)
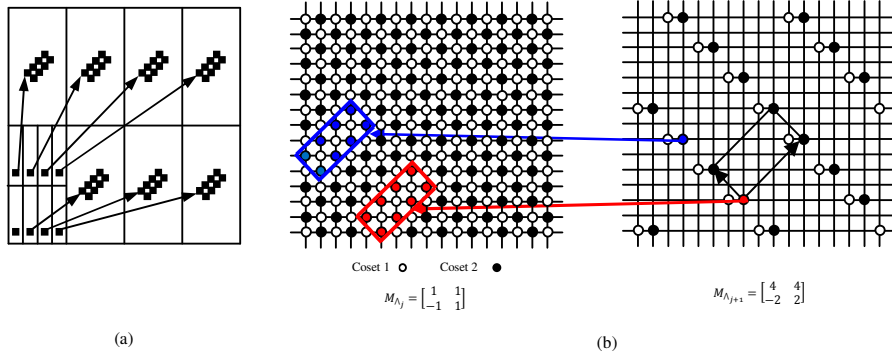
Figure 4.11 (a) The parent child relationships for DT($\mathbf{M}_{\Lambda J}, 2, 1$). (b)The subbands at the coarser scale $j +1$ are defined across the lattice Λ_{j+1} with the generator matrix $M_{\Lambda_{j+1}}$. Each coefficient has a set of children at the next finer scale j.

The MAP filtering is a powerful estimation strategy for the random processes affected by noise. However, it needs a precise knowledge of the *pdf* of the random processes that are involved. Let $P_g(\boldsymbol{g})$, $P_f(\boldsymbol{f})$ and $P_v(\boldsymbol{v})$ represent the *pdf* of the interscale dependence vectors of DT coefficients of the noisy image, noise free image and noise components respectively. Then, the MAP estimation of the process f_j is

$$\hat{f}_j = \arg\max P_{f/g}(\boldsymbol{f_j}|\boldsymbol{g_j}) \tag{4.34}$$

Using Baye's formula, this can be written as

$$\hat{f}_j = \arg\max[\, P_{g/f}(\boldsymbol{g_j}|\boldsymbol{f_j}) \cdot p_f(\boldsymbol{f_j})] \tag{4.35}$$

$$\hat{f}_j = \arg\max[\, p_v(\boldsymbol{g_j} - \boldsymbol{f_j}) \cdot p_f(\boldsymbol{f_j})] \tag{4.36}$$

Here the estimate of noise free image is represented in terms of the probability density functions of interscale dependence vectors of noise and the signal coefficient. As it can be seen, finding a solution to the above equation needs *pdf* of both the signal and noise coefficients. Due to the orthogonal property of the DT, the noise in the transform domain remains zero mean Gaussian with a standard deviation σ_v. So the noise *pdf* can be written as

$$p_v(v_j) = \frac{1}{\sqrt{2\pi}\sigma_v}\, e^{-\left(\frac{v_j^2}{2\sigma_v{}^2}\right)} \tag{4.37}$$

It was established that WT coefficients of natural images have highly non-Gaussian heavy tailed distribution [153]. The *pdf* for wavelet coefficients is often modeled using a Generalized Gaussian Distribution (GGD) as follows:-

$$p_f(f)] = K(s,p)e^{-\left|\frac{f}{s}\right|^p} \tag{4.38}$$

where $s\,\&\,p$ are the parameters for this model, and $K(s,p)$ is the parameter-dependent normalization constant. Since DT is an extended WT operation, the DT coefficients of natural images also follow a non-Gaussian statistics with heavy tailed distributions. This non-Gaussian statistics can be modelled by using different heavy tailed *pdf*s. There are many marginal distributions proposed in literature. However these marginal models cannot effectively model the statistical dependencies between wavelet coefficients. It was established that there are strong

inter and intra scale dependencies between WT coefficients of natural images. Four different non-Gaussian models to characterize this dependency between a coefficient and its parent were proposed by Sendur et. al. and the corresponding bivariate MAP estimators based on noisy wavelet coefficients were derived [49]. But all these models were made based on the dependency of a coefficient and its parent at adjacent coarser scale locations and at adjacent spatial locations only. The children at the adjacent finer scale locations are not considered. Here a new joint non-Gaussian model is presented which characterizes the dependency between a coefficient and its parent at coarser scale and children at finer scale, and derives the corresponding bivariate MAP estimators. The Bayesian estimation problem is modified to take into account the statistical dependency between a coefficient and its parent and children. Thus the joint probability density functions for the noise and signal coefficients have to be considered by taking into account the parent child relationship. The noise is assumed to be independent and identically distributed. Then the corresponding joint *pdf* of noise vector $v_j = \left(A_{v_{jpc}}, v_j \right)$ can be written as a bivariate *pdf* as

$$p_v(v_j) = \frac{1}{\left(\sqrt{2\pi}\sigma_v\right)^2} \ e^{-\left(\frac{A_{v_{jpc}}{}^2 + v_j^2}{2\sigma_v{}^2}\right)} \tag{4.39}$$

The joint *pdf* for the signal coefficient vector $f_j = \left(A_{f_{jpc}}, f_j \right)$ can be defined as

$$p_f(f_j) = \frac{3}{\left(\sqrt{2\pi}\sigma\right)^2} \ e^{-\left(\frac{\sqrt{3}}{\sigma}\sqrt{A_{f_{jpc}}{}^2 + f_j{}^2}\right)} \tag{4.40}$$

Here the model fitting performance of this proposed model to the statistics of natural images has to be studied. The histogram of *Lena* and *Barbara* images at two different subbands and levels are considered here. These are shown in figure 4.12 and 4.13. The proposed estimated *pdf* are also shown in red colour in each plot. These figures show that the proposed model provides a very good fit to the histogram of directionlet transform coefficients at different subbands and levels of these images. Also, for a quantitative evaluation of the closeness of fit, the Kullback-Leibler (KL) distance [150] is used to measure the difference between normalised histogram and the estimated *pdf*. It is a non-symmetric measure of the difference between two probability distributions *P* and *Q*. Specifically, the Kullback–Leibler divergence of *Q* from *P*, denoted as $D_{KL}(P\|Q)$, is a measure of

the information lost when Q is used to approximate P. For discrete probability distributions P and Q, the KL divergence of Q from P is defined to be

$$D_{KL}(P\|Q) = \sum_i ln\left(\frac{P(i)}{Q(i)}\right) P(i) \tag{4.41}$$

The KL distance of the proposed *pdf* in (4.40) and the histograms of DT coefficients at different subbands and resolution levels of *Lena* and *Barbara* images are given in Table 4.5. This also shows that the proposed model has very good model fitting performance. Based on this analysis, the proposed model can very well be used in the MAP estimation process.
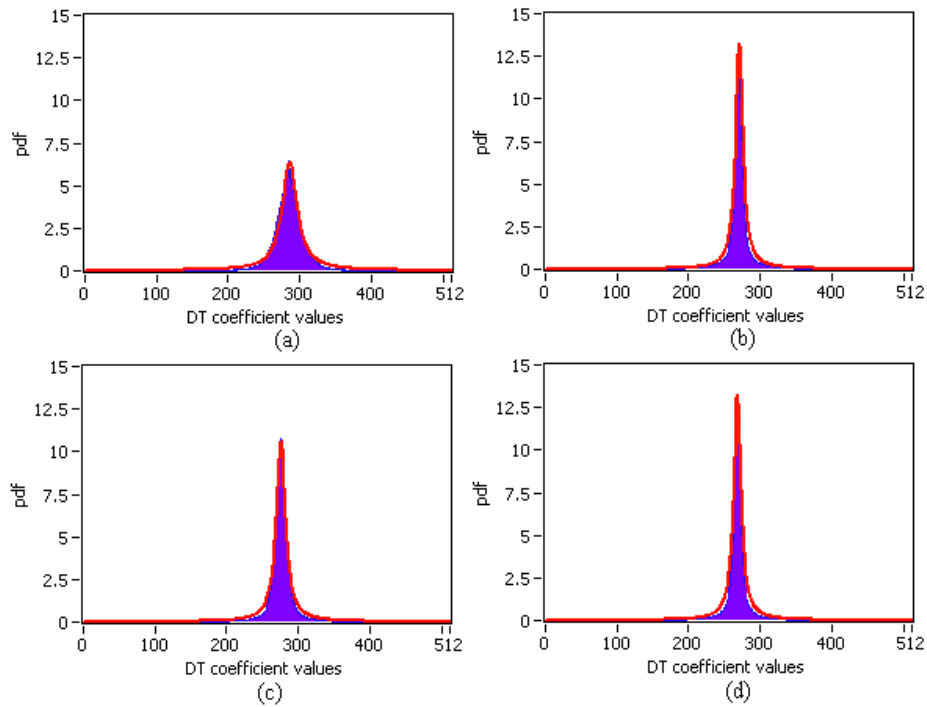
Figure 4.12 Histogram of the DT coefficients of '*Lena*' image & the estimated bivariate *pdf* (a) *HHH* subband at level 1 (b) *HHH* subband at level 2 (c) *HLH* subband at level 1 (d) *HLH* subband at level 2
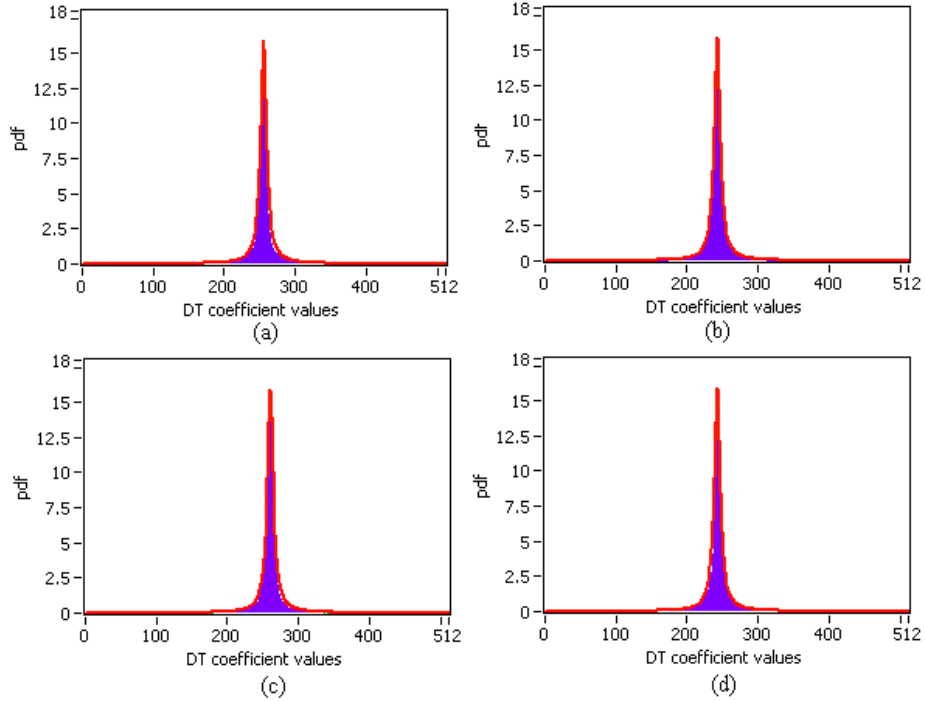
Figure 4.13 Histogram of the DT coefficients of '*Barbara'* image & the estimated bivariate *pdf* (a) *HHH* subband at level 1 (b) *HHH* subband at level 2 (c) *HLH* subband at level 1 (d) *HLH* subband at level 2

Table 4.5 Values of the K-L distance between the normalised histogram and estimated *pdf*

Image	HHH		HLH	
	Level 1	Level 2	Level 1	Level 2
Lena	3.51	3.18	2.95	3.03
Barbara	2.33	3.12	2.02	2.91

Using equation (4.36) with (4.39) and (4.40), the MAP estimator of f_j is derived as

$$\hat{f}_j(A_{g_{jpc}}, g_j) = \frac{\left(\sqrt{A_{g_{jpc}}{}^2 + g_j^2} - \frac{\sqrt{3}\sigma_\vartheta^2}{\sigma} \right)_+}{\sqrt{A_{g_{jpc}}{}^2 + g_j^2}} \cdot g_j \qquad (4.42)$$

121

Here the parameters required for this estimator are only signal and noise variances, σ^2 and σ_v^2 respectively. By using these parameters, the estimate of the noise free DT coefficients can be computed from the noisy observations of the same coefficients at adjacent scales.

4.4.2 Denoising Algorithm

The DT can have directional vanishing moments along any two directions with rational slopes. Thus the dominant directions in an image have to be identified first to select the two transform directions. Since directionality in an image is a local feature which varies over space, it is ideal to identify it after spatially segmenting the image into small blocks.

Here the input image is first divided into small spatial segments. Then a local texture-direction detector is constructed by measuring directional variance [146], using equation (4.16) to identify the pair of transform directions. Here the $DirVar$ is computed along eight different directions with $(x, y) = (1, 0)$, $(2, 1)$, $(1, 1)$, $(1, 2)$, $(0, 1)$, $(-1,2)$, $(-1, 1)$ and $(-2,1)$ which corresponds to 0º, 30º, 45º, 60º, 90º, 120º, 135º and 150º. This was carried out for each spatial segment of the image and the directions corresponding to the two minimum $DirVar$ are identified as the optimal pair of directions for computing the DT. The segments where the $DirVar$ for all the directions comes within 5% are considered to have no apparent dominant directions. For such segments, the pair (0º, 90º) is assigned by default as the transform directions for the reason of simplicity of implementation of DT.

The directionlets apply transform separately on each coset of the integer lattice given by the chosen generating matrix, and by definition no interaction is allowed between these cosets. Here based on the computational efficiency point of view, the generating matrices are selected in such a way that they will not form more than one coset. To satisfy this condition, the direction vectors d_1 and d_2 are considered such that $|det\ (M_\Lambda)| = 1$. One useful subset of matrices with $|det\ (M_\Lambda)| = 1$ are of the form $M_\Lambda = \begin{bmatrix} 1 & 0 \\ p & 1 \end{bmatrix}$ and $M_\Lambda = \begin{bmatrix} 0 & 1 \\ 1 & p \end{bmatrix}$ where $p \in \mathbb{Z}$. Varying p leads to large number of transform directions. Based on the eight

directions considered earlier for $DirVar$ computation, thirteen different generating matrices can be formed as follows which will satisfy the above condition.

$$M_{\Lambda 1} = \begin{bmatrix} 1 & 0 \\ 0 & 1 \end{bmatrix}, M_{\Lambda 2} = \begin{bmatrix} 1 & 0 \\ 1 & 1 \end{bmatrix}, M_{\Lambda 3} = \begin{bmatrix} 1 & 0 \\ 2 & 1 \end{bmatrix}, M_{\Lambda 4} = \begin{bmatrix} 1 & 0 \\ -1 & 1 \end{bmatrix}, M_{\Lambda 5} = \begin{bmatrix} 1 & 0 \\ -2 & 1 \end{bmatrix},$$

$$M_{\Lambda 6} = \begin{bmatrix} 0 & 1 \\ 1 & 1 \end{bmatrix}, M_{\Lambda 7} = \begin{bmatrix} 0 & 1 \\ 1 & 2 \end{bmatrix}, M_{\Lambda 8} = \begin{bmatrix} 2 & 1 \\ 1 & 1 \end{bmatrix}, M_{\Lambda 9} = \begin{bmatrix} 1 & 1 \\ 1 & 2 \end{bmatrix}, M_{\Lambda 10} = \begin{bmatrix} -1 & 2 \\ 0 & 1 \end{bmatrix},$$

$$M_{\Lambda 11} = \begin{bmatrix} -1 & 2 \\ -1 & 1 \end{bmatrix}, M_{\Lambda 12} = \begin{bmatrix} -1 & 0 \\ 1 & 1 \end{bmatrix}, M_{\Lambda 13} = \begin{bmatrix} -1 & 1 \\ -2 & 1 \end{bmatrix}$$

Using these generator matrices the DT decomposition is carried out for each spatial segment along the content directionality. Pairs of directions that would result in $|det\ (M_{\Lambda})| > 1$ and thereby form multiple cosets are not considered here to avoid the division of spatially adjacent pixels into different cosets. Symmetric boundary extension at the borders of the segment is carried out while taking the transform, to avoid the boundary errors. As compared to the periodic extension, the symmetric extension has shown to yield better performance.

The noise free DT coefficients are then computed using the estimator given in equation (4.41). It may be noted here that, since the undecimated DT decomposition generates redundant representation, there are correlations exist between the decomposition coefficients. Thus the $i.i.d$ models explained in the previous section are not justified and the derivation of MAP estimator is not possible. To overcome this, the DT coefficients are separated into four sets of uncorrelated coefficients namely $g^i_{j+1}(2x, 2y), g^i_{j+1}(2x + 1, 2y), g^i_{j+1}(2x, 2y + 1)$ and $g^i_{j+1}(2x + 1, 2y + 1)$. For the mth level decomposition, the coefficients can be separated into $2^{(n_1+n_2)m}$ sets, each containing uncorrelated coefficients, and they are $i.i.d$ within each set as well. This approach lets us still use the independent noise assumption and circumvent the issue of denoising correlated signal coefficients with correlated noise.

The estimator in equation (4.42) requires the prior knowledge of the noise variance σ_v^2 and marginal variance σ^2 for each directionlet coefficient. The noise variance can be computed from the high frequency sub band coefficients at the finest scale (HHH_1) in the directionlet decomposition as

$$\sigma_v = \frac{Median\ (|g_1|)}{0.6745}, where\ g_1 \in HHH_1 \tag{4.43}$$

The marginal variance can be estimated using a locally adaptive scheme [50]. From the observation model of equation (4.30), one gets $\sigma_g^2 = \sigma^2 + \sigma_v^2$, where σ_g^2 is the marginal variance of noisy observations, g_j. Since g_j is modelled as zero mean, σ_g^2 can be calculated as follows

$$\sigma_g^2 = \frac{1}{M}\Sigma_{g_i \in N_o(k)}\, g_i^2 \tag{4.44}$$

where M is the size of the oriented neighbourhood, $N_o(k)$, which is defined as all coefficients within an anisotropic neighbourhood oriented along the transform direction and centered at the kth coefficient. In the case of undecimated DT since the down samplers are discarded in the decomposition process, the transform coefficients in the nearest neighbor spatial locations are highly correlated and they provide only redundant information. Therefore, estimation of marginal variance based on the closest neighborhood is not too efficient. For that reason, a sparser neighborhood is chosen, that is, the neighborhoods of coefficients with the relative coordinates to the coordinate of the referent coefficient scaled by the distance factor, $\delta = 2^j$ while the dimensionality of the neighborhood is retained the same. Here the orientation is matched with the transform direction.

Using σ_g^2 and σ_v^2, σ can be estimated as

$$\sigma = \sqrt{\left(\sigma_g^2 - \sigma_v^2\right)_+} \tag{4.45}$$

Since the DT coefficients at the first level do not have any children the noise free coefficients at this level are computed using the standard bivariate shrinkage procedure given in [50]. Now inverse DT is applied on the denoised directionlet coefficients to get the noise free image. The denoising algorithm presented here is referred as *DT-Interscale* and is summarised in three steps as follows:-

Step 1: **Spatial Segmentation & Identification of dominant direction**
- Spatially segment the noisy image into small blocks.
- Compute optimal pair of directions for each spatial segment using *DirVar*.

Step 2: **Multi scale DT computation and estimation of noise free coefficients**
- Apply multilevel undecimated DT to the segments along the optimal pair of directions.

- Calculate the noise variance σ_v^2 from HHH_1 subband coefficients using equation (4.43).
- For each DT coefficient compute the marginal variance σ^2 using (4.45).
- Estimate the new DT coefficient using equation (4.42) except for the DT coefficients at level 1.
- Estimate the new coefficients at level 1 using standard bivariate shrinkage procedure of [50]

Step 3: **Reconstruction**
- Reconstruct the image from the modified DT coefficients using directional information and inverse DT

4.4.3 Experimental Results & Analysis

Standard 8-bit greyscale images of size 512 x 512 are used for evaluating the performance of the developed algorithm. The test images are contaminated with zero mean white Gaussian noise with variance 10, 15, 20, 25 & 30. The performance of the proposed method is compared with Bayesian thresholding in wavelet domain (BayesShrink) [43], SURE linear expansion of thresholding in wavelet domain (SURELET) [51], bivariate shrinkage in DTCWT domain (BiShrink) [50], steerable pyramid based oriented denoising (BLS-GSM) [54] and the DTCWT based scheme using three scales of dependency (DTWT-3) [53]. The BLS-GSM algorithm uses fully steerable pyramid decomposition with five levels and eight oriented sub bands at each level. BiShrink uses six levels and DTWT-3 uses three levels of DTCWT. The performance improvement was quantified in terms of Peak Signal to Noise Ratio (PSNR). The PSNR comparison of *Lena, Boat* and *Barbara* images is given in Table 4.6.

In the proposed method the image was spatially segmented into small blocks of size 32x32 and three levels of decomposition using undecimated DT with an anisotropic ratio of 1:2 was carried out. The biorthogonal-9/7 filter bank was used for DT decomposition and a 5x5 window was used as the neighbourhood window for marginal variance estimation. The segment size and the neighbourhood window size will greatly affect the quality of processed images. If the segment size is too small, the algorithm may not work well and may lead to unwanted block-like

artifacts. On the other hand, if the segment size is too large, the region containing image features will also become large with relatively more number of directions. This will adversely affect the denoising performance. It was also found that as the size of neighborhood window increases the image is getting more smoothened with diminishing features. Our experiments indicate that a window of size three or five is an ideal choice. The selection of biorthogonal wavelet is due to two reasons; regularity and symmetry. Regularity deals with sparse representation, i.e. a wavelet shall generate relatively few significant coefficients after decomposition. The regularity of a wavelet usually increases with the number of its vanishing moments. The symmetry is related to visual quality. The preference of symmetrical wavelets is due to the fact that our visual system is more tolerant of symmetric errors than asymmetric ones.

Table.4.6. PSNR (dB) Comparison of DT-Bivariate scheme with other efficient schemes

				Lena			
σ	Noisy	BayesShrink [43]	SURELET [51]	BiShrink [50]	DTWT-3 [53]	BLS GSM [54]	DT-Interscale
10	28.13	33.33	34.56	35.32	35.32	35.60	**35.96**
15	24.61	31.39	32.68	33.64	33.60	33.90	**34.25**
20	22.11	30.15	31.37	32.41	32.36	32.66	**32.95**
25	20.17	29.21	30.36	31.38	31.38	31.68	**31.90**
30	18.59	28.48	29.56	30.51	30.56	30.88	**31.03**
				Boat			
10	28.13	31.78	32.91	33.12	33.23	33.58	**33.95**
15	24.61	29.84	30.80	31.34	31.35	31.68	**32.03**
20	22.11	28.43	29.47	30.09	30.01	30.35	**30.74**
25	20.17	27.37	28.44	29.02	28.98	29.33	**29.67**
30	18.59	26.56	27.63	28.33	28.16	28.49	**28.81**
				Barbara			
10	28.13	30.84	32.18	33.35	33.66	34.02	**34.38**
15	24.61	28.50	29.66	31.28	31.49	31.83	**32.17**
20	22.11	27.11	27.97	29.81	29.97	30.27	**30.64**
25	20.17	26.00	26.76	28.58	28.78	29.07	**29.41**
30	18.59	25.14	25.83	27.62	27.84	28.07	**28.30**

Though the performance difference is marginal as compared to BLS-GSM scheme the *DT-Interscale* outperformed the compared schemes for all the test images. It

outperforms the classical *Bayes Shrink* by more than 2 dB on low and medium frequency images like *Lena* and *Boat* and more than 3 dB on high frequency image like *Barbara*. The interscale dependency modeling in directionlet domain for high frequency images give better results as it adaptively captures the oriented features like edges and contours in these images which correspond to high frequency information. It can also be seen from the results that the performance improvement of the *DT-Interscale* scheme as compared to the other schemes is narrowing down as the noise variance increases. This can be attributed to the fact that as the noise variance increases the accurate identification of dominant directions in the image is getting adversely affected. Thus the improvement of the quality of denoised images using *DT-Interscale* scheme, when compared to the results of the wavelet and DTCWT based schemes is significant, especially at lower noise levels.

The visual quality of the denoised images is also used to evaluate the performance. Most of the image denoising algorithms achieve high visual quality in smooth regions. The difference is mainly in the preservation of image edges and textures. In Figure 4.14 and Figure 4.15 extracted portions of *Barbara* and *Lena* images are shown for visual comparison of the proposed scheme with BiShrink [50]. The visual quality of the denoised image using the proposed algorithm is evidently better because of sharper edges and texture. To emphasize this gain, portions of the denoised images of *Barbara* containing the stripes of the scarf and *Lena* containing the lines of the hat are zoomed in for both the methods. It can be noticed that the stripes in the scarf of *Barbara* image and the cross lines in the hat of *Lena* image are more clear and distinct in the denoised images of *DT-Interscale* scheme.

In Figure 4.16, three different regions of *Lena* image containing smooth, edge and texture areas are extracted and the performance is compared with BiShrink and BLS-GSM algorithms. The visual quality with the *DT-Interscale* scheme in the smooth region is almost same as that with BiShrink scheme. In the areas where there are edges and textures, the performance of the *DT-Interscale* algorithm is similar to that of BLS-GSM. The performance is slightly inferior in segments where both edges and smooth regions are equally dominant. This is because the oriented denoising will adversely affect the smooth areas in a segment. So the selection of segment size plays a major role in the denoising performance.

Figure 4.14 Image denoising results of part of *Barbara* image (a) noise free image (b) noisy image with $\sigma_v = 20$ (c) denoised image using BiShrink and (d) denoised image using DT-Interscale (e) selected enlarged portion of '(c)' (e) selected enlarged portion of '(d)'
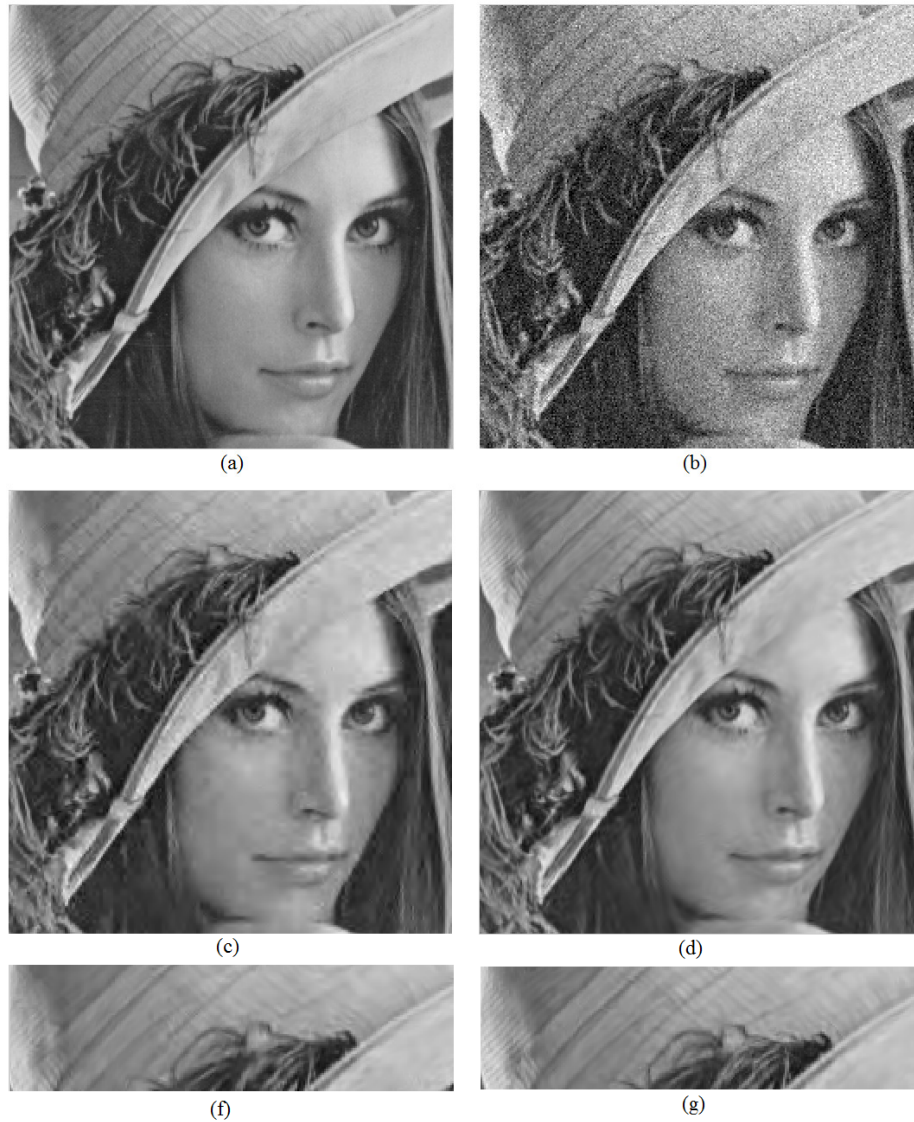
Figure 4.15 Image denoising results of part of *Lena* image (a) noise free image (b) noisy image with $\sigma_v = 20$ (c) denoised image using BiShrink and (d) denoised image using DT-Interscale (e) selected enlarged portion of '(c)' (e) selected enlarged portion of '(d)'
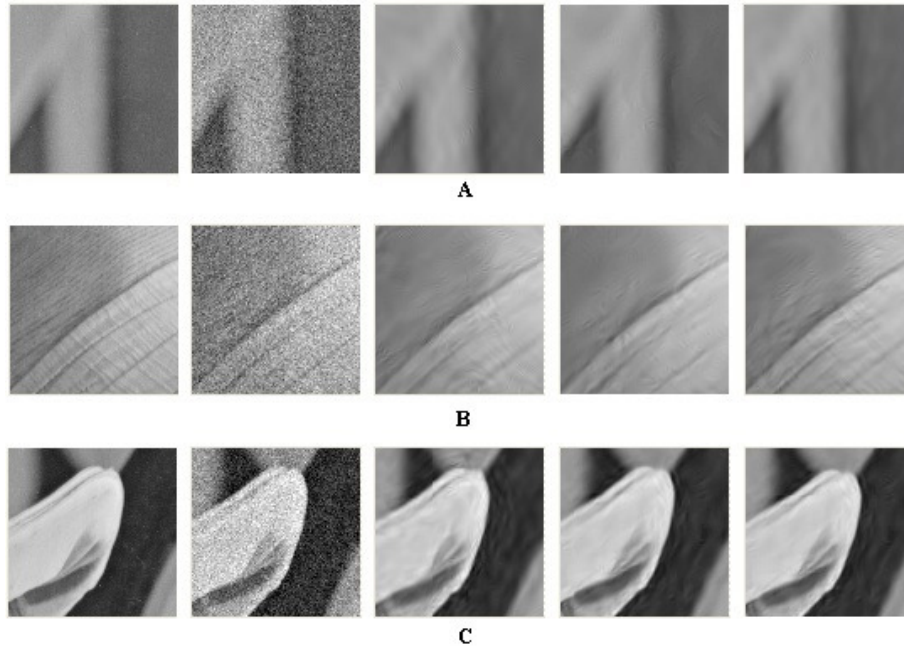
Figure 4.16. Image denoising results of smooth (A), texture (B) and edge (C) regions of *Lena* image using BiShrink, BLS-GSM & DT-Bivariate schemes. The images are arranged from left to right in order from Noise free image, noisy image with noise variance 20, denoised image using BiShrink, denoised image using BLS-GSM and denoised image using DT-Interscale scheme.

An analysis of the computational complexity of the presented scheme is carried out here. The computational cost of the scheme consists of the cost of image segmentation, identification of dominant directions, image decomposition using DT, filtering process and reconstruction. Here the additional computation as compared to the BiShrink and DTWT-3 schemes is due to the identification of dominant directions using *DirVar*. For k pairs of directions the computation of *DirVar* requires one addition and one multiplication per direction, per pixel. So for an image with N pixels, the computation of *DirVar* requires only $k \times N$ additions and the same number of multiplications. In BLS-GSM scheme eight directions and five levels are used leading to a total of forty 2-D non-separable filtering stages. The 2-D filtering of BLS-GSM scheme is much more complex than the separable

1-D filtering of the *DT-interscale* scheme. The computation cost of variance estimation is almost same in all the schemes. This analysis shows that the transform in the case of directionlets is computationally simpler than the steerable pyramids with 2-D directional filter-banks used in BLS-GSM scheme. However the proposed scheme is computationally more complex than the other two schemes based on DTCWT, mainly due to the mandatory requirement of spatial segmentation of the input image and identification of local dominant directions. The actual time taken by the four algorithms in an Intel Core i5 CPU @ 2.4 GHz with 4GB RAM for *Barbara* image of size 512x512 with a noise level of $\sigma = 20$ is given in Table 4.7. This shows that the proposed scheme takes less than one third of the time of BLS-GSM scheme with performance better than that of BLS-GSM.

Table 4.7 Computation times taken by different algorithms

Method	BiShrink [50]	DTWT-3 [53]	BLS GSM [54]	DT-Interscale
Time (sec)	1.3	1.5	30.1	9.4

4.4.4 Conclusion

In this section an effective image denoising technique based on inter and intra scale dependency of directionlet transform coefficients is presented. The scheme suitably adjusts the transform directions based on content directionality of spatially segmented images and successfully captures the oriented features. It uses the joint statistics of the DT coefficients of natural images and a non-linear threshold function is derived using Bayesian MAP estimator. It was established that, allowing for spatial segmentation and choosing transform directions in each segment independently, directionlets outperform the DTCWT and BLS-GSM in image denoising. Even though the computational complexity of this scheme is less than one third of that of BLS-GSM scheme, it is much higher when compared to the other two schemes based on DTCWT. This may limit the practical applicability of the proposed algorithm. Thus the requirement is a computationally efficient scheme which can provide good denoising performance while preserving the edges and textures efficiently.

4.5 Denoising based on Adaptive Spatial Segmentation and Classification in Directionlet Domain

In this section a statistical model based denoising scheme is presented. This scheme is different from the earlier scheme in two aspects. One is the adaptive spatial segmentation of the image based on local dominant directions to identify the transform directions. This will improve computational efficiency and provide better sparse representation of the image. The second change is in the local variance estimation based on classification of DT coefficients using context modelling.

The image to be denoised is first spatially segmented based on the content directionality and the dominant directions in each segment are identified. Then an undecimated version of DT is applied to effectively capture the directional features and edge information of these segments. The DT coefficients so obtained are then modelled using a simple bivariate distribution and the noise free coefficients are computed using MAP estimator. By employing bivariate *pdf*, the heavy-tail behaviour of natural images is accurately modelled and the interscale properties of DT coefficients are properly exploited. In addition, the local variance parameter of the model is estimated based on classification of DT coefficients using context modelling. Due to this the intrascale dependency of directionlets is also well exploited in the enhancement process.

4.5.1 Adaptive Spatial Segmentation

By adapting the transform directions to the local content directions as close as possible, the DT concentrates the signal information to the low frequency approximation sub band as much as possible. However the DT can have directional vanishing moments only along two directions with rational slopes. Thus to get the best benefit out of DT, the dominant directions in an image have to be identified in advance to select the transform directions.

The content directionality in an image varies over space. Therefore it is ideal to find out the directionality in an image locally after spatially segmenting it into small blocks. Here a segmentation scheme adaptive to the content directionality is proposed. First, the input image is divided into four equally sized segments in a

step of the quad-tree spatial segmentation. Then for each spatial segment, the directional variance, *DirVar* [146] is computed along eight different directions with *(x, y)* = (1, 0), (2, 1), (1, 1), (1, 2), (0, 1), (-1,2), (-1, 1) and (-2,1). Even though more directions are possible, in practice, it was observed that these eight directions are enough to achieve a good performance.

For segments with uniform region or texture which don't have specific directionality, the *DirVar* doesn't vary much from direction to direction. This particular behaviour of *DirVar* can be used to differentiate the uniform and texture regions from the regions with specific directionality. If the value of *DirVar* along all eight directions are within 5% then that segment need no further division. The segments with more than two dominant directions are further quad tree segmented and the process is repeated till the predetermined maximal segmentation depth is reached. The two dominant directions of each segment are then selected as the transform and alignment directions. This way the transform directions are adapted independently in each spatial segment allowing for more efficient capturing of geometrical information. For segments having no apparent dominant directions, the transform directions are selected as (0º, 90º) for simplicity of implantation of DT. The optimal segmentation and the choice of transform and alignment directions for a simulated circle image is shown in figure 4.17.
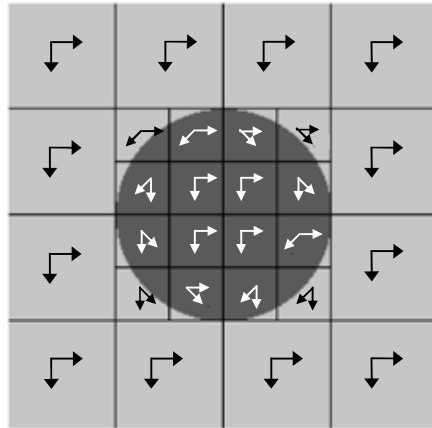
Figure 4.17 The optimal segmentation and choice of transform directions in each segment identified by Directional variance for simulated circle image

As in the previous scheme the generating matrices for the DT decomposition are selected in such a way that the determinant of the generating matrices value is one so that it will not form more than one coset. At every level of the transform only one level of 1-D transform is applied along each direction to avoid computational complexity. This will generate an isotropic decomposition. Even though anisotropic nature provides a faster asymptotic approximation rate it will result in a small number of scales and, therefore, the multi-scale dependence of the coefficients cannot not be properly captured. Symmetric extension at the borders of the segment was carried out while taking the transform, to avoid boundary errors.

4.5.2 Image Modelling & MAP Estimation

The image modelling and MAP estimation are similar to the earlier section except in the interscale dependency modelling. Here the parent coefficients only are considered for estimating the noise free coefficients. This is basically to make the system more computationally efficient. By considering only the parent coefficient in the estimation process, the estimate of the noise free coefficient can be obtained as follows

$$\hat{f}_j(g_j, g_{j+1}) = \frac{\left(\sqrt{g_j^2 + g_{j+1}^2} - \frac{\sqrt{3}\sigma_v^2}{\sigma}\right)_+}{\sqrt{g_j^2 + g_{j+1}^2}} \cdot g_j \qquad (4.46)$$

where g_j and g_{j+1} are the noisy DT coefficients at two adjacent scales, σ_v^2 is the noise variance and σ^2 is the marginal variance. So if we know the noise and signal variances, the estimate of the noise free DT coefficients can be computed from the noisy observations of the same coefficient and its parent at adjacent scale.

4.5.3 Signal Variance Estimation through Context Modelling

The signal variance is estimated here using the context modelling technique as explained in [44]. In the case of decimated DT, since the coefficients in a subband are de-correlated, the $i.i.d$ models are largely justified and thus the derivation of a MAP estimator is facilitated. However undecimated DT decomposition generates redundant representation, and there are correlations between the decomposition coefficients. For example, at the first level of decomposition, the odd and even

coefficients in each direction are correlated. So in this case the realistic statistical modelling of coefficients is far more difficult. To solve this issue the coefficients have to be separated into four sets of uncorrelated coefficients, namely $g_j^i(2k, 2l)$, $g_j^i(2k + 1, 2l)$, $g_j^i(2k, 2l + 1)$ and $g_j^i(2k + 1, 2l + 1)$. For the sth level decomposition, the coefficients can be separated into $2^{(n_1+n_2)s}$ sets, each containing uncorrelated coefficients, and they are $i.i.d$ within each set as well. This approach lets us still use the independent noise assumption and circumvent the issue of denoising correlated signal coefficients with correlated noise. The coefficients from each of these groups are further classified based on context modelling to differentiate and gather coefficients with some similarities, but not necessarily spatially adjacent. Consider one particular group from a subband with N number of coefficients $g_j[k, l]$. Here the context value, $c_j(k, l)$ of noisy DT coefficient, $g_j[k, l]$ is calculated as the weighted average of the absolute values of its neighbours.

$$c_j(k, l) = u_j^{k,l} w_j \qquad (4.47)$$

where $u_j^{k,l}$ is a 1×8 vector whose elements are the absolute value of $g_j[k, l]$'s eight nearest neighbors. Here the parent coefficient at scale $j + 1$ is not considered as it is already accounted in the bivariate shrinkage function. Here w_j is a 1×8 weight vector, which can be found by using the least squares estimation as

$$w_j = (U_j^T U_j)^{-1} U_j^T |g_j| \qquad (4.48)$$

where U_j is a $N \times 8$ matrix with each row being $u_j^{k,l}$ and g_j is an $N \times 1$ vector containing all elements of $g_j[k, l]$. Now the context values are sorted in ascending order and the corresponding DT coefficients are clustered. The DT coefficients with similar natures are now arranged together and are assumed to have same statistics. Now the variance of a DT coefficient $g_j[k_0, l_0]$ can be estimated from $g_j[k, l]$ whose context $c_j(k, l)$ falls near to it. The pixel values can be selected by L closest points in value above $c_j[k_0, l_0]$ and L closest points in value below, resulting in a total of $2L$ points. These $2L$ points can be considered as a cluster Θ_j^i. The variance of DT coefficient can be estimated from this cluster as

$$\hat{\sigma}_{f_j}^2 = Max \left(\frac{1}{2L} \sum_{g_j(k,l) \in \Theta_j^i} g_j^2(k, l) - \sigma_v^2, 0 \right) \qquad (4.49)$$

Here σ_v^2 is the noise variance which needs to be subtracted because $g_j(k,l)$ are the noisy observations and the noise is independent of the signal. The noise variance can be computed from the high frequency sub band coefficients at the finest scale in the decomposition (HHH_1) using equation (4.43). The selection of the value of L is very important here. Too small or too large values adversely affect the performance.

4.5.4 Denoising Algorithm

The full denoising algorithm presented in this section is referred as *DT-Adaptive* and is summarized in three steps as follows

Step 1: **Adaptive Spatial Segmentation & Identification of dominant direction**
- The input image is first divided into four equally sized segments
- Compute $DirVar$ for each spatial segment along eight directions
- If the $DirVar$ for all directions lies within 5%, then leave the segment as such, else check whether there are more than two dominant directions in that segment. If it is so, then further divide it into four equally sized segments and go back to the previous step until a pre defined segmentation depth is reached.

Step 2: **Multi scale Directionlet Transform computation and Estimation of noise free coefficients**
- Apply 3-level undecimated DT to the segments having dominant directions along the optimal pair of directions to get the multi scale DT coefficients.
- Apply 3-level isotropic undecimated WT to the segments having no apparent dominant directions
- For each transform coefficients, compute the noise variance σ_v^2 using equation (4.43) and marginal variance σ^2 using equation (4.49).
- Estimate the noise free transform coefficient using equation (4.46).

Step 3: **Reconstruction**
- Reconstruct the image from the modified DT and WT coefficients using directional information of each segment and inverse DT and WT.

4.5.5 Experimental Analysis & Results

The performance of the presented algorithm is verified by using standard 8-bit grey scale images of *Lena, Boat* and *Barbara* of size 512 x 512. The *Lena* and *Boat* images contain smooth regions and edges while the *Barbara* image has abundant inhomogeneous structures. These images are contaminated with zero mean white Gaussian noise with standard deviation of 10, 15, 20, 25 & 30. The performance of the *DT-Adaptive* scheme was compared with that of interscale dependency model based schemes like BiShrink [50] and DTWT-3 [53]. Both these schemes are based on DTCWT.

In *DT-Adaptive* scheme, the image is quad tree segmented based on the content directionality and a maximum segmentation depth of 32x32 is fixed. The segmentation depth greatly affects the quality of processed images. If it is too small, the output image will have block like artefacts, which are seen as artificial edges at the segment boundaries. On the other hand, if the segment size is too large, the segment will have more number of dominant directions making it difficult to select the optimum transform directions. This will adversely affect the denoising performance. A segmentation depth of 32x32 is found to be an ideal choice. After segmentation, each segment is decomposed using undecimated DT up to three levels with biorthogonal-9/7 filter bank. The signal variance required to estimate the noise free coefficient is computed based on context modelling of the DT coefficients. Through this the intra scale dependency of the DT coefficients is also incorporated in the estimation process. The performance improvement of the *DT-Adaptive* scheme is quantified in terms of Peak Signal to Noise Ratio (PSNR). The values obtained are given in Table 4.8 for different noise realizations**.** The PSNR values provided are the average of ten different noise realizations for each standard deviation.

From the results it is clear that the *DT-Adaptive* method outperformed the DTCWT based schemes for all the test images, but the performance is slightly inferior as compared to *DT-Interscale* scheme. The visual quality of the denoised images is also used to evaluate the performance. The difference in visual quality is mainly in the preservation of image edges and textures. In figure 4.18 and figure 4.19, extracted portions of the *Lena* and *Barbara* images are compared with BiShrink in

DTCWT domain. The visual quality of the denoised image using the proposed algorithm is evidently better because of sharper edges and texture.

Table 4.8. PSNR (dB) comparison of DT-Adaptive scheme with other denoising schemes

Lena					
σ	Noisy	DTWT-3 [53]	BiShrink [50]	DT-Interscale	DT-Adaptive
10	28.13	35.32	35.32	**35.96**	35.82
15	24.61	33.60	33.64	**34.25**	34.08
20	22.11	32.36	32.41	**32.95**	32.80
25	20.17	31.38	31.38	**31.90**	31.78
30	18.59	30.56	30.51	**31.03**	30.94
Boat					
10	28.13	33.23	33.12	**33.95**	33.81
15	24.61	31.35	31.34	**32.03**	31.89
20	22.11	30.01	30.09	**30.74**	30.58
25	20.17	28.98	29.02	**29.67**	29.56
30	18.59	28.16	28.33	**28.81**	28.69
Barbara					
10	28.13	33.66	33.35	**34.38**	34.19
15	24.61	31.49	31.28	**32.17**	32.00
20	22.11	29.97	29.81	**30.64**	30.54
25	20.17	28.78	28.58	**29.41**	29.30
30	18.59	27.84	27.62	**28.30**	28.22

Here the computational efficiency of this algorithm is compared with the *DT-Interscale* scheme presented in previous section and also with DTCWT based schemes. The actual time taken by these algorithm in an Intel Core i5 CPU @ 2.4 GHz with 4GB RAM for *Barbara* image of size 512x512 with a noise variance of 20 is given in Table 4.9. This shows that the *DT-Adaptive* scheme is computationally more efficient than the *DT-Interscale* scheme but with a slight degradation in performance.

Table 4.9. Computation times taken by different algorithms

Method	BiShrink [50]	BLS GSM [54]	DT-Interscale	DT-Adaptive
Time (sec)	1.3	30.1	9.4	4.8
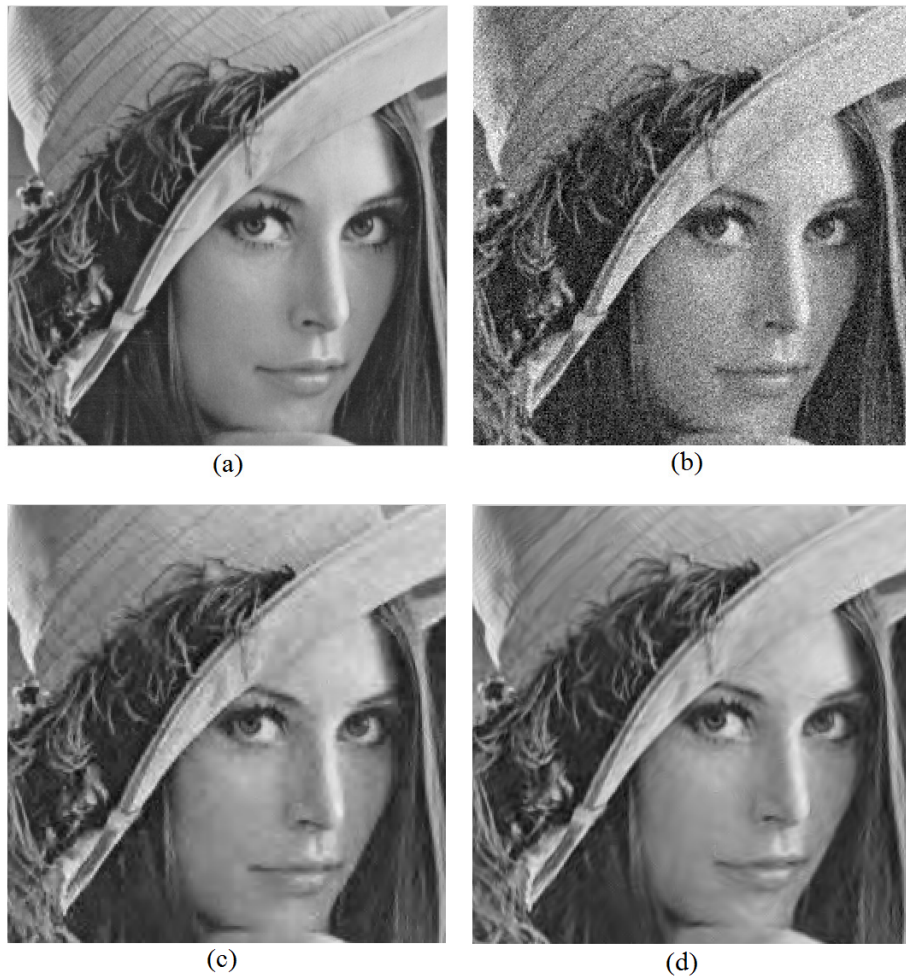
Figure 4.18 Visual comparison of Image denoising results of part of *Lena* image (a) noise free image (b) noisy image with $\sigma_v = 20$ (c) denoised image using BiShrink (d) denoised image using *DT-Adaptive*

Figure 4.19 Visual comparison of Image denoising results of part of *Barbara* image (a) noise free image (b) noisy image with $\sigma_v = 20$ (c) denoised image using BiShrink and (d) denoised image using *DT-Adaptive*

Spatially Adaptive SAR Image Despeckling in Directionlet Domain

---

This chapter presents the contributions of this thesis to SAR image despeckling. Here six different despeckling schemes in directionlet domain are presented, which include threshold based schemes and statistical model based schemes. The effectiveness of these schemes are established by comparing them with the state of the art technologies available for original SAR images and standard benchmark images corrupted with noise.

5.1 Introduction

Speckle in SAR images is generally modelled as multiplicative random noise, whereas most available filtering algorithms are developed for additive white Gaussian noise (AWGN) as additive noise is most common in imaging and sensing systems. To take advantage of the available noise models and wavelet based denoising techniques for AWGN, it is necessary to apply a logarithmic transform to convert the multiplicative noise model into an additive one. As a nonlinear operation, the logarithmic transform totally changes the statistics of SAR images, and thus the original speckle statistics cannot be directly applied to log-transformed images. SAR images are usually available in intensity format or amplitude format. The statistical modelling and parameter estimation techniques for the log-transformed multi-look speckle noise in these formats are explained in chapter 2.

In this chapter the main contributions of this thesis in the area of SAR image despeckling are presented. The basic principle of despeckling in directionlet

domain is illustrated in Figure 5.1. It mainly consists of four steps. The first step is the spatial segmentation of the image and identification of two dominant directions. The second step involves DT computation along these dominant directions. The third step is the manipulation of the DT coefficients and the final step is the computation of the inverse DT using the modified coefficients. Since the speckle noise is multiplicative in nature, a pre-processing step consisting of a logarithmic transformation is mandatory to separate the noise from the original image. The manipulation of DT coefficients can be done in two ways. One is thresholding and the other is statistical model based Bayesian estimation. Depending upon the manipulation of coefficients, the despeckling schemes can be divided in to two: the threshold based ones and the statistical model based ones. The threshold based methods involve the computation of a proper threshold, which is troublesome in many cases. Statistical model based methods involve modeling of image and noise coefficients using suitable *pdf*. The success of these schemes depends on the closeness of these models to the actual distribution. In this chapter six different despeckling schemes in directionlet domain are presented. The first three are threshold based schemes and the last three are statistical model based schemes. These schemes suitably adjust the transform directions based on local dominant directions of spatially segmented image and successfully capture the oriented features.
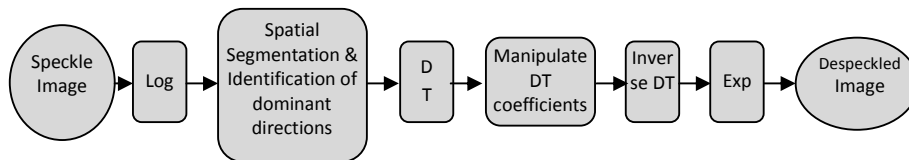
Figure. 5.1. Block diagram of directionlet based speckle suppression algorithm

In many threshold based despeckling scheme, the prior knowledge of noise variance is required for the proper computation of an optimal threshold. Unfortunately, this is not available in most of the cases. To avoid this limitation, Generalized Cross Validation (GCV) technique [45] is used here to estimate the optimal threshold without using the prior knowledge of the noise variance. GCV is based on the input data only and its minimum is a good approximation for the optimal threshold. The first scheme is a simple GCV thresholding in directionlet

domain. The second scheme efficiently extracts edge information along dominant directions from the spatially segmented SAR image. Then an optimal scale dependent subband adaptive threshold based on GCV technique is applied to the edge removed image. The despeckled image is finally synthesized using the extracted edge information to preserve sharpness of edges and texture. In the third scheme the adjacent DT coefficients are multiplied to amplify the significant signal features and thresholding is applied to these multiscale products to better differentiate edge structures from noise. The proposed schemes are compared with the similar schemes in wavelet domain and also with other directional transform based despeckling schemes.

 Among the statistical model based schemes proposed here, the first one uses a simple Laplacian-Gaussian modelling of the DT coefficients and the noise free coefficients are estimated using MAP criterion. The performance of despeckling schemes based on multi-resolution analysis can be improved significantly by taking into account the multi-scale correlation among the transform coefficients. Here the last two schemes are based on bivariate modelling of the directionlet coefficients, which takes into account the multi-scale correlation among the transform coefficients. In the first scheme the signal and the noise coefficients are modelled using Cauchy-Gaussian bivariate distributions which take into account the statistical dependence between the adjacent scale coefficients. In the second scheme the interscale dependency of the DT coefficients is modelled using a non-Gaussian bivariate distribution with a local variance parameter. The nonlinear threshold functions derived from these models employing a *maximum a posteriori* (MAP) estimator are then used for estimating the noise-free coefficients. Since the directionlets possess spatial anisotropy and better directional capabilities, statistical interscale dependency modelling in directionlet domain results in visually appealing despeckling results, with improved performance parameters. The details of these despeckling schemes are presented in the following sections.

5.2 Despeckling using GCV Thresholding

Here a simple yet efficient despeckling scheme in directionlet domain is presented. As in any transform based despeckling schemes, the directionlet based despeckling also involves mainly three steps. First transform the input image using an

orthogonal transform, then threshold the transform coefficients using a non-linear algorithm and finally reconstruct the image using the modified coefficients. The effectiveness of a threshold based denoising algorithm basically depends on two factors- one is the efficient representation of the image to be denoised using a local, directional and multi resolution expansion and the other is the efficient computation of an optimal threshold. Here the first requirement is met by using a locally adaptive directionlet transform and the second by optimal threshold computation using Generalized Cross Validation (GCV) technique.

5.2.1 Speckle noise model

It may be assumed that the observed signal follows the following model

$$G = F.V \tag{5.1}$$

where G is the observed signal, F is the speckle-free reflectivity that we would like to estimate and V is the multiplicative speckle noise. Here a logarithmic transformation is carried out to convert the multiplicative nature of speckle noise to an additive one. However this results in a mean shift which has to be corrected after processing. After logarithmic transformation the equation (5.1) becomes

$$g = f + v \tag{5.2}$$

where g, f and v are the logarithms of G, F and V respectively. Owing to the linearity of DT, a multi-resolution decomposition of g results in

$$g_j = f_j + v_j \tag{5.3}$$

where g_j, f_j and v_j are the DT coefficients at level j of g, f and v respectively. The directionlet transform concentrates the important image features in a limited number of coefficients and the noise energy to all the coefficients. So the noise has small influence on the large signal coefficients. To reduce the contribution of these small noisy coefficients, a soft thresholding operation is applied to all the coefficients except those of the lowest scale. A soft threshold operation will set all the directionlet coefficients g_j below the threshold, λ (between $-\lambda$ to $+\lambda$) to zero, while others are shrunk in absolute value to obtain $g_{j\lambda}$.

$$g_{j\lambda} = sign(g_j)(\left|g_j\right| - \lambda)_+ \tag{5.4}$$

Finally, the speckle-reduced image is obtained from the synthesis part of the DT of the enhanced subband image $g_{j\lambda}$. The main problem here is the selection of an appropriate threshold. If this threshold is large, important image features will be lost. On the other hand, a small threshold will result a still noisy image. Thus an optimal threshold, $\lambda_{k,opt}$ is required which optimizes the mean square error $R_k(\lambda)$.

$$R_k(\lambda) = \frac{1}{N_k} \left\| G_{k,\lambda} - F_k \right\|^2 \qquad\qquad (5.5)$$

where N_k is the number of coefficients in the subband k, $G_{k,\lambda}$ is the vector of threshold applied noisy coefficients and F_k is the vector of noise-free coefficients. Here, because F_k is unknown the function $R_k(\lambda)$ is not computable and hence it cannot be used in practical applications to compute the optimal threshold $\lambda_{k,opt}$.

5.2.2 Thresholding based on Generalized Cross Validation

Since piecewise smooth true images have sparse representations with respect to wavelet basis functions, wavelet denoising methods have been intensively researched over the past two decades. Donoho and Johnstone [17] provided an asymptotically optimal choice for a single thresholding parameter under soft thresholding with an assumption of white noise. Following their work, Nason [147] and Jansen et al [45] proposed cross validation (CV) and generalized cross validation (GCV) techniques, respectively, for threshold parameter estimation. Johnstone and Silverman [148] suggested schemes for dealing with correlated noise by grouping wavelet coefficients according to their resolution levels and then selecting the threshold parameters separately for each resolution level. Jansen and Bultheel [149] subsequently revised the GCV technique to accommodate correlated noise.

In GCV technique, the original image f is assumed to be regular so that the ith component of it, f_i can be approximated by a linear combination of its neighbours. So by considering $\tilde{g}_i$, as a combination of its neighbours, the noise in this particular component can be eliminated. That is a pixel value is replaced by the weighted average of its neighbours to smooth the noise in that pixel. This value can be used in the computation of an approximation for mean square error, $R_k(\lambda)$ of equation

(5.5). This way the modified signal $\tilde{g}$ is obtained by replacing the ith component g_i with $\tilde{g}_i$. Now we have to consider the ability of $\tilde{g}_{i,\lambda}$ to predict the value of g_i as a measure for the optimality of the choice of threshold, λ. For small values of λ, the difference $g_i - \tilde{g}_{i,\lambda}$ is dominated by noise while for large values of λ, the signal itself is affected. This can be repeated for all the components and the compromise can be estimated as Ordinary Cross Validation (OCV).

$$OCV = \frac{1}{N} \sum_{i=1}^{N} \left(g_i - \tilde{g}_{i,\lambda}\right)^2 \qquad (5.6)$$

The $\tilde{g}_i$ can be computed in many ways. One of the most obvious choices is

$$\tilde{g}_i = \frac{1}{2} \left[g_{i-1} + g_{i+1}\right] \qquad (5.7)$$

If $\tilde{g}_{i,\lambda}$ is taken as $Max_i \, g_i$ then $\tilde{g}_{i,\lambda} \le \tilde{g}_i$ and if $\tilde{g}_{i,\lambda}$ is taken as $Min_i \, g_i$ then $\tilde{g}_{i,\lambda} \ge \tilde{g}_i$. The OCV in equation (5.6) can be approximated as

$$OCV = \frac{1}{N} \sum_{i=1}^{N} \left(g_i - g_{i,\lambda}\right)^2 . \, w_i^{\,2}(\lambda) \qquad (5.8)$$

where $\quad w_i(\lambda) = \frac{1}{(1-A'_{ii})} \quad$ and $\quad A'_{ii} = \frac{g_{i,\lambda} - \tilde{g}_{i,\lambda}}{g_i - \tilde{g}_i} \approx \frac{\partial g_{i,\lambda}}{\partial g_i}$

This cannot be used in practical computations as A'_{ii} is 0 or 1. Thus a mean value of $w_i(\lambda)$ can be taken as

$$w_i(\lambda) = w(\lambda) = \frac{1}{\frac{1}{N} \sum_{i=1}^{N} (1 - A'_{ii})} \qquad (5.9)$$

With this generalisation, the OCV will become a Generalized Cross Validation (GCV) as

$$GCV = \frac{1}{N} \sum_{i=1}^{N} \frac{\left(g_i - g_{i,\lambda}\right)^2}{\left(\frac{1}{N} \sum_{i=1}^{N} (1 - A'_{ii})\right)^2} \qquad (5.10)$$

This can be written as

$$GCV(\lambda) = \frac{\frac{1}{N}\|g - g_\lambda\|^2}{\left[\frac{N_0}{N}\right]^2} \qquad (5.11)$$

where, N_0 is the number of coefficients that were replaced by zero. For orthogonal transforms, this formula can be used as such for the transform coefficients also. Thus GCV can be applied as such to both wavelet transform and directionlet transform coefficients. In the transform domain for a subband *k,* the GCV as a function of threshold λ is defined as

$$GCV_k(\lambda) = \frac{\frac{1}{N_k}\|g_{jk} - g_{jk,\lambda}\|^2}{\left[\frac{N_{k0}}{N_k}\right]^2} \qquad (5.12)$$

where N_{k0} is the number of coefficients that were replaced by zero, g_{jk} is the transform coefficients at level j in the subband k. $g_{jk,\lambda}$ is the threshold applied transform coefficient g_{jk}. This is a function of known parameters of the input noisy image only and is independent of the noise variance. It was established that, under certain conditions, this threshold choice is asymptotically optimal, i.e., for a large number of wavelet coefficients, the minimizer of $GCV(\lambda)$ also minimizes the mean square error function (or risk function) $R(\lambda)$ [45]. Thus the value corresponding to the minimum of the GCV function can be used as the optimal threshold value. The main advantage of such an approach is that the prior knowledge about the amount of noise energy is not necessary here. The amount of computation for this minimization is comparable to or even less than that for the wavelet transform.

If E denotes the expectation operator, and λ^* and $\tilde{\lambda}$ are the estimated thresholds based on the minimum of mean square error, $R(\lambda)$ and minimum of Generalized Cross Validation, $GCV(\lambda)$ respectively then,

$$\lambda^* = \arg\min R(\lambda) \qquad (5.13)$$

$$\tilde{\lambda} = \arg\min GCV(\lambda) \qquad (5.14)$$

Then for $N,$ the total number of coefficients, tending to ∞

$$\frac{ER(\tilde{\lambda})}{ER(\lambda^*)} \downarrow 1 \qquad (5.15)$$

and in the neighborhood of λ^*

$$E\,GCV(\lambda) \approx ER(\lambda) + \sigma^2 \qquad\qquad (5.16)$$

Figure.5.2 illustrates this principle. Here the GCV and mean square error, R are plotted against threshold for a noisy image with a variance of 3. It can be seen from the figure that the minimum of both GCV and mean square error, R corresponds to the same threshold. However the mean square error is not computable from the available data but GCV is.
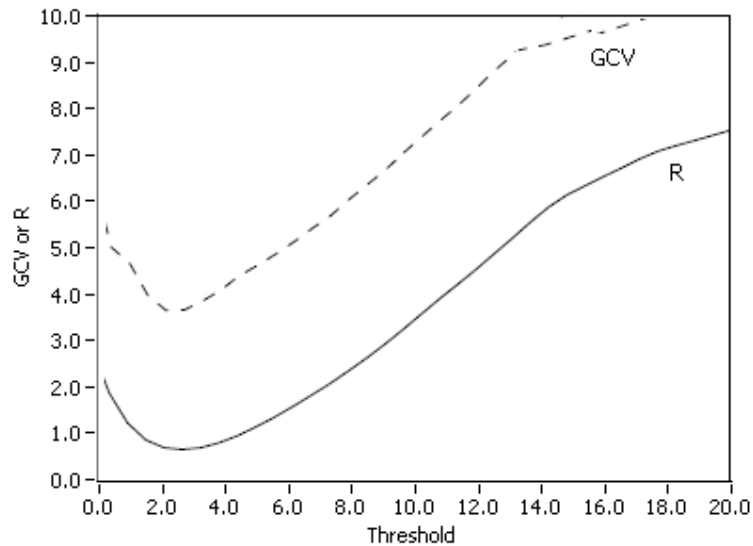
Figure 5.2 GCV and mean square error, R are plotted against threshold

The denominator in the GCV function counts the transform coefficients below the threshold and therefore behaves discontinuously as a function of the threshold value. This causes unpleasant jumps in the GCV plot, especially at small threshold values, since most coefficients are small. Typically, most discontinuities appear up to thresholds equal to the noise deviation. It was established that for a typical signal, 1000 sample values are sufficient for the minimum risk threshold to be far enough from the noise deviation. In that case the threshold will be in a region of smooth GCV behavior and can thus be easily estimated [45].

It was proven that the GCV procedure fails in cases with correlated noise. It is obvious that a wavelet threshold method fails when the noise on the coefficients is not stationary. The optimal choice of the threshold depends on the present noise energy. If the amount of noise is different for different coefficients, it is difficult to remove it decently by using a single threshold. The threshold computation methods are always based on the assumption that the noise is *i.i.d,* means it is stationary. A non orthogonal transform yields a non-stationary noise in transform domain even if the noise is stationary and white in time domain. Thus an orthogonal wavelet is required to be used for decomposition. The wavelet transform of stationary correlated noise is stationary within each resolution level. Since stationarity is a condition for a successful GCV-estimation of the optimal threshold, this result suggests choosing a different threshold for each resolution level. Although a level-dependent threshold selection works fine for correlated noise, problems may occur from the fact that the GCV-estimation is only asymptotically optimal. Indeed, the number of available coefficients decreases if the scale gets coarser, because of the subsampling step in the transform algorithm. A non-decimated transform or stationary transform has no subsampling step and therefore keeps the same number of coefficients at each level. Moreover, unlike the decimated transform, the redundant transform is translation invariant. The main drawback with such an approach is the increase in computational complexity.

For large images the computation of GCV may be time consuming. To deal with this problem, one can base the computation of GCV not on all pixels, but on a well selected, representative part of it. One way of doing it is selecting the pixels using an equidistant sampler.

5.2.3 Despeckling Algorithm

A transform based on direction of texture with edge information in an image can greatly improve its sparse representation and also the precision of estimation of correct threshold. Thus it is important to identify the dominant direction of texture before thresholding. As discussed earlier, the directionality in an image is a local feature which varies over space. Therefore it is ideal to find out the directionality in an image locally after spatially segmenting it into small patches. The directionlet

transform can have anisotropy and directional vanishing moments along any two directions with rational slopes. Here the input image is first spatially segmented in a quad tree structure and directionlet transform is taken along multiple directions from the set $D = \{(0°, 90°), (0°, 45°), (0°, -45°), (90°, 45°), (90°, -45°)\}$. These sets are chosen in such a way that the cubic lattice is not divided into more cosets in the lattice based implementation of DT [37]. The best pair of directions $d_n^* \in D$ is chosen for each segment indexed by *n* as follows [37].

$$d_n^* = arg\,min_{d \in D} \sum_i \left| W_{n,i}^d \right|^2 \qquad (5.17)$$

where $W_{n,i}^d$ represent the wavelet coefficients which are produced by applying directionlets to the nth segment along the pair d of directions. The assigned pair of transform directions of each patch across the input image forms a directional map of that image and provides the best matching between transform and locally dominant directions for that segment. For segments with no apparent dominant directions, the pair $(0°, 90°)$ is assigned by default to smooth the segments, for the reason of simplicity of implementation of the directionlet.

After identifying the dominant direction in each spatial segment, multi scale directionlet transform is applied along the dominant directions and the directionlet coefficients are selected for thresholding using GCV. In the directionlet decomposition, the subbands *HHH$_j$, HHL$_j$, HLH$_j$, HLL$_j$, LHH$_j$, LHL$_j$* and *LLH$_j$, j=1, 2, 3….J* are called the *details*, where *j* is the *scale*, with *J* being the largest scale in the decomposition. The subband *LLL$_J$* is the low resolution residual. The directionlets retain orthogonality from standard wavelet transform and the coefficients in the subbands are independent and identically distributed with zero mean. Thus the image noise model presented in section 5.2.1 is applicable for directionlets also. The directionlet coefficient g_{jk} from the detail subbands are used for optimal threshold computation using GCV technique to obtain $\tilde{g}_{jk}$. The denoised estimate is then $\hat{f} = D^{-1}\tilde{g}_{ij}$, where D^{-1} is the inverse directionlet transform operator.

It may be noted here that, since the undecimated DT decomposition generates redundant representation there are correlations between the decomposition coefficients. Thus the $i.i.d$ models explained in the previous section are not

justified. To overcome this, a level dependent threshold is used here. That is the thresholds for each subband at each level are computed separately.

The despeckling algorithm proposed here is referred as *DT-GCV* and is summarised in three steps as follows

Step 1: **Directionlets and Directional Map**
- The noisy image is first quad tree segmented till a desired level of segmentation is achieved.
- Make a logarithmic transformation (log (*g*+1.0)) of the segmented image to convert multiplicative noise to additive noise. Here 1 is added to prevent zero become -∞ after logarithmic transformation.
- Apply directionlet transform to the segments along the pair of directions $D = \{(0°, 90°), (0°, 45°), (0°, -45°), (90°, 45°), (90°, -45°)\}$
- Compute optimal pair of directions for each segment using equation (5.17)
- Compute the multi scale directionlet transform along the dominant directions

Step 2: **Threshold Computation**
- At each level for each subband, except the LLL_J subband, compute the GCV threshold which minimizes the parameter $GCV_k(\lambda)$, given in equation (5.12).
- Apply the computed threshold to the subband coefficients using soft thresholding rule to estimate the best value for the noise-free coefficients

Step 3: **Reconstruction**
- Reconstruct the image from the above processed sub-bands and the low-pass residual (LLL_J) using inverse directionlet transform and the directional map.
- Invert the logarithmic transformation to obtain the despeckled image

5.2.4 Results and Discussions

In SAR image denoising, due to the lack of the original noiseless signal, performance assessment is quite a challenging task. Different indicators have already been explained in chapter 2 to measure smoothness of smooth areas as well as sharpness of edges and details, but they are largely empirical and provide little insight about how to balance image smoothness and preservation of critical

information. Therefore, following the approach widely used in the literature, experiments have been carried out on optical images corrupted by simulated speckle. Through this, objective performance figures like PSNR have been obtained which allow a sound comparison among different despeckling algorithms. Experiments have been conducted with actual SAR images also. In this case Equivalent Number of Looks (ENL) is used as the performance parameter for assessing the performance of speckle reduction over a homogeneous area in the image. However ENL is not a good measure of despeckling performance in heterogeneous areas of an image. Thus the subjective quality of the despeckled image through visual examination is also important. A parameter called Edge Save Index (ESI) is also used to assess the edge preservation capability of the algorithm. It reflects the edge save ability in horizontal (ESI_H) or vertical (ESI_V) direction of the despeckling algorithm.

The proposed scheme is compared with similar scheme in wavelet domain (WT-GCV) [45]. The well-known traditional spatial filters like Frost filter [4] and Lee filter [6] are also considered here. These filters, although pretty aged, are the *de facto* standard, included in many image processing software packages, and used routinely by photo interpreters of military and civil space agencies. A 3x3 mask was used in both these spatial filters. For a fair comparison, three levels of decomposition using db4 wavelet was carried out both in WT-GCV and DT-GCV schemes. The subband coefficients in both these methods were shrunk using soft thresholding with a threshold value computed for each subband and resolution level through GCV technique. The *LL* subband in WT and *LLL* subband in directionlet scheme are kept unchanged. To reduce computational complexity, the GCV is computed only for 512 pixels for a segment of size 32x32. These pixels are selected using an equidistant sampler.

The resolution cell of the SAR system describes the smallest object the system is able to recognize and its size depends on the azimuth and range resolution. Each ground resolution cell is composed of a large number of elementary reflectors backscattering the radar wave in the sensor direction following different paths. The total component backscattered by the resolution cell is the vectorial sum of these elementary backscattered electrical fields. Interference caused by different

scattering waves can be both constructive and destructive. So SAR images are characterized by dark spots, corresponding to destructive interferences, and clear spots, due to constructive ones. These are seen as speckle in SAR images. The speckle noise can be modelled as a white noise with a Gamma distribution, whose parameter is the number of looks, L. The noise variance is inversely proportional to the number of looks, i.e., as the number of looks increases, the quality of image becomes better. Here in order to assess the quality of the presented algorithm, synthetically speckled images are used. These are generated from standard benchmark noise-free images added with speckle noise. Here 1, 2, 4 and 16-look amplitude speckled *Lena* and *Boat* images of size 512x512 disturbed by fully developed speckle are taken for experiments. The worst case corresponding to the input image with the number of looks, $L = 1$ and the best case corresponding to the image with number of looks, $L = 16$. The PSNR values obtained with different algorithms are given in table 5.1. Visual effects of these algorithms are shown in figure 5.3 for *Lena* image. Figure 5.3 (a) and (b) are noise-free *Lena* image and its speckled versions respectively. Figure 5.3 (c) – (e) shows the despeckled images obtained by Lee filter, wavelet based GCV thresholding and the proposed directionlet based scheme respectively. As they appear, the Lee filtered version has lower despeckling effects, because many homogeneous regions are not smoothed enough. The one-dimensional data extracted from 50th and 150th row of this test image is given in figure 5.4. It shows a comparison of the one-dimensional variation of noise less pixel values of *Lena* image and artifacts in despeckling results of same image with speckle noise using different algorithms. It can be seen from this figure that the pixel values of the despeckled image using DT-GCV follows the original one very smoothly. But in case of Lee filter and WT-GCV, there are many spikes in the despeckled pixel values. This clearly indicates that the noise reduction is much better in directionlet based scheme than the other schemes.

The performance of the scheme was also verified by using original SAR images in amplitude and intensity formats. Here an X-band, 2-looks, amplitude SAR image of Bedfordshire [151] and a Ku-band, 4-looks, intensity SAR image relevant to Horse track, near Albuquerque, New Mexico with 1-m resolution [152] are considered. Figure 5.5 and figure 5.6 show the visual comparison of the despeckled images obtained by different methods with these images. Two homogeneous

regions each in these images are used to compute the ENL. These areas are highlighted in the noisy SAR images. The ENL and ESI values obtained by the different schemes are listed in Table 5.2. It can be noted that the *DT-GCV* scheme provides a substantial improvement in terms of ENL and ESI over the other methods for both these images. Also the visual quality of the despeckled image using the proposed scheme is evidently better because of sharper edges and texture. The Gamma MAP filter smoothes speckle noise and gives better ENL among traditional schemes, but edges are blurred here and regions around the edges contain significant artefacts which are visible as dark spots. Even though the wavelet based scheme removes speckle effectively Gibbs phenomena exists in uniform regions and also the edges in this case are blurred.
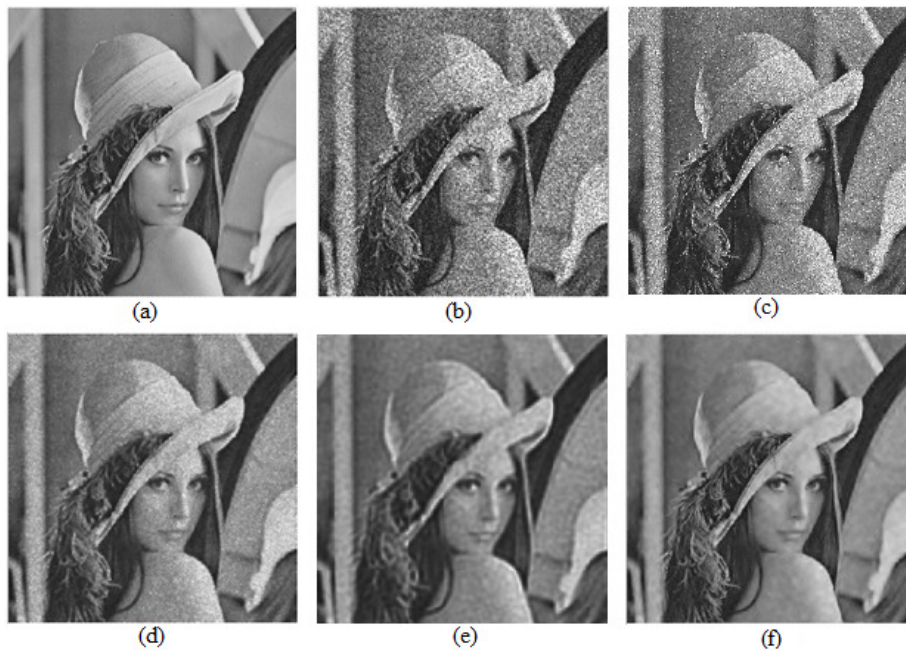
Figure 5.5 Despeckling results of Synthetic SAR image of *Lena* in amplitude format with *L=4* (a) Original noise free Image (b) Noisy image (c) Despeckled image using Frost filter (d) Despeckled image using Lee filter (e) Despeckled image using WT-GCV (f) Despeckled image using *DT-GCV*
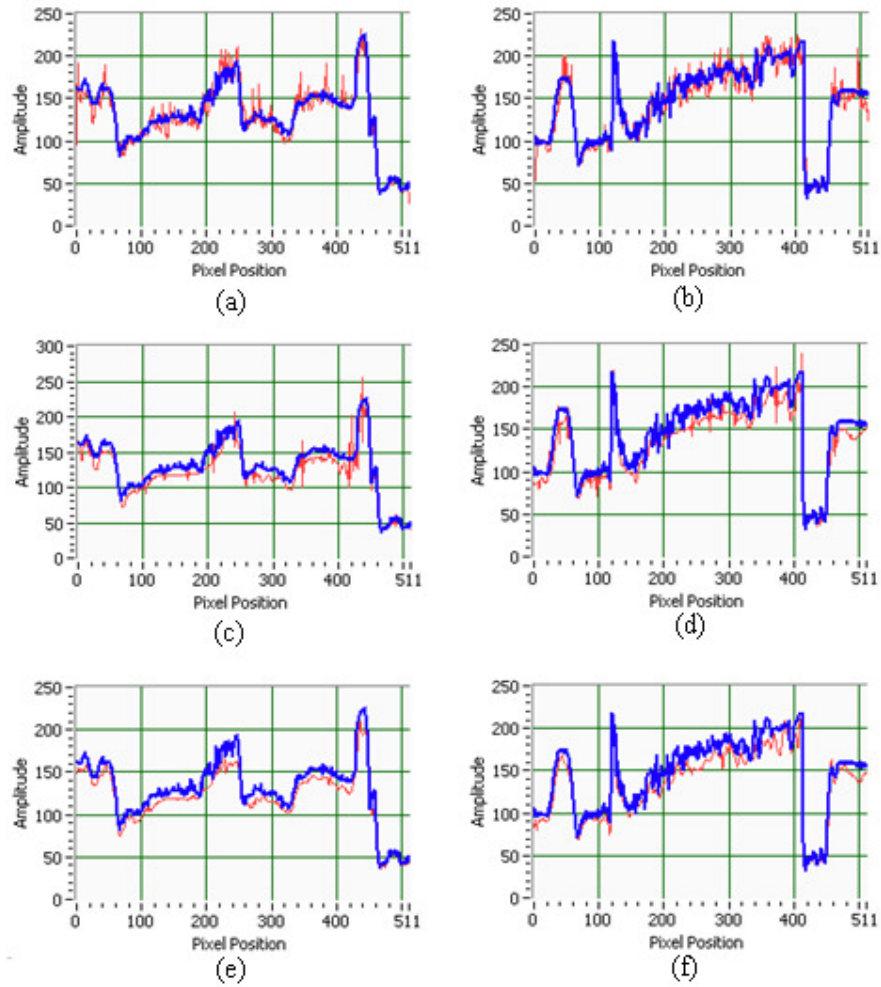
Figure 5.6 One-dimensional data extracted from 50th & 150th rows of synthetic SAR image of *Lena* in amplitude format with *L=4*. Original image pixels are shown in blue colour and despeckled image in red colour.(a) (b) Despeckled image using Lee filter, (c) (d) Despeckled image using WT-GCV and (e) (f) Despeckled image using *DT-GCV*

155

Table 5.1. Despeckling results (PSNR) for synthetic SAR images of *Lena & Boat* (512x512) in amplitude format

Looks/Method	Lena				Boat			
	1	2	4	16	1	2	4	16
Synthetic SAR Image	12.11	14.89	17.80	23.76	11.77	14.55	17.46	23.42
Frost [4]	19.16	23.32	26.32	30.60	18.64	22.56	25.22	28.33
Lee [6]	20.82	23.86	26.19	29.34	17.25	20.31	23.53	28.09
WT-GCV [45]	24.86	27.01	28.68	32.10	23.00	24.61	26.15	29.60
DT-GCV	**25.38**	**27.54**	**29.21**	**32.90**	**23.59**	**25.26**	**26.86**	**30.48**
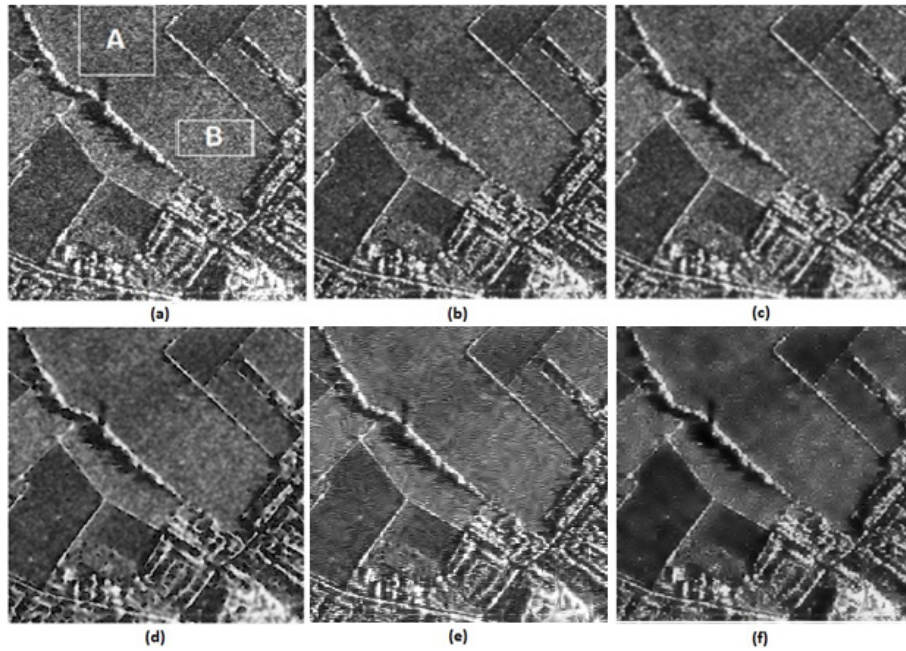
Figure. 5.7. (a) The original SAR image of *Bedfordshire* (b) de-speckled image using Frost filter (c) de-speckled image using Lee filter (d) de-speckled image using Gamma MAP filter (e) de-speckled image using WT-GCV and (f) despeckled image using DT-GCV.
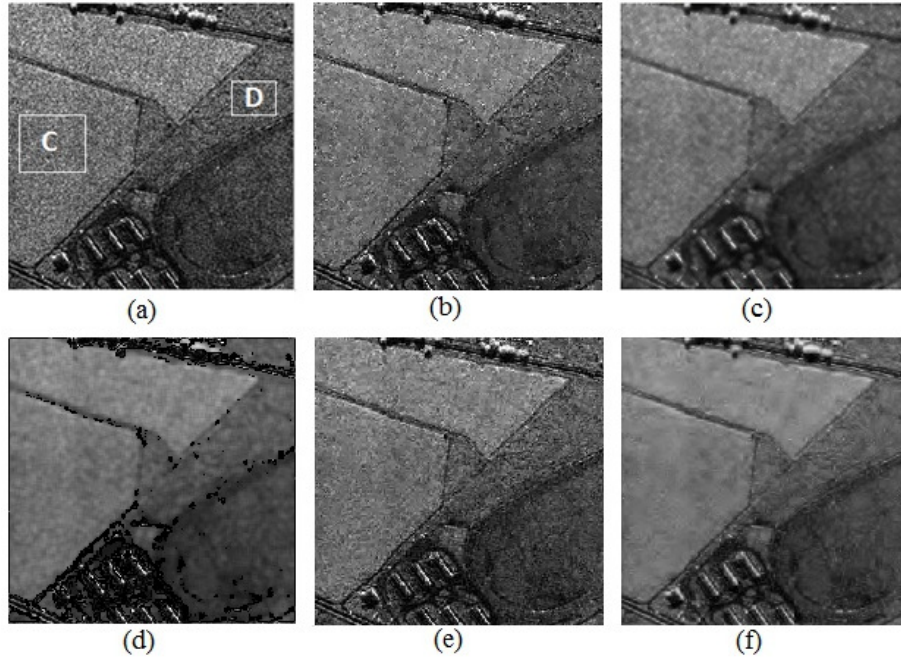
Figure. 5.8. (a) The original SAR image of *Horse track* (b) de-speckled image using Frost filter (c) de-speckled image using Lee filter (d) de-speckled image using Gamma MAP filter (e) de-speckled image using WT-GCV and (f) despeckled image using DT-GCV.

Table 5.2 Comparison of ENL & ESI values of DT-GCV and other despeckling schemes applied on original SAR images

Despeckling Scheme	Bedfordshire Image (Amplitude format, L=2)				Horse Track image (Intensity format, L=4)			
	ENL		ESI		ENL		ESI	
	Reg. A	Reg. B	ESI_H	ESI_V	Reg. C	Reg. D	ESI_H	ESI_V
Real SAR Image	2.94	3.28	1	1	14.11	9.76	1	1
Frost [4]	13.56	21.10	0.370	0.332	116.8	82.45	0.261	0.270
Lee [6]	15.67	22.69	0.365	0.328	125.1	91.33	0.253	0.262
WT-GCV [45]	24.91	48.11	0.371	0.301	182.6	90.21	0.268	0.256
DT-GCV	**32.60**	**63.58**	**0.428**	**0.394**	**214.8**	**98.70**	**0.313**	**0.385**

5.3 Despeckling with Edge detection

The human visual system is highly sensitive to edge structures, which involves a large quantity of information, and thus the key point for the image denoising algorithms is to remove noise while preserving the original edge structures. Here an edge detection and despeckling algorithm in directionlet domain is presented. The algorithm adapts the transform directions to dominant directions across the image domain and efficiently captures the geometrical information present in images. Due to this the transform generates sparser representation allowing for more robust estimation of edge characteristics and optimal threshold for despeckling.

5.3.1 Edge Detection and Despeckling Algorithm

The despeckling of image causes smoothing the edges. Most of the reported despeckling methods are a compromise between edge preservation and speckle reduction. In transform domain despeckling schemes, as the level of decomposition increases the image becomes smoother and the despeckling becomes more effective at the cost of blurring the edges. To tackle this problem, here the edge information in the image is first removed before despeckling.

Here an undecimated version of DT is used for edge detection and despeckling. The input image is first divided into spatial segments of smaller size. Then a local texture-direction detector is constructed by measuring directional variance to identify the pair of transform directions. The directional variance is computed along the rational directions, $(x, y) = (1, 0), (2, 1), (1, 1), (1, 2), (0, 1), (-1,2), (-1, 1)$ and $(-2,1)$ which corresponds to 0º, 30º, 45º, 60º, 90º, 120º, 135º and 150º. This is carried out for each spatial segment of the image and the directions corresponding to the two minimum directional variances are identified as the optimal pair of directions for computing the undecimated DT. The pairs of directions are selected so that the cubic lattice is not divided into more cosets.

The undecimated DT with an anisotropic ratio of 1:2 is first taken along the dominant directions for each spatial segment of the image $G(x, y)$. This will produce eight subbands viz. *HHH, HHL, HLH, HLL, LHH, LHL, LLH, and LLL.*

The corresponding directionlet coefficients at level j are represented as $W_d^j(x, y)$ where $d = HHH_j, HHL_j, HLH_j, . HLL_j, LHH_j, LHL_j, LLH_j, LLL_j$. The DT modulus matrix, $M(x, y)$ is computed as

$$M(x, y) = \sqrt{\Sigma_d \left| \Pi_{j=1}^J W_d^j(x, y) \right|^2}$$ (5.18)

The local maxima of the DT modulus correspond to the edges. So the edge information $E(x, y)$ is obtained by thresholding $M(x, y)$. Here $T = 3\sigma$ is selected as the approximate threshold.

$$E(x, y) = \begin{cases} 1. & if\ M(x, y) > T \\ 0, & otherwise \end{cases}$$ (5.19)

where

$$T = 3\sigma = \frac{3*Median\ (|G_1|)}{0.6745}, where\ G_1 \in HHH_1$$ (5.20)

Now multiply this edge positions with the image to get the final edge. The next step involved is despeckling the edge removed image. Here a logarithmic transformation is carried out to convert the multiplicative noise to an additive one. Then multi scale DT is taken along the dominant directions as identified earlier. The GCV threshold is then computed and applied to the DT coefficients as per the procedure explained in the previous scheme.

Because of the independent processing of spatial segments, the despeckled image is affected by blocking effect, which is visible as sharp artificial edges along the segment boarders. Symmetric extension at the borders of the segment is carried out while taking the transform, to avoid this blocking artefact. The despeckling scheme presented in this section is referred as *DT-Edge* and the whole algorithm is summarised here.

Step 1: **Segmentation & Identification of dominant directions**
- Spatially segment the input image to the required level.
- Identify optimal pair of directions for each segment by computing directional variance.

Step 2: **Edge detection and removal**
- Compute 3-level DT along dominant directions.
- Identify the edge information using equation (5.19).
- Subtract the edge information from the noisy image

Step3: **Multi scale Directionlet and Threshold Computation**
- Make a logarithmic transformation of the edge removed image to convert multiplicative noise to additive one.
- Apply DT to the edge removed segments along the optimal pair of directions to get the multi scale DT coefficients.
- For each subband, except the LLL_J subband, compute the GCV threshold which minimizes $GCV_d(\lambda)$
- Apply the computed threshold to the DT coefficients using soft thresholding rule to estimate the noise-free coefficients.

Step 4: **Reconstruction**
- Reconstruct the image from the processed sub-bands and the low-pass residual (LLL_J) using inverse DT
- Invert the logarithmic transformation
- Add the edge information to the reconstructed image to obtain the final image.

5.3.2 Results and discussions

To demonstrate the efficacy of the proposed method an original 2-looks amplitude SAR image of *Bedfordshire* [151] and 1-look intensity SAR image of *Horse track* [152] are used. Equivalent Number of Looks (ENL) and Edge Save Index (ESI) are used as the performance parameters. The proposed method was compared with traditional Lee filter [6] and wavelet [45] and bandlet [71] based schemes with edge preservation. A 3x3 mask was used in the Lee filter. Here the image was spatially segmented to 32x32 patches and three levels of decomposition using dB4 wavelet was carried out. The edges detected by the proposed scheme are shown in figure 5.7 for Bedfordshire and Horse track images. The despeckling results are given in Table 5.3 and visual comparison is shown in figure 5.8 for Bedfordshire and in figure 5.9 for Horse track images. As they appear, the despeckled image using WT-GCV has lower despeckling effects, because many homogeneous regions are not smoothed enough. The other two schemes viz. bandlet and

directionlet based ones are adaptive methods and have better performance in visual result. But it still can be easily observed that the despeckled image using DT-Edge is smoother in homogeneous areas than that of Bandlet based scheme.

(a)   (b)
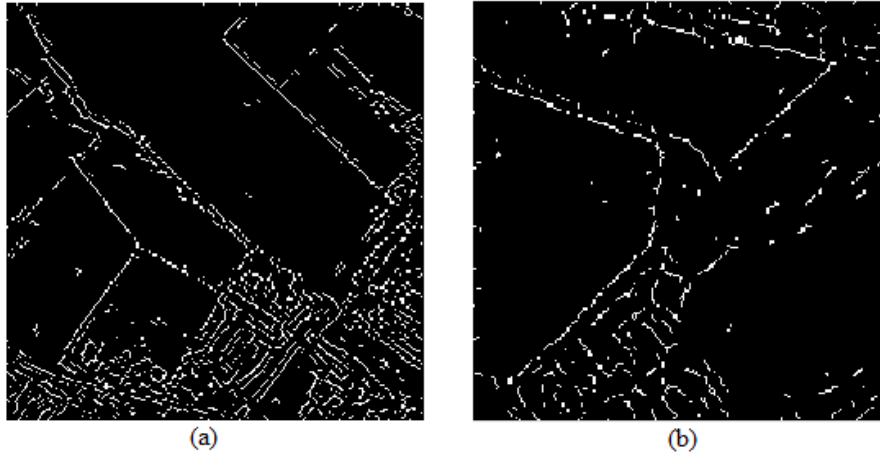
Figure 5.7 Edges detected by the DT-Edge scheme for (a) Bedfordshire image and (b) Horse track image.

Table. 5.3. Comparison of ENL & ESI values of DT-Edge and other despeckling schemes applied on original SAR images

Despeckling Scheme	Bedfordshire Image (Amplitude format, L=2)				Horse Track image (Intensity format, L=4)			
	ENL		ESI		ENL		ESI	
	Reg. A	Reg. B	ESI_H	ESI_V	Reg. C	Reg. D	ESI_H	ESI_V
Real SAR Image	2.94	3.28	1	1	14.11	9.76	1	1
Frost [4]	13.56	21.10	0.370	0.332	116.8	82.45	0.261	0.270
Lee [6]	15.67	22.69	0.365	0.328	125.1	91.33	0.253	0.262
WT-GCV [45]	24.91	48.11	0.371	0.301	182.6	90.21	0.268	0.256
Bandlet [71]	66.14	146.9	0.518	0.441	402.6	141.2	0.318	0.411
DT-Edge	**72.08**	**165.18**	**0.681**	**0.621**	**482.31**	**172.87**	**0.395**	**0.479**

161
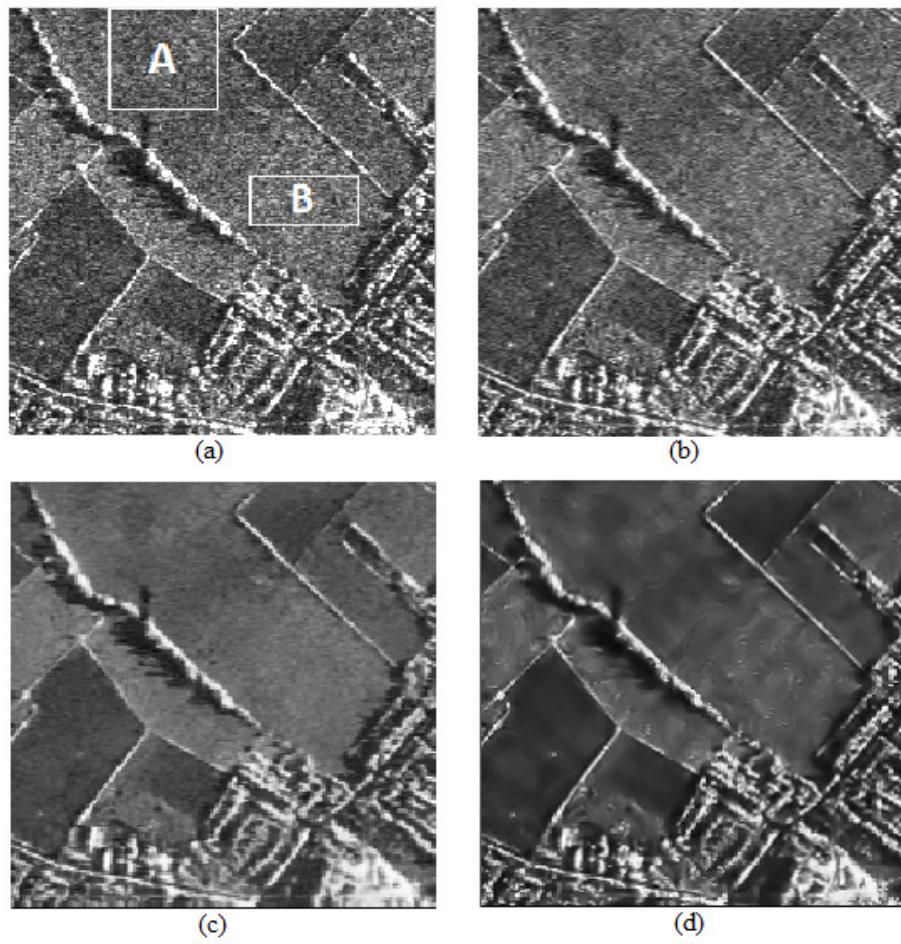
Figure 5.8 Despeckling results of *Bedfordshire* image (a) Original Image (b) Despeckled image using WT-GCV (c) Despeckled image using Bandlet (d) Despeckled image using DT-Edge
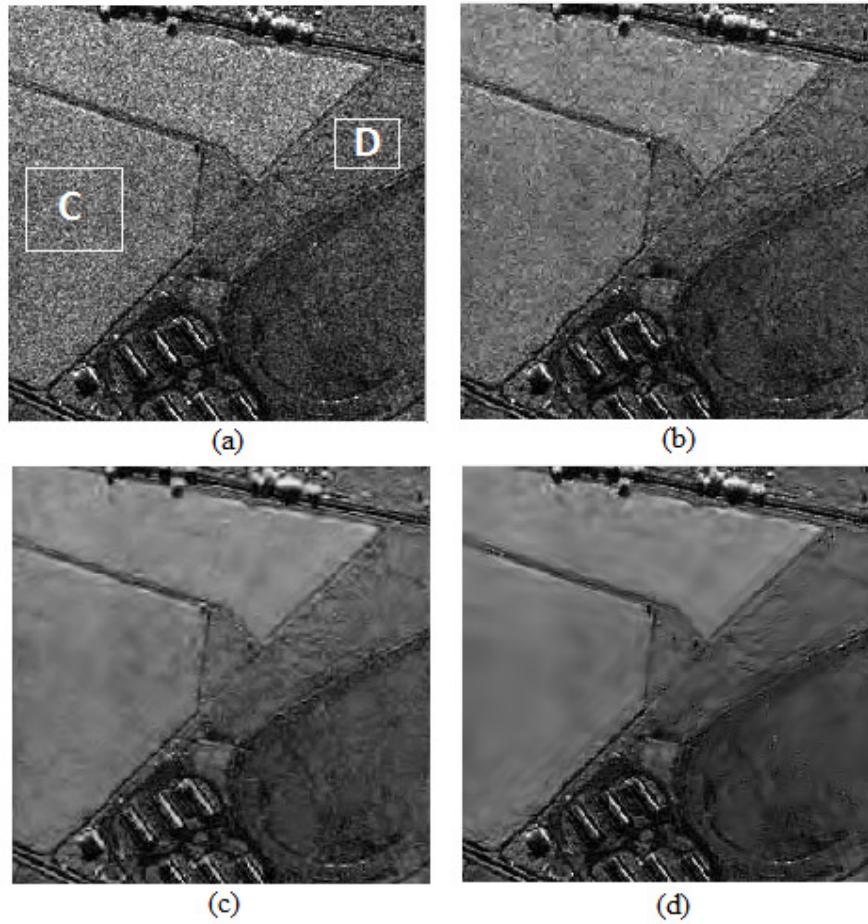
Figure 5.9 Despeckling results of *Horse track* image (a) Original Image (b) Despeckled image using WT-GCV   (c) Despeckled image using Bandlet (d) Despeckled image using DT-Edge

An enlarged portion of horse track image and synthetic *Lena* image are shown in figure 5.10 and 5.11 respectively to highlight the edge saving capability of DT-edge scheme as compared to WT-GCV and bandlet based despeckling schemes. As shown in these figures, DT-Edge scheme possesses a good preserving performance of the edges both regular and irregular compared with WT-GCV scheme. This is clearly visible along the lines in *horse track* image and in edges of hat and eyes of *Lena* image. Bandlet based algorithm attains a similar preserving performance but with some artifacts in the homogeneous zones of *horse track* image. Also for *Lena* image there are some intensity variations in the homogeneous zones, some textures of the hat are lost and some fine contours are over smoothed.
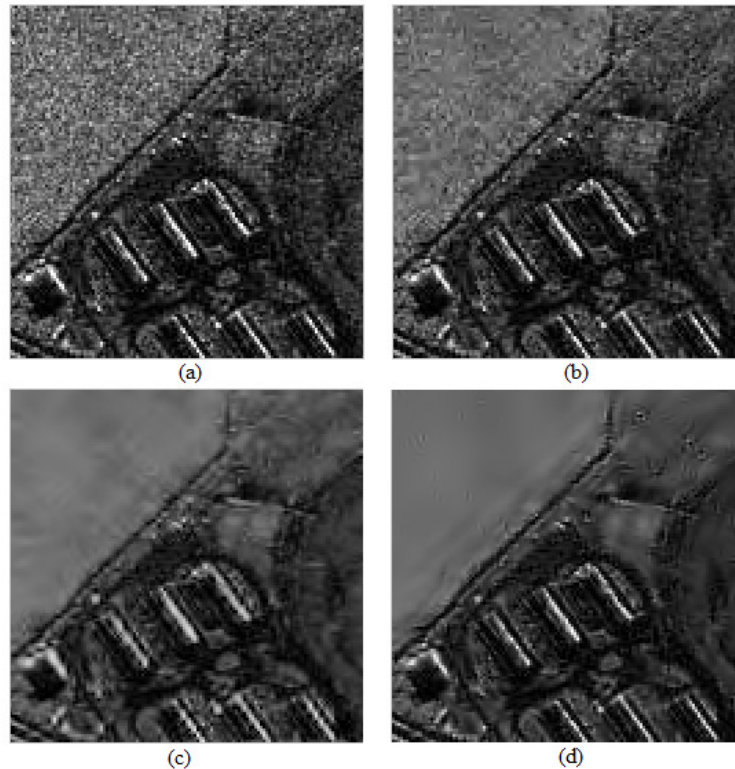
Figure 5.10 Despeckling results of enlarged portion of *Horse track* image (a) Original Image (b) Despeckled image using WT-GCV (c) Despeckled image using Bandlet (d) Despeckled image using DT-Edge
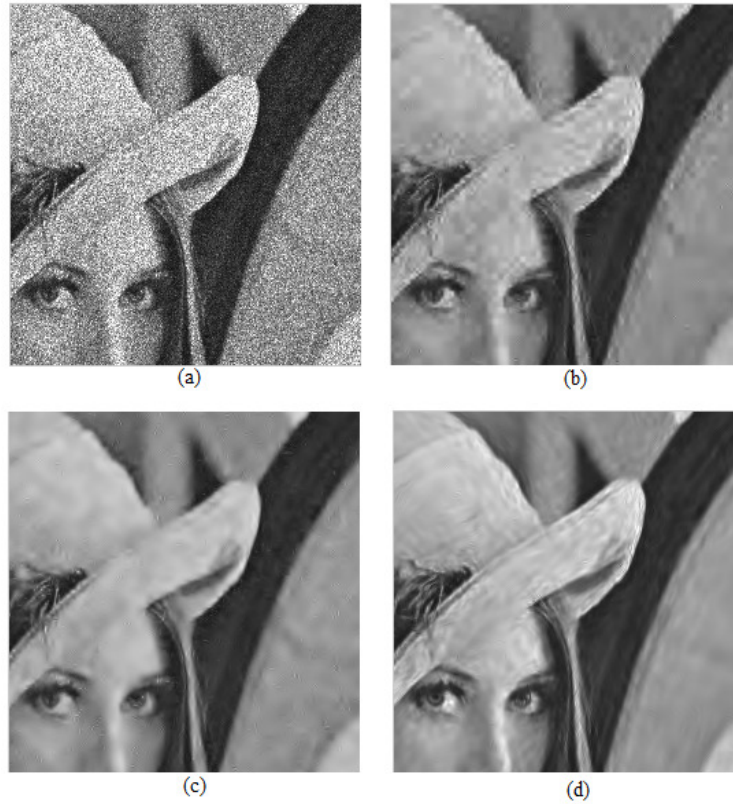
Figure 5.11 Despeckling results of enlarged portion of synthetic *Lena* image (a) Noisy Image (b) Despeckled image using WT-GCV (c) Despeckled image using Bandlet (d) Despeckled image using DT-Edge

Due to the anisotropic basis functions of DT, the edge details can be captured exactly by less number of DT coefficients. Thus the directionlet based scheme preserve the edges efficiently while providing very good despeckling performance. The numerical results indicate that the *DT-Edge* possesses remarkable speckle-suppression and radiometric preservation capabilities. Since the directionlets possess spatial anisotropy and better directional capabilities, edge detection and GCV thresholding in directionlet domain results in visually appealing despeckling results, with improved performance parameters.

5.4 Despeckling using multiscale products thresholding

In most of the transform based multi resolution denoising methods the correlation of the coefficients across the scales is not considered in the thresholding process even though there are strong dependency between adjacent scale coefficients. The performance of despeckling schemes based on multi resolution analysis would be significantly improved if the multiscale correlation among the transform coefficients is taken into account. If a DT coefficient generated by true signal has large magnitude at a finer scale, its ascendants at coarser scales will likely be significant as well, while the magnitude of noise coefficients may decay rapidly along the scales. So the multiscale products at adjacent scales of DT would strengthen the significant features while diluting noise. Unlike many traditional schemes that directly threshold the transform coefficients, here a despeckling algorithm in directionlet domain is presented which multiplies the adjacent scale DT coefficients to amplify the significant features. GCV technique is then used to find out the optimum threshold from these multiscale products to better differentiate edge structures from noise.

5.4.1 Despeckling algorithm

The speckle noise can typically be modelled as a multiplicative independent and identically distributed random noise. Here first a logarithmic transformation is carried out to convert the multiplicative noise to an additive one. The local dominant directions in the image are identified by computing a parameter called directional variance. The multi scale DT is then taken along the identified dominant directions and the multiscale products are computed. A subband adaptive optimal threshold is then computed from these products using GCV technique.

As in earlier schemes here also the first step involved in the despeckling algorithm is the spatial segmentation of SAR image into small blocks and identification of the local dominant directions in that area for fixing the transform directions. The directional information is obtained by computing directional variance along the rational directions $(x, y) = (1, 0), (2, 1), (1, 1), (1, 2), (0, 1), (-1,2), (-1, 1)$ and $(-2,1)$ which corresponds to 0º, 30º, 45º, 60º, 90º, 120º, 135º and 150º. The directions corresponding to the two minimum directional variances are identified as the

optimal pair of directions for computing the DT for each segment to make the DT adaptive to the image to be despeckled.

In transform domain the signal and noise behave very differently. Multiplying the DT coefficients at adjacent scales would amplify the edge structures while diluting noise. The undecimated DT is first taken along the dominant directions for each spatial segment of the image $G(x, y)$. This will produce eight subbands viz. *HHH, HHL, HLH, HLL, LHH, LHL, LLH, and LLL*. The corresponding directionlet coefficients at level j are represented as $W_d^j(x, y)$ where $d = HHH_j, HHL_j, HLH_j,. HLL_j, LHH_j, LHL_j, LLH_j, LLL_j$. The multiscale product of $W_d^j(x, y)$, $P_d(x, y)$ is computed as

$$P_d(x, y) = \prod_{j=1}^{J} W_d^j(x, y) \qquad (5.21)$$

where J is the number of levels.

Finding an optimal threshold plays a key role in the transform domain filtering. The GCV technique used in the earlier schemes for estimating the optimum threshold is employed here also but with a small modification. The GCV is computed here using the multiscale products. In the transform domain for a subband *d,* the GCV as a function of threshold λ is defined as

$$GCV_d(\lambda) = \frac{\frac{1}{N_d}\|P_d - P_{d,\lambda}\|^2}{\left[\frac{N_{d0}}{N_d}\right]^2} \qquad (5.22)$$

Where N_d is the number of DT coefficients in the subband *d*, P_d is the multiscale product of noisy coefficients, $P_{d,\lambda}$ is the threshold applied P_d and N_{d0} is the number of coefficients that were replaced by zero. The minimum of $GCV_d(\lambda)$ is found by iteration. The value of λ corresponding to minimum of $GCV_d(\lambda)$ is selected as the threshold for each subband and the DT coefficients of subbands except that of LLL subband are modified with this threshold. A significant DT coefficient, $\widehat{W}_d^l(i, j)$ is identified if its corresponding multiscale products value $P_d^l(i, j)$ is greater than or equal to an adaptive threshold λ_d^l. that is

$$\widehat{W}_d^l(i, j) = \begin{cases} W_d^l(i, j). & if\ P_d^l(i, j) \geq \lambda_d^l \\ 0, & otherwise \end{cases} \qquad (5.23)$$

Because of the independent processing of spatial segments, the despeckled image is affected by blocking effect, which is visible as sharp artificial edges along the segment boarders. Symmetric extension at the borders of the segment was carried out while taking the transform, to avoid this blocking artefact.

This despeckling scheme presented here is referred as *DT-Multiscale* and the whole algorithm is summarised below

Step 1: **Segmentation & Identification of dominant directions**
- Spatially segment the input SAR image into small blocks of size 32x32.
- Compute optimal pair of directions for each block using directional variance.

Step2: **Multi scale Directionlet and Threshold Computation**
- Make a logarithmic transformation of the segmented image to convert multiplicative noise to additive noise.
- Apply 3-level UDT to the segments along the optimal pair of directions to get the multiscale DT coefficients.
- Compute the multiscale product for each block and subband.
- For each subband, except the LLL_J subband, compute the GCV threshold from the multiscale products which minimizes $GCV_d(\lambda)$.
- Apply the computed subband adaptive threshold to the DT coefficients, except those in the LLL_J subband to estimate the noise-free coefficients.

Step 3: **Reconstruction**
- Reconstruct the image from the above processed sub-bands and the low-pass residual (LLL_J) using inverse DT
- Invert the logarithmic transformation

5.4.2 Results and discussions
The performance of the proposed algorithm is analyzed using original SAR images of *Bedfordshire* and *horse track*. Equivalent Number of Looks (ENL) and Edge Save Index (ESI) are used as the performance parameters. The scheme is compared with wavelet [45] and bandlet [71] based schemes with edge preservation. The despeckling results are shown in figures 5.12 and 5.13 and the performance parameters are given in Table 5.4, with the best results highlighted in bold font. It shows that the proposed scheme outperforms the other compared methods in terms

of numeric and visual qualities. As compared to the DT-Edge scheme presented in the previous section, this scheme is better in terms of speckle removal but worse in terms of edge preservation.
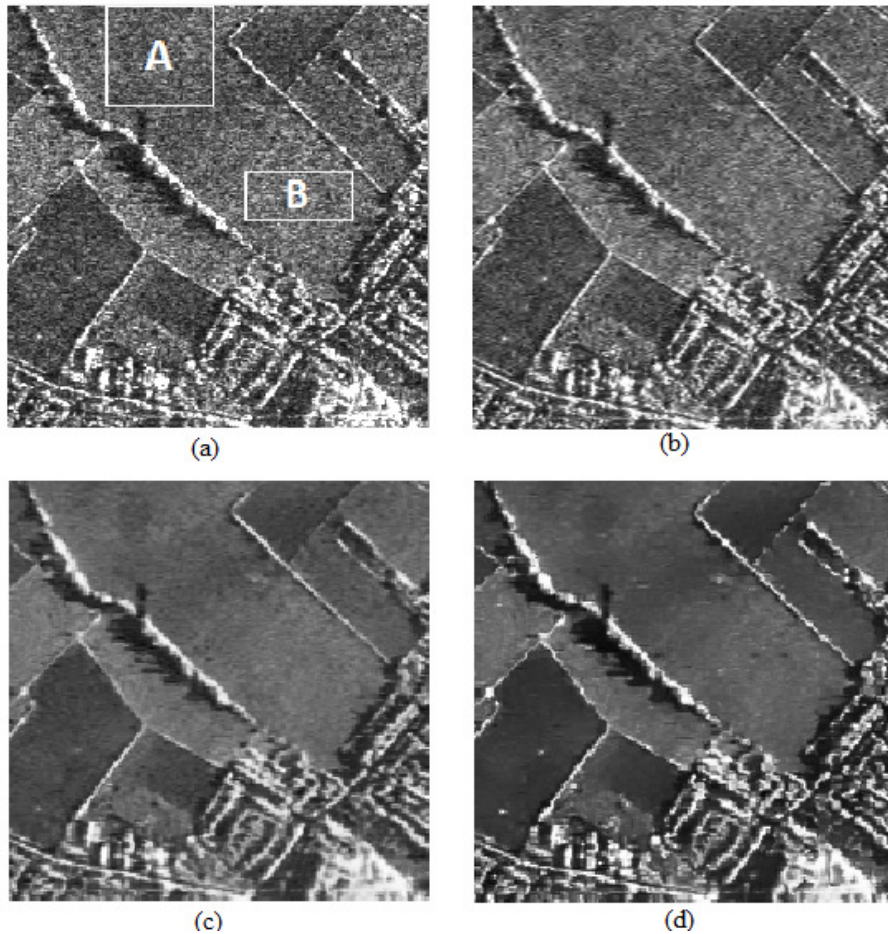
Figure 5.12 Despeckling results of Bedfordshire image (a) Original Image (b) Despeckled image using WT-GCV (c) Despeckled image using Bandlet (e) Despeckled image using DT-Multiscale.
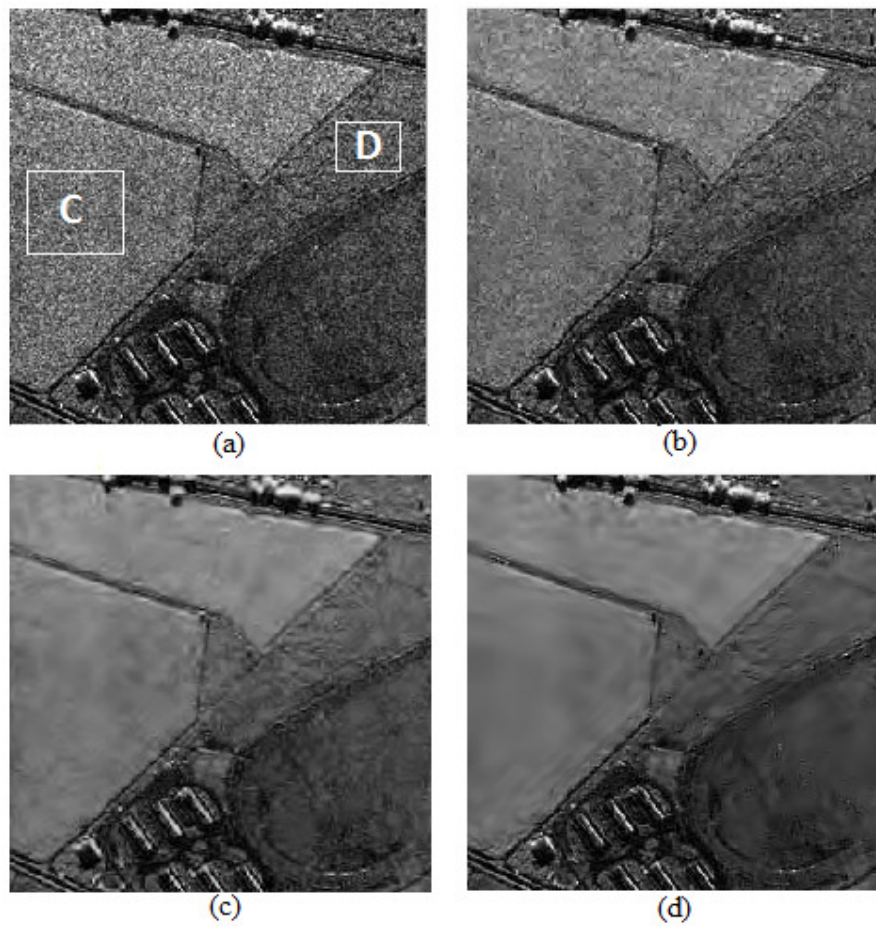
Figure 5.13 Despeckling results of horse track image (a) Original Image (b) Despeckled image using WT-GCV (c) Despeckled image using Bandlet (e) Despeckled image using DT-Multiscale.

Table 5.4 Comparison of ENL & ESI values of DT-Multiscale and other despeckling schemes applied on original SAR images

Despeckling Scheme	Bedfordshire Image (Amplitude format, L=2)				Horse Track image (Intensity format, L=4)			
	ENL		ESI		ENL		ESI	
	Reg. A	Reg. B	ESI_H	ESI_V	Reg. C	Reg. D	ESI_H	ESI_V
Real SAR Image	2.94	3.28	1	1	14.11	9.76	1	1
Frost [4]	13.56	21.10	0.370	0.332	116.8	82.45	0.261	0.270
Lee [6]	15.67	22.69	0.365	0.328	125.1	91.33	0.253	0.262
WT-GCV [45]	24.91	48.11	0.371	0.301	182.6	90.21	0.268	0.256
Bandlet [71]	66.14	146.9	0.518	0.441	402.6	141.2	0.318	0.411
DT-Multiscale	**76.57**	**171.24**	**0.612**	**0.569**	**511.56**	**196.22**	**0.387**	**0.470**

5.5 Despeckling using Laplacian-Gaussian Modelling

The despeckling schemes presented in the earlier three sections are based on thresholding of directionlet coefficients. Here a simple statistical model based despeckling scheme based on Bayesian *maximum a posteriori* (MAP) estimator is presented. The MAP solution is based on the assumption that directionlet coefficients have a known distribution. In literature different distributions have been used for modeling the signal coefficients and Gaussian distribution for the noise coefficients. Here a new modeling of the statistics of directionlet coefficients is proposed based on experimental observations. Observations of the estimated generalized Gaussian shape parameters relative to the reflectivity and to the speckle noise in SAR images suggest that their distributions can be approximated as a Laplacian and a Gaussian function, respectively. Under these hypotheses, a closed form solution of the MAP estimation in directionlet domain is presented for SAR despeckling.

5.5.1 Image Speckle Model

It is assumed that the observed signal follows the following model

$$G = F.V \qquad (5.24)$$

where G is the observed signal, F is the speckle-free reflectivity that we would like to estimate and V is the speckle noise. Here a logarithmic transformation is carried out to convert the multiplicative nature of speckle noise to an additive one. However, this results in a mean shift which has to be corrected after processing. After logarithmic transformation, the equation (5.24) becomes

$$g = f + v \qquad (5.25)$$

where g, f and v are the logarithms of G, F and V respectively. Owing to the linearity of DT, a multi-resolution decomposition of g results in

$$g_j = f_j + v_j \qquad (5.26)$$

where g_j, f_j and v_j be the undecimated directionlet transforms of g, f and v at level j respectively. Here the aim is to estimate f_j from the noisy observation g_j. Based on Bayesian *maximum a posteriori* (MAP) estimator, the estimate of f_j is given by

$$\hat{f}_j = \arg\max P_{f/g}(f_j|g_j) \qquad (5.27)$$

$$\hat{f}_j = \arg\max[P_{g/f}(g_j|f_j).p_f(f_j)] \qquad (5.28)$$

$$\hat{f}_j = \arg\max[p_v(g_j - f_j).p_f(f_j)] \qquad (5.29)$$

It was established that WT coefficients of natural images have highly non-Gaussian heavy tailed distribution [122]. The *pdf* for wavelet coefficients is often modelled using a Generalized Gaussian Distribution (GGD). The zero mean GG distribution can be written as

$$p_{GG}(\theta)] = \frac{\upsilon\eta}{2\Gamma\left(\frac{1}{\upsilon}\right)} e^{-\eta|\theta|^p} \qquad (5.30)$$

where η is the scale parameter and υ is the shape parameter. The above GG distribution coincides with the Laplacian distribution when the shape parameter assumes a value of one and with the Gaussian distribution when the shape parameter assumes a value of two.

When a particular *pdf* is considered for modeling the statistics of a set of data, there are basically two factors which need to be considered. One is the amount of complexity involved in the estimation of its parameters and the other is the model fitting performance. Here a simple Laplacian *pdf* is considered for modeling the noise free directionlet coefficients. As far as Laplacian *pdf* is considered, there are only two parameters which need to be estimated; the scale parameter and the shape parameter. The model fitting performance can be assessed by conducting some experiments. Here images from different databases are taken and their histograms are plotted along with the standard model *pdf*. Then one can visually analyze and assess the closeness of fit. In addition to this quantitative analysis also can be carried out by computing various parameters which measure the difference between the normalized histogram and estimated *pdf*. *Kullback-Leibler* (K-L) distance [150] is one such parameter, which is explained in section 4.4.1. Here both these methods are used for analyzing the closeness of fit of the Laplacian *pdf* with the histogram of DT coefficients.

The histogram of the DT coefficients at two different subbands and two different resolution levels for noise free *Lena* image is shown in figure 5.14 in blue colour. The standard Laplacian *pdf* is also plotted along with the histograms in each case in red colour. Here the scale and the shape parameters of the model are adjusted to make it close to the histograms. As can be seen from these plots that these histograms roughly approach Laplacian distribution. A similar analysis is done for *Barbara* image and the result is shown in figure 5.15. The observation holds good in this case also. It can be seen that a similar behavior has been also encountered for different subbands and different decomposition levels for both the images. This observation was found to be true for most of the natural images including SAR images. The *Kullback-Leibler* (K-L) distance measured in these cases is given in Table 5.5. This also indicates a good model fitting performance.

Table 5.5. Values of the K-L distance between the normalised histogram and estimated *pdf*

	HHH		HLH	
	Level 1	Level 2	Level 1	Level 2
Lena	8.51	10.31	3.65	10.11
Barbara	8.33	10.11	4.22	11.11

Figure 5.14 Histogram of the DT coefficients of '*Lena*' image (blue colour) & the estimated Laplacian *pdf* (red colour) (a) *HHH* subband at level 1 (b) *HHH* subband at level 2 (c) *HLH* subband at level 1 (d) *HLH* subband at level 2

Based on this analysis, the directionlet coefficients related to the speckle-free signal and to the signal-dependent noise can be assumed to be distributed as a Laplacian and as a Gaussian function, respectively. Based on this assumption the solution of the MAP equation of (5.29) can be found in a closed form. The f and v can be modeled as

$$p_f(f) = \frac{1}{\sqrt{2}\sigma_f} e^{-\frac{\sqrt{2}|f-\mu_f|}{\sigma_f}} \tag{5.31}$$

$$p_v(v) = \frac{1}{\sqrt{2\pi}\sigma_v} e^{-\frac{|v-\mu_v|}{2\sigma_v^2}} \tag{5.32}$$

Here μ_f and μ_v are mean and σ_f and σ_v are the standard deviations of clean image and noise respectively. By substituting this to equation (5.29), we get the estimate of f_j as follows

$$\hat{f}_j = \begin{cases} g_j - \frac{\sqrt{2}\sigma_v^2}{\sigma_f}, & if \ g_j > \mu_f + \frac{\sqrt{2}\sigma_v^2}{\sigma_f} \\ g_j + \frac{\sqrt{2}\sigma_v^2}{\sigma_f}, & if \ g_j > \mu_f - \frac{\sqrt{2}\sigma_v^2}{\sigma_f} \\ \mu_f, & elsewhere \end{cases} \qquad (5.34)$$
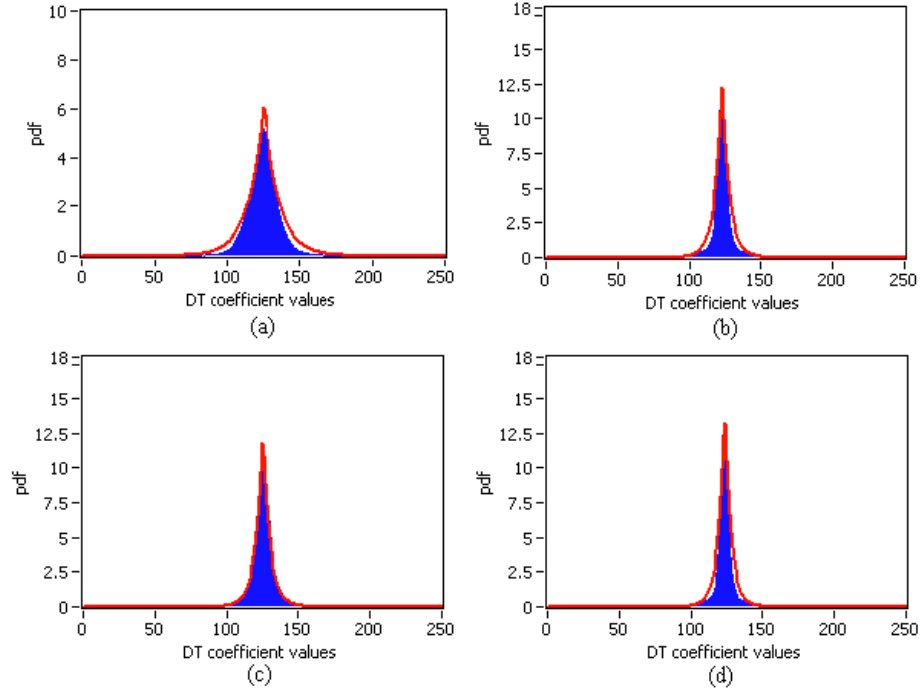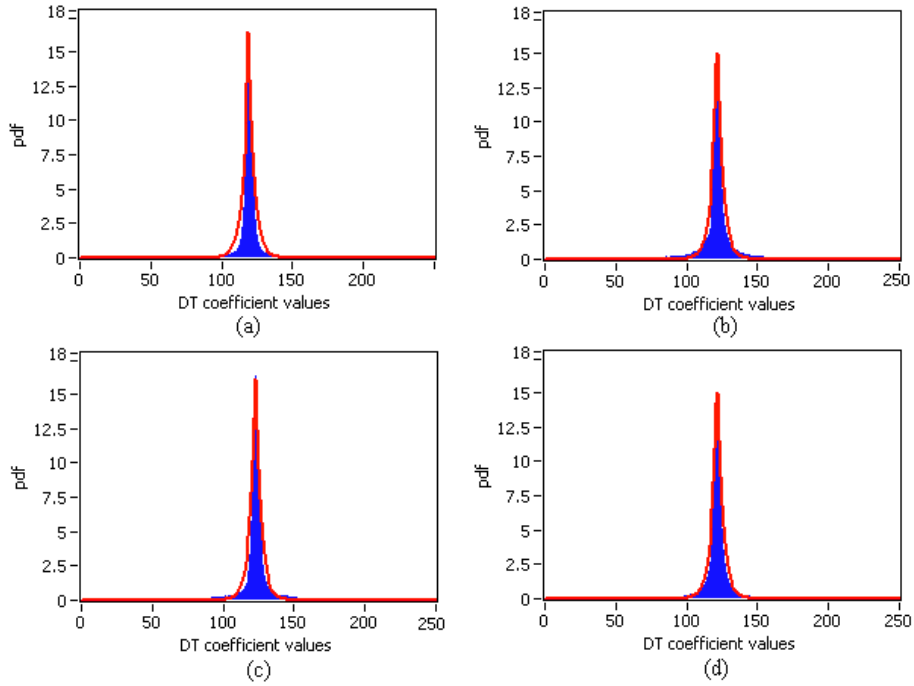

Figure 5.15 Histogram of the DT coefficients of '*Barbara*' image (blue colour) & the estimated Laplacian *pdf* (red colour) (a) *HHH* subband at level 1 (b) *HHH* subband at level 2 (c) *HLH* subband at level 1   (d) *HLH* subband at level 2

5.5.2 Despeckling algorithm

Directionlets can have directional vanishing moments along any two directions only. Also directionality in any image is a local feature which varies over space. So a spatial segmentation of the input image is first carried out to identify two local dominant directions. The local dominant directions are identified by computing directional variance as explained in the previous schemes. Here for each spatial segment, the directional variance is computed along eight different directions with (x, y) = (1, 0), (2, 1), (1, 1), (1, 2), (0, 1), (-1,2), (-1, 1) and (-2,1) which corresponds to 0º, 30º, 45º, 60º, 90º, 120º, 135º and 150º. Two directions corresponding to two minimum directional variances in each segment are identified as the optimal pair of directions for computing the DT. The estimate of the noise free DT coefficients is then computed using equation (5.34). The noise variance is estimated from the HHH_1 subband as the robust median estimator as

$$\sigma_v = \frac{Median\ (|g_1|)}{0.6745}, where\ g_1 \in HHH_1 \qquad (5.35)$$

From the observation model of equation (5.25), one gets $\sigma_g^2 = \sigma_f^2 + \sigma_v^2$, where σ_g^2 is the marginal variance of noisy observations g_j. Here g_j is modelled as zero mean and thus σ_g^2 can be calculated as

$$\sigma_g^2 = \frac{1}{M}\Sigma_{g_i \in N_o(k)}\ g_i^2 \qquad (5.36)$$

where $N_o(k)$ is a directional window oriented along the transform direction with M members from an anisotropic neighbourhood and centered at the kth coefficient. In case of undecimated DT since the down samplers are discarded, the transform coefficients in the nearest neighbor spatial locations are highly correlated and they provide only redundant information. Therefore, estimation of marginal variance based on the closest neighborhood is not too efficient. Thus sparser neighborhoods, that is, the neighborhoods of coefficients with the relative coordinates to the coordinate of the referent coefficient scaled by the distance factor, $\delta = 2^j$, with the orientation matched with the transform direction are chosen. For DT with anisotropic ratio of n_2:n_1 and orientation θ, the neighborhood around the coefficient in the location (x', y') is defined as the set of the coefficients at the same scale in the locations as

$$x' = [(x + n\delta)\cos\theta - (y + m\delta)\sin\theta] \qquad (5.37)$$

$$y' = [(x + n\delta)\sin\theta - (y + m\delta)\cos\theta] \qquad (5.38)$$

$$\text{for } n \in \{-3, -2, \ldots.2, 3\} \text{ if } m = 0 \text{ and } n \in \{-1, 0, 1\} \text{ if } m \in \{-1, 1\}$$

Here, [ ] is the rounding function, which ensures that the coordinates of the neighbor coefficients are integers. Based on this neighborhood definition there are thirteen members in this anisotropic neighborhood. The selection of a neighborhood along -45° for $\delta = 2$ is shown in figure 5.16 (b). Here the neighborhood used is anisotropic and oriented as against the isotropic neighborhood in the case of WT shown in figure 5.16 (a). Neighborhoods with different sizes can also be defined. The size of the neighborhood will greatly affect the quality of processed images. If the neighborhood size is too small, the algorithm may not work well and may lead to unwanted block-like artifacts. On the other hand, if it is too large, the region containing edges and contours will also become large, resulting in relatively large variances. This will lead to the poor denoising performance nearby edges and contours. The neighborhood size of 13 is found to be good choice here.

(a)   (b)
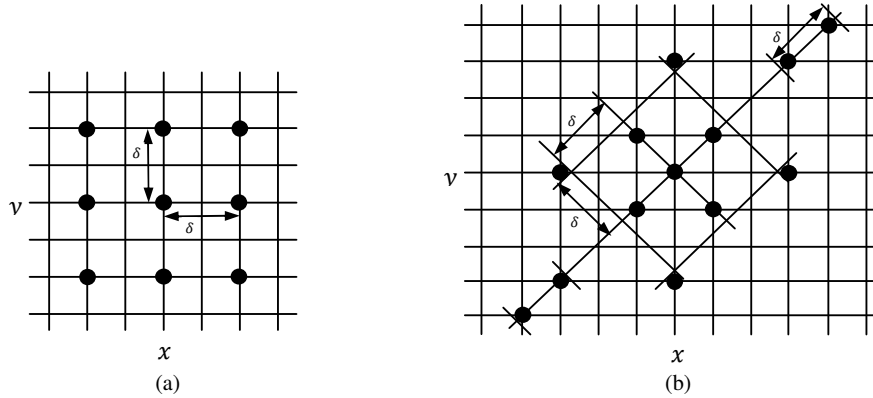
Figure 5.16 (a) The isotropic neighborhood of WT (b) The anisotropic neighborhood of DT for $\theta = -45°$, and $\delta = 2$. The orientation of the neighborhood is matched with the orientation of the transform in case of DT.

The standard deviation of clean image, σ_f can be computed from the standard deviations of noisy image and noise as follows

$$\sigma_f = \sqrt{\left(\sigma_g^2 - \sigma_v^2\right)_+} \tag{5.39}$$

The mean of the clean image, μ_f is equal to the mean of the noisy observation, μ_g. Thus it can be computed directly from the noisy observation.

This scheme is referred here as *DT-LG* and the whole despeckling algorithm is described in three steps as follows

Step 1: **Segmentation & identification of dominant directions**
- Spatially segment the SAR image into small blocks.
- Compute optimal pair of directions for each segment using directional variance.

Step2: **Multi scale DT computation and MAP estimation**
- Convert the multiplicative speckle noise to additive one by doing a logarithmic operation.
- Compute 3-level DT along the optimal pair of directions for each segment to get the multi scale DT coefficients.
- Estimate the noise free coefficients using equation (5.34) for all subbands except *LLL_J*

Step 3: **Reconstruction**
- Reconstruct the image from the above processed sub-bands and the low-pass residual (*LLL_J*) using inverse DT
- Invert the logarithmic operation and carry out a mean correction.

5.5.3 Results and Discussions

As in earlier schemes, here also the performance of the presented scheme is verified by using original and synthetic SAR images. In the proposed scheme the segment size was selected as 32x32 and three levels of decomposition using db4 wavelet was carried out along the dominant directions for each segment. The proposed method is compared with wavelet based schemes LGMAP-S [63] and GGMAP-S [60]. The traditional Lee filter is also used for comparison with its local window being set up as 3x3. For generating synthetic SAR images, standard grey scale images of *Lena* and *Boat* of size 512x512 are used. These images are corrupted by multiplying simulated spatially uncorrelated speckle noise. The PSNR

values obtained with different schemes for these images at four different noise levels (four number of looks) are listed in Table 5.6 with the highest PSNR values highlighted. The PSNR provided is an average of ten noise realizations. The experiment was repeated ten times under exactly the same settings except that speckle was realized using different random seeds, but with the same distribution. As can be seen from the table, the proposed method consistently outperforms the other wavelet-based denoising algorithms in all the cases. Figure 5.17 presents the comparison of the denoised *Lena* image corrupted with speckle noise (*L=4*) in amplitude format. It can be seen that many isolated specks are present in smooth regions of despeckled image using wavelet based LGMAP-S scheme as shown in figure 5.17 (c). These are disappeared in figure 5.17 (d) due to the spatially adaptive directionlet based filtering.

Table 5.6. Despeckling results (PSNR) for synthetic SAR images of *Lena* & *Boat* (512x512) in amplitude format

Looks/Method	Lena				Boat			
	1	2	4	16	1	2	4	16
Synthetic SAR Image	12.11	14.89	17.80	23.76	11.77	14.55	17.46	23.42
Lee [6]	20.82	23.86	26.19	29.34	17.25	20.31	23.53	28.09
GGMAP-S [60]	26.33	28.03	29.75	33.29	23.98	25.43	27.05	30.48
LGMAP-S [63]	26.20	27.80	29.51	33.24	23.71	25.20	26.91	30.40
DT-LG	**26.45**	**28.24**	**30.08**	**33.88**	**24.14**	**25.69**	**27.38**	**30.89**

Shown in figure 5.18 (a) is a 256x256 original X-band, 2-looks SAR image of *Bedfordshire* in amplitude format [151] and in figure 5.19 (a) is a 256x256 size portion of Ku-band, 4-looks, intensity SAR image relevant to *Horse track*, near Albuquerque, New Mexico with 1-m resolution [152]. Since the noise-free images are not available in these cases, ENL is used to assess the different algorithms' noise reduction performance in homogeneous areas. As highlighted in these figures, two uniform areas each are selected for the analysis. Table 5.7 lists the

ENL values before and after filtering. It can be seen that in all the cases, the DT-LG scheme outperforms the other ones with the highest ENL values, which is consistent with the simulation results. In terms of feature preservation, ESI parameter is computed for vertical and horizontal directions for each scheme and compared. It is indicated that the proposed method provides very good edge preservation performance as compared to other schemes. Visual comparisons of these schemes shown in figure 5.18 and figure 5.19 also show the superiority of the DT-LG scheme.

Table. 5.7. Comparison of ENL, ESI & MRI values of DT-LG and other despeckling schemes applied on original SAR images

Despeckling Scheme	Bedfordshire Image (Amplitude format, L=2)				Horse Track image (Intensity format, L=4)			
	ENL		ESI		ENL		ESI	
	Reg. A	Reg. B	ESI_H	ESI_V	Reg. C	Reg. D	ESI_H	ESI_V
Real SAR Image	2.94	3.28	1	1	14.11	9.76	1	1
Frost [4]	13.56	21.10	0.370	0.332	116.8	82.45	0.261	0.270
Lee [6]	15.67	22.69	0.365	0.328	125.1	91.33	0.253	0.262
GGMAP-S [60]	31.47	77.21	0.309	0.284	328.45	77.55	0.315	0.377
LGMAP-S [63]	30.2	70.6	0.295	0.269	303.83	104.47	0.272	0.322
DT-LG	**70.11**	**160.81**	**0.507**	**0.424**	**531.86**	**192.01**	**0.347**	**0.412**

Even though the performance improvement of the scheme with respect to GGMAP-S scheme is only marginal for synthetic SAR images, the computational complexity of the scheme is much less here as compared to GGMAP-S. Also it can be seen that the *DT-LG* algorithm is becoming more competitive with increasing number of looks. The DT-LG scheme takes only 12 sec for filtering a synthetically speckled image of *Lena* of size 512x512 with *L=4*, whereas GGMAP-S takes 64 sec for the same image by a Core i5 CPU @ 2.4 GHz with 4GB RAM. The denoising performance of the proposed method can be further improved by incorporating the interscale dependency in the modeling process.

Figure 5.17 Despeckling result for synthetic speckle image of Lena (four-look amplitude). (a) Original Lena image (b) Speckled Lena image (c) Despeckled image using wavelet based LGMAP-S (d) Despeckled image using *DT-LG* scheme.
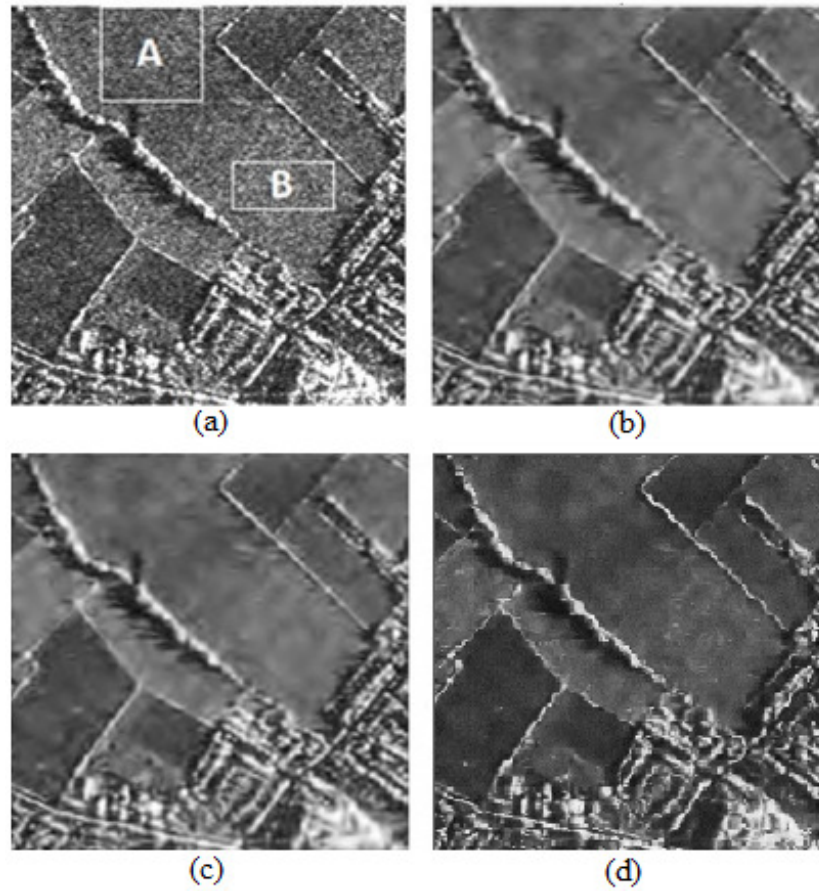
Figure 5.18 Despeckling results of Bedfordshire image (a) Original Image (b) Despeckled image using wavelet based GGMAP-S (c) Despeckled image using wavelet based LGMAP-S (d) Despeckled image using *DT-LG* scheme.
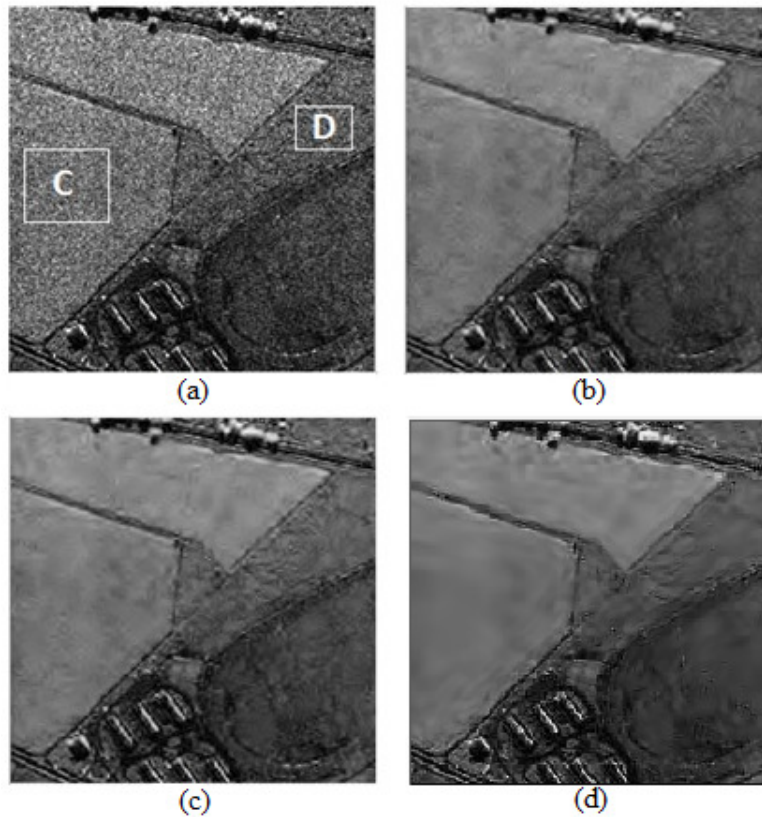
Figure 5.19 Despeckling results of Horse track image (a) Original Image (b) Despeckled image using wavelet based GGMAP-S (c) Despeckled image using wavelet based LGMAP-S (d) Despeckled image using DT-LG scheme.

5.6 Despeckling using Cauchy-Gaussian modelling with interscale dependence

In the previous scheme a simple statistical model was presented for SAR images and dependent noise. There the interscale dependency of the transform coefficients in the multi resolution representation was not considered in the modelling process. The performance of despeckling schemes based on multi-resolution analysis can be improved significantly by taking into account the multi-scale correlation among the

transform coefficients. Here a novel directionally adaptive despeckling algorithm for SAR images is presented which takes into account the statistical inter scale dependency of Cauchy-Gaussian modelled DT coefficients. The noise free coefficients are computed using Bayesian MAP estimator. Since the directionlets possess spatial anisotropy and better directional capabilities, statistical interscale dependency modelling in directionlet domain results in visually appealing de-speckling results, with improved performance parameters.

5.6.1 Speckle Model & MAP Estimator

The noise model explained in the previous section is considered here also. Let us recall the equation (5.26)

$$g_j = f_j + v_j \tag{5.26}$$

Here an undecimated DT is used to decompose the image. So there is one to one dependency between the adjacent scale coefficients. To model the interscale dependency, each DT coefficient is represented by interscale dependence vectors $\boldsymbol{g_j}, \boldsymbol{f_j}$ and $\boldsymbol{v_j}$. So

$$\boldsymbol{g_j} = \boldsymbol{f_j} + \boldsymbol{v_j} \tag{5.43}$$

where $\boldsymbol{g_j} = (g_j, g_{j+1}), \boldsymbol{f_j} = (f_j, f_{j+1})$, and $\boldsymbol{v_j} = (v_j, v_{j+1})$

Here the aim is to estimate f_j from the noisy observation g_j. This can be done by Bayesian *maximum a posteriori* (MAP) estimator. The typical MAP estimate of f_j is

$$\hat{f}_j(g, g_{j+1}) = \arg\max P_{\boldsymbol{f/g}}(\boldsymbol{f_j}|\boldsymbol{g_j}) \tag{5.44}$$

$$\hat{f}_j(g_j, g_{j+1}) = \arg\max[P_{\boldsymbol{g/f}}(\boldsymbol{g_j}|\boldsymbol{f_j}) \cdot p_f(\boldsymbol{f_j})] \tag{5.45}$$

$$\hat{f}_j(g_j, g_{j+1}) = \arg\max[p_v(\boldsymbol{g_j} - \boldsymbol{f_j}) \cdot p_f(\boldsymbol{f_j})] \tag{5.46}$$

Now the inter scale dependency of the signal and noise coefficients has to be modelled using a suitable *pdf*. It was established that the distribution of the wavelet coefficients of the log-transformed reflectance can be accurately described by a symmetric alpha stable *pdf*. There are some theoretical reasons for such an assumption. Stable random variables satisfy the stability property, which states that

linear combinations of jointly stable variables are indeed stable. Also stable processes arise as limiting processes of sums of independent and identically distributed random variables via the generalized central limit theorem. Strong empirical evidence suggests that many data sets in several physical and economic systems exhibit heavy tail features. The heavy tail characteristic justifies the use of symmetric alpha stable densities for modeling signals that are impulsive in nature. Only two special cases of the alpha stable *pdf* have a closed form expression, namely, the Gaussian and the Cauchy *pdf*. However, the Gaussian *pdf* is obviously not suitable to represent the wavelet coefficients. On the other hand, the Cauchy *pdf* is unimodal and symmetric, having a sharp peak around zero with heavy tails and so is an ideal choice.

The log transformed SAR image has significant non-Gaussian behaviour which can be best described by the families of heavy tailed distribution such as the Cauchy distribution [122]. H. H Arsenault et al. [115] have modelled the impulsive heavy-tailed behaviour of high resolution SAR images using Cauchy distribution. Later J. J. Ranjani et al [65] have developed a statistical interscale dependency model based on the parent child relationship using Cauchy distribution and applied it to DTCWT coefficients. Since DT is an extended WT operation, it can be established that the statistical distribution of DT coefficients is same as that of WT coefficients. So this scheme can be extended to the directionlet domain. However before finalizing such a distribution for DT coefficients, an experimental analysis has to be carried out to arrive at a parameter distribution for the DT coefficients of natural images. The histograms obtained for noise free images at different subbands and resolution levels are approximated here to a bivariate Cauchy distribution with interscale dependency. The histogram and *pdf* plots for *Lena* and *Barbara* images are shown in figure 5.20 and figure 5.21 respectively.

In addition to the standard images used for analysis, a Lee filtered SAR image of *horse track* is also analyzed as it can be approximated to the noise free SAR image. The corresponding histogram and *pdf* plots are shown in figure 5.22. It can be seen that a similar behavior has been encountered for this image also. This validates the generalization of the *pdf* approximation as explained above. In addition, for a quantitative evaluation, the *Kullback–Leibler* (K-L) distance [150] is also used to

measure the difference between the normalized histogram and the estimated *pdf*, which is shown in Table 5.5. This table also shows that the bivariate Cauchy *pdf* model has the best model fitting performance w.r.t the DT coefficients of natural images. Also it can be seen that this model is closer to the normalized histogram of DT coefficients, than the Laplacian model presented in the previous section. The K-L distance measure also substantiates this. The K-L distance is found to be more for Lee filtered SAR image as in this case the histograms are more close to a Gaussian distribution. This can be attributed to the fact that the Lee filtering is not much effective in despeckling.
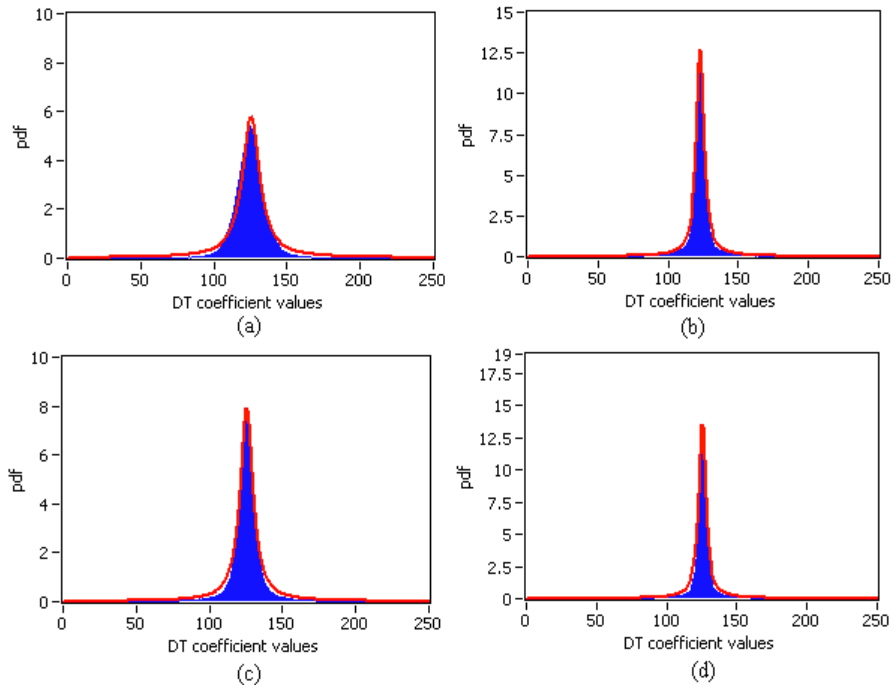
Figure 5.20 Histogram of the DT coefficients of '*Lena*' image & the estimated bivariate Cauchy *pdf* (a) *HHH* subband at level 1 (b) *HHH* subband at level 2 (c) *HLH* subband at level 1   (d) *HLH* subband at level 2

Table 5.8. Values of the K-L distance between the normalised histogram and estimated *pdf*

	HHH		HLH	
	Level 1	Level 2	Level 1	Level 2
Lena	6.85	5.61	5.25	4.15
Barbara	6.53	5.69	5.14	4.31
Horse track	22.12	20.56	21.34	21.01
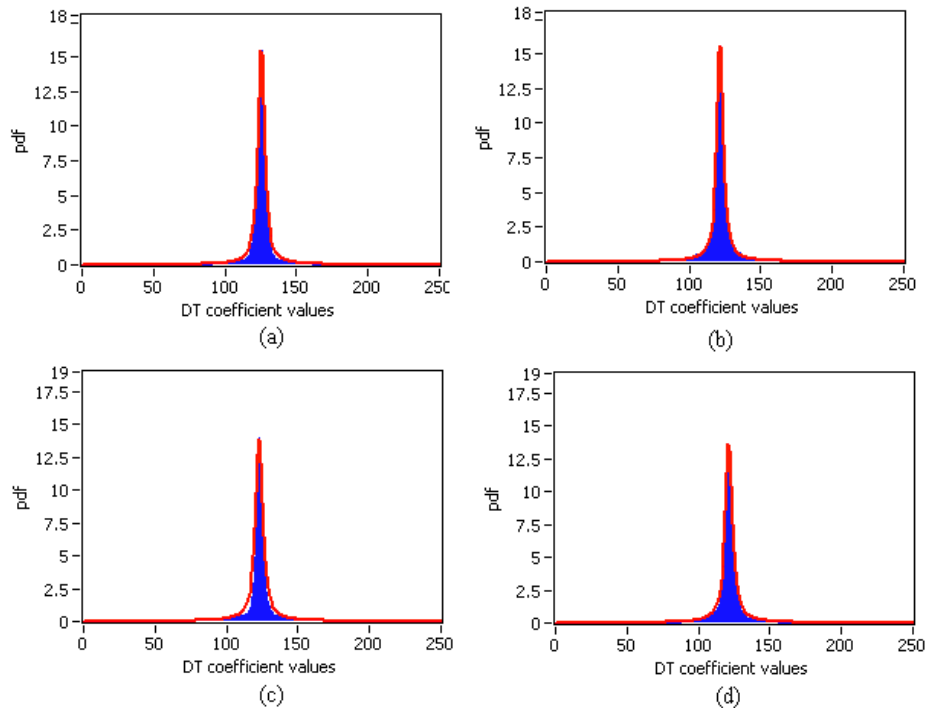
Figure 5.21 Histogram of the DT coefficients of '*Barbara'* image & the estimated bivariate Cauchy *pdf* (a) *HHH* subband at level 1 (b) *HHH* subband at level 2 (c) *HLH* subband at level 1   (d) *HLH* subband at level 2

Based on the above analysis, the joint probability density function for the signal coefficient vector $\boldsymbol{f_j} = (f_j, f_{j+1})$ can be defined as a bivariate Cauchy *pdf* as

$$p_f(\boldsymbol{f_j}) = \frac{\gamma_j}{2\pi(f_j^2 + f_{j+1}^2 + \gamma_j^2)^{3/2}} \quad for\ j = 1\ to\ J \tag{5.47}$$

where γ_j is the dispersion parameter at scale j and J is the decomposition level. This parameter can be computed using central moments of the noisy observations in (5.43) through Mellin transform [65] as

$$\gamma_j = \left(\left(\frac{1}{N} \sum_{i=1}^{N} [g_j(i)] - \frac{\sigma_v^2}{4\pi} \right) \frac{\Gamma\left(\frac{3}{2}\right)}{\Gamma\left(-\frac{1}{2}\right)} 8\pi \right)^{1/2} \quad for\ j = 1\ to\ J \tag{5.48}$$

where N is the number of coefficients of g_j.
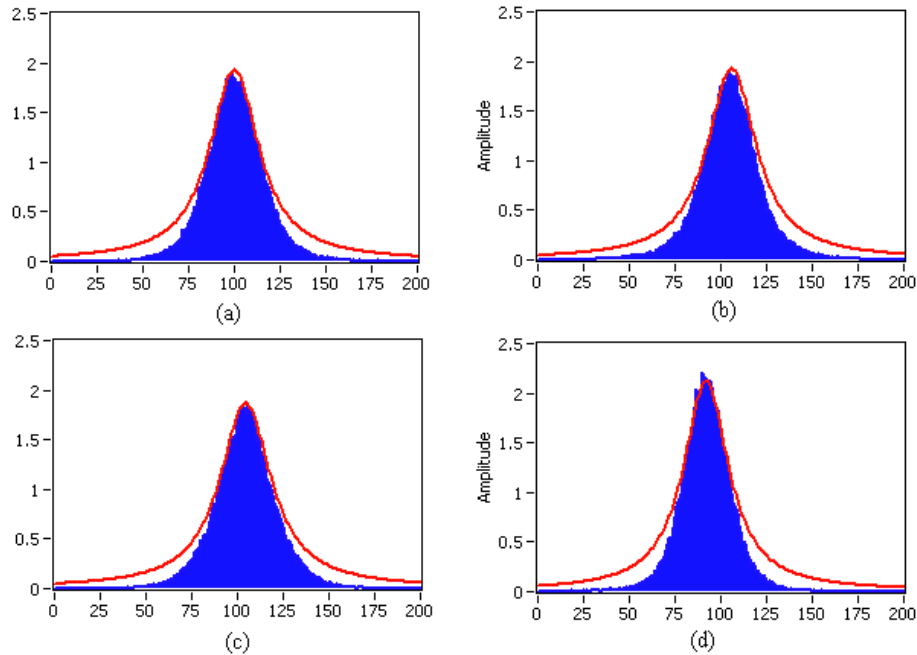
Figure 5.22 Histogram of the DT coefficients of Lee filtered '*Horse track*' image & the estimated bivariate Cauchy *pdf* (a) *HHH* subband at level 1 (b) *HHH* subband at level 2 (c) *HLH* subband at level 1 (d) *HLH* subband at level 2

Several authors have shown that the distribution of the log transformed speckle can be well modelled by a Gaussian distribution. Thus the logarithmic speckle is assumed to be independent and identically distributed. So the joint probability density function of noise vector $\boldsymbol{v_j} = (v_j, v_{j+1})$ can be written as a bivariate Gaussian *pdf* as

$$p_v(\boldsymbol{v_j}) = \frac{1}{(\sqrt{2\pi}\sigma_v)^2} \, e^{-\left(\frac{v_j^2 + v_{j+1}^2}{2\sigma_v{}^2}\right)} \tag{5.49}$$

Now the *pdf* of signal and noise are known. By applying (5.47) & (5.49) to the MAP estimator given in equation (5.46), the estimate of f_j can be obtained as [65]

$$\hat{f}_j = sign(g_j) \, Max\left(0, \left|\frac{g_j}{1 + \frac{3\sigma_v^2}{(x_j^2 + x_{j+1}^2 + \gamma_j^2)}}\right|\right) \quad for \; j = 1 \; to \; J \tag{5.50}$$

where,

$$x_j = \frac{d_j}{3} + \left(-\frac{q_j}{2} + \left(\frac{q_j^2}{4} + \frac{p_j^3}{27}\right)^{1/2}\right)^{1/3} + \left(-\frac{q_j}{2} - \left(\frac{q_j^2}{4} + \frac{p_j^3}{27}\right)^{1/2}\right)^{1/3} \tag{5.51}$$

with

$$p_j = \left[\frac{\gamma_j^2 + 3\sigma_n^2}{1 + \frac{d_{j+1}^2}{d_j^2}}\right] - \frac{d_j^2}{3} \tag{5.52}$$

and

$$q_j = -\frac{\gamma_j^2 d_j}{1 + \frac{d_{j+1}^2}{d_j^2}} + \frac{1}{27} * \left[9 d_j \frac{\gamma_j^2 + 3\sigma_n^2}{1 + \frac{d_{j+1}^2}{d_j^2}} - 2 d_j^3\right] \tag{5.53}$$

5.6.2 Despeckling Algorithm

As explained in previous section, the DT will be effective for a sparse representation of an image if the transform directions are matched with the local dominant directions in the image. Thus the input image is first spatially segmented and the dominant directions are identified by computing directional variance before taking the DT. As in previous schemes, here also the directional variance is computed along 0º, 30º, 45º, 60º, 90º, 120º, 135º and 150º. The directions corresponding to the two minimum directional variances are identified as the optimal pair of directions for computing the DT for each segment to make the DT adaptive to the image to be despeckled.

The estimate of the noise free coefficients is obtained from the noisy coefficients and its next level coefficients using equation (5.50). The noise variance required in the estimator is computed using equation (5.35) as in previous scheme.

The DT coefficient from the detail subbands are only used for modelling and MAP estimation. The despeckled image is then obtained by performing an inverse DT operation. The logarithmic transformation carried out at the beginning will cause a mean shift which needs to be corrected at the end. The full despeckling algorithm is referred here as *DT-CG* and is summarized below

- Spatially segment the SAR image into small blocks.
- Compute optimal pair of directions for each segment using directional variance.
- Make a logarithmic transformation of the segmented image to convert multiplicative noise to additive noise.
- Apply 3-level DT to the segments along the optimal pair of directions to get the multi-scale DT coefficients.
- Compute the noise variance σ_v^2 from the high frequency sub band coefficients at level1 (HHH_1).
- Compute the estimate of noise-free coefficients using equation (5.50) for all subbands except LLL_J.
- Reconstruct the image from the above processed sub-bands and the low-pass residual (LLL_J) using inverse DT.
- Invert the logarithmic transformation and do a mean correction.

5.6.3 Experimental Results

The performance of the proposed algorithm was analyzed using original SAR images of *Horse track* and *Bedfordshire*. Synthetic speckle images of *Lena* and *Boat* in amplitude format are also used for performance analysis. In case of original SAR images, Equivalent Number of Looks (ENL) and Edge Save Index (ESI) are used as the performance parameter for assessing the performance of speckle reduction and edge preservation. For synthetic speckle images, PSNR is used as the performance parameter as in this case the reference images are available.

The performance was compared with the state of the art despeckling schemes like GGMAP [60] and LGMAP [63] in wavelet domain and also with a DTCWT based scheme with interscale dependency [65]. Here the image is spatially segmented to blocks of size 32x32 and three levels of decomposition using Daubechies' length eight wavelet (Db4) is carried out. The despeckling results are shown in figure 5.23, 5.24 and 5.25, and the performance parameters in Table 5.9 and 5.10, with the best results highlighted in bold font. It shows that the DT-CG scheme outperforms the other compared methods in terms of numeric and visual qualities. Also it can be noted that the WT based schemes provide good smoothing but with blurring of edges. The edge retaining capacity of DT-CG scheme is much better than the wavelet based schemes. DTCWT based scheme provides both better despeckling and edge preservation but as compared to directionlet based scheme, it is slightly inferior. This is more evident in the comparison with real SAR images. Since the directionlets possess spatial anisotropy and better directional capabilities, directionally adaptive interscale dependency modelling in directionlet domain results in visually appealing despeckling results, with improved performance parameters.

Upon critical analyze of the results it can be seen that as the number of looks decreases, the performance improvement of the proposed scheme is narrowing down. This can be mainly attributed to two reasons. First one is that as the noise level increases, the log-transformed speckle noise deviates strikingly from the Gaussian distribution, and secondly, the identification of dominant directions using directional variance computation is adversely affected as the noise level increases.

Table 5.9. Despeckling results (PSNR) for synthetic SAR images of *Lena* & *Boat* (512x512) in amplitude format

Looks/Method	Lena				Boat			
	1	2	4	16	1	2	4	16
Synthetic SAR Image	12.11	14.89	17.80	23.76	11.77	14.55	17.46	23.42
LG MAP-S [63]	26.20	27.80	29.51	33.24	23.71	25.20	26.91	30.40
GGMAP-S [60]	26.33	28.03	29.75	33.29	23.98	25.43	27.05	30.48
DTCWT [65]	26.37	28.11	29.93	33.61	24.06	25.55	27.21	30.59
DT-GG	**26.49**	**28.29**	**30.16**	**33.97**	**24.20**	**25.78**	**27.47**	**31.00**

Table. 5.10. Comparison of ENL & ESI values of DT-CG and other despeckling schemes applied on original SAR images

Despeckling Scheme	Bedfordshire Image (Amplitude format, L=2)				Horse Track image (Intensity format, L=4)			
	ENL		ESI		ENL		ESI	
	Reg. A	Reg. B	ESI_H	ESI_V	Reg. C	Reg. D	ESI_H	ESI_V
Real SAR Image	2.94	3.28	1	1	14.11	9.76	1	1
GGMAP-S [60]	31.47	77.21	0.309	0.284	328.45	77.55	0.315	0.377
LGMAP-S [63]	30.2	70.6	0.295	0.269	303.83	104.47	0.272	0.322
DTCWT [65]	40.1	61.11	0.424	0.383	366.34	121.78	0.332	0.408
DT-CG	**71.41**	**163.52**	**0.511**	**0.438**	**536.15**	**194.64**	**0.356**	**0.432**

Figure 5.23 Despeckling result for synthetic speckle image of Lena (four-look amplitude). (a) Original *Lena* image (b) Speckled *Lena* image. (c) Despeckled image using GGMAP-S algorithm. (d) Despeckled image using DT-CG
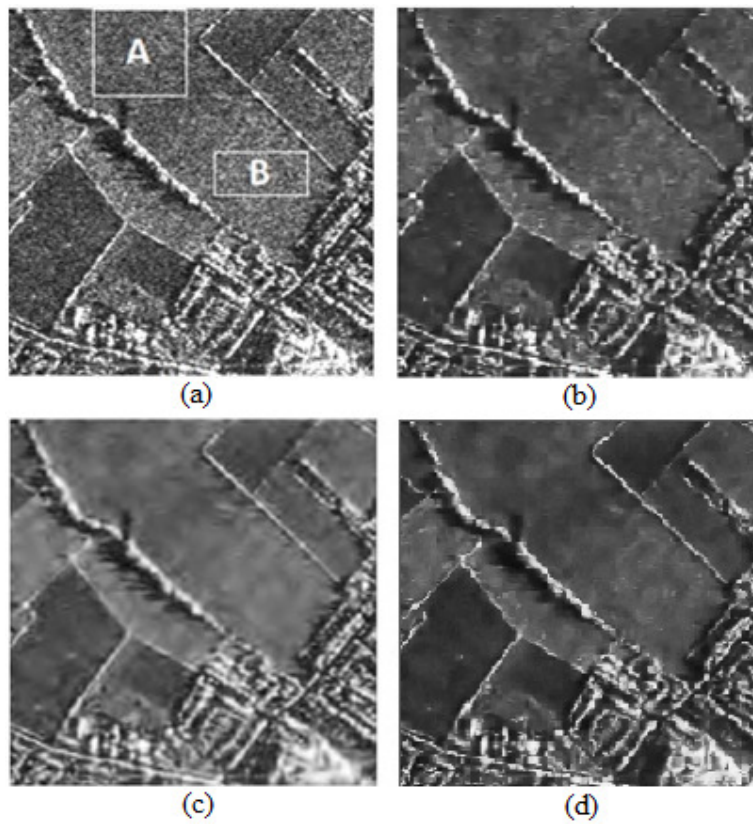
Figure 5.24 Despeckling results of Bedfordshire image (a) Original Image (b) Despeckled image using DTCWT (c) Despeckled image using GGMAP-S in wavelet domain (d) Despeckled image using DT-CG scheme.
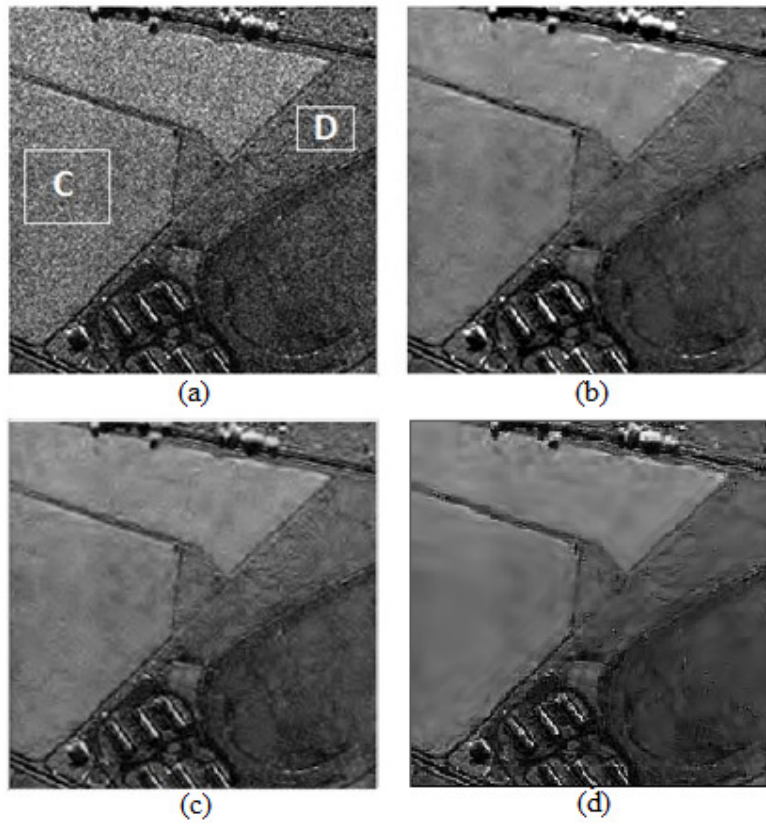
Figure 5.25 Despeckling results of Horse track image (a) Original Image (b) Despeckled image using DTCWT (c) Despeckled image using GGMAP-S (d) Despeckled image using DT-CG scheme.

5.7 SAR Despeckling using Bivariate Modelling in Directionlet Domain

As explained earlier, simple marginal models cannot properly model the statistical dependence between transform coefficients. There are strong dependency between the adjacent scale coefficients and neighbour coefficients in a multi resolution representation. This is due to the fact that in a multi resolution representation, the next scale of coefficients is derived from the parent scale. Thus the dependency between the adjacent scale coefficients is significant. However, in most of the image processing schemes based on multi resolution analysis, the interscale dependence between the coefficients is neglected. Sendur et al analysed the dependency of WT coefficients across adjacent scales and modelled the heavy-tailed behaviour using a bivariate *pdf* [49]. This is based on the parent child relationship in the wavelet domain. They have used more than two hundred images from Corel image database to compute the joint empirical coefficient-parent histogram and proposed a joint probability density function for the WT coefficients of adjacent scales. This model was successfully used for denoising images corrupted with Gaussian noise [50]. Here an interscale dependency model of the DT is presented in line with this scheme and the model fitting performance is analysed. Using this statistical model a shrinkage function using MAP estimator is presented and a despeckling algorithm in directionlet domain is developed.

5.7.1 Despeckling Model

The multiplicative noise model used in the previous section is used here also. As explained in chapter 2, a simple logarithmic transformation is required to convert the multiplicative noise model of SAR images to an additive one. As in previous section, to model the interscale dependency, each DT coefficient is represented by interscale dependence vectors $g_j,$ f_j and v_j. So

$$g_j = f_j + v_j \tag{5.43}$$

Here the joint probability density functions are required which take into account the parent child relationship for the noise and signal coefficients. Since the noise is

assumed to be independent and identically distributed the joint probability function of noise vector $\boldsymbol{v_j} = (v_j, v_{j+1})$ can be written as a bivariate *pdf* as

$$p_v(\boldsymbol{v_j}) = \frac{1}{\left(\sqrt{2\pi}\sigma_v\right)^2} e^{-\left(\frac{v_j^2 + v_{j+1}^2}{2\sigma_v^2}\right)} \qquad (5.54)$$

It is well known that the high-resolution SAR images exhibit impulsive behaviour indicative of underlying heavy-tailed distributions. Since DT is an extended WT operation, it can be established that the statistical distribution of DT coefficients is same as that of WT coefficients. This is experimentally proven here by analyzing the histogram of natural images.

Let f_{j+1} is the directionlet coefficient at the same position as f_j, but at the next coarser scale, then f_{j+1} can be considered as the parent of f_j. The joint probability density function for the signal coefficient vector $\boldsymbol{f_j} = (f_j, f_{j+1})$ can be defined as

$$p_f(\boldsymbol{f_j}) = \frac{3}{\left(\sqrt{2\pi}\sigma\right)^2} e^{-\left(\frac{\sqrt{3}}{\sigma}\sqrt{f_j^2 + f_{j+1}^2}\right)} \qquad (5.55)$$

Figure 5.26 illustrates the histogram of the directionlet coefficients computed from *Lena* and *Barbara* images. The red line shows estimated bivariate *pdf* and blue line, the histogram. From the figure it is clear that the distribution of DT coefficients is very close to the bivariate *pdf*. The *Kullback-Leibler* (KL) distance [150] measure in each case is given in Table 5.11. This also shows a good model fitness. From this measure it can be seen that this model is very close to the histogram of natural images than the other models considered in previous sections.

The estimate of the noise free coefficients can be obtained by applying *pdf* equations of (5.54) and (5.55) to the MAP estimator in equation (5.46). The estimate is given as

$$\hat{f}_j(g_j, g_{j+1}) = \frac{\left(\sqrt{g_j^2 + g_{j+1}^2} - \frac{\sqrt{3}\sigma_v^2}{\sigma}\right)_+}{\sqrt{g_j^2 + g_{j+1}^2}} \cdot g_j \qquad (5.56)$$

where g_j and g_{j+1} are the noisy DT coefficients at two adjacent scales, σ_v^2 is the noise variance and σ^2 is the marginal variance.
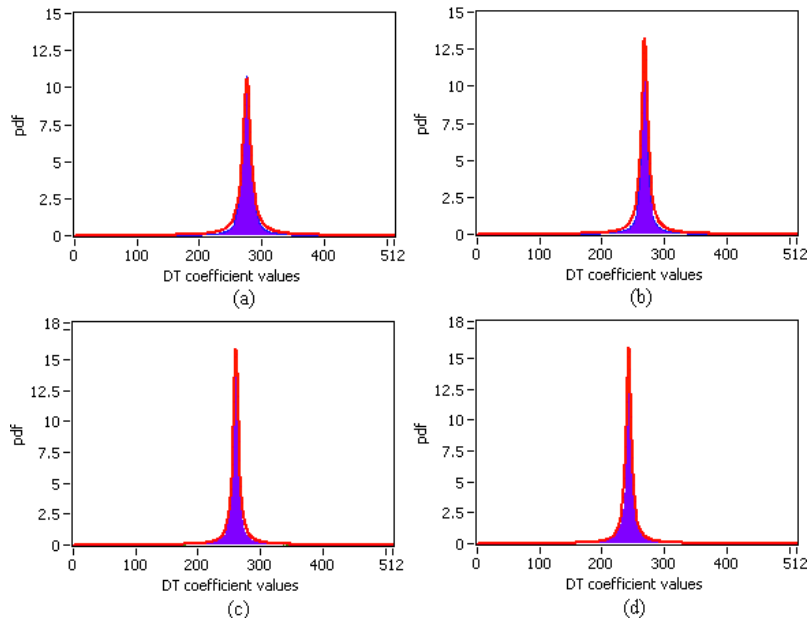
Figure 5.26 Histogram of the DT coefficients of '*Lena*' and '*Barbara*' images & the estimated bivariate *pdf* (a) *HLH* subband at level 1 of '*Lena*' (b) *HLH* subband at level 2 of '*Lena*' (c) *HLH* subband at level 1 of '*Barbara*' (d) *HLH* subband at level 2 of '*Barbara*'

Table 5.11. Values of the K-L distance between the normalised histogram and estimated *pdf*

	HHH		HLH	
	Level 1	Level 2	Level 1	Level 2
Lena	3.60	3.26	3.03	3.11
Barbara	2.38	3.19	2.14	2.96

5.7.2 Despeckling Algorithm

The first step in the proposed scheme is the spatial segmentation of the image to identify the local dominant directions. This is done as in earlier schemes by computing directional variance. The directions corresponding to two minimum directional variances are identified as the dominant directions. After identifying the dominant direction in each spatial segment, multi scale undecimated DT is applied

along these directions. The noise free DT coefficients are then computed using the estimator given in equation (5.56). It requires the prior knowledge of the noise variance σ_v^2 and marginal variance σ^2 for each directionlet coefficient. These parameters can be computed using the procedure followed in the previous section. The scheme presented in this section is referred as *DT-Bivariate* and the whole algorithm is summarised here.

Step 1: **Segmentation & identification of dominant directions**
- Spatially segment the SAR image into small blocks.
- Compute optimal pair of directions for each segment using directional variance.

Step2: **Multi scale DT computation and MAP estimation**
- Convert the multiplicative speckle noise to additive one by doing a logarithmic operation.
- Compute 3-level DT along the optimal pair of directions for each segment to get the multi scale DT coefficients.
- Estimate the noise free coefficients using equation (5.56) for all subbands except *LLL_J*

Step 3: **Reconstruction**
- Reconstruct the image from the above processed sub-bands and the low-pass residual (*LLL_J*) using inverse DT
- Invert the logarithmic operation and do a mean correction.

5.7.3 Results and discussions

In the presented scheme the image is spatially segmented into small patches of size 32x32. The transform directions are chosen by identifying the dominant directions through the computation of directional variance for each spatial segment. Here three levels for DT decomposition with an anisotropic ratio of 1:2 is used. The number of levels in DT is limited by the segment size, which in turn limits the segmentation process and hence possibly affects the denoising performance. For segments having no dominant directions, three levels of decomposition was done using an undecimated WT. Here a 5x5 window was used as the neighbourhood window for marginal variance estimation. In both the cases the filtering was done using db4 wavelet. Symmetric extension at the borders of the image was carried out to reduce the impact of border effects. The major parameters of the algorithm

like segment size, anisotropic ratio, number of levels of decomposition, window size for marginal variance estimation etc. are tuned based on simulation on different images.

The performance of the proposed algorithm is analyzed using original and synthetic SAR images. The performance is compared with the state of the art despeckling schemes like wavelet based GGMAP-S [60] and LGMAP-S [63], directional transform based schemes like NSCT [68] and NSST [69] and interscale dependency model based schemes like DTCWT [65]. The GGMAP-S and LGMAP-S use three levels of decomposition using db4 wavelet. In both these schemes the wavelet coefficients are segmented according to their texture energy to provide better results. NSCT filter uses 3-levels of decomposition, and the number of directional subbands is 8, 8 and 4 from finer to coarser level. In NSST scheme, the number of decomposition level is set to 4, the numbers of shearing directions are chosen to be 4, 4, 4 and 4 from finer to coarser, the bin sizes for the histograms used to compute prior ratio and likelihood ratio are set to 4, and the bin size used to compute the normalized distribution is set to 0.01 for all scales.

The performance of the scheme is analyzed in terms of both image quality and computational complexity. Synthetically speckled image are generated from a noise-free images of '*Lena*' and '*boat*' of size 512x512 pixels with different number of looks say, 1, 2, 4, and 16. These noisy images are made in amplitude format as explained in [2]. Table 5.12 shows the objective performance index in terms of PSNR measured on these images. The PSNR values provided are the average of ten different noise realisations for each case. It can be seen from the results that for both the test images the proposed scheme perform better than the compared schemes. Two original SAR images are also taken for evaluating the performance of the proposed scheme. The first image is an X-band, 2-looks, amplitude SAR image of *Bedfordshire* and the second one is a Ku-band, 4-looks, intensity SAR image of *Horse track*. Table 5.13 shows the ENL and ESI values measured on these two real SAR images.

PSNR figures for simulated SAR images and ENL & ESI values for real SAR images help understanding major trends, but must be complemented by visual

inspection. Therefore, in figure 5.27 the output of the various despeckling algorithms on the synthetic *Lena* image (*L=4*) and in figure 5.28 and figure 5.29 that on two real SAR images are shown. The DT-Bivariate scheme provides the best speckle rejection followed by DTCWT, both by visual inspection and in terms of performance indices. It can be seen that most of these schemes are very effective for homogeneous regions. But they have the common limitation, that is, edges and point targets are also strongly and smoothly suppressed in despeckling. In directional transform based schemes the speckles are effectively reduced, and the texture feature are very well preserved, but scratches are seen in homogeneous areas of NCST filtered image and edges and strong point objects are blurred in NSST filtered images. On the other hand, wavelet based schemes, GGMAP-S & LGMAP-S and in a lesser measure DTCWT also, over smooth the image, leaving traces of signal structures in the ratio images shown in figure 5.30. It can be seen from the ratio images generated from Bedfordshire SAR image that the one by the DT-Bivariate looks much noisier and shows the least number of details among all the methods.

Table 5.12 Despeckling results (PSNR) for synthetic SAR images of *Lena & Boat* (512x512) in amplitude format

Looks/Method	Lena				Boat			
	1	2	4	16	1	2	4	16
Synthetic SAR Image	12.11	14.89	17.80	23.76	11.77	14.55	17.46	23.42
Lee [6]	20.82	23.86	26.19	29.34	17.25	20.31	23.53	28.09
DTCWT [65]	26.37	28.11	29.93	33.61	24.06	25.55	27.21	30.59
GGMAP-S [60]	26.33	28.03	29.75	33.29	23.98	25.43	27.05	30.48
LG MAP-S [63]	26.20	27.80	29.51	33.24	23.71	25.20	26.91	30.40
NSCT [68]	26.02	27.12	29.01	32.78	23.50	24.64	26.37	30.02
NSST [69]	26.28	27.87	29.66	33.41	23.76	25.35	27.00	30.61
DT-Bivariate	**26.66**	**28.44**	**30.28**	**34.22**	**24.39**	**26.01**	**27.73**	**31.45**

Figure 5.27 Despeckling results of Synthetic SAR image of *Lena* in amplitude format with *L=4* (a) Original noise free Image (b) Noisy image (c) Despeckled image using Lee filter (d) Despeckled image using NSCT (e) Despeckled image using NSST and (f) Despeckled image LGMAP-S (g) Despeckled image GGMAP-S (h) Despeckled image DT-Bivariate

Table 5.13 Comparison of ENL, ESI & MRI values of DT-Bivariate and other despeckling schemes applied on original SAR images

Despeckling Scheme	Bedfordshire Image (Amplitude format, L=2)					Horse Track image (Intensity format, L=4)				
	ENL		ESI		MRI	ENL		ESI		MRI
	Reg. A	Reg. B	ESI_H	ESI_V		Reg. C	Reg. D	ESI_H	ESI_V	
Real SAR Image	2.94	3.28	1	1	-----	14.11	9.76	1	1	-----
Lee [6]	15.67	22.69	0.365	0.328	0.926	125.1	91.33	0.253	0.262	0.930
NSCT [68]	30.78	42.11	0.421	0.381	0.942	204	70.34	0.311	0.384	0.926
NSST [69]	44.46	52.56	0.456	0.397	**1.005**	212	76.75	0.320	0.401	0.997
DTCWT [65]	40.1	61.11	0.424	0.383	0.986	366.34	121.78	0.332	0.408	0.963
GGMAP-S [60]	31.47	77.21	0.309	0.284	0.972	328.45	77.55	0.315	0.377	0.990
LGMAP-S [63]	30.2	70.6	0.295	0.269	0.969	303.83	104.47	0.272	0.322	0.951
DT-Bivariate	**76.7**	**178.2**	**0.534**	**0.453**	1.006	**569.21**	**205.76**	**0.386**	**0.468**	**1.011**

Shown in figure 5.31 is a 256x256 portion of *Horse track* image and the despeckled images using directional transform based schemes NSCT and NSST. This portion of the image is taken as it contains lot of structural information. An enlarged part of the despeckled image is shown in figure 5.32. The visual examination of these figures shows that the DT-Bivariate scheme provides a very high edge preservation performance and speckle reduction as compared to other two schemes.

It can also be seen from the results that the performance improvement of the proposed scheme is narrowing down as the noise variance increases or the number of looks, *L* decreases. This is basically due to two reasons. The first one is that at lower values of *L*, the noise variance is more which adversely affects the detection of local dominant directions in the image and the second reason is that as the number of looks, *L* increases, the noise in the log transformed image tend to become more Gaussian making the homomorphic filtering more effective. The

performance is also affected by the length of the wavelets. The Db4 wavelet gives slightly better results than Haar wavelet due to the fact that it effectively smoothes out the noise in flat regions due to the good support of its scaling function.

Figure 5.28 Despeckling results of *Bedfordshire* image (a) Original Image (b) Despeckled image using Lee filter (c) Despeckled image using DTCWT (d) Despeckled image using LGMAP-S (e) Despeckled image using GGMAP-S and (f) Despeckled image using DT-Bivariate.

Computational complexity is a serious problem in the SAR field, since systems of the last generation produce high-resolution images of hundreds of megapixels. Several recent papers focus on fast SAR despeckling techniques. In order to compare the computational burden of the different algorithms, a computer with a core i5 CPU@2.4GHz with 4GB RAM is used. A synthetic SAR image of *Lena* of size 512X512 with *L=4* is used to compare computation time. The computational

times needed to run the different algorithms are shown in Table 5.14. It can be seen that the computation time of NSCT is the largest, say, 400 Sec. LG-MAP-S algorithm takes the smallest computation time of 10 sec among the compared schemes. This is because the LG-MAP-S algorithm uses wavelet transform, which is having lower complexity as compared with other directional transforms like NSCT, NSST, directionlet etc. Among the directional transform based schemes, DT-Bivariate and DTCWT are best in terms of computational efficiency.
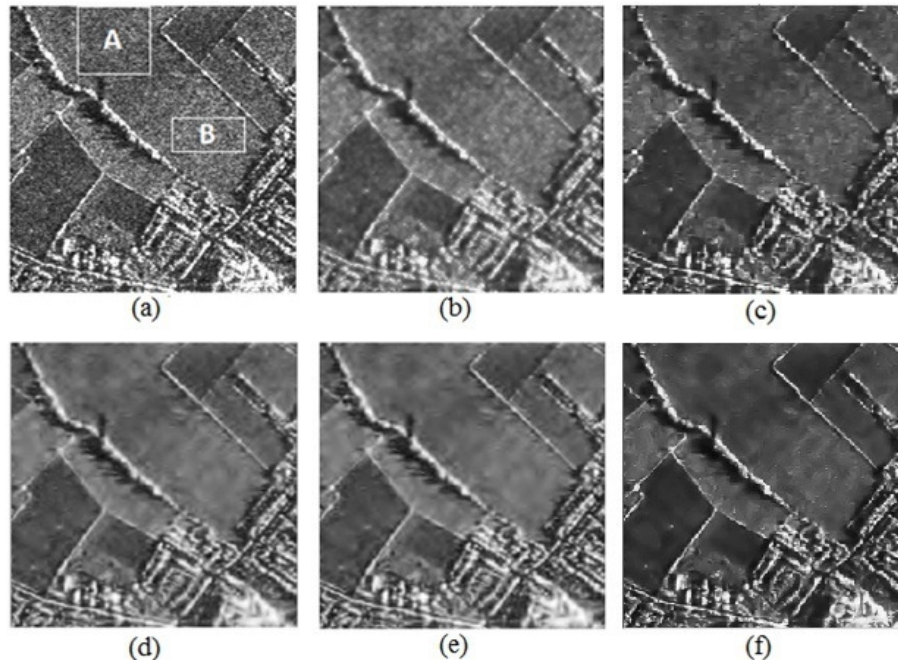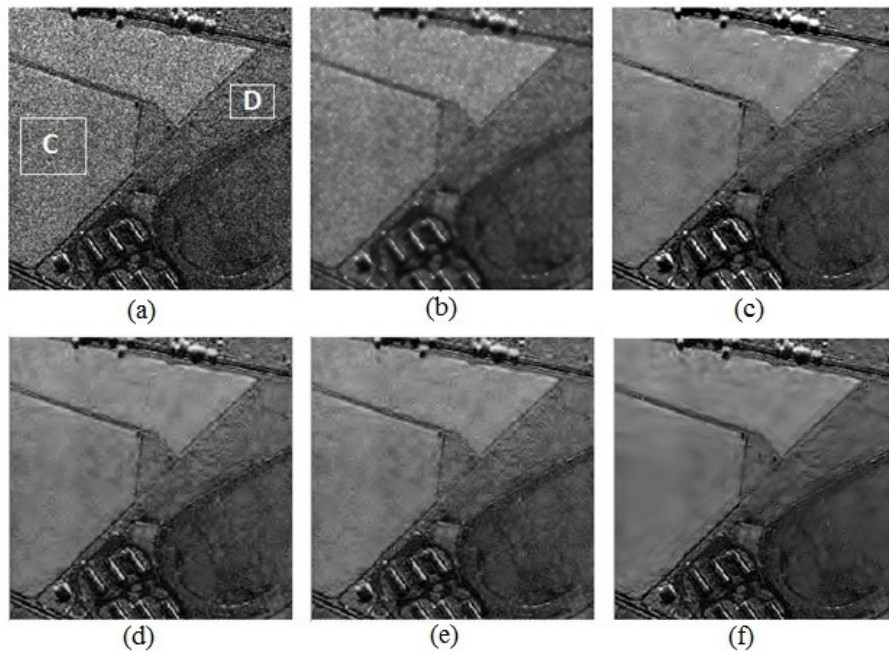

Figure 5.29 Despeckling results of *Horse track* image (a) Original Image (b) Despeckled image using Lee filter (c) Despeckled image using DTCWT (d) Despeckled image using LGMAP-S (e) Despeckled image using GGMAP-S and (f) Despeckled image using DT-Bivariate scheme.
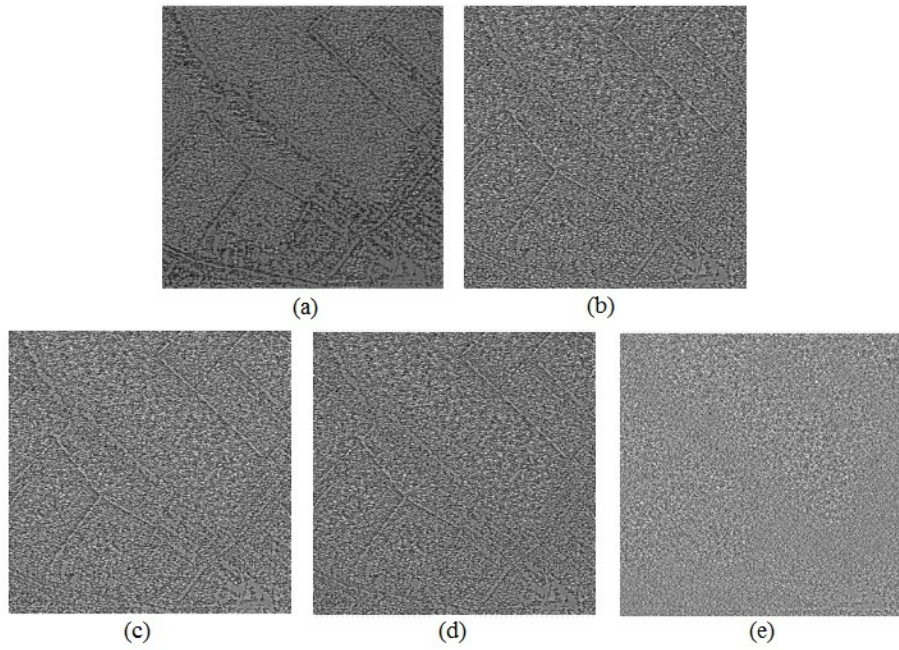
Figure 5.30 Ratio images of despeckled result of *Bedfordshire* image (a) Lee filter (b) DTCWT (c) LGMAP-S (d) GLGMAP-S and (e) DT-Bivariate

Table. 5.14. Approximate computation time taken by different despeckling schemes

Scheme	Lee [6]	NSCT [68]	NSST [69]	DTCWT [65]	GGMAP-S [60]	LG MAP-S [63]	DT-Bivariate
Time(sec.)	20	400	69	11	64	**10**	12
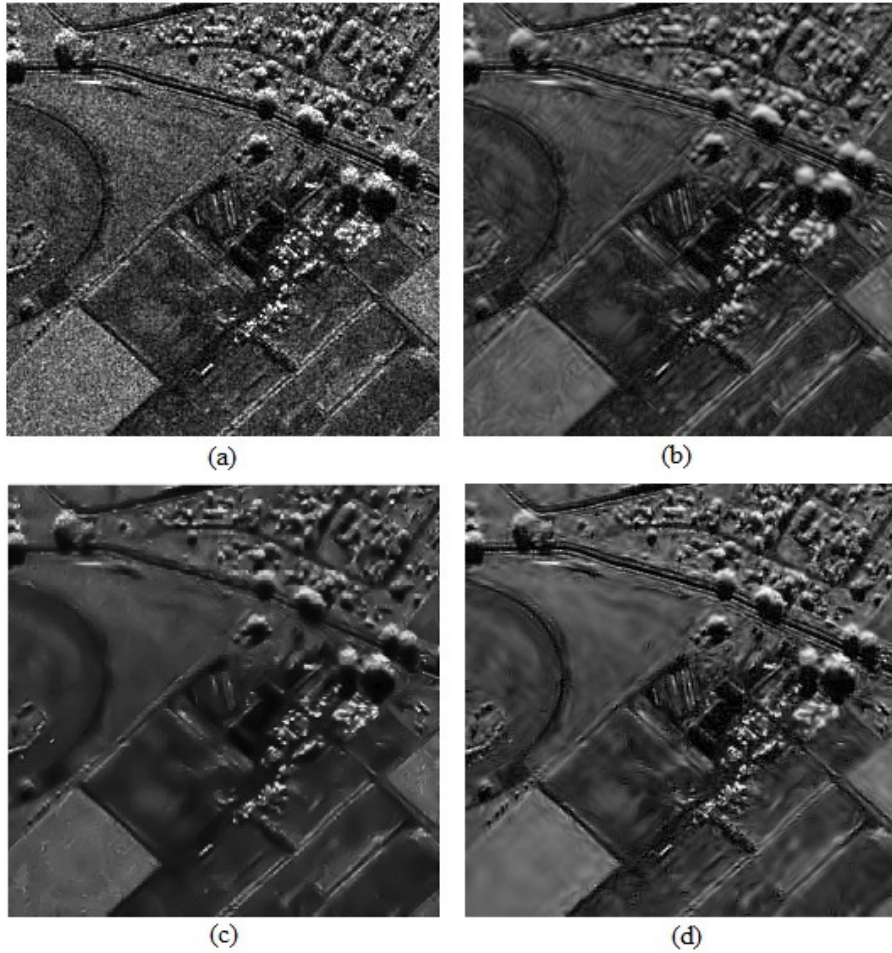
Figure 5.31 Despeckling results of *Horse track 1* image a) Original Image b) Despeckled image using NSCT c) Despeckled image using NSST d) Despeckled image using DT-Bivariate
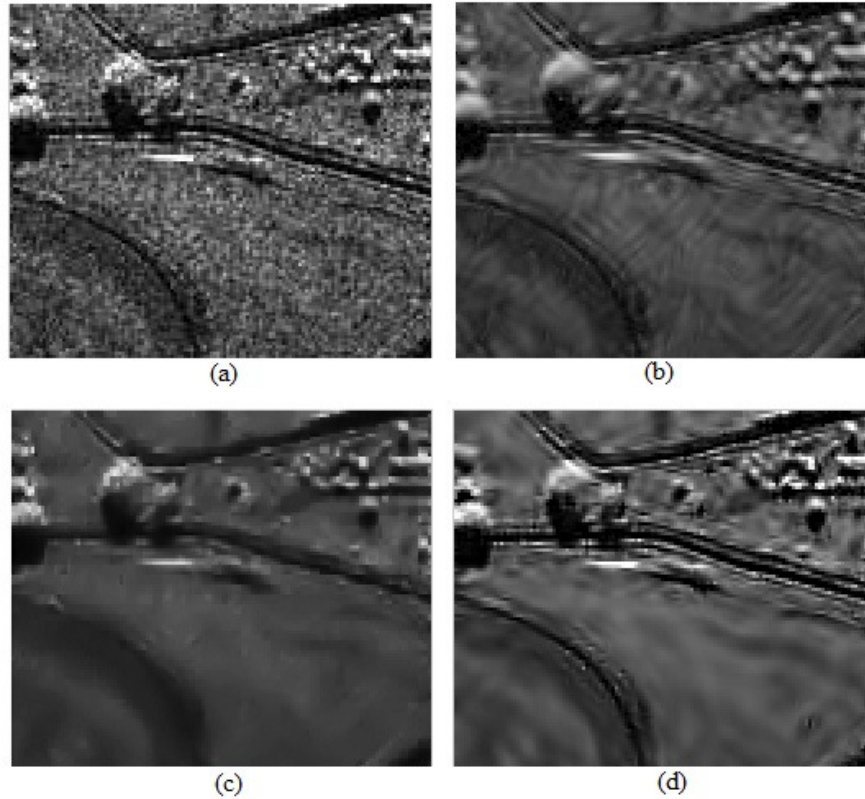
Figure 5.32 The enlarged detail parts corresponding to *Horse track 1* image. (a) Original (b) NSCT (c) NSST (d) DT-Bivariate

5.8 Comparison of Presented Despeckling Schemes in Directionlet Domain

In this section an overall comparison of all the developed despeckling schemes in directionlet domain is carried out. The comparison is done in terms of PSNR for synthetic SAR images and ENL & ESI values for original SAR images. The comparison of computational complexity in terms of the actual time taken by a standard computer environment is also done. Table 5.15 gives the PSNR values achieved by different despeckling schemes in directionlet domain for synthetic

SAR image of *Lena* and *Boat* with different number of looks. Also the comparison is made with two real SAR images in amplitude and intensity formats, of *Bedfordshire* and *horse track*. Here the ENL & ESI are used as the performance measures. The mean of ratio image (MRI) is also used for performance assessment. Table 5.16 gives a comparison of these parameters for the original SAR images. The computation time taken by these schemes on a computer with a core i5 CPU@2.4GHz with 4GB RAM is listed in Table 5.17.

Table 5.15. Despeckling results (PSNR) for synthetic SAR images of *Lena* & *Boat* (512x512) in amplitude format

Looks/Method	Lena				Boat			
	1	2	4	16	1	2	4	16
Synthetic SAR Image	12.11	14.89	17.80	23.76	11.77	14.55	17.46	23.42
DT-GCV	25.38	27.54	29.21	32.90	23.59	25.26	26.86	30.48
DT-Edge	25.83	27.86	29.43	33.65	23.62	25.45	27.18	30.60
DT-Multiscale	25.90	27.91	29.58	33.79	23.72	25.57	27.35	30.79
DT-LG	26.45	28.24	30.08	33.88	24.14	25.69	27.38	30.89
DT-CG	26.49	28.29	30.16	33.97	24.20	25.78	27.47	31.00
DT-Bivariate	**26.66**	**28.44**	**30.28**	**34.22**	**24.39**	**26.01**	**27.73**	**31.45**

In addition to the denoising techniques and the statistical models used, the choice of the underlying wavelet family, as well as the length of the wavelet filter, is also important for the overall denoising performance. The length of a wavelet filter is related to smoothness and localization properties. The primary advantage of short-wavelet filters, such as the Haar wavelet, is their compact spatial support; in contrast, longer-wavelet filters are preferred for smoothness. Furthermore, computational time of the wavelet transform is approximately proportional to the length of the wavelet filter. To compromise, Daubechies' maximally flat wavelet of length eight (db4) is used throughout this work. To allow for robust and reliable parameter estimation, the minimum segment size is maintained at 32x32. The

decomposition level of directionlet transform is limited to three in all the cases. Another concern of segmented processing is managing the problem of image border distortion. Here symmetric extension of the boarders is carried out to avoid discontinuities along borders. At each decomposition level, the denoising algorithm was applied separately to all the detail subbands, while the approximation subband was left intact.

Table 5.16 ENL, ESI & MRI values for the different Despeckling schemes applied on original SAR images

Despeckling Scheme	Bedfordshire Image (Amplitude format, L=2)					Horse Track image (Intensity format, L=4)				
	ENL		ESI		MRI	ENL		ESI		MRI
	Reg. A	Reg. B	ESI_H	ESI_V		Reg. C	Reg. D	ESI_H	ESI_V	
Real SAR Image	2.94	3.28	1	1	-----	14.11	9.76	1	1	-----
DT-GCV	32.60	63.58	0.428	0.394	0.971	214.81	98.70	0.313	0.385	0.982
DT-Edge	72.08	165.18	**0.681**	**0.621**	0.979	482.31	172.87	**0.395**	**0.479**	0.986
DT-Multi	76.57	171.24	0.612	0.569	0.988	511.56	196.22	0.387	0.470	0.978
DT-Bivariate	**86.78**	**195.79**	0.544	0.463	1.006	**569.21**	**205.76**	0.386	0.468	1.011
DT-CG	71.41	163.52	0.511	0.438	**1.005**	536.15	194.64	0.356	0.432	**1.004**
DT-LG	70.11	160.81	0.507	0.424	1.008	531.86	192.01	0.347	0.412	1.007

Table 5.17 Approximate computation time taken by different despeckling schemes in directionlet domain

Scheme	DT-GCV	DT-Edge	DT-Multiscale	DT-LG	DT-CG	DT-Bivariate
Time(sec)	8.2	9.4	9.3	11.2	13.6	12.1

From the computed performance measures, it can be concluded that the DT-bivariate scheme provides the best despeckling performance in terms of noise smoothing with a reasonable computation time. The DT-Edge scheme provides the best edge retaining capability whereas the DT-GCV (with dominant direction identification using *DirVar*) takes the lowest computation time among the schemes.

Chapter 6

Conclusions and Future Perspectives

In this concluding chapter the whole work is summarised and the achievements of the research work is highlighted. The directions for future study are also discussed here.

6.1 Thesis Highlights and Contributions

This chapter stands as a brief conclusion of the thesis. It highlights the objectives of the study and the achievements. The aim of the thesis was to design and develop spatially adaptive denoising techniques with edge and feature preservation, for images corrupted with additive white Gaussian noise and SAR images affected with speckle noise.

Image denoising is a well researched topic. It has found multifaceted applications in our day to day life. Image denoising based on multi resolution analysis using wavelet transform has received considerable attention in recent years. However due to limited directional selectivity, the wavelet based multi resolution techniques cannot easily cater to the growing requirements of effective denoising with edge and feature preservation. Digital photography, satellite imaging, medical imaging etc are the thrust application areas which need edge and feature preserving denoising algorithms. The intense research efforts to tackle this problem with better adaptive schemes by combining ideas from geometry and traditional multi-scale analysis have resulted in a family of multi scale geometrical transforms. A special member of this emerging family is the directionlet transform, which has strong directional character and its elements are highly anisotropic at all scales.

Given the diversity of the problems posed and addressed, this thesis presented different denoising algorithms in directionlet domain for images corrupted with additive white Gaussian noise and SAR images affected by speckle noise. To

211

address the multiplicative nature of speckle noise, the speckle contribution is made additive by a linear decomposition. All the presented methods suitably adjust the transform directions based on local dominant directions of spatially segmented image and successfully capture the oriented features. The developed methods include two sub band adaptive threshold based schemes, based on SURE risk and Bayes shrink. Since these schemes require the prior knowledge of the noise variance and signal variance to compute the threshold, a Generalized Cross Validation (GCV) based optimal threshold estimation scheme in directionlet domain is developed. This scheme computes the optimal threshold from the noisy input data without using the knowledge of the noise variance. Here three despeckling schemes based on GCV thresholding are presented in directionlet domain. The first scheme applies simple GCV thresholding to the directionlet coefficients of a spatially segmented image. The second scheme efficiently extracts edge information along dominant directions from the spatially segmented SAR image. Then an optimal scale dependent subband adaptive threshold is applied to the edge removed image. The despeckled image is finally synthesized using the extracted edge information to preserve sharpness of edges and texture. In the third scheme, the adjacent scale directionlet coefficients are multiplied to amplify the significant signal features and thresholding is applied to these multiscale products to better differentiate edge structures from noise. All the presented schemes provided better results as compared to the WT based schemes and other state of the art techniques.

The statistical model based schemes use the joint statistics of the DT coefficients across scales and non-linear threshold functions are derived using Bayesian MAP estimator. The interscale dependency of the DT coefficients is modelled here using different probability distributions. Three different distributions have been considered. These are selected based on the analysis of the original signal and noise distributions in directionlet domain. It was observed that the heavy tailed behaviour of the natural images can be effectively modelled by using different bivariate distributions with inter and intra scale dependency. Denoising and despeckling schemes have been developed using these bivariate distributions. In one of the despeckling schemes Cauchy *pdf* was utilized as a prior for modelling the heavy tailed nature of the log-transformed reflectance. The statistical inter scale

dependency of DT coefficients was also considered in the modelling process. Laplacian-Gaussian model based MAP despeckling was also developed which has provided reasonably good results with better computational efficiency. Adaptive spatial segmentation and processing based on content directionality was tried in one of the schemes which have improved the computational efficiency with a slight reduction in performance.

Altogether ten different denoising schemes were developed within the frame work of directionlet transform and all these schemes were compared with the state of the art technologies available for standard benchmark images and original images corrupted with noise. It is well established that, allowing for spatial segmentation and choosing transform directions in each segment independently, directionlets outperform the standard 2D WT and other oriented transforms in image denoising. The performance improvement can be basically attributed to two reasons. One is the application of multi directional DT, which adapts to the local dominant directions resulting in an efficient sparse representation and there by retaining the image specific features like edges and contours after denoising. The other reason for the improvement is the interscale dependency model based denoising of DT coefficients using locally adaptive marginal variance and oriented neighbourhood.

6.2 Future Perspectives

The directionlet based denoising schemes presented in this thesis are effective in preserving the image specific features like edges and contours in denoising. Scope of this research is still open in areas like further optimization in terms of speed and extension of the techniques to other related areas like colour and video image denoising. Such studies would further augment the practical use of these techniques.

Several aspects of the proposed algorithm may still be improved. A more complex spatial segmentation, which is capable of extracting the dominant directions in images with more flexibility, may improve the performance of the proposed schemes. A more efficient adaptive spatial segmentation of the image based on the

local dominant directions to identify the transform directions can further improve the computational efficiency and provide better sparse representation.

The anisotropic ratio and the maximum number of levels in the DT decomposition are now limited by the segment size, which can affect the overall performance of DT based denoising schemes. The optimal selection of these parameters based on content directionality may improve the performance.

The identification of dominant directions in the case of images contaminated with large amount of noise is a challenging task. The estimation of dominant directions based on the computation of directional variance may not yield a good result in such cases. This needs further study.

In the case of SAR despeckling, the performance analysis showed different results when the algorithm is applied on simulated or real SAR images; the reason behind is that the speckle statistics of actual SAR images, especially at high resolution, often deviate from the simplified models used in this work, as well as in most of the literature. The accurate modelling of the statistics of SAR images is a challenging task. The performance of statistical model based despeckling schemes is heavily dependent on the models selected. As a future improvement, optimization of the statistical model based denoising algorithm by incorporating generalized statistical models with variable parameters can be tried out.

Yet another scope of future research is to extend the proposed algorithms for colour image denoising and video image denoising. This will find more practical applications to the presented schemes.

References

[1] Rafeal. C . Gonzalez and Richard E. Woods, "Digital image processing", Addison Wesley Longman, 1999.

[2] J.W. Goodman, "Some fundamental properties of speckle," J. Opt. Soc. Amer., vol. 66, pp. 1145–1150, Nov. 1976.

[3] C. Oliver and S. Quegan, "Understanding Synthetic Aperture Radar Images", Norwood, MA: Artech House, 1998.

[4] V. S. Frost, J. A. Stiles, K. S. Shanmugan, and J. C. Holtzman, "A model for radar images and its application to adaptive digital filtering of multiplicative noise," IEEE Trans. Pattrn Anal. Machn Intell., vol.4, pp.157–166, 1982.

[5] D. T. Kuan, A. A. Sawchuk, T. C. Strand, and P. Chavel, "Adaptive noise smoothing filter for images with signal-dependent noise," IEEE Trans. Pattern Anal. Machine Intell., vol. 7, pp. 165–177, 1985.

[6] J. S. Lee, "Digital image enhancement and noise filtering by use of local statistics," IEEE Trans. Pattern Anal. Mach. Intell., vol. 2, no. 2, pp. 165–168, Mar. 1980.

[7] G. Lee, "Refined filtering of image noise using local statistics," Comput. Graph. Image Process., vol. 15, no. 4, 1981.

[8] A. Lopès, R. Touzi, and E. Nezry, "Adaptive speckle filters and scene heterogeneity," IEEE Trans. Geosci. Remote Sens., vol. 28, no. 6, pp. 992–1000, Nov. 1990.

[9] A. Lopès, E. Nezry, R. Touzi, and H. Laur, "Maximum a posteriori speckle filtering and first order texture models in SAR images," in Proc. IGARSS, Washington, DC, vol. 3, pp. 2409–2412, May 1990.

[10] A. Baraldi and F. Parmigiani, "A refined Gamma MAP SAR speckle filter with improved geometrical adaptivity," IEEE Trans. on Geosci.and Remote Sensing, vol. 33, pp. 1245–1257, Sept. 1995.

[11] M. R. Azimi-Sadjadi and S. Bannour, "Two-dimensional adaptive block Kalman filtering of SAR imagery," IEEE Trans.Geosci.Remote Sensing, vol. 29, pp. 742–753, 1991.

[12] I. Daubechies "The Wavelet transform, time frequency localization and signal analysis", IEEE Trans. Inform. Theory Vo1.36, pp.961- 100S, Sep. 1990.

[13] M.Vetterii and C.Harley "Wavelets and filter banks: theory and design", IEEE Trans. Signal Processing Vo1.40, No.9, pp.2207-2232, Dec.l993.

[14] E. Hervet, R. Fjortoft, P. Marthon and A. Lopes, "Comparison of Wavelet-based and Statistical Speckle Filters," EUROPTO Conference on SAR Image Analysis, Modeling, and Techniques. Barcelona, Spain, Sep. 1998.

[15] L. Gagnon and A. Jouan, "Speckle filtering of SAR images-A comparative study between complex-wavelet based and standard filters," Proc. SPIE, vol. 3169, pp. 80–91, 1997.

[16] D. L. Donoho and I. M. Johnstone, "Ideal spatial adaptation via wavelet shrinkage," Biometrika, vol. 81, pp. 425–455, 1994.

[17] D. L. Donoho, "De-noising by soft-thresholding", IEEE Trans. Inform. Theory, vol. 41, no. 3, pp. 613–627, May 1995.

[18] D. L. Donoho and I. M. Johnstone, "Adapting to unknown smoothness via wavelet shrinkage," Journal of the American Statistical Assoc., vol. 90, no. 432, pp. 1200–1224, December 1995.

[19] E. P. Simoncelli, "Bayesian denoising of visual images in the wavelet domain," in Bayesian Inference in Wavelet Based Models, P. Müller and B. Vidakovic, Eds. New York: Springer-Verlag, 1999.

[20] E. J. Candés and D. L. Donoho, "Curvelets-A surprisingly effective non adaptive representation for objects with edges," in Curve and Surface Fitting, A. Cohen, C. Rabut, and L. L. Schumaker, Eds. Saint-Malo, France: Vanderbilt Univ. Press, 1999.

[21] M. N. Do and M. Vetterli, "The contourlet transform: An efficient directional multi resolution image representation," IEEE Trans. Image Process., vol. 14, no. 12, pp. 2091–2106, 2005.

[22] R. H. Bamberger and M. J. T. Smith, "A filter bank for the directional decomposition of images: Theory and design," IEEE Trans. Signal Process., vol. 40, no. 4, pp. 882–893, 1992.

[23] D. L. Donoho, "Wedgelets: Nearly minimax estimation of edges"' Ann. Statist., vol. 27, pp. 859–897, 1999.

[24] J. K. Romberg, M. Wakin, and R. Baraniuk, "Multiscale wedgelet image analysis: fast decompositions and modelling," In Proc. IEEE International Conference on Image Processing (ICIP2002), pp. 585–588, Rochester, NY, September 2002.

[25] N. G. Kingsbury, "Complex wavelets for shift invariant analysis and filtering of signals," Appl. Compt. Harmon. Anal., pp. 234–253, 2001.

[26] D. Taubman and A. Zakhor, "Orientation adaptive subband coding of images," IEEE Trans. Image Process., vol. 3, no. 4, pp. 421–437, 1994.

[27] W. Ding, F. Wu, X. Wu, S. Li, and H. Li, "Adaptive directional lifting based wavelet transform for image coding," IEEE Trans. Image Process., vol. 16, no. 2, pp. 416–427, 2007.

[28] C.-L. Chang and B. Girod, "Direction-adaptive discrete wavelet transform for image compression," IEEE Trans. Image Process., vol. 16, no.5, pp. 1289–1302, 2007.

[29] G. Kutyniok and D. Labate, "Resolution of the wave front set using continuous shearlets," Trans. Amer. Math. Soc., vol. 361, no. 5, pp. 2719–2754, May 2009.

[30] G. Easley, D. Labate, and W. Lim, "Sparse directional image representations using the discrete Shearlet transform," Appl. Comput. Harmon. Anal., vol. 25, no. 1, pp. 25–46, Jan. 2008.

[31] G. Kutyniok and T. Sauer, "From wavelets to Shearlets and back again," in Approximation Theory XII (San Antonio, TX, 2007). Nashville, TN: Nashboro Press, pp. 201–209, 2008.

[32] D. Wang, L. Zhang, A. Vincent, and F. Speranza, "Curved wavelet transform for image coding," IEEE Trans. Image Process., vol. 15, no. 8, pp. 2413–2421, 2006.

[33] E. Le Pennec and S. Mallat, "Sparse geometric image representations with bandelets," IEEE Trans. Image Processing, vol. 14, pp. 423–438, April 2005.

[34] S. Mallat and G. Peyré, "A review of bandelets methods for geometrical image representation," Numer. Alg., vol. 44, pp. 205–234, Mar. 2007.

[35] G. Peyré and S. Mallat, "Orthogonal bandelet bases for geometric images approximation," Commun. Pure Appl. Math., vol. 61, no. 9, pp. 1173– 1212, 2008.

[36] V. Velisavljevic´, B. Lozano, M. Vetterli, and P. L. Dragotti, "Directionlets: Anisotropic multi-directional representation with separable filtering," IEEE Trans. Image Process., vol. 15, no. 7, pp. 1916–1933, 2006.

[37] V. Velisavljevi´c, "Directionlets: Anisotropic multi-directional representation with separable filtering," Ph.D. dissertation, School Comput. Commun. Sci., Swiss Federal Inst. Technol. Lausanne (EPFL), Lausanne, Swiz, 2005.

[38] Dakala Jayachandra and Anamitra Makur, "Directionlets Using In-Phase Lifting for Image Representation", IEEE Trans. Image Process, Vol. 23, No. 1, 2014.

[39] A.P. Reji and T. Thomas, "Directionally adaptive single frame image super resolution", Int. J. Innovative Computing and Applications, Inderscience Publishers, Vol. 3, No. 3, pp.117–125, 2011.

[40] X. Zhou, X. Yin, R. Liu, and W. Wang, "Infrared and visible image fusion technology based on directionlets transform," EURASIP J. Wireless Commun. Netw., vol. 20, no. 1, pp. 1–4, Feb. 2013.

[41] S. Ananda, R. Shantha Selva Kumaria, S. Jeevab, and T. Thivyac, "Directionlet transform based sharpening and enhancement of mammographic

X-ray images," Biomed. Signal Process. Control, vol. 8, no. 9, pp. 391–399, Jul. 2013.

[42] C. Stein, "Estimation of the mean of a multivariate normal distribution," Ann. Statist., vol. 9, pp. 1135–1151, 1981.

[43] S. G. Chang, B. Yu, and M. Vetterli, "Adaptive wavelet thresholding for image denoising and compression," IEEE Trans. Image Processing, vol.9, no. 9, pp. 1532–1546, Sept. 2000.

[44] S. G. Chang, B. Yu, and M. Vetterli, "Spatially adaptive wavelet thresholding with context modelling for image denoising," IEEE Trans. Image Processing, vol. 9, no. 9, pp.1522– 1531, Sept. 2000.

[45] M. Jansen, M. Malfait and A. Bultheel, "Generalized cross validation for wavelet thresholding," Signal Processing, vo. 56, no. 1, pp. 33-44, Jan 1997.

[46] Chen, G.Y., Bui, T.D, "Multiwavelet denoising using neighbouring coefficients," IEEE Signal Process. Lett., vol.10, no. 7, pp. 211–214, 2003.

[47] Chen, G.Y., Bui, T.D., Krzyzak A, "Image denoising with neighbour dependency and customized wavelet and threshold," Pattern Recognit., vol. 38, no. 1, pp. 115–124, 2005

[48] Crouse, M.S., Nowak, R.D., Baraniuk, R.G, "Wavelet-based signal processing using hidden markov models," IEEE Trans. Signal Process., vol. 46, no. 4, pp. 886–902, 1998.

[49] Sendur, L., Selesnick, I.W, "Bivariate shrinkage functions for wavelet based denoising exploiting interscale dependency," IEEE Trans. Signal Process., vol. 50, no.11, pp. 2744–2756, 2002.

[50] Sendur, L., Selesnick, I.W, "Bivariate shrinkage with local variance estimation," IEEE Signal Process. Lett., vol. 9, no. 12, pp. 438–441, 2002.

[51] Luisier, F., Blu, T., Unser, M, "A new SURE approach to image denoising: inter-scale ortho-normal wavelet thresholding," IEEE Trans. Image Process., vol. 16, no. 3, pp. 593–606, 2007.

[52] E. P. Simoncelli, W. T. Freeman, E. H. Adelson, and D. J. Heeger, "Shiftable multiscale transforms," IEEE Trans. Inform. Theory, vo. 38, pp. 587–607, March 1992.

[53] G. Chen, W. P. Zhu, W. Xie, "Wavelet-based image denoising using three scales of dependency," IET Image Process., Vol. 6, Iss. 6, pp. 756–760, 2012.

[54] J. Portilla, V. Strela, M. J. Wainwright, and E. P. Simoncelli, "Image denoising using scale mixtures of Gaussians in the wavelet domain," IEEE Trans. Image Process., vol. 12, no. 11, pp. 1338–1351, Nov. 2003.

[55] J.-L. Starck, E. J. Candès, and D. L. Donoho. The curvelet transform for image denoising. IEEE Trans. Image Processing, vol. 11, no. 6, pp. 670–684, June 2002.

[56] Z. F. Zhou and P. L. Shui, "Contourlet-based image denoising algorithm using directional windows," Electronics Letters, Vol. 43, No. 2, Jan. 2007.

[57] G. Liu, X. Zeng and Y. Liu, "Image denoising by random walk with restart Kernel and non-subsampled contourlet transform," IET Signal Process., vol. 6, no. 2, pp. 148–158, 2012.

[58] Glenn R. Easley, Demetrio Labate, and Flavia Colonna, "Shearlet-Based Total Variation Diffusion for Denoising," IEEE Transactions on Image Processing, vol. 18, no. 2, Feb. 2009

[59] F. Argenti, T. Bianchi, and A. Alparone, "Multiresolution MAP despeckling of SAR images based on locally adaptive generalized Gaussian pdf modeling," IEEE Transactions on Image Processing, vol. 15, no. 11, pp. 3385–3399, Nov. 2006.

[60] F. Argenti, T. Bianchi, and A. Alparone, "Segmentation-based MAP despeckling of SAR images in the undecimated wavelet domain," IEEE Transactions on Geoscience and Remote Sensing, vol. 46, no. 9, pp. 2728–2742, Sep. 2008.

[61] H. Rabbani, M. Vafadust, P. Abolmaesumi, and S. Gazor, "Speckle noise reduction of medical ultrasound images in complex wavelet domain using mixture priors," IEEE Trans. Biomed. Eng., vol. 55, no. 9, pp. 2152–2160, Sep. 2008.

[62] F. Argenti, T. Bianchi, A. Lapini, and L. Alparone, "Bayesian despeckling of SAR images based on Laplacian-Gaussian modeling of undecimated wavelet coefficients," in ICASSP 2011, pp. 1445 –1448, May 2011.

[63] F. Argenti, T. Bianchi, A. Lapini, and L. Alparone, "Fast MAP despeckling based on Laplacian - Gaussian modeling of wavelet coefficients," IEEE Geosci. Remote Sens. Lett., vol 9, no. 1, pp. 13–17, Jan. 2012.

[64] M. Bhuiyan, M. Ahmad, and M. Swamy, "Spatially adaptive wavelet based method using the Cauchy prior for denoising the SAR images," IEEE Transactions on Circuits and Systems for Video Technology, vol. 17, no. 4, pp. 500–507, Apr. 2007.

[65] J. J. Ranjani and S. J. Thiruvengadam, "Dual tree complex wavelet transform based despeckling using interscale dependence," IEEE Trans. Geosci. Remote Sens., vol.48, no.6, pp. 2723–2731, Jun. 2010.

[66] J. J. Ranjani and S. J. Thiruvengadam, "Generalized SAR Despeckling Based on DTCWT Exploiting Interscale and Intrascale Dependences" IEEE Geoscience And Remote Sensing Letters, Vol. 8, No. 3, May 2011

[67] Biao Hou, Honghua Liu, Licheng Jiao, "The Despeckling of SAR Image Based on Curvelet Transform" Proceedings of APSAR 2009, 2nd Asian-Pacific Conference on Synthetic Aperture Radar, 2009. pp. 1080 – 1083

[68] F. Argenti, T. Bianchi, G. M. di Scarfizzi, and L. Alparone, "LMMSE and MAP estimators for reduction of multiplicative noise in the non-subsampled contourlet domain," Signal Process., vol. 89, no. 10, pp. 1891–1901, Oct. 2009.

[69] Biao Hou, Xiaohua Zhang, Xiaoming Bu, and Hongxiao Feng, "SAR Image Despeckling Based on Non subsampled Shearlet Transform", IEEE Journal Of Selected Topics In Applied Earth Observations And Remote Sensing, Vol. 5, No. 3, June 2012.

[70] Biao Hou, Shuang Wang, Ronghua Shang, Wenge Zhang, Fang Liu and Licheng Jiao, "SAR Image Despeckling Using Edge Detection and Feature Clustering in Bandelet Domain," IEEE Geoscience And Remote Sensing Letters, vol. 7, no. 1, Jan. 2010.

[71] W G Zhang, Q Zhang and C S Yang, "Edge detection with multiscale products for SAR image despeckling," Electronic letters, vol. 48, no.4, Feb. 2012.

[72] Rafael C. Gonzalez, Richard E. Woods, "Digital Image Processing," Pearson Prentice Hall, 2007.

[73] Hazewinkel, Michiel, ed., "Normal Distribution", Encyclopaedia of Mathematics, Springer, 2001.

[74] Horowitz, Paul and Winfield Hill, "The Art of Electronics," 2nd edition. Cambridge (UK): Cambridge University Press, 1989

[75] J. W. Goodman, "Statistical Properties of Laser Speckle Patterns," Heidelberg, Germany: Springer-Verlag, 1980.

[76] F. Ulaby and M. C. Dobson, "Handbook of Radar Scattering Statistics for Terrain," Norwood, MA: Artech House, 1989.

[77] D. H. Hoekman, "Speckle ensemble statistics of logarithmically scaled data," IEEE Trans. Geosci. Remote Sensing, vol. 29, pp. 180–182, Jan. 1991.

[78] D. Kaplan and Q. Ma, "On the statistical characteristics of log-compressed Rayleigh signals," in Proc. IEEE Ultrason. Symp., pp. 961–964, 1993.

[79] Hua Xie, Leland E. Pierce, and Fawwaz T. Ulaby, "Statistical Properties of Logarithmically Transformed Speckle," IEEE Transactions On Geosciences And Remote Sensing, vol. 40, no. 3, March 2002.

[80] M. Abramowitz and I. A. Stegun, "Handbook of Mathematical Functions With Formulas, Graphs, and Mathematical Tables," New York: Dover, 1973.

[81] I. S. Gradshteyn and I. M. Ryzhik, "Table of Integrals, Series, and Products," New York: Academic, 1980.

[82] S. Mallat, "A theory for multiresolution signal decomposition: the wavelet representation," IEEE Transactions on Pattern Analysis and Machine Intelligence, vol. 11, no. 7, pp. 674–693, Jul. 1989.

[83] G. Tzagkarakis and P. Tsakalides, "Bayesian compressed sensing of a highly impulsive signal in heavy-tailed noise using a multivariate Cauchy prior," in Proc. 17th EUSIPCO, pp. 2293–2297, Aug. 2009.

[84] E. E. Kuruoglu and J. Zerubia, "Modeling SAR images with a generalization of the Rayleigh distribution," IEEE Trans. Image Process., vol. 13, no. 4, pp. 527–533, Apr. 2004.

[85] S. Foucher, G. B. Bénié, and J.-M. Boucher, "Multiscale MAP filtering of SAR images," IEEE Trans. Image Processing, vol. 10, pp. 49–60, Jan. 2001.

[86] A. Achim, A. Bezerianos, and P. Tsakalides, "Novel Bayesian multiscale method for speckle removal in medical ultrasound images," IEEE Trans. Medical Imaging, vol. 20, no. 8, pp. 772-783, Aug 2001.

[87] P. Moulin and J. Liu, "Analysis of multiresolution image denoising schemes using generalized gaussian and complexity priors," IEEE Trans. Inform. Theory, vol. 45, pp. 909–919, Apr 1999.

[88] A. Buades, B. Coll, and J. Morel, "A review of image denoising algorithms, with a new one," SIAM interdisciplinary journal: Multiscale Modeling and Simulation, vol. 4, no. 2, pp. 290–530, 2005.

[89] A. Buades, B. Coll., and J. Morel, "A non local algorithm for image denoising," in Proc. Int. Conf. Computer Vision and Pattern Recognition (CVPR), vol. 2, pp. 60–65, 2005.

[90] N. Azzabou, N. Paragias, and G. F., "Image Denoising Based on Adapted Dictionary Computation," in Proc. of IEEE International Conference on Image Processing (ICIP), San Antonio, Texas, USA, pp. 109–112, Sept. 2007.

[91] C. Kervrann, J. Boulanger, and P. Coupé, "Bayesian Non-Local Means Filter, Image Redundancy and Adaptive Dictionaries for Noise Removal," in Proc. Int. Conf. on Scale Space and Variational Methods in Computer Visions (SSVM'07), Ischia, Italy, pp. 520–532, 2007.

[92] A. Dauwe, B. Goossens, H. Luong, and W. Philips, "A Fast Non-Local Image Denoising Algorithm," in Proc. SPIE Electronic Imaging, vol. 68, no. 12, Jan 2008.

[93] C. Kervrann and J. Boulanger, "Optimal spatial adaptation for patch-based image denoising," IEEE Trans. Image Processing, vol. 15, no. 10, pp. 2866–2878, 2006.

[94] T. Brox and D. Cremers, "Iterated Nonlocal Means for Texture Restoration," in Proc. Int. Conf. on Scale Space and Variational Methods in Computer Visions (SSVM'07), vol. 44, no. 85, Springer, 2007.

[95] M. Mahmoudi and G. Sapiro, "Fast image and video denoising via nonlocal means of similar neighborhoods," IEEE Signal Processing Letters, vol. 12, no. 12, pp. 839–842, Dec. 2005.

[96] J. Wang, Y. Guo, Y. Ying, Y. Liu, and Q. Peng, "Fast non-local algorithm for image denoising," in Proc. of IEEE International Conference on Image Processing (ICIP), pp. 1429–1432, 2006.

[97] B. R. C. and M. Vehvilainen, "Fast nonlocal means for image denoising," in Proc. SPIE Digital Photography III, R. A. Martin, J. M. Di Carlo, and N. Sampat, Eds., vol. 65, no. 1, 2007.

[98] Y. Wu, B. Tracey, P. Natarajan, J. P. Noonan, "James-Stein type center pixel weights for non-local means image denoising," IEEE Signal Processing Letters, vol. 20, no. 4, pp. 411-414, 2013.

[99] K. Dabov, A. Foi, V. Katkovnik, K. Egiazarian, "Image denoising by sparse 3D transform-domain collaborative filtering," IEEE Transactions on Image Processing, vol. 16, no. 8, pp. 2080-2095, 2007.

[100] S. Ghael, A. Sayeed, and R. Baraniuk, "Improved wavelet denoising via empirical wiener filtering," in Proc. SPIE, vol. 5, pp. 389–399, Jul. 1997.

[101] Y.C. Pati, R. Rezaiifar, and P.S. Krishnaprasad, "Orthogonal matching pursuit: Recursive function approximation with applications to wavelet decomposition," In IEEE Conference Record of The Twenty-Seventh Asilomar Conference on Signals, Systems and Computers, pp. 40-44, 1993.

[102] M Aharon, M Elad, and A. Bruckstein, "K-SVD: An Algorithm for Designing Over complete Dictionaries for Sparse Representation," IEEE Transactions on signal Processing, vol. 54, no. 11, pp. 4311-4322, 2006.

[103] M. Elad, M. Aharon, "Image denoising via sparse and redundant representations over learned dictionaries," IEEE Transactions on Image Processing, vol. 15, no. 12, pp. 3736-3745, 2006.

[104] J. Mairal, F. Bach, J. Ponce, G. Sapiro, and A. Zisserman, "Non-local sparse models for image restoration," In International Conference on Computer Vision (ICCV), IEEE, 2010.

[105] J.A. Tropp, A.C. Gilbert, and M.J. Strauss, "Algorithms for simultaneous sparse approximation, Part I: Greedy pursuit," Signal Processing, vol. 86, no. 3, pp.572-588, 2006.

[106] D. Zoran and Y. Weiss, "From learning models of natural image patches to whole image restoration," In International Conference on Computer Vision (ICCV), IEEE, 2011.

[107] R. Touzi, "A review of speckle filtering in the context of estimation theory," IEEE Transactions on Geoscience and Remote Sensing, vol. 40, no. 11, pp. 2392–2404, Nov. 2002.

[108] Mariana Poderico, "Denoising of SAR Images", a Ph.D thesis from University of Naples Federico II, Naples, Italy, 2012

[109] D. T. Kuan, A. A. Sawchuk, T. C. Strand, and P. Chavel, "Adaptive restoration of images with speckle," IEEE Transactions on Acoustics, Speech, and Signal Processing, vol. 35, pp. 373–383, Jan. 1987.

[110] S. M. Kay, "Fundamentals of statistical signal processing: estimation theory," Englewood Cliffs, NJ: Prentice Hall, 1993.

[111] R. Touzi, A. Lopes, and P. Bousquet, "A statistical and geometrical edge detector for SAR images," IEEE Transactions on Geoscience and Remote Sensing, vol. 26, no. 6, pp. 764–773, Nov. 1988.

[112] E. Nezry, A. Lopes, and R. Touzi, "Detection of structural and textural features for SAR image filtering," in Proceedings of IEEE International Geoscience and Remote Sensing Symposium, vol. 3, pp. 2169– 2172, 1991.

[113] G. Gao, "Statistical modeling of SAR images: a survey," Sensors, vol. 26, pp. 775– 794, Jan. 2010.

[114] R. Coifman and D. L. Donoho, "Translation-invariant de-noising," in Wavelets and Statistics. ser. Lecture Notes in Statistics, A. Antoniadis, Ed. Berlin, Germany: Springer-Verlag, vol. 103, pp. 125–150, 1995.

[115] H. H. Arsenault and G. April, "Properties of speckle integrated with a finite aperture and logarithmically transformed," J. Opt. Soc. Am., vol. 66, no. 11, pp. 1160–1163, 1976.

[116] H. Xie, L. Pierce, and F. Ulaby, "Statistical properties of logarithmically transformed speckle," IEEE Transactions on Geoscience and Remote Sensing, vol. 40, no. 3, pp. 721–727, Mar. 2002.

[117] J. Sveinsson and J. Benediktsson, "Almost translation invariant wavelet transformations for speckle reduction of SAR images," IEEE Transactions on Geoscience and Remote Sensing, vol. 41, no. 10, pp. 2404–2408, Oct. 2003.

[118] S.Fukuda and H.Hirosawa, "Smoothing effect of wavelet-based speckle filtering: the Haar basis case," IEEE Transactions on Geoscience and Remote Sensing, vol. 37, pp. 1168–1172, Mar. 1999.

[119] S. Solbø and T. Eltoft, "Γ-WMAP: A statistical speckle filter operating in the wavelet domain," Int. J. Remote Sens., vol. 25, no. 5, pp. 1019–1036, Mar. 2004.

[120] A. Achim, P. Tsakalides, and A. Bezarianos, "SAR image denoising via Bayesian wavelet shrinkage based on heavy-tailed modeling," IEEE Transactions on Geoscience and Remote Sensing, vol. 41, no. 8, pp. 1773–1784, Aug. 2003.

[121] S. Solbø and T. Eltoft, "Homomorphic wavelet-based statistical despeckling of SAR images," IEEE Transactions on Geoscience and Remote Sensing, vol. 42, no. 4, pp. 711–721, Apr. 2004.

[122] H. Xie, L. Pierce, and F. Ulaby, "SAR speckle reduction using wavelet denoising and markov random field modeling," IEEE Transactions on Geo science and Remote Sensing, vol. 40, pp. 2196–2212, Oct. 2002.

[123] M. C. Mihçak, I. Kozintsev, K. Ramchandran, and P. Moulin, "Low complexity image denoising based on statistical modeling of wavelet coefficients," IEEE Signal Processing Lett., vol. 6, pp. 300–303, Dec.1999.

[124] H. Xie, L. Pierce, and F. Ulaby, "Despeckling SAR images using a low complexity wavelet denoising process," in Proceedings of IEEE International Geoscience and Remote Sensing Symposium, vol. 1, pp. 321–324, Nov. 2002.

[125] Argenti F, Alparone L., "Speckle removal from SAR images in the undecimated wavelet domain. IEEE Trans. On Geosci. Remote Sensing," vol. 40, no. 11, pp. 2363–2374, Nov. 2002.

[126] M. Dai, C. Peng, A. K. Chan, and D. Loguinov, "Bayesian wavelet shrinkage with edge detection for SAR image despeckling," IEEE Trans. Geosci. Remote Sens., vol. 42, no. 8, pp. 1642–1648, Aug. 2004.

[127] H. Zhong, J. Xu, and L. Jiao, "Classification based nonlocal means despeckling for SAR image," in proc. of SPIE, vol. 7495, Oct. 2009.

[128] C. Deledalle, L. Denis, and F. Tupin, "Iterative weighted maximum likelihood denoising with probabilistic patch-based weights," IEEE Transactions on Image Processing, vol. 18, no. 12, pp. 2661–2672, Dec. 2009.

[129] J. Polzehl and V. Spokoiny, "Propagation-separation approach for local likelihood estimation," Probability Theory and Related Fields, vol. 135, no. 3, pp. 335–362, 2006.

[130] S. Parrilli, M. Poderico, C. V. Angelino, and L. Verdoliva, "A nonlocal SAR image denoising algorithm based on LLMMSE wavelet shrinkage," IEEE Transactions on Geo science and Remote Sensing, vol. PP, pp. 1–11, 2011.

[131] Gerardo Di Martino, Mariana Poderico, Giovanni Poggi, Daniele Riccio Luisa Verdoliva, "Benchmarking Framework for SAR Despeckling", IEEE Trans. Geo. And Rem. Sen, vol. 52, no. 3, March 2014

[132] Tang, L.L., Jiang, P., Dai, C.D., Thomas, J.J, "Evaluation of smoothing filters suppressing speckle noise on SAR images," Remote Sens. Environ., China, vol. 11, no. 3, pp. 206–211, 1996.

[133] F. Sattar, L. Floreby, G. Salomonsson, and B. Lovstrom, "Image enhancement based on a nonlinear multiscale method," IEEE Trans. Image Process., vol. 6, no. 6, pp. 888–95, Jan. 1997.

[134] Z. Wang, A. C. Bovik, H. R. Sheikh, and E. P. Simoncelli, "Image quality assessment: From error visibility to structural similarity," IEEE Trans. Image Process., vol. 13, no. 4, pp. 600–612, Apr. 2004.

[135] W. K. Pratt, Digital Image Processing. New York, NY, USA: Interscience, 1978.

[136] J. S. Lee, I. Jurkevich, P. Dewaele, P. Wambacq, and A. Oosterlinck, "Speckle filtering of synthetic aperture radar images: A review," Remote Sens. Rev., vol. 8, no. 4, pp. 313–340, Jan. 1994.

[137] H. Feng, B. Hou, and M. Gong, "SAR image despeckling based on local homogeneous-region segmentation by using pixel-relativity measurement," IEEE Trans. Geosci. Remote Sens., vol. 49, no. 7, pp. 2724–2737, Jul. 2011.

[138] R. D. Nowak and R. G. Baraniuk, "Wavelet-based transformations for nonlinear signal processing," IEEE Trans. Signal Process., vol. 47, no. 7, pp. 1852–1865, Jul. 1999.

[139] C. P. Rosiene and T. Q. Nguyen, "Tensor-product wavelet vs. Mallat decomposition: A comparative analysis," in Proc. IEEE Int. Symp. Circuits and Systems, Orlando, FL, pp. 431–434, Jun. 1999.

[140] J. E. Bresenham, "Algorithm for computer control of a digital plotter," IBM Syst. J., vol. 4, no. 1, pp. 25–30, 1965.

[141] J. D. Foley, A. V. Dam, S. K. Feiner, and J. F. Hughes, "Computer Graphics" Principles and Practice," Reading, MA: Addison-Wesley, 1990.

[142] T. S. Chan and R. K. K. Yip, "Line detection algorithm," in Proc. IEEE Int. Conf. Pattern Recognition, vol. 2, pp. 126–130, 1996.

[143] J. H. Conway and N. J. A. Sloane, "Sphere Packings, Lattices and Groups," New York: Springer, 1998.

[144] M. Vetterli and J. Kovačević, "Wavelets and Subband Coding," Englewood Cliffs, NJ: Prentice-Hall, 1995.

[145] G. Wackersreuther, "On two-dimensional polyphase filter banks," IEEE Trans. Acoust., Speech, Signal Processing, ASSP, vol. 34, no. 1, pp. 192–199, February 1986.

[146] D. Jayachandra and A. Makur "Directional Variance: A Measure to Find the Directionality in a Given Image Segment," Proc. of IEEE Int. Symp. on Circuits And Systems, pp. 1551-1554, 2010.

[147] G. P. Nason, "Wavelet shrinkage using cross validation," J. Roy. Stat. Soc. B, vol. 58, pp. 463–479, 1996.

[148] I. M. Johnstone and B.W. Silverman, "Wavelet threshold estimators for data with correlated noise," J. Roy. Stat. Soc. B, vol. 59, pp. 319–351, 1997.

[149] M. Jansen and A. Bultheel, "Multiple wavelet threshold estimation by generalized cross validation for images with correlated noise," IEEE Trans. Image Process., vol. 8, no. 7, pp. 947–953, Jul. 1999.

[150] A. M. Uso, F. Pla, J. M. Sotoca, and P. Garcia-Sevilla, "Clustering-based hyper spectral band selection using information measures," IEEE Trans. Geosci. Remote Sens., vol. 45, no. 12, pp. 4158–4171, Dec. 2007.

[151] H. Maître, "Processing of Synthetic Aperture Radar Images," London, U.K.: Wiley Publishers, 2008.

[152] www.sandia.gov/RADAR/imagery.htm

[153] M. A. T. Figueiredo, R. D. Nowak, "Wavelet-based image estimation: An empirical Bayes approach using Jeffrey's non-informative prior," IEEE Trans. Image Processing, vol. 10, no. 9, pp. 1322–1331, 2001.

[154] A. Hyvarinen, "Sparse code shrinkage denoising of non Gaussian data by maximum likelihood estimation," Neural Comput., vol. 11, no. 7, pp. 1739–1768, Oct. 1999.

List of Publications

1. Journals Papers

1.1 Sethunadh R & Tessamma Thomas, 'Spatially Adaptive Image Denoising using Interscale Dependence in Directionlet Domain', *Journal on Image Processing, IET (UK)*, May 2014, Accepted

1.2 Sethunadh R & Tessamma Thomas, 'Spatially adaptive despeckling of SAR image using bivariate thresholding in directionlet domain', *Electronics Letters*: 4th January 2014 Vol. 50 No. 1: Available in IEEE Explorer

1.3 Sethunadh R & Tessamma Thomas, 'Spatially Adaptive Image Denoising using Undecimated Directionlet Transform', *International Journal of Computer Applications* (0975 – 8887) Volume 84 – No 11, Dec. 2013: Selected as Editors' Choice paper for the issue

1.4 Sethunadh R & Tessamma Thomas, 'SAR image despeckling using adaptive multiscale products thresholding in directionlet domain', *Electronics Letters:* 29th August 2013 Vol. 49 No. 18: Available in IEEE Explorer

1.5 Sethunadh R & Tessamma Thomas, 'SAR image despeckling in directionlet domain based on edge detection', *Electronics Letters:* 14th March 2013 Vol. 49 No. 6: Available in IEEE Explorer

1.6 Sethunadh R & Tessamma Thomas, 'Image Denoising Using SURE-Based Adaptive Thresholding In Directionlet Domain', *Signal & Image Processing: An International Journal (SIPIJ)* Vol.3, No.6, December 2012

1.7 Sethunadh R & Tessamma Thomas, 'Locally Adaptive De-Speckling of SAR Image using GCV Thresholding in Directionlet Domain', *International Journal of Computer Applications* (0975 – 8887) Volume 60– No.17, Dec 2012

1.8 Sethunadh R & Tessamma Thomas, 'Image Denoising Based On Adaptive Spatial Segmentation and Correlation in Directionlet Domain', *Int. Journal of Computer Vision & Robotics*, Inderscience Publishers: Communicated.

1.9 Sethunadh R & Tessamma Thomas, 'SAR image Despeckling based on Laplacian-Gaussian modelling of directionlet coefficients', *Submitted to an international Journal.*

2. Conference Paper

2.1 Sethunadh R & Tessamma Thomas, 'Directionally Adaptive Despeckling of SAR Image Using Interscale Dependence', *International Conference on Recent Advances in Computational Systems Proceedings of IEEE RAICS-2013* Dec 19-21, 2013, Trivandrum, India. Available in IEEE Explorer

Resume of Author

Sethunadh
Scientist/Engineer-SF
Head, Baseband Telemetry Systems Section
QDTE/Systems Reliability
Vikram Sarabhai Space Centre
ISRO, Trivandrum

Phone: 9496820044
E mail: r_sethunadh@vssc.gov.in

EDUCATION

Course	Year	University	Institution	Class
Ph D	Currently pursuing	Cochin University of Science & Technology (CUSAT)	Department of Electronics, CUSAT	
M Tech Digital Electronics	2005-2007	Cochin University of Science & Technology (CUSAT)	Department of Electronics, CUSAT	First Rank with CGPA of 9.5 out of 10
B Tech Electronics & Communication	1990-1994	University of Kerala	T K M College of Engineering, Kollam.	First class with distinction

WORK EXPERIENCE
1. Defence Research & Development Organisation (DRDO), CEMILAC, Bangalore Employed as **Scientist 'B'** during Dec 1995 to Oct 1997. • Airworthiness certification of avionics packages of fighter planes. • Involved in the development of automatic test system for Accident Data Recorder for LCA.
2. Indian Space Research Organisation (ISRO), Vikram Sarabhai Space Centre, TVM Employed as **Scientist /Engineer** since Oct 1997. • Developed automatic test systems for launch vehicle avionics • Generated test & evaluation plans • Carried out qualification and acceptance tests of avionics packages for launch vehicles **Holding the position of Head, Baseband Telemetry System Section** since March 2011 Managing the Automatic test system development and test and evaluation activities of power system packages, baseband telemetry packages and sensors for launch vehicles.
AWARDS/ HONOURS
• ISRO team award 2007 for realization of Advanced Avionics Module.
• Prof. K G Nair Endowment award for securing highest mark in M. Tech from Department of Electronics at CUSAT during the year 2006-07
• Finalist in international paper contest on best applications of measurement and automation in Aerospace/Defence category conducted by M/s National Instruments USA, in Aug 2001.

PATENT & PUBLICATIONS
A patent (Patent No. 251042) was granted by Indian patent office in April 2007 to the invention entitled 'A system and method for calibration of signal processing electronics' Published more than 17 papers in international and national journals

MEMBERSHIP
Member, Institution of Electrical & Electronic Engineers (IEEE) Life member, Society for Aerospace Quality & Reliability (SAQR)

AREAS OF INTEREST
Image Processing, Signal Processing, Test Automation and Virtual Instrumentation

PERSONAL INFORMATION
Date of birth : 25 March 1973 Permanent Address : 'SAIJ', Mathilil P O, Perinad, Kollam, Kerala- 691601

REFERENCES	
Dr. Tessamma Thomas Professor Department of Electronics Cochin University of Science & Technology (CUSAT)	**Dr. P P Mohanlal** Director ISRO Inertial Systems Unit Vikram Sarabhai Space Centre